Rear Surface passivation for High Efficiency Silicon Solar Cells

Alban Jean-Joël PEREAU

A dissertation submitted for the degree of

Doctor of Philosophy

Heriot-Watt University

School of Engineering and Physical Sciences

<June> <2013>

Abstract

In order to adapt laser grooved buried contact (LGBC) solar cells to a thinner silicon substrate than usually used, we have investigated the reduction of charge carrier loss at the rear surface of p-type silicon wafers by plasma-enhanced chemical vapour deposition (PECVD) of a-Si:H and SiN_x films. The efficiency of these passivating films has been measured via the surface recombination velocity (SRV) which is wanted as low as possible. The SRV values of our samples have been compared with the expected theoretical values given by the Shockley-Read Hall (SRH) recombination model. SRH theory is a description of the electron-hole recombination via defects inducing energy levels in the forbidden bandgap. This way of recombination is the predominant mode for semiconductors with indirect bandgaps like silicon. Two influential factors in regard to SRV can be understood from this theory. These two factors are the electron to hole capture cross section ratio and the fixed charge density Q_f at the silicon substrate / film interface. These two factors induce an asymmetry between the electron and the hole recombination and are responsible for the excess charge carrier concentration dependence of the SRV. In other words, the SRV depends on the illumination intensity. In this work, the SRV has been measured for an excess charge carrier injection level in the 1.10^{13}-1.10^{16} cm^{-3} range and then it has been compared with the theoretical value given by the SRH theory in order to determine the fixed charge density and have an estimation of the defect characteristics including its density. Simulations of LGBC cells under one sun illumination have then been performed using the PC1D5 software. The measured SRV value corresponding to one sun has been integrated in the simulation and the expected efficiency has been extracted as a function of the wafer thickness. It results from this study that 150µm LGBC solar cells can theoretically have an efficiency of 19% by the integration of passivating SiN_x films. A second aspect of this work is an effort to understand the relation between the passivating film quality, structure, and the PECVD parameters during deposition. The films have been characterized principally by ellipsometry and also by XPS. All of our SiN_x films are located in the Si-rich region ($x<1.1$) and the passivating quality increases with x.

Dedication

To my wife and my family,

Acknowledgements

Firstly, I would like to express my gratefulness to Professor John I.B. Wilson my thesis director, for his concern. He gave a great attention on this work and has made it pleasant. Our discussions enable to highlight some interesting aspects and at the same time he let me the freedom on the way to do it. I would like to thank my supervisor Gudrun Kocher with whom we spent time on doing the experiment, who introduced me to the PECVD technique always with a certain sense of humour. I would like also to thank my supervisor professor Bryce S. Richards who gave me the opportunity to do this thesis. Finally, I would like to thank the National Research Energy Center (NaREC) who is at the origin of this collaboration with Heriot Watt University, and particularly Dominique Morrison.

Table of contents

List of Publications

[1] Development of Laser Fired Contact (LFC) Rear Passivated Laser Groove Buried Contact (LGBC) Solar Cells Using Thin Wafers ,
D.J. Morrison S.E. Devenport , A. Cole, K.C. Heasman, G. Kocher, A. Pereau, B.S. Richards, J.Wilson, Conference C93 of the Solar Energy Society, Heriot-Watt University, Edinburgh, 6-8 April 2011

[2] Rear surface passivation of Si solar cells by plasma deposited dielectric films
A. Pereau, G. Kocher, B.S. Richards, D. Morrison, J.I.B. Wilson, Conference C91 of the Solar Energy Society, Chilworth Manor, University of Southampton 24-26 March 2010

[3] Development of Laser Fired Contact (LFC) Rear Passivated Laser Groove Buried Contact (LGBC) Solar Cells Using Thin Wafers ,
D. Morrison, A. Cole, S. Devenport, J. Delve, K. Heasman, G. Kocher, A. Pereau, B. Richards, J.Wilson**,** Conference C90 of the Solar Energy Society, Glyndwr University, Wales UK 1-3 April 2009

POSTERS

[1] a-Si:H and Alloy Thin Film Deposition by PEVCD for Rear surface passivation of Si Solar Cells
A. Pereau, G. Kocher, B.S. Richards, J.I.B. Wilson, D. Morrison, Conference: New Generation: Powering the future, Heriot-Watt University, 2 February 2011

[2] Plasma deposited dielectrics for rear surface passivation of Si solar cells
A. Pereau, G. Kocher, B.S. Richards, D. Morrison, J.I.B. Wilson, TPW Glasgow, 13-15 December 2009.

Symbol	Description	Unit
E_d	Defect energy level	eV
Δ	Phase difference between the parallel and orthogonal electric field component	Deg
Δn	Excess electron concentration	cm^{-3}
Δp	Excess hole concentration	cm^{-3}
μ_n	Electron mobility	$cm^2.V^{-1}s^{-1}$
μ_p	Hole mobility	$cm^2.V^{-1}s^{-1}$
AM 1.5	Solar irradiance function versus wavelength for one sun intensity through the atmosphere with an incidence angle of 48.2°	$W.cm^{-2}$
B	Radiative constant	$cm^{-3}.s^{-1}$
B_p	Magnetic field component parallel to the incident plane	T
B_r	Magnetic field component orthogonal to the incident plane	T
C	Resonance peak broadness	eV
C_a	Rate constant of hydrogen abstraction	$cm^{-3}.s^{-1}$
C_{Hyd}	Hydrogen concentration in the film	cm^{-3}
d	Layer thickness	cm
D	Defect energy level density	$cm^{-3}.eV^{-1}$
D_n	Electron diffusion coefficient	$cm^2.s^{-1}$
D_p	Hole diffusion coefficient	$cm^2.s^{-1}$
E	Electric field	$V.cm^{-1}$
E_a	Activation energy	eV
E_B	Binding energy	eV
E_c	Lowest energy level of conduction band	eV
E_F	Fermi level	eV
E_{FN}	Energy of electron quasi-Fermi level	eV
E_{Fp}	Energy of hole quasi-Fermi level	eV
E_G	Energy band gap	eV
E_i	Energy corresponding to mid-gap	eV
E_K	Kinetic energy	eV
e_n	Electron emission probability	
E_{n0}	Resonance energy	eV
E_p	Electric field component parallel to the incident plane	$V.cm^{-1}$
e_p	Hole emission probability	
E_s	Electric field component orthogonal to the incident plane	$V.cm^{-1}$
E_t	Transition energy	eV
E_u	Urbach absorption tail	eV
E_V	Highest energy level of valence band	eV
F	Flux of photon	$cm^{-2}.s^{-1}$

Symbol	Description	Unit
f	Fermi statistics	
G_n	Electron generation rate	$cm^{-3}.s^{-1}$
G_p	Hole generation rate	$cm^{-3}.s^{-1}$
I	Current	mA
I_0	Saturation current (dark current)	mA
I_L	Photogenerated current	mA
I_{SC}	Short circuit current	mA
J	Current density	$mA.cm^{-2}$
J_L	Photogenerated current density	$mA.cm^{-2}$
J_n	Electron current density	$mA.cm^{-2}$
J_p	Hole current density	$mA.cm^{-3}$
J_S	Saturation current density	$mA.cm^{-2}$
k	Imaginary part of refractive index	
k_H	Spring constant	$kg.s^{-2}$
L	Distance between the positive and negative charge barycentre in a dipole	m
L_n	Electron diffusion length	cm
L_p	Hole diffusion length	cm
m_e	Electron mass	kg
MW	Micro Wave	GHz
n	Electron concentration in the conduction band	cm^{-3}
n_1	Contribution of defects to electron concentration in the conduction band	cm^{-3}
Na	Acceptor concentration	cm^{-3}
N_C	Energy level density in the conduction band	cm^{-3}
N_{crit}	Critical value density	cm^{-3}
Nd	Donor concentration	cm^{-3}
n_d	Electron concentration at the edge of the depletion region on the p-region	cm^{-3}
n_e	Electron concentration in the plasma	m^{-3}
n_f	Real part of refractive index	
N_H	Concentration of sites bonded with H on the film surface	cm^{-3}
n_i	Electron concentration in the conduction band for an intrinsic semiconductor	cm^{-3}
n_{p0}	Electron concentration in the p-region at equilibrium	cm^{-3}
N_s	Sticking site concentration on the film surface	cm^{-3}
N_V	Energy level density in the valence band	cm^{-3}
P	Electric polarisation	$C.m^{-2}$
p	Hole concentration in the valence band	cm^{-3}
p_1	Contribution of defects to hole concentration in the valence band	cm^{-3}
p_d	Hole concentration at the edge of the depletion region on the p-region	cm^{-3}

Symbol	Description	Unit
p_{n0}	Hole concentration in the n-region at thermal equilibrium	cm^{-3}
q	Elementary charge (1.6x10-19 C)	C
Q_f	Fixed charge density at the interface	$C.cm^{-2}$
Q_{si}	Charge density induced into the silicon substrate by interface charge density	$C.cm^{-2}$
R	Reflection coefficient	
R_p	Parallel resistance (shunt resistance)	ohm
r_p	Fresnel reflection coefficient (incident plane)	
R_p	Reflectance related to the parallel component of the electric field	
R_S	Series resistance	ohm
r_s	Fresnel reflection coefficient (othogonal plane)	
R_s	Reflectance related to theprthogonal component of the electric field	
S	Surface recombination velocity	$cm.s^{-1}$
S_n	Electron surface recombination velocity	$cm.s^{-1}$
S_n	Electron surface recombination velocity at very high injection level	$cm.s^{-1}$
S_p	Electron surface recombination velocity	$cm.s^{-1}$
S_p	Electron surface recombination velocity at very high injection level	$cm.s^{-1}$
SRV	Surface Recombination Velocity	$cm.s^{-1}$
t_p	Fresnel transmission coefficient (incident plane)	
t_s	Fresnel transmission coefficient (orthogonal plane)	
U	Net recombination rate	$cm^{-3}.s^{-1}$
U_e	Net recombination rate of electron	cm^{-3}
U_{ec}	Electron capture transiton rate	$cm^{-3}.s^{-1}$
U_{ee}	Electron emission transition rate	$cm^{-3}.s^{-1}$
U_{eh}	Hole emission transition rate	$cm^{-3}.s^{-1}$
U_h	Net recombination rate of hole	cm^{-3}
U_{hc}	Hole capture transition rate	$cm^{-3}.s^{-1}$
U_n	Electron recombination rate	$cm^{-3}.s^{-1}$
U_p	Hole recombination rate	$cm^{-3}.s^{-1}$
U_{rad}	Radiative recombination rate	$cm^{-3}.s^{-1}$
V	Electric potential difference between n and p-region	V
V_b	Bias voltage	V
V_{bi}	Built-in potential	V
VHF	Very High Frequency	MHz
V_{OC}	Open circuit voltage	V
V_{pp}	Peak to peak voltage	V
v_{sat}	Saturation velocity	$cm.s^{-1}$
v_{th}	Thermal velocity	$cm.s^{-1}$

Symbol	Description	Unit
W	Wafer thickness	cm
W_{dep}	Depletion region width	cm
x	Position	cm
α	Absorption coefficient	cm^{-1}
Γ_v	Viscosity coefficient	s^{-1}
δ	Optical path difference	cm
δ_p	Phase of the parallel electric field component	
δ_s	Phase of the orthogonal electric field component	
ε	Dielectric permittivity	$F.cm^{-1}$
ε_{Si}	Dielectric constant of silicon	$F.cm^{-1}$
θ_B	Brewster angle	rad
θ_{SiH3}	Concentration of SiH3 radical at the film surface	cm^{-3}
λ	Wavelength	nm
λ_0	Wavelength in vacuum	nm
μ	Dipole momentum	C.m
ν	Photon frequency	Hz
ν_c	Collision frequency	MHz
ρ	Ratio between parallel Fresnel coefficient and orthogonal Fresnel coefficient	
σ	Full width at half maximum of defect density	eV
σn	Electron capture cross section	cm^{-2}
σ_p	Hole capture cross section	cm^{-2}
τ	Lifetime of charge carrier	ms
τ_b	Bulk lifetime	ms
τ_{eff}	Effective life time	ms
τ_n	Lifetime of electron	ms
τ_p	Lifetime of hole	ms
τ_{SRH}	Lifetime of minority charge carrier for SRH recombination	ms
ϕ_n	Electric potential of the n-region	V
ϕ_p	Electric potential of the p-region	V
χ	Electronic susceptibility	eV
ψ	Electric potential of intrinsic level	V
ψ	Angle between the axis orthogonal to incident plane and the electric field axis	
ψ_S	Surface potential	V
ω	Angular velocity	$rad.s^{-1}$
ω_p	Plasma frequency	MHz
A	Dielectric function amplitude	

ACRONYM AND ABBREVIATION	Definition
a-Si:H	Hydrogenated amorphous silicon
BSF	Back Surface Field
C_H	Rate constant of hydrogen desorption
c-Si	Crystalline silicon
CVD	Chemical Vapour Deposition
Cz	Czochralski
EMA	Effective Medium Approximation
FF	Fill factor
FWHM	Full Width at Half Maximum
FZ	Float-Zone
LGBC	Laser Groove Buried Contact
PECVD	Plasma Enhanced Chemical Vapour Deposition
PV	Photovoltaic
RF	Radio Frequency
SiN_x	Hydrogenated silicon nitride
SRH	Shockley Read Hall
XPS	X-ray Photoelecton Spectroscopy

Chapter 1

<INTRODUCTION>

The work for this thesis took place in the context of a project of EPSRC/TSB and the National Renewable Energy Center (NaREC) of the U.K for contributing to the improvement of the photovoltaic (PV) technology based on silicon solar cells. Indeed Photovoltaic technologies are grouped into three categories referred to as 1st, 2nd and 3rd generation in regards with their chronological apparition. The 1st is the technology based on crystalline silicon (c-Si) wafer, the 2nd generation is based on better material utilization concept using thin film absorbers and the 3rd generation is based on better utilization of solar spectrum using multi-junction or tandem solar cells. This category also includes novel PV technology like concentrating PV and organic PV. The 1st generation itself can be divided into 2 groups which are monocrystalline and multicrystalline silicon. The best laboratory PV efficiency for 1st generation has been obtained with monocrystalline wafer and is equal to 24.7 % [1.1] whereas laboratory efficiency is 20.3% for multicrystalline wafer [1.2]. However it has to be recalled for a same technology there is actually 3 different PV efficiencies: the module, the commercial cell and the record efficiencies. Module efficiency is lower than the commercial cell efficiency which is itself lower than the record efficiency (or best laboratory efficiency). For monocrystalline the range of commercial cell efficiency is 13-19% and for multicrystalline 12-15%. The c-Si based technology provides the high efficiency but the production cost is still high compared with other technologies. The efforts for improving this 1st generation consist in increasing the efficiency and lowering the manufacturing cost mainly by using thinner c-Si-wafer. The 2nd generation is based on thin film with thickness around1µm whereas for 1st generation the wafer thickness is usually 300-500µm. Thin film based solar cells are divided in four sub-technologies. The first one is based on amorphous silicon (a-Si) material. The best laboratory efficiency is 10.1% [1.3] whereas the commercial cell efficiency only ranges on 4-8%. However, the lower efficiency is balanced by the very low manufacturing cost. The second ones are solar cell based on multijunction a-Si/µc (nc)-Si or and a-Si/ µc(nc)-SiGe where µc(nc) means microcrystalline (or nanocrystalline). Using two different materials as an active layer for PV generation allows absorbing a wider range of the solar spectrum. The best laboratory efficiency is 13.4 % [1.3] whereas module efficiencies are between 6.5-9%. The 3rd one is based on cadmium-telluride (CdTe) films with a relatively low manufacturing cost and relatively high module efficiency

over 11%. For this technology the highest record laboratory efficiency is 19.6% after a high deposition temperature which increases the manufacturing cost. The fourth is the solar cell based on heterojunction of copper-indium-gallium-selenide (CIGS) films. This technology corresponds to the highest thin film technology efficiency with a laboratory efficiency of 20.4% and 13-14% for commercial solar cell. However manufacturing process is more complex and costlier than other thin film technologies. The 3rd generation includes multijunction solar cells based on III-V materials viz GaAs and its alloys with a triple junction have achieved more than 38% efficiency already. This category may also include all of the innovating process like concentrating PV (CPV), organic solar cell and advanced inorganic thin film. CPV technology focuses the direct sunlight on high efficiency solar cell by using optical tracking concentrator. Efficiency record is 27.6 % [1.3] with Si solar cells for concentration of 92 suns and 44.4% [1.3] with thin-film technology for high concentration of 302 suns intensity. The second main technology for 3rd generation is dye-sensitised solar cells (DSSC). Laboratory record efficiency for liquid junction based cells is 11.9% [1.3] for DSSC and commercial efficiency only around 4%. In a recent breakthrough around 16% efficient solid state DSSCs have been developed which are based on the perovskite absorber based materials [1.4]. On the other hand, the organic solar cells have also achieved about 10% efficiency for single junction. Another disadvantage is the bad stability of organic solar cell over time but this disadvantage is relatively compensated by a very low manufacturing and material cost.

The aims of EPSRC/TSB and NaREC project was to produce low-cost, high-efficiency crystalline silicon (c-Si) solar cells based on the laser groove buried contact (LGBC) process with a reduction of the silicon wafer thickness compared to the standard LBGC solar cells [1.5-1.9]. Achieving this goal requires much higher quality rear surface passivation than the aluminium BSF used in classical LGBC cells. Indeed, the relative effect of interface recombination is more important with a low thickness because the interface thickness remains the same whereas the wafer thickness decreases. It was proposed that this improvement be provided by plasma enhanced chemical vapour deposition (PECVD) of thin-film silicon alloys. The choice of plasma technology was made to limit the production cost since it allows low temperature deposition, in the range 200 – 400°C. Finally the cost should be 30% lower than standard LGBC standard solar cells. Two kinds of material have been deposited for investigating the passivation effect, hydrogenated amorphous silicon (a-Si:H) and silicon nitride (SiN_x). Indeed with

these films a successful commercial process would be available as shown by previous study on PECVD passivation for instance by the works of Vetter [1.10] who obtained a SRV of 60 cm/s with a-Si:H, Lauinger [1.11] or Kintzel [1.12] who obtained a SRV of respectively 4 cm/s and 32 cm/s with SiN_x. Passivation with SiN_x has also been studied by authors like Aberle [1.13], Kerr [1.14] or Schmidt [1.15].

Surface passivation quality is improved if the number of surface defects generating energy levels within the bandgap - and thus losses of charge carriers due to recombination - is lower. The effect of the deposition of the mentioned films is to remove a part of these inter-gap energy levels. The PEVCD system used in Heriot-Watt University has the convenience of allowing work both with RF, VHF and microwave frequencies. This presents the advantage of working at different frequency ranges with the same system and thus limiting variations in the other conditions, since it is known that deposited film quality is closely dependent on the system itself. The first aim of this study was to study the effect of PECVD deposition at different frequencies in the VHF range. However, after an extensive literature survey, it appears that the adaptation required for converting the system to VHF frequencies (like plasma diagnostic for impedance calculation and the building of a matching network) [1.16-1.18] was too time consuming and we decided to limit the study to 13.56 MHz RF and 2.45 GHz frequencies.

In the first step, we concentrated on the sample production and the optimisation of PECVD conditions in order to reach a high passivation quality as fast as possible. The choice of the PECVD parameters was closely related to what was found in the literature and the measurement of the sample quality was based on standard industrial methods. In a second stage, questions appeared on the relevance of this measurement method in the particular conditions of this work. This led us to study the principles of surface passivation measurement. Since measurement is actually the result of the probing of a sample, it is interesting to understand how results are produced by interaction of the probe and the sample. Moreover, the measurement methods are calibrated to give a correct result only if the conditions of measurement are suitable, with some previous assumptions. Therefore a correct understanding of the method's background can allow extension to other cases.

This thesis is divided into 7 chapters including introduction and conclusion. The second chapter describes the photovoltaic process. From the fundamental principle of charge conservation expressed by the continuity equation relating the charge carrier generation and recombination rates and the current density, together with the diffusion process relating current density with charge carrier concentration, the short circuit current and open circuit voltage characterising photovoltaic efficiency are extracted. The solar cell structure as an applied device of these processes is described with a focus on the improvement brought by the LGBC technology. Since an aim of this work was to reduce the wafer thickness without a loss of efficiency, by improving the passivation quality, simulations including LGBC cell parameters have been done in order to determine the evolution of efficiency with wafer thickness for different rear surface recombination rates. Surface recombination rate is determined by a parameter that is surface recombination velocity (SRV). Both optimal wafer thickness and maximum SRV required for keeping the same efficiency as for standard thickness have been deduced from simulation. Thus this chapter establishes the main objective.

After having highlighted the necessity of achieving low SRV for keeping a good efficiency, the notion of SRV is developed in the third chapter. It begins by a simple description of the interaction between electrons and holes in a direct bandgap semiconductor and the way they recombine together. Then the theory of Shockley, Read and Hall is explained regarding carrier loss in indirect bandgap semiconductors – which is the case of silicon - where recombination occurs mainly by recombination via a single intra-bandgap energy level defect. This leads to the expression of the relation linking some of the sample characteristics and charge carrier density with the recombination rate and the SRV. Photogenerated charge carrier density, called more simply "injection level", is a value which varies with the light intensity whereas the sample characteristics are fixed for a given sample; then the SRV is expressed as a function of the injection level. Numerical methods are then used to include in this theory the effect on SRV of surface charge and to extend it to a quasi-continuum of energy levels. This chapter also describes the method and the industrial device used for measuring the SRV. However since the determination of SRV from carrier lifetime supposed some conditions that some of our samples do not fulfil, the method has been adapted for extracting the SRV from the calculation of the recombination rate instead of lifetime. Eventually some of our samples' characteristics have been deduced by fitting the experimental SRV data with the results of the simulation. The two main characteristics are the defect density

and the surface charge density. The defect density is a mark of the film quality whereas the surface charge density acts as a factor increasing or decreasing the surface recombination at low injection level.

After having determined a SRV value to reach for the injection level corresponding to the real processing conditions of the solar cell, chapter 3 shows that different causes can be the reason for the same value of SRV. Moreover when a given sample parameter has a positive effect on the SRV for one type of sample, it can have a negative effect for another. For instance a fixed charge which lowers the SRV for high resistivity samples can increase it for low resistivity samples. Thus the deposition of a film with the same characteristics will result in better passivation in the former case while worse in the latter case.

The fourth chapter describes spectroscopic ellipsometry which is a method for extracting the optical characteristics of a thin film and which allows one to determine a model of this film. It starts with a recall of electromagnetic waves and the way they interact with a dielectric. Then we introduce the notion of polarisation and its modification after passing through several media. From these considerations, equations are established between polarisation changes and complex refractive indices of these media. Then the principle of ellipsometry measurement is explained as well as the dielectric function used to determine the optical characteristics and a model. A numerical method has been used to simulate the results from a given model and compare it with experimental values of our samples. Although commercial software was included with the measurement device, we have developed a code based on the mentioned equations. This presents the advantage to do manipulation directly into the equation whereas software is limited to the changes of parameters. Eventually the simulations have been fitted with experimental results. However the accurate modelling of our films would require a whole thesis and only the films closest to standard structures are accurately modelled. Despite this weakness, the positive point is that those correctly modelled films also coincide with the best passivation quality.

This chapter ends with a part regarding X-ray photoelectron spectroscopy (XPS) because this technique adds information to the film structure interesting for completing the ellipsometry interpretation. The negative point of this latter part is that due to difficulty for access to XPS, the measurements have only been done during the mid

period of our sample production whereas the correctly fitted sample matches the last produced samples.

After considering the structure of the sample in the third and fourth chapter, the fifth chapter treats the passivating film production by PECVD, explaining the way to make an adequate structure. Firstly, the steps of the PECVD process and the main phenomena occurring in each of these steps are described. The aim of this chapter is to describe the effects of the external conditions on the film structure and to find the optimal set of parameters for having a structure corresponding to the best passivating film. Whereas all of the previous chapters end with a comparison with experimental results, this chapter is closed only with a description of the PECVD system.

Indeed experimental results of this chapter concern characterisation of the film in all of the aspects described in the previous chapters and for this reason they are interpreted in chapter 6 which is a synthesis of the thesis. This last chapter ends with a photovoltaic efficiency simulation, seen in the second chapter, including the experimental SRV and shows that efficiency can remain at the same level when reducing the wafer thickness, when SiN_x films are deposited on Cz 1 ohm.cm wafers with the optimal conditions.

BIBLIOGRAPHY CHAPTER 1

[1.1] J. Zhao *et al*, 24·5% Efficiency silicon PERT cells on MCZ substrates and 24.7% efficiency PERL cells on FZ substrates, Prog. Photovolt: Res.Appl., **7** (6), 471-4, (1999).

[1.2] O. Schultz *et al*., Multicrystalline Silicon Solar Cells Exceeding 20 % Efficiency, Prog. Photovolt: Res. Appl., **12** (7), 553-8, (2004).

[1.3] M.A. Green *et al*. ,Solar cell efficiency tables (version 42), Prog. Photovolt: Res. Appl. 21 827–837 (2013)

[1.4] H.M. Upadhyaya *et al.* , Recent progress and the status of dye-sensitised solar cell (DSSC) technology with the state-of-art conversion efficiencies, Solar Energy Materials and Solar Cells (2013) http://dx.doi.org/10.1016/j.solmat.2013.08.031

[1.5] A. Cole *et al.,* Front contact modelling of monocrystalline silicon laser grooved buried contact solar cells, 4th International Conference on Solar Concentrators for the Generation of Electricity or Hydrogen, Mar. 12-16, 2007, San Lorenzo de El Escorial, SPAIN.

[1.6] K.C. Heasman *et al.*, Development of laser buried contact solar cells for use at concentration factors up to 100x, 4th International Conference on Solar Concentrators for the Generation of Electricity or Hydrogen, Mar. 12-16, 2007, San Lorenzo de El Escorial, SPAIN.

[1.7] D. Morrison *et al.*, Development of Laser Fired Contact (CFC) Rear Passivated Laser Groove Buried Contact (LGBC) Solar cells Using Thin Wafers, International Solar Energy Society UK section conference C 90, 101-104 (2009)

[1.8] N.B. Mason *et al.,* The selection and performance of monocrystalline silicon substrates for commercially viable 20% efficient lid-free solar cells, 19th PVSEC, Paris, (2004)

[1.9] A. Cole et *al.,* Progress of the LAB2LINE Laser Grooved Buried Contact Screen Printed Solar Cells Hybrid p-type Monocrystalline Process, PVSAT 5 (2009)

[1.10] M. Vetter, Surface passivation by RF magnetron-sputtered silicon nitride films, Thin Solid Films 337, 118-122(1999)

[1.11]T. Lauinger, Record Low Surface Recombination Velocities on 1 ohm.cm p-silicon using Remote Plasma Silicon Nitride Passivation. Appl. Phys. Lett. 68 (9), 1996.

[1.12] W. Kintzel *et al.*, Efficient surface passivation by silicon nitride using a large area deposition system, 29th IEEE Photovoltaic Specialists Conf., New Orleans, USA (2002)

[1.13]A.G. Aberle, Overview on SiN surface passivation of crystalline, silicon solar cells, Solar Energy Materials & Solar Cells 65, 239-248(2001)

[1.14] 10] M.J. Kerr *et al.*, Simplified PERC solar cells passivated with PECVD silicon nitride, Glasgow, Scotland (2000)

[1.15] J Schmidt *et al.*, Highest-quality surface passivation of low-resistivity p-type silicon using stoichiometric PECVD silicon nitride, PVSEC 11^{th}, Technical digest of the 11^{th} international photovoltaic science and engineering conference, Sapporo, 581-582 (1999)

[1.16] I. Sumpono *et al.*,VHF-PECVD impedance matching network design for the fabrication of nanocrystalline silicon, J. Solid St. Sci and Technol. Letters 13, 260-265 (2006)

[1.17] C.Beneking, Power dissipation in capacitively coupled RF discharges, J.Appl. Phys. 68(9), 4461-4473 (1990)

[1.18] W.C. Tan *et al.*, Optical properties of amorphous silicon nitride thin-films prepared by VHF-PECVD using silane and nitrogen, J. Mater. Sci: Mater Electron 20, S15-S18(2009)

Chapter 2

<OPTIMISATION OF PHOTOVOLTAIC EFFICIENCY >

First of all a remark has to be made about the exponent notation used in the graphs in all of the chapters. Most of these graphs have been drawn with excel software which uses the notation 1.E±N for $1x10^{\pm N}$. Despite trying to fix this notation problem we realised that it required to implement an excel macro and in order to save time it has been decided to leave this notation.

The aim of rear surface passivation is to contribute to the optimisation of high efficiency solar photovoltaic cells. For understanding the relative importance of passivation it is first necessary to describe the mechanism of a solar cell and the optimal condition for converting solar energy into electric energy. In the ideal case the totality of solar energy would be converted into electric energy but this is not the case because of both fundamentals and technical reasons. We will describe the constraints which limit the photovoltaic (PV) conversion at different levels, from intrinsic constraints relating to the different factors which are involved in the photovoltaic process (solar radiation, intrinsic properties of the base material and their interaction), to the limitations due to the technology. This will allow understanding about important aspects of a high efficiency solar cell structure and show that although passivation is not one of the most important factors for having a good PV conversion it can make a significant difference in high efficiency solar cell optimisation.

2.1 General principles of a solar cell

When a photon from solar radiation is absorbed in a semiconductor material constituting the base of the solar cell (Si for instance), an electron-hole pair is generated if the photon energy is higher than the band gap energy of the semiconductor. Due to the asymmetric structure of the solar cell electrons and holes are spatially separated by an electric field and driven to an external circuit, providing electrical power. Charge carriers are lost by electron-hole recombination in the bulk, the front and the rear surface. This recombination process which opposes to electron-hole generation will be detailed in chapter 3 because of its central importance in this work. Although different types of solar cell exist, only P-N junction diode types have been considered for this study.

2.1.1 Carrier concentration in semiconductors

Due to quantum physics, each atom is defined by an atomic number and can be characterised by discrete electronic energy levels. When a large number of a given atom is assembled in a solid material, these discrete energy levels are differentiated due to Pauli principle and give bands of quasi-continuum energy. Each band corresponding to the initial energy level of the isolated atom is separated by a gap of forbidden energy which means that an electron cannot have energy with value between two energy bands. Since electrons follow Fermi distribution, only two electrons can have the same energy and the number of electrons in a band is limited [2.1]. At 0 K the electrons are distributed in a way that fills the lowest energy levels. The highest energy band at 0 K determines the electrical property. A conductor is a material where this band is not full and then electrons can flow easily between the free levels of this quasi-continuum energy band. On the other hand an insulator is a material where the highest energy band at 0 K is full and then there is no conduction of electrons. However if an electron absorbs an energy higher than the energy bandgap it can move to an upper band where it can move quasi freely. For this reason this latter band is called the conduction band while the highest full band is called the valence band. When an electron is excited from the valence band to the conduction band it leaves a vacancy in the valence band which is equivalent to a hole, positively charged, contributing to the total current. The edge of the valence band is the valence energy E_V and the edge of the conduction band is E_C. Therefore the energy bandgap E_G between the conduction and the valence bands is E_V-E_C. A semiconductor is an insulator at 0K but its energy bandgap is low enough to allow electrons into the conduction band at ambient temperature. This corresponds to energy bandgaps in the order of 1 eV like silicon which has a bandgap equal to 1.12 eV [2.2]. Although thermal energy corresponding to 300 K is only 0.025 eV, a few electrons occupy the conduction band due to Boltzmann statistics. Since an electron passing from the valence band to the conduction band leaves a hole in the valence band it results that for a pure silicon material or in other words intrinsic silicon, the electron concentration, n, in the conduction band is the same as the hole concentration, p, in the valence band and is equal to the intrinsic concentration n_i. This equality is broken when the silicon is doped with phosphorus or a boron atom concentration in order to add in the former case an electron for each phosphorus atom in the conduction band and in the latter case a hole in the valence band for each boron atom. Thermal equilibrium can be described in

three terms which are equilibrium of electron population in conduction band, of hole population in valence band and between the electrons and the holes in conduction and valence bands. Equations 2.1 and 2.2 synthesise this

$$n = n_i . e^{-\frac{E_i - E_F}{k.T}} \quad (2.1)$$

$$p = n_i . e^{-\frac{E_F - E_i}{k.T}} \quad (2.2)$$

The equilibrium between electrons and holes is implicit by the fact that the Fermi level is the same for both charge carriers:

$$n . p = n_i^2 \quad (2.3)$$

If the equilibrium between the bands is disturbed while equilibrium in conduction band and valence band is conserved, the Fermi levels of electrons and holes are not equal anymore and the population of electrons and holes respectively in the conduction and in the valence bands becomes:

$$n = n_i . e^{-\frac{E_i - E_{F_n}}{k.T}} \quad (2.4)$$

$$p = n_i . e^{-\frac{E_{F_p} - E_i}{k.T}} \quad (2.5)$$

2.1.2 P-N junction

This section will extract the three major factors which are necessary for determining the efficiency of PV conversion which are, the short circuit current I_{SC}, the open circuit voltage V_{OC} and the fill factor FF.

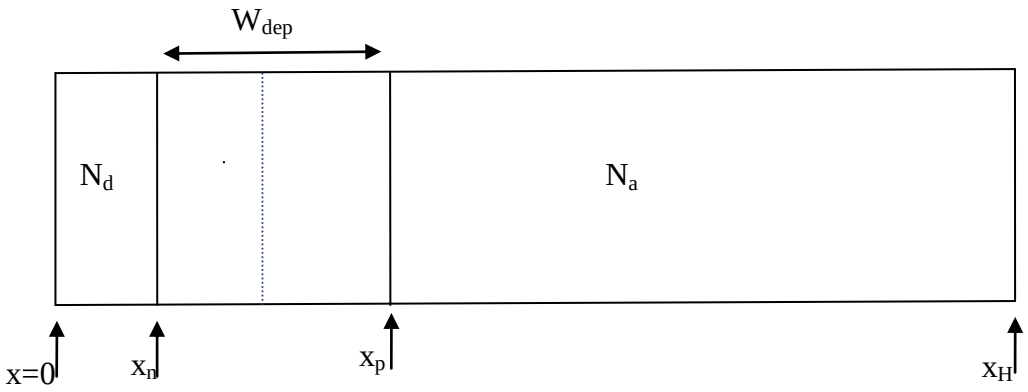

Figure 2.1 A schematic representation of a P-N junction exhibiting its space charge region spread across the bulk: In this figure the position x=0 corresponds to the front surface and $x=x_H$ to the rear surface. Region N corresponds to a doping with donors N_d and region P to a doping with acceptors N_a. The region from x_n to x_p is the depletion region.

Figure 2.1 represents a P-N junction, on this figure the position x = 0 corresponds to the front surface and $x = x_H$ to the rear surface of the cell. A P-N junction is the result of the contact between a p-type and an n-type semiconductor. These regions starts from x = 0 to x_p and $x = x_n$ to $x = x_H$ for respectively the n and the p region. The doping of the n and the p region are respectively N_d and N_a. The electron excess in the n-type region flows by diffusion toward the p-type region whereas the hole excess in the p-type region diffuses into the n-region. Since there is initially charge neutrality in both regions, the lack of electrons and hole respectively near n-region and p-region of the junction, leave a positive charge in the n-region and a negative in the p-region generating an electric field that opposes the diffusion. Equilibrium is reached when diffusion and drift are balanced. Thus, the electric field influence becomes lower as the position is far from the junction. Therefore three regions can be distinguished in a P-N diode: the n-region, the charge zone region (or depleted region in the approximation of abrupt junction) and the p-type region. The width of the depleted region, W_{dep} on figure 2.1 is actually several orders lower than the regions n and p. Outside the depleted region, the potential remains constant. The difference of potential between the n and p-regions is the built-in potential V_{bi} and only depends, at a given temperature, on the doping of n and p-regions, respectively N_d and N_a:

$$V_{bi} = \frac{k.T}{q}.\ln\left(\frac{N_a.N_d}{n_i^2}\right) \qquad (2.6)$$

From V_{bi}, the depletion width W in a semiconductor of permittivity ε can be determined:

$$W = \sqrt{\frac{2.\varepsilon}{q}.V_{bi}\left(\frac{1}{N_a}+\frac{1}{N_d}\right)} \tag{2.7}$$

The built-in potential V_{bi} can be seen as the maximum potential provided by a P-N region of an ideal solar cell with no recombination and no losses.

2.1.3 Determination of I_{SC}, V_{OC} and FF

This section has been adapted from the works of Sze [2.3] and Green [2.4]

i) The short circuit current I_{sc}

The short circuit current I_{SC} can be identified with the total photo-generated current I_L. This latter is deduced from the combination of continuity equation (equations 2.8 and 2.9) and the relation between current density, electric field and diffusion coefficient (equations 2.10 and 2.11).

$$G_n - U_n + \frac{1}{q}.\frac{dJ_n}{dx} = 0 \tag{2.8}$$

$$G_p - U_p + \frac{1}{q}.\frac{dJ_p}{dx} = 0 \tag{2.9}$$

U_n and U_p are the recombination rates of respectively excess electrons and holes and G_n and G_p are the generation rate of respectively electron and hole. J_n and J_p are respectively the electron and hole current densities. The current density is given by two semi-classical carrier equations derived from Boltzmann transport equation with the following assumptions. The temperature is uniform in the material. The two charge carriers flow independently, in other words there is no carrier-carrier scattering. They are in thermal equilibrium with the surrounding crystal lattice, that is, there are no hot

carriers. The mobility of the carriers is isotropic. The effect on energy band structure of carrier transitions after excitation is negligible. The magnetic field is negligible. With these assumptions current density is given by:

$$J_n = q.n.\mu_n.E + q.D_n\frac{\partial \Delta n}{\partial x} \quad (2.10)$$

$$J_p = q.p.\mu_p.E - q.D_p\frac{\partial \Delta p}{\partial x} \quad (2.11)$$

The first part of the right hand side of the equation is the drift current related to the electric field E whereas the second part is the diffusion current related to the carrier gradient. For the purpose of this study, the model of the abrupt P-N junction can be used. In the abrupt junction approximation, all the free charge carriers are repelled toward the region where they are in majority; therefore there is no free charge carrier concentration in the depleted region. At the edges of the depletion region x_p (figure 2.1), the excess minority carrier concentration is therefore assumed to be equal to 0. Furthermore, the edges of the depletion region are determined by the spatial limit of the electric field influence in the emitter and the base, and then the electric field can be neglected out of the depletion region. Combining both current density and continuity equations leads to equations 2.12 and 2.15:

$$D_n\frac{d^2\Delta n}{dx^2} - U_n + G_n = 0 \quad (2.12)$$

$$D_p\frac{d^2\Delta p}{dx^2} - U_p + G_p = 0 \quad (2.13)$$

At low injection where $U=\Delta n/\tau$ [2.5], τ being the lifetime of the excess charge carriers, the resolution of equation 2.12 leads to equation 2.14 assuming that the recombination rate is constant.

$$\Delta n = Ae^{\frac{x}{L_n}} + Be^{\frac{-x}{L_n}} + C \quad (2.14)$$

Where A, B and C are constants and L_n is the diffusion length of the electrons. The relation between L_n, D_n and τ_n is given by equation 2.15

$$L_n = \sqrt{D_n . \tau_n} \tag{2.15}$$

And similarly for Δp, D_p , τ_p and L_p.

For a wafer thickness where $x_H >> L_n$ (figure 1.1), without loss of charge except bulk recombination, the resolution of equation 2.14 at x_H induces A=0 for avoiding divergence and $C=G_n . \tau_n$.

At x_p in the frontier between P region and the depletion region, $n=n_{p0}.e^{qV/kT}$ where n_{p0} is the electron density in the P region at equilibrium and $V=\phi_p - \phi_n$ where ϕ_n and ϕ_p are respectively the potential of the n and p regions. The resolution of equation 2.14 with A=0 and $C=G_n . \tau_n$ results in equation 2.16.

$$\Delta n = n_{p0}\left(e^{\frac{qV}{kT}} - 1\right)e^{\frac{x_p - x}{L_n}} + G_n . \tau_n \left(1 - e^{\frac{x_p}{L_n}}\right) \tag{2.16}$$

Similarly the boundary conditions for Δp drive to equation 2.17.

$$\Delta p = p_{n0}\left(e^{\frac{qV}{kT}} - 1\right)e^{\frac{x_n - x}{L_p}} + G_p . \tau_p \left(1 - e^{\frac{x_n}{L_p}}\right) \tag{2.17}$$

The current density is determined by using equation 2.10 and 2.11 at the boundaries of the depletion region where the electrostatic field is null.

$$J_p = -q . D_p \frac{\partial \Delta p}{\partial x} \tag{2.19}$$

When the sample is placed in the dark, the photo-generation rate is null and the summation of the electron and hole currents density is called the dark current density. The expression of the dark current density in equation 2.20 is obtained from the resolution of equation 2.18 at x_p and equation 2.19 at x_n with Δn and Δp given by respectively equations 2.16 and 2.17. J_s is the saturation current density.

$$J = J_n + J_p = J_S\left(e^{\frac{qV}{kT}} - 1\right) \tag{2.20}$$

$$J_S = \frac{q.D_n.n_{p0}}{L_n} + \frac{q.D_p.p_{n0}}{L_p} \tag{2.21}$$

On the other hand, under illumination a photogenerated current density J_L occurs due to the contribution of $G_n.\tau_n\left(1 - e^{\frac{x_p}{L_n}}\right)$ and $G_p.\tau_p\left(1 - e^{\frac{x_n}{L_p}}\right)$. Under short circuit condition, V is null and $J_{SC} = J_L$ thus the short circuit current corresponds to the current flow from photogenerated charges.

$$J = J_S\left(e^{\frac{qV}{kT}} - 1\right) - J_L \tag{2.22}$$

i) The open circuit voltage V_{OC}

Open circuit voltage corresponds to a total current J equal to 0, thus by resolving equation 2.22 with J=0, V_{OC} can be determined by the relation 2.23

$$V_{OC} = \frac{kT}{q}\ln\left(\frac{J_L}{J_S} - 1\right) \tag{2.23}$$

ii) The photovoltaic efficiency

- **Dark characteristic**

The current voltage characteristic of a photovoltaic cell is similar to the I - V characteristic of a diode shown in the left of figure 2.2. Its equivalent scheme is shown to the right in figure 2.2.

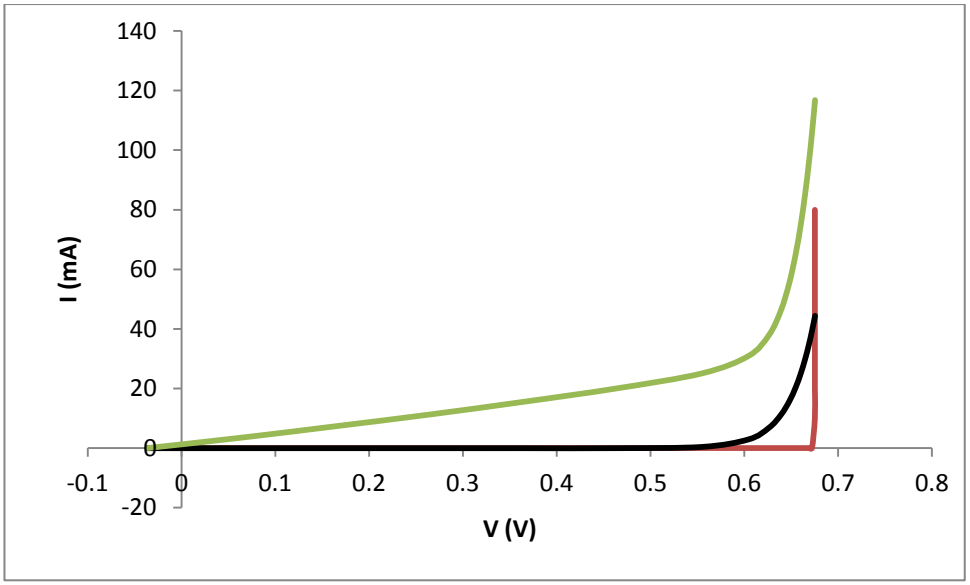

Figure 2.2 I-V characteristic of a P-N junction in the dark. The red curve represents the ideal I-V characteristics that is when the series resistance R_s =0 and the shunt (or parallel) resistance R_p is "infinite". The black curve is for a moderate R_s and the green for a moderate R_s and low R_p. The effects of R_s and R_P are to add a slope respectively to the horizontal and vertical part of the I-V characteristic. These I-V characteristics correspond to the equivalent circuit on figure 2.3 when the illumination current I_L=0

The blue curve represents an ideal diode whose characteristic is to let the current flow one-way from n to p i.e. if $V = \phi_N - \phi_P > 0$. The series resistance R_S is the sum of the silicon substrate resistivity contribution and the contact resistance between the cell and the metallic contacts. It reduces the slope of the curve, i.e. the current. R_P, the parallel resistance is responsible for current leakage between the front and rear of the cell. The slope of the I-V curve is $1/R_p$ if V is below a threshold and $1/R_S$ if V is beyond this threshold. In the ideal case, R_S is null and R_P is "infinite", I is null below this threshold and tends toward infinity beyond this threshold.

- **Illumination characteristic**

When the photovoltaic cell is illuminated, the I-V dark characteristic is shifted vertically downward toward negative current by I_L which is the photogenerated current. This current acts as an intensity dependent source. The resulting power is negative which is equivalent to say that the power is produced by the cells. On the other hand a positive power corresponds to a power received by the cells. In the ideal case (R_s null and R_p infinite), the maximum power is the product of the I_{SC} and V_{OC}.

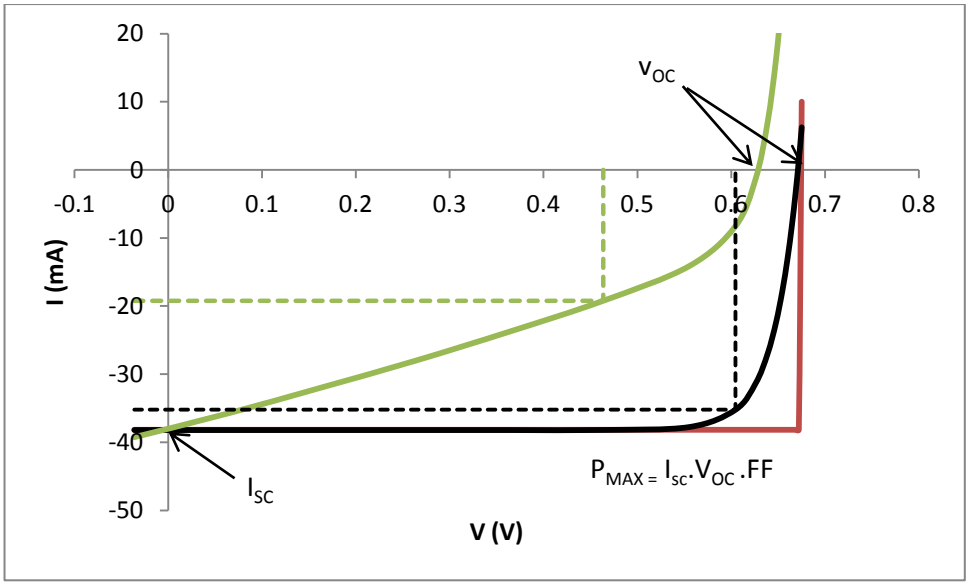

Figure 2.4 I-V characteristic of a solar cell under one sun illumination. The I-V characteristics are the same as on figure 2.2 except that the curves are shifted by a current intensity equal to the illumination current. For the ideal characteristic in red, the fill factor FF is equal to 1. The series and the parallel resistances respectively R_s and R_p reduce FF which result in a loss of electric power.

Figure 2.4 represents the I-V characteristic of a photoelectric cell subject to a luminous flux for 3 cases. It has been previously seen that I_{SC} on figure 2.4 is quasi-equivalent to I_L. The ideal case is for $R_s = 0$ and R_p infinite. The second case is obtained from PC1D5 simulation with an R_s equal to $1x10^{-6}$ ohm and a bulk carrier lifetime of 1 ms. The last case corresponds to an R_s of 1 ohm and a bulk carrier lifetime of 10^{-6} µs. Although this latter lifetime is very low compared to the reality, it has been chosen for emphasizing the effect of R_p. The dashed line represents the point where the power is maximal.

2.1.4 Factors limiting efficiency

In 1960, W. Shockley and H.J. Queisser have shown that the maximum efficiency of an ideal solar cell is 30% [2.6].

It has been seen that three parameters are involved for characterising performance of a P-N junction solar cell: I_{SC}, V_{OC} and FF. Since FF actually depends on V_{OC}, limitations of the two other parameters are discussed.

i) Limitation in I_{SC}

I_{SC} results from the flow of photogenerated charge carriers flowing in the circuit. In ideal conditions all the photons from the solar spectrum with energy higher than the energy bandgap are absorbed and give rise to an electron-hole pair each charge of which is collected and driven in the external circuit. Thus, it is easy to understand that I_{SC} is high if the energy bandgap is low. There is also the possibility of generated secondary electron-hole pairs with very high energy photons (several times the energy bandgap) where these latter give an electron-hole pair with a kinetic energy high enough to ionise atoms of the semiconductor and generating another electron-hole pair. However, these very high energy photons represent a very little part of the solar spectrum and the creation of secondary carriers can therefore be neglected. Actually the absorption of the radiation by the semiconductor varies as a function of electromagnetic wavelength. Therefore the probability of the sunlight photon to generate an electron-hole pair decreases for wavelengths corresponding to low absorption coefficients.

Another cause of efficiency limitation is the loss of charge carriers by electron and hole recombination. These fundamental limitations are intrinsic to the nature of the material, the solar spectrum and their interaction process and cannot therefore be removed.

On the other hand, the structure of a solar cell is also a cause of efficiency loss and can be improved by optimising the solar cell design. Recombination increases with impurity in the semiconductor material. The major parameter of this latter process is the diffusion length that is the mean path of a charge carrier before recombination. As interfaces between the cell and the air, front and rear surfaces of the cell have a large number of defects with energy levels inside the energy band gap, this leads to very high recombination rates at the surfaces of the cell. Furthermore a part of solar power is lost by reflection at the front surface of the cell and due to the shading of electric contacts. The shading effect represents a loss of around 5%. The laser groove buried contact (LGBC) solar cells [2.7] used antireflection coating and texturisation of the front surface which reduces considerably the loss by reflection which can be limited at 4%. The burying of electric contacts used in this technology divides the shading effect by 5

(cf. section 2.2). The charge carrier recombination in the bulk and at the front and rear surfaces reduces the collected current at the base and the emitter and thus I_{SC}.

ii) Limitation in V_{OC}

The expression of the open circuit voltage is given by

$$V_{OC} = \ln\left(\frac{I_L}{I_0} + 1\right) \tag{2.24}$$

As it has been seen previously, I_L is the photogenerated current that reaches the external circuit and I_L can be identified with I_{SC}. I_0 is the saturation current or the dark current which is the residual current when the generation rate is null. Recombination in the depletion region is neglected in the upper relation but actually recombination current has to be added to I_0 which results in a decrease of V_{OC}. Furthermore and of particular interest for this study, SRV of rear surface decreases the V_{OC} with an effect as high as the wafer is thin [2.8].

2.2 General structure of a silicon solar cell

2.2.1 Generalities

The P-N structure of the cell is obtained from a silicon p-type substrate which is called the base. Into a very thin depth near the surface which receives solar radiation (front surface), the material has been highly doped by donor impurity diffusion. This n-region where the donor concentration is very much higher than the acceptor concentration in p-region is called the emitter. Metallic contacts on the front and on the rear surface of this P-N junction allow collecting electrons and holes respectively at the rear and at the front contacts.

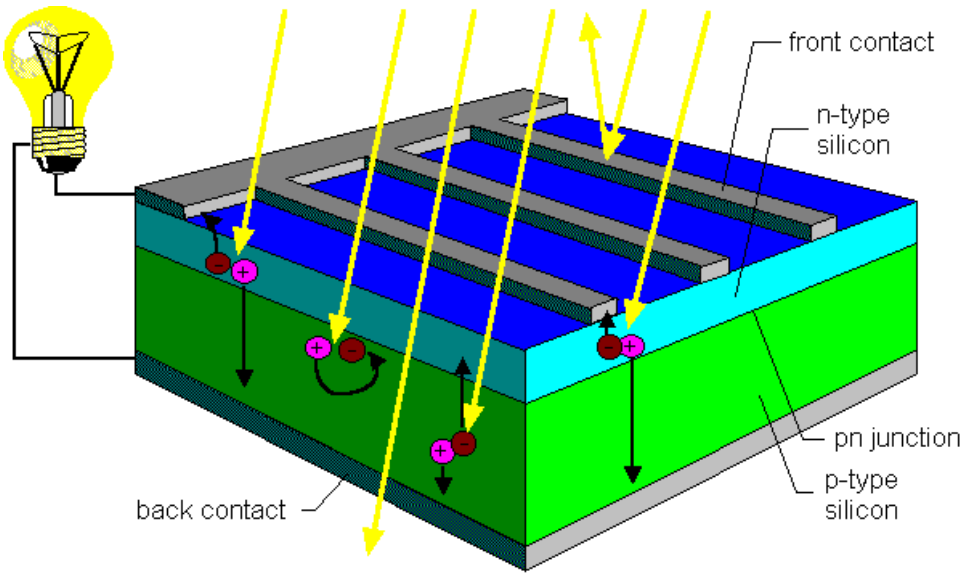

Figure 2.5 Simplified representation of a silicon solar cell (cf. text).The top and the bottom of the figure correspond to the front and the rear surfaces. The front surface is covered with metallic finger and the rear with a metallic uniform deposition in order to collect the photo-generated charges.

Figure 2.5 represents a basic conventional solar cell with a p region in the bulk (the base of the solar cell, and an n region (the emitter) near the front surface. Metallic contacts are put on the front and the rear surfaces.

2.2.2 *Laser grooved buried contact (LGBC) solar cell*

The manufacturing process for screen-printed photovoltaic cells is both easy to implement and cheap [2.7]. However, the height of the metal contacts over the surface of the cell is greater than 150 µm. Because of the relatively high fingers, the losses due to their shadows projected on the surface are not negligible. Thus the space between the fingers should be at least 3mm for limiting these shadows and for having acceptable loss. This separation requirement limits the number of electrical contacts. To compensate for the fewer electrical contacts, electrical conductivity must be increased which requires a level of doping which prejudices quality. Indeed with a high level of doping, the number of majority carriers from the dopant atoms becomes large enough to interfere significantly in the recombination of photo-generated carriers. It follows that the contribution of photons absorbed at the surface becomes small. Since photons of small wavelengths are mostly absorbed at the surface, the high-energy photons do not contribute to the photovoltaic performance significantly. Furthermore, when the metal contacts are located only on top of the surface, the photons of longer wavelength, which are principally absorbed deeply into the cell, are also lost unless the length of diffusion

is about the thickness of the cell which requires very high minority carrier life time. The process of burying electrical contacts invented by S. R. Wenham and M. Green is a way to minimize these disadvantages. The description of the structure of a solar cell with this type of contact will show how this technique improves the efficiency of solar cells.

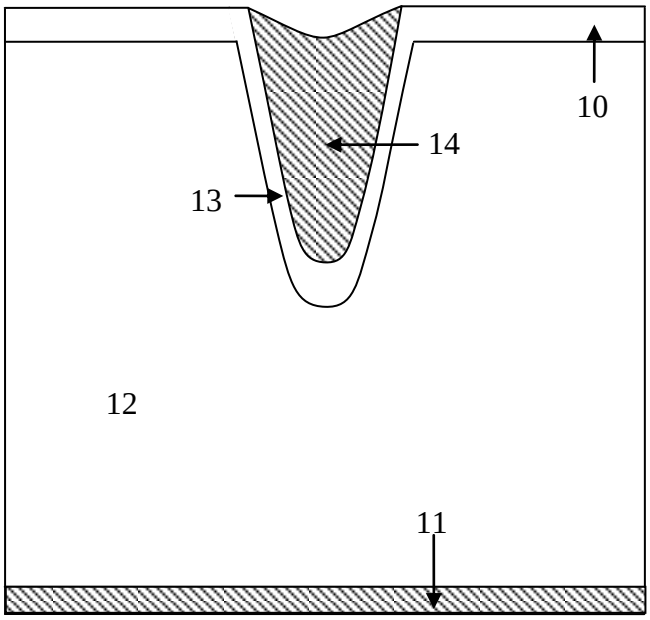

Figure 2.6 Laser Groove Buried Contact solar cell design: the principle is the same as in figure 2.5. The P-N junction is formed by the junction between the emitter region doped with donor atoms (10) and the base doped with acceptors atoms (12). The particularity of LGBC solar cell is the fact that the metallic fingers (14) are buried into the base. Adapted from reference [2.7]

As can be seen in figure 2.6 where the different part of the cells are labelled by a number, the substrate which constitutes the silicon wafer is p-type (labelled 12 on figure 2.6), the surface including the emitter (10) is n-type due to the diffusion of phosphorus. Grooves are formed on the surface by laser inscription and etching (13). These trenches are then filled with a metal paste (14). Finally, the rear surface of the wafer is covered with a metal which constitutes the counter electrical contacts (11).

The contacts are buried at a depth of approximately 100µm and emerge 30 µm above the surface against 150 µm with the usual method described above. The patent for this invention identifies 7 improvements of the process [2.7]. Among these, it can be noted the following point:

1) Losses due to shading are 5 times lower which results in an improvement of 8% in the photovoltaic power generated.

2) Shading relatively low compared to the usual contacts allows a significant reduction of the space between the metal contacts, thus the electrical conductivity does not need to be as high and the required doping is lower. Thus the loss of short wavelength photons described above is limited. The result is a power gain of 5-10% which combined with the decrease of shading can save 15-20% of photovoltaic power.

3) Furthermore, the burial depth of these contacts also improves the response to long wavelengths. Indeed, the P-N junction induced by the grooves can collect a portion of the charge carriers generated at significant depth. The increasing density of contacts enhances the ability to carry high current making it a good structure for solar concentrators.

The settings are:

1) R=60 ohm/cm^2 for the emitter

If the resistivity of the emitter is less than 60 ohm/cm^2 (i.e. if the doping is too high), the response to shorter wavelengths is rapidly deteriorating.

2) The height of the grooves above the surface must be greater than 25 µm to ensure good collection and less than 60 µm to minimize shading.

3) The depth of the grooves must be less than half the thickness of the Si not to reduce the effectiveness of the substrate.

4) The space between the fingers should be between 1.5 and 2.5 µm according to their height above the surface.

- **NaREC (Highpoint) process**

In the Highpoint process, the grooves of the upper surface are formed by laser ablation and then the metal is plated in these grooves for forming the electrical contact. An interface of silica and copper plating is used to minimize contact resistance and metal diffusion, resulting in limiting the series resistance R_s (figure 2.2). As seen previously, since the electrical contacts are closer, conductivity does not need to be so high. This is an indirect benefit for the contribution of high-energy photons. Moreover, these trenches are highly doped n^{++} prior to their metal coating, which gives rise to a P-N junction with a high electric field that enhances the collection of the charge carriers. In standard LGBC solar cell, passivation of the rear surface is provided by an aluminium

doping p^{++} which generates an electric field, the so-called back-surface-field (BSF) that repels the charge carriers towards the bulk of the material. This passivation is called Al-BSF. Although Al-BSF is enough for standard LGBC cell wafer thickness (300µm), the reduction of the wafer thickness requires a better passivation. Table 2.1 gives the characteristic of the P-N junction constituting the solar cell. The bulk is the p-region or the base and the emitter is the n-region of the cells.

Parameter	Value
Dopant	Boron
Bulk Resistivity	1Ω-cm
Bulk Lifetime	30µs
Emitter Sheet Resistivity	90.Ω/□.

Table 2.1 Process Parameters used for the simulation of solar cell behavior [1.3]

2.3 Influence of surface recombination

The relation between generation rate, recombination rate and carrier concentration has been seen in section 2.1. In this previous section, generation rate was assumed to be constant and recombination rate independent of the wavelength. In the usual condition of solar cell operation, the light comes from the sun and has a spectrum (cf. section 2.3) whose intensity is a function of the wavelength. Moreover, the generation of electron-hole pairs is conditioned by the photon absorption and the absorption probability in a given material is also a function of the wavelength. Eventually a part of the light is reflected by the material and the reflection coefficient also depends on the wavelength. For having a consistent equation, total recombination rate U(x) has to be decomposed into a sum of U(x, λ) which represents the recombination rate of excess carriers generated by a ray with a wavelength λ. This is expressed in the following equations.

$$G(x,\lambda) - U_n(x,\lambda) + D_n \frac{d^2 n}{dx^2} = 0 \qquad (2.26\ a)$$

$$G(x,\lambda) - U_p(x,\lambda) + D_p \frac{d^2p}{dx^2} = 0 \qquad (2.26\ b)$$

The recombination rate is assumed to be equal for electrons and holes. Its expression is

$$G(x,\lambda) = \alpha(\lambda).F(\lambda).\big(1 - R(\lambda)\big)e^{-\alpha(\lambda).x} \qquad (2.27)$$

R and α are respectively the reflection and absorption coefficient of silicon, F is the flux of photons per wavelength.

2.3.1 Generation

i) AM 1.5 spectrum

AM 1.5 direct spectrum corresponds to incident sunlight with an intensity one sun through an atmosphere thickness of 1.5 which means that due to the angle of incidence of around 48.2° from the vertical, the direct light path is 1.5 times higher than the thickness of atmosphere. Figure 2.7 represents the AM 1.5 spectrum and the corresponding number of incident photons per cm^2, which is referred to as F.

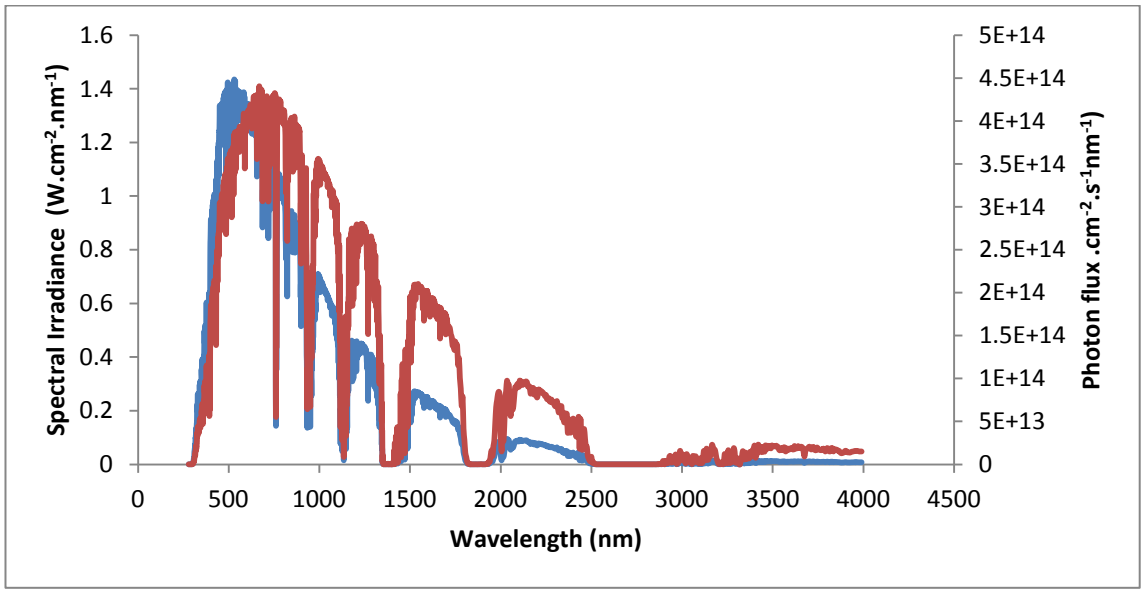

Figure 2.7 In blue: spectral irradiance corresponding to AM 1.5 solar spectrum (cf. text). In red: photon flux corresponding to AM 1.5 spectrum. Photon flux is used for the calculation of the generation rate (cf. equation 2.31). The photon flux has been deduced from the spectral irradiance.

ii) ***Optical constants of silicon***

Figure 2.8 represents the dispersion of the imaginary part k and real part n_f of the complex refractive index of silicon which has been used in chapter 4.

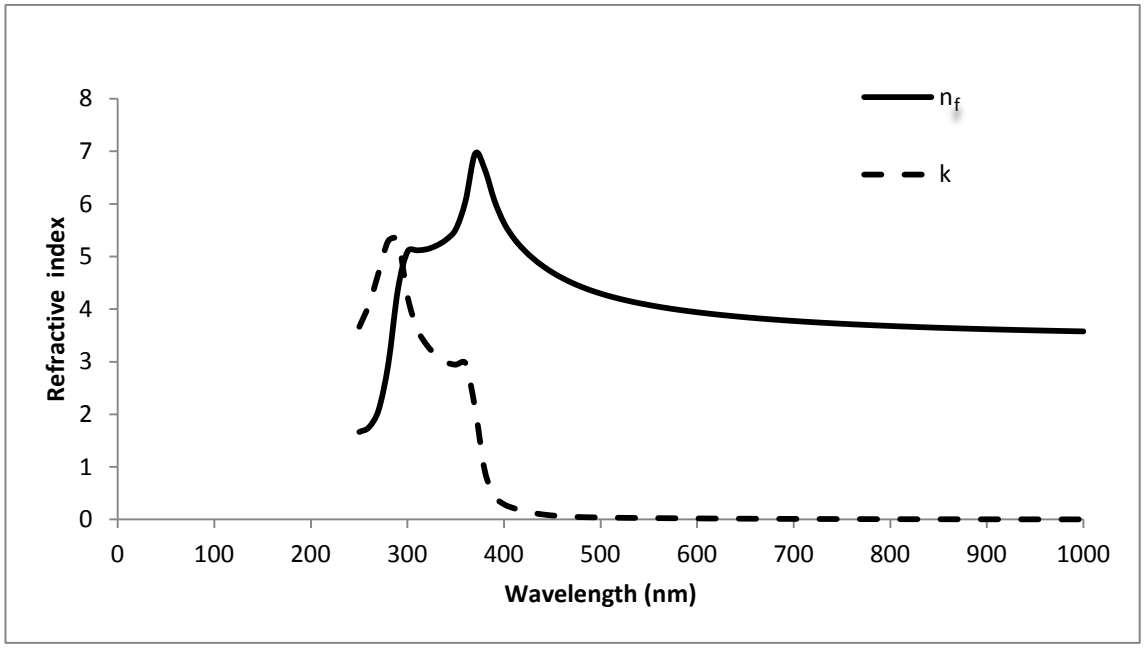

Figure 2.8 Real part (n_f) and in dash imaginary part (k) of the c-Si refractive index. The real part of the refractive index is used for the determination of the reflection resulting in a loss of carrier generation. The imaginary part is used for the calculation of the absorption coefficient and thus the part of the photon flux which contributes to the charge carrier generation

iii) Coefficient of absorption

Absorption coefficient (figure 2.9) is determined from equation 2.28

$$\alpha = \frac{4.\pi.k}{\lambda_0} \tag{2.28}$$

The imaginary part k as a function of the wavelength lambda of the complex refractive index $N = n_f - ik$ has been extracted from the data of Jellison. It can be noticed that the same data have been used for the ellipsometry measurement. However these data are measured for wavelengths spaced with a step of 10 nm whereas the data of light power as a function of λ in the AM 1.5spectra are measured with a step of 0.5 nm for the low wavelengths. Therefore in order to fit with the AM 1.5 spectra, the missing data of silicon optical constants have been interpolated assuming a linear variation between the

measured data. Although this first order assumption is a strong simplification it is enough for this purpose.

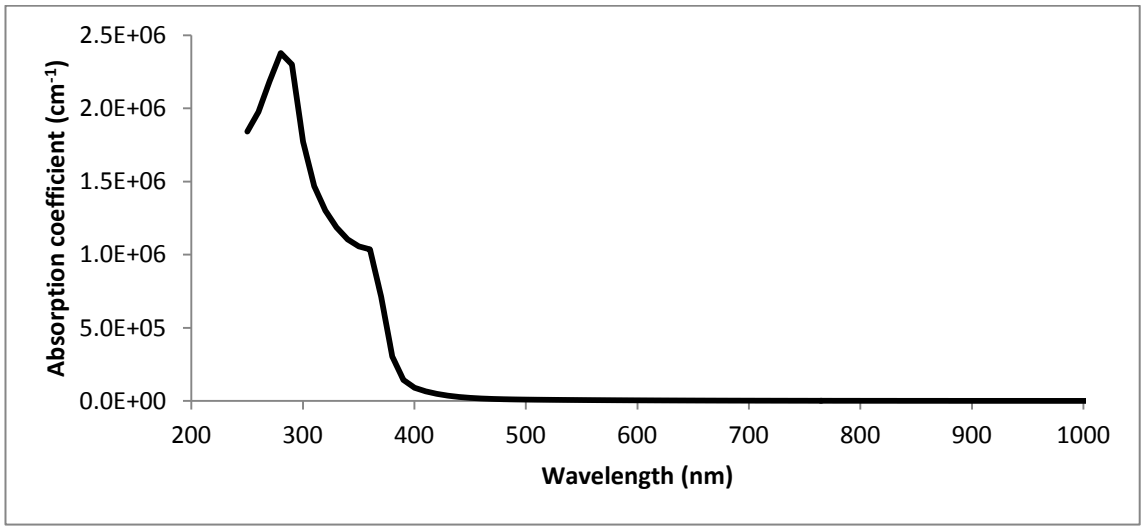

Figure 2.9 Typical representation of the variation of absorption coefficient of c-Si with respect to wavelength.

iv) Coefficient of reflection

The reflection coefficient at the interface of two media with a refractive index of respectively n_{f1} and n_{f2} is given for a normal incidence by the relation:

$$R = \frac{(n_{f1} - n_{f2})^2}{(n_{f1} + n_{f2})^2} \tag{2.29}$$

Since the first medium is the air $n_{f1} = 1$,

$$R(\lambda) = \frac{\left(1 - n_f(\lambda)\right)^2}{\left(1 + n_f(\lambda)\right)^2} \tag{2.30}$$

The total generation rate is given by the summation of $G(x,\lambda)$ over the whole AM 1.5 spectrum

$$G(x) = \int_{\lambda_{min}}^{\lambda_{max}} \alpha(\lambda).F(\lambda).\big(1 - R(\lambda)\big)e^{-\alpha(\lambda).x}.d\lambda \qquad (2.31)$$

The following figure is the result of calculation from the data of AM 1.5 spectrum, $n_f(\lambda)$ and $\alpha(\lambda)$ given in the previous figures. The first curve is for bare silicon whereas the second curve is for a textured surface with an antireflection (AR) coating of Si_3N_4. On this latter case, $R(\lambda)$ is reduced to 4%.

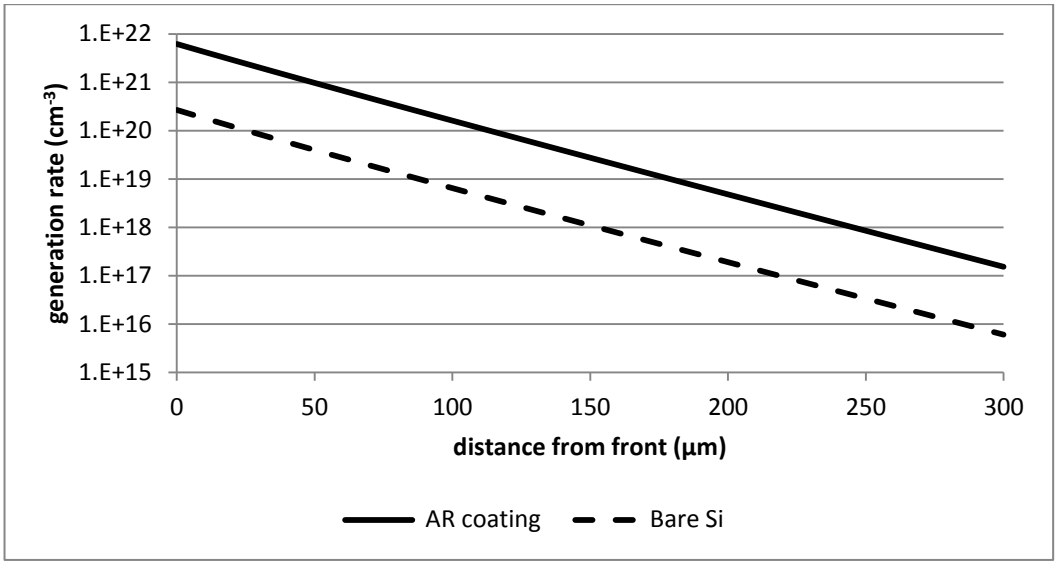

Figure 2.10 Generation rate versus distance from the front surface. Due to a higher reflection at the front surface, the generation rate is lower for uncoated silicon wafer (bare Si) than for a-Si covered with antireflection (AR) coating.

2.3.2 Calculation of I_{SC}

- ***Resolution of continuity equation for low injection***

Low injection corresponds to an excess electron concentration $\Delta n << N_{dop}$ where N_{dop} is the p or n doping respectively at the base and the emitter. The Shockley-Read-Hall (SRH) model describing the recombination via defects will be seen in more detail in the section about SRV. The recombination rate U is determined from SRH theory by the following relation

$$U_n = \frac{\Delta n}{\tau_{SRH}} \tag{2.32}$$

τ_{SRH} is the lifetime of the minority carrier, that is the mean time between a carrier generation and its recombination; this lifetime is a function of Δn. For an excess carrier concentration very far below the doping concentration, τ_{SRH} becomes independent of Δn. Therefore continuity equation in the region p becomes:

$$\alpha(\lambda).F(\lambda).\big(1 - R(\lambda)\big)e^{-\alpha(\lambda).x} - \frac{\Delta n(\lambda)}{\tau_n} + D_n \frac{d^2\Delta n}{dx^2} = 0 \tag{2.33}$$

Similarly for the hole excess Δp in the n-region

$$\alpha(\lambda).F(\lambda).\big(1 - R(\lambda)\big)e^{-\alpha(\lambda).x} - \frac{\Delta p(\lambda)}{\tau_p} + D_p \frac{d^2\Delta p}{dx^2} = 0 \tag{2.34}$$

This latter equation can be analytically solved and its results is

$$\Delta n = A.\cosh\left(\frac{x}{L_n}\right) + B\sinh\left(\frac{x}{L_n}\right) - \frac{\alpha.F(1-R).\tau_n}{\alpha^2.{L_n}^2 - 1}e^{-\alpha x} \tag{2.35}$$

The diffusion length is determined by the diffusion coefficient D_n of electrons in the base:

$$L_n = \sqrt{D_n.\tau_n} \tag{2.36}$$

- **Boundary conditions at the base**

The continuity of electron excess concentration in the depletion region and in the p region implied that $\Delta n = 0$ at the depletion edge since $\Delta n = 0$ in the depletion region.

(2.37)

$$(\Delta n)_{x_p} = 0 \quad (2.37)$$

Furthermore, the electron current density at the rear surface is given by

$$J_n = q.S_n.\Delta n \quad (2.38)$$

Or

$$-D_n\left(\frac{d\Delta n}{dx}\right)_{x_H} = S_n.(\Delta n)_{x_H} \quad (2.39)$$

- **At the emitter of the cells (zone N)**

The current density of holes at the front surface is given by

$$-D_p\left(\frac{d\Delta p}{dx}\right)_0 = S_p.(\Delta p)_0 \quad (2.40)$$

Equations 2.39 and 2.40 show clearly that the loss of carrier concentration at the front and rear surfaces increases with the effective SRV which is obvious by the negative sign.

Similarly to condition for electrons at x_p the hole concentration at the depletion edge x_n is equal to 0:

$$(\Delta p)_{x_n} = 0 \quad (2.41)$$

The solution of equations 2.33 and 2.34 can be found in reference [2.3]. Although interesting for understanding the physical processes occurring in a solar cell and the effect of surface recombination, these equations obtained by analysis are based on approximation which cannot give a true estimation of the photovoltaic performance. Therefore software using numerical method has been used for simulating the

performance of our cells [2.9]. The most important point of this section is what results from equations 2.39 and 2.40 that is a reduction of Δn at the rear surface due to higher recombination rate than in the bulk. Actually the rear surface is a thin volume in the interface between the wafer and the exterior of the cell. Thus it is easy to understand that effect of rear surface recombination increases with the interface thickness to the wafer thickness ratio. Although rear interface is very thin compared to the wafer thickness, the effect of the surface recombination becomes sensitively higher when this ratio increases. Thus the reduction of the wafer thickness requires a better passivation in order to compensate the effect of the higher thickness ratio.

2.4 Simulation with PC1D5

PC1D-5 [2.9] is reference software for simulating solar cells behaviour based on silicon technology.

In a work done by NaREC [1.3] for the determination of the optimal thickness of the Si wafer in order to keep high efficiency when reducing the thickness PC1D-5 software has been used to simulate the evolution of photovoltaic efficiency at different values of SRV. It has been shown that for a SRV lower than 300 cm/s, efficiency does not decrease when the thickness is reduced from 300 to 150 μm. However, the present work has revealed that the SRV value determined by NaREC does not take in to account the SRV dependence with injection level due to fixed charge density at the c-Si /film interface. This will be explained in details in chapter 3. The SRV considered by NaREC and in PC1D-5 simulation is actually the SRV at very high injection level where the effect of fixed charge density becomes negligible. For 1 ohm.cm wafers, fixed charge density can increase more than 10 times the SRV for an injection level corresponding to an intensity of one sun. On section 2.4.2 a method for substituting effective SRV (including fixed charge density effect) will be proposed.

2.4.1 Numerical method used in PC1D5

The details in this section about the calculation are only given for highlighting the difference between the conditions used in numerical calculation and the assumptions of the analytical problem. In particular, the Poisson equation is used in the numerical method since the electric field is not assumed to be null and because there is a change in the local charge density due to the photogenerated charge carriers and their recombination. It can also be remarked that the mobility is also a function of the electric field which in turn depends on the charge distribution – via the Poisson equation- and

thus on mobility. It results in a self-consistent and interdependent system of equations which can only be resolved by numerical method.

The software is based on five fundamental equations [2.9, 2.10], the two equations of current density including drift current and diffusion current that have been used previously (the assumptions are the same). Each unknown variable is expressed as a function of three potentials: the electric potential ψ, the quasi-Fermi levels of electrons and holes respectively V_n and $V_{p.}$ These 5 equations are combined, leaving only three equations with these three unknown variables. The system is discretised and solved by the method of Newton using Jacobian matrix. After determination of these three potentials, all parameters can be deduced from their values.

$$J_n = q.n.\mu_n.E + q.D_n\frac{\partial n}{\partial x} \tag{2.42}$$

$$J_p = q.p.\mu_p.E - q.D_p\frac{\partial p}{\partial x} \tag{2.43}$$

$$E=\text{grad}\ \psi \tag{2.44}$$

Introducing the quasi-Fermi level, E_{FN}, of the electrons and E_{FP} of the holes the two upper equations can be rewritten:

$$J_n = q.n.\mu_n.\frac{\partial E_{FN}}{\partial x} \tag{2.45}$$

$$J_p = q.p.\mu_p.\frac{\partial E_{FP}}{\partial x} \tag{2.46}$$

The continuity equation is used but while this latter was previously at equilibrium, here, the continuity equations are time dependent and become:

$$\frac{\partial n}{\partial t} = G_n - U_n + \frac{1}{q}.\frac{dJ_n}{dx} \quad (2.47) \qquad (2.47)$$

$$\frac{\partial p}{\partial t} = G_p - U_p + \frac{1}{q}.\frac{dJ_p}{dx} \qquad (2.48)$$

The generation rate in PC1D5 includes effect of light trapping by textured front structure. The absorption coefficient is improved by taking into account absorption of the free carriers. The recombination model includes Auger recombination. Field enhanced recombination by trap assisted tunneling is also included using Hurkx model [2.11]. The last equation is Poisson equation giving the relation between charge density and electric potential.

$$\nabla.(\varepsilon.\nabla\psi) = -\left({N_d}^+ - {N_a}^- + p - n\right) \qquad (2.49)$$

The material is assumed to be not degenerate and therefore the Fermi distribution function can be approximated by Boltzmann expression. At a position where electric potential is taken as reference (labeled R) and equal to zero:

$$n = N_C.\exp\left(-\frac{E_c - E_{FN}}{k.T}\right) \qquad (2.50)$$

$$p = N_V.\exp\left(-\frac{E_{FP} - E_v}{k.T}\right) \qquad (2.51)$$

E_{FN} and E_{FP} are the position of the quasi-Fermi potentials at the position x=0 corresponding to the cell front. Indeed in PC1D5 the reference intrinsic Fermi level is taken at x=0. E_c and E_v represent the band–edge potentials respectively of the conduction and the valence band at x=0, since these two band-edges are related to the electric potential and spatial variation in the energy band structure. Spatial variation in the material composition and bandgap narrowing (due to heavy doping) induce shift of the band edge toward the centre of the bandgap. For taking account of this spatial variation, PC1D5 introduces two band edge potentials V_N and V_P respectively for the conduction and the valence band. The expressions of V_N and V_P are:

$$\phi_N(x) = \frac{k.T}{q}.\ln\left(\frac{N_C(x)}{N_{CR}}\right) + \frac{\chi(x) - \chi_R}{q} + \Delta Eg_C(x) \qquad (2.52)$$

$$\phi_P(x) = \frac{k.T}{q}.\ln\left(\frac{N_V(x)}{N_{VR}}\right) + \frac{Eg(x) - EgR}{q} + \frac{\chi(x) - \chi_R}{q} + \Delta Eg_v(x) \qquad (2.53)$$

Since all the parameters of these equations are known, V_N and V_P are directly determined by these two independent relations. Since the material is the same in the whole cell, the logarithm part of the relation is not involved. However, this presents the possibility to include dielectric films of a-Si: H and SiN_x in the simulation and it would be interesting to use a model with these film characteristics instead of fixing a SRV value on the rear surface, and then to extract the rear SRV from the simulation. This would require knowing the density of states of conduction and valence bands in the film, the bandgap and the dielectric susceptibility. The bandgap narrowing is calculated with the model of Del Alamo:

$$\Delta Eg = A_{Gap}.\ln\left(\frac{N_D}{N_{ref}}\right) \text{ if } N_D \geq N_{ref} \qquad (2.54)$$

N_{ref} and A_{gap} depend on the material. N_{ref} is equal to $7.10^{17}cm^{-3}$ and A_{gap} to $1.87.10^{-2}$ eV for Si material. Since the emitter, N-region, of the solar cells in this work is around 4.10^{19} cm^{-3}, bandgap narrowing occurs in this region. It has to be noticed that bandgap

narrowing was not taken into account in the previous calculation. At a position x, the expressions for carrier density become

$$n(x) = n(0).\exp\left(\frac{q(\psi - \phi_{N)} - E_{FN}}{k.T}\right) \tag{2.55}$$

$$p(x) = p(0).\exp\left(\frac{q(-\psi + \phi_{P)} + E_{FP}}{k.T}\right) \tag{2.56}$$

The electric potential $\psi(x)$ is determined by solving the Poisson equation in its integral form (reduced solution) after discretisation of the problem.

The mobility is described by equation 2.57 with E=grad ψ:

$$\mu(x, E) = \frac{\mu(x, 0)}{\left[1 + \left(\frac{\mu(x, 0).E}{v_{sat}}\right)^{\beta}\right]^{1/\beta}} \tag{2.57}$$

In PC1D5, β=2, v_{sat} is the saturation velocity which is around 10^7cm/s. This mobility variation affects the field as follows:

$$\psi(x) + \phi_N(x) \;\Rightarrow\; \zeta_n(x) = \psi(x) + \phi_N + \frac{kT}{q}.\ln\left(\frac{\mu(x, E)}{\mu(x, 0)}\right) \tag{2.58}$$

Therefore the expressions for electron and hole density becomes:

$$n(x) = n(0).\exp\left(\frac{q\zeta_n - E_{FN}}{k.T}\right) \tag{2.59}$$

$$p(x) = p(0).\exp\left(\frac{-q\zeta_p - E_{FN}}{k.T}\right) \tag{2.60}$$

The expressions for carrier density are injected into the current density transport equations and Poisson equation. After discretisation of the problem, the system is thus solved by the method of Newton using Jacobian matrix. I_{sc}, V_{oc} , FF and PV efficiency can therefore be determined.

2.4.2 Modelling of the LGBC solar cells

A detail description of the simulation process can be found in reference [2.12]. The cell is composed of a base with a p-type doping N_a with a diffusion N_d of a very high n-type doping at the front surface. The doping is chosen to be uniform and starting from the top of the cells until a depth of 2 µm. The n-type doping is $4.1x10^{19}$ cm^{-3} which gives a sheet resistance of 90 ohm/square. The front surface is textured with a depth texture of 3µm and angle of 54.74°. The silicon nitride coat can reduce the light reflectance under 2% as shown by a work on front surface passivation by silicon nitride [2.15]. The electrical contacts on the emitter are grooved, and the loss of light which represents around 5% in a classical solar cell can be divided by 5. In the simulation both reflection and shading effects are taken in account by setting the front reflectance to 5%. The recombination at the front surface is fixed at a relatively high value of 5000cm/s for the SRV which corresponds to a non passivated surface. The bulk recombination is fixed at 1000 µs for the FZ wafer of 8000 ohm.cm and at 30 µs for the Cz wafer of 1 ohm.cm. The spectrum is AM 1.5G corresponding to a total illuminating power of $0.1W/cm^2$. The optical characteristic of the wafer is the characteristic of silicon that has a band gap equal to 1.124 eV, a refractive index of 3.58 at 632.8 nm, and a relative dielectric constant of 11.9. All the characteristics are taken at 300 K. After having fixed these parameters, only two parameters are changed during simulation, first the doping N_A which is equal to $1.5x10^{16}$ cm^{-3} for Cz 1ohm.cm and $2.6x10^{11}$ cm^{-3} for FZ 8000ohm.cm and the parameters that we study, the SRV at the rear surface. Figure 2.11 represents the PC1D5 interface where all the parameters of the cell are fixed by the user. On the top-right of this figure, the red region at the top represents the emitter (n-region) and the bottom in blue the base (p-region).

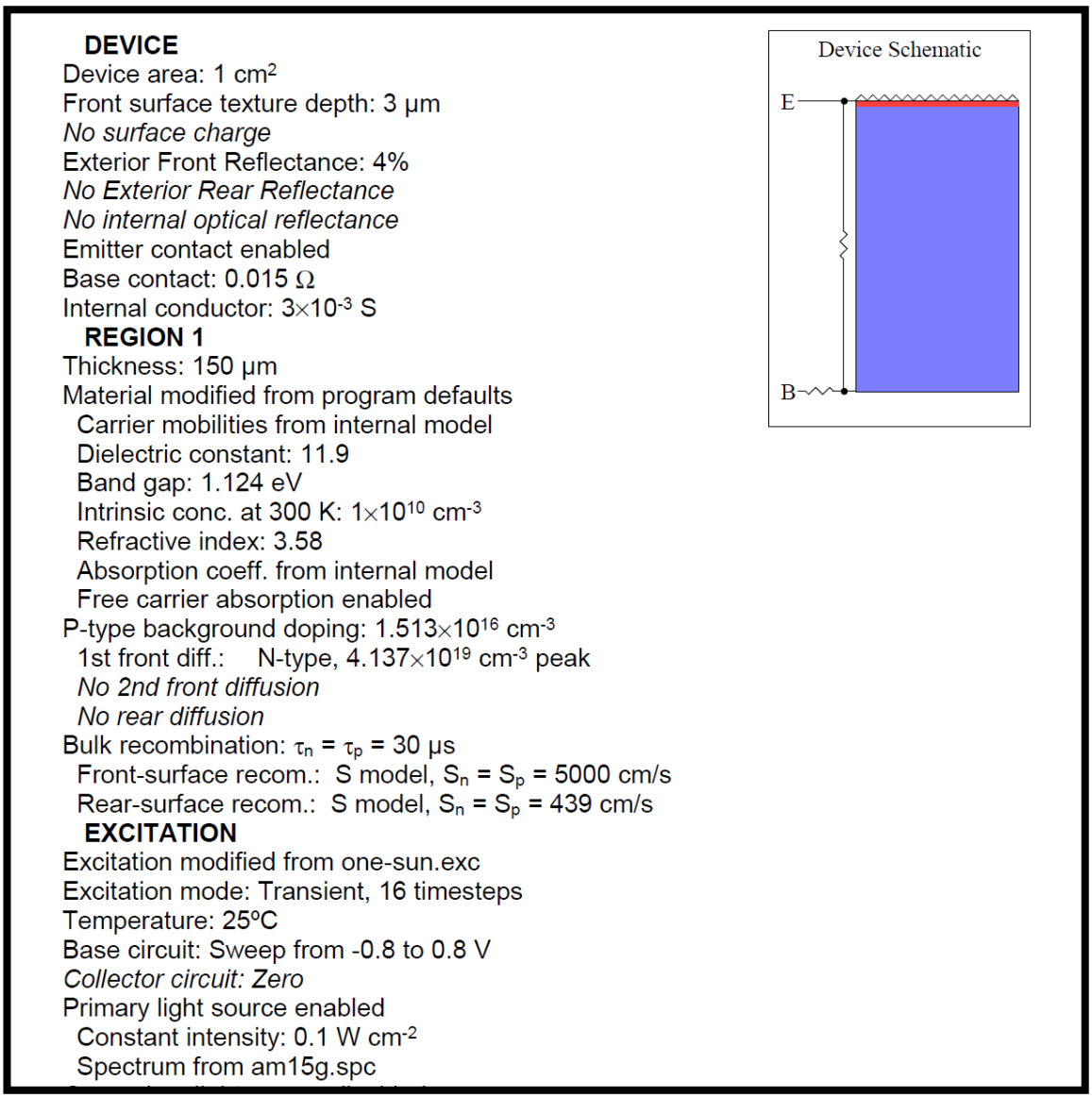

Figure 2.11 Interface of the PC1D5 software with all the parameters used for the simulation of this work. On the device schematic, E and B mean respectively emitter and base. Dielectric constant, energy bandgap, refractive index and intrinsic carrier concentration corresponds to standard values for silicon. Doping of the base and of the emitter correspond to NaREC parameters. Front surface texture depth is taken from usual value [2.12-14]. The excitation parameters correspond to the spectral irradiation AM 1.5 with an intensity one sun. The bulk recombination is 30µs for Cz wafer. The surface velocity recombination is fixed to 5000 cm/s at the front. S_n and S_p (S_{n0} and S_{p0} in the text) have been determined to fit with the effective SRV (cf. text).

Regarding the surface recombination, it has to be emphasised that the effective SRV can actually not be directly chosen but it is the factors S_{n0} and S_{p0} that are given by the following relations.

$$S_{n0} = N_d . \sigma_n . \upsilon_{th} \tag{2.61}$$

$$S_{p0} = N_d . \sigma_p . \upsilon_{th} \tag{2.62}$$

The surface recombination is calculated by the relation

$$U_S = \frac{S_{n0} . S_{p0}(n.p - n_i^2)}{S_{n0}(n + n_i e^{\frac{E_d}{k.T}}) + S_{p0}(p + n_i e^{-\frac{E_d}{k.T}})} \tag{2.63}$$

E_d , the energy level of the defect relatively to the mid-gap level E_i, S_{n0} and S_{p0} can be chosen by the operator. Compared to our simulation in chapter 3, there is only one level defect E_d whereas we used a quasi continuum of defect energy levels. Furthermore, due to the positive fixed charge which attracts the electrons and repels the holes, the charge carrier densities at the surface n_s and p_s are not the same as n and p in the bulk. For taking this into account, the order of injection level in the bulk Δn is determined by the simulation. The value S_{eff} of the measured SRV is taken at this injection level and the experimental R_s is deduced from $U_s = S_{eff}.\Delta n$. S_{n0} and S_{p0} are considered as equal (which is false since $\sigma_p/\sigma_n \sim 100$) and E_d=0. Thus

$$S_{eff} . \Delta n = \frac{S_0(n.p - n_i^2)}{n + p + 2.n_i} \tag{2.64}$$

This relation is only accurate for a given Δn and is only an artificial way for having the same surface recombination. A further investigation could be done using software as SCAPS [2.16] or ASA (Amorphous Semiconductors Analysis) which include the possibility of simulating a density of states in the bandgap [2.17]. However since efficiency has to be determined only for one sun illumination using PC1D-5 with equation 2.64 is enough for including effective SRV.

2.4.3 Results

i) Injection level

As shown on figure 2.12, the injection level stays approximately between 2 and $3.5x10^{14}$ cm^{-3} Cz 1ohm.cm wafer (samples 2527-2530) and between 1 and $3x10^{15}$ cm^{-3} for FZ 8000 ohm.cm wafer (samples 43-45). The injection level difference between Cz and FZ wafer is mainly due to the fact that the bulk lifetime is around 30µs for the former and beyond 1ms for the latter which is in agreement with the fact that an illumination of 1 sun corresponds, for a wafer with bulk lifetime higher than 1ms, to an injection level of 10^{15} cm^{-3} [2.18] Knowing the density of photogenerated charge carriers, S_0 can be extracted for a given S_{eff}. Figure 2.12 gives the injection level obtained with PC1D5 using the values of our experimental samples (samples 2527-2530 and 43-45) given in chapter 6. The dependence of S_0 with the injection level is only sensitive with its value order i.e. 10^{14} and 10^{15} cm^{-3}respectively for1 ohm.cm Cz and 8000 ohm.cm FZ wafers and thus a correct value of S_0 does not require performing the simulation for each effective SRV value.

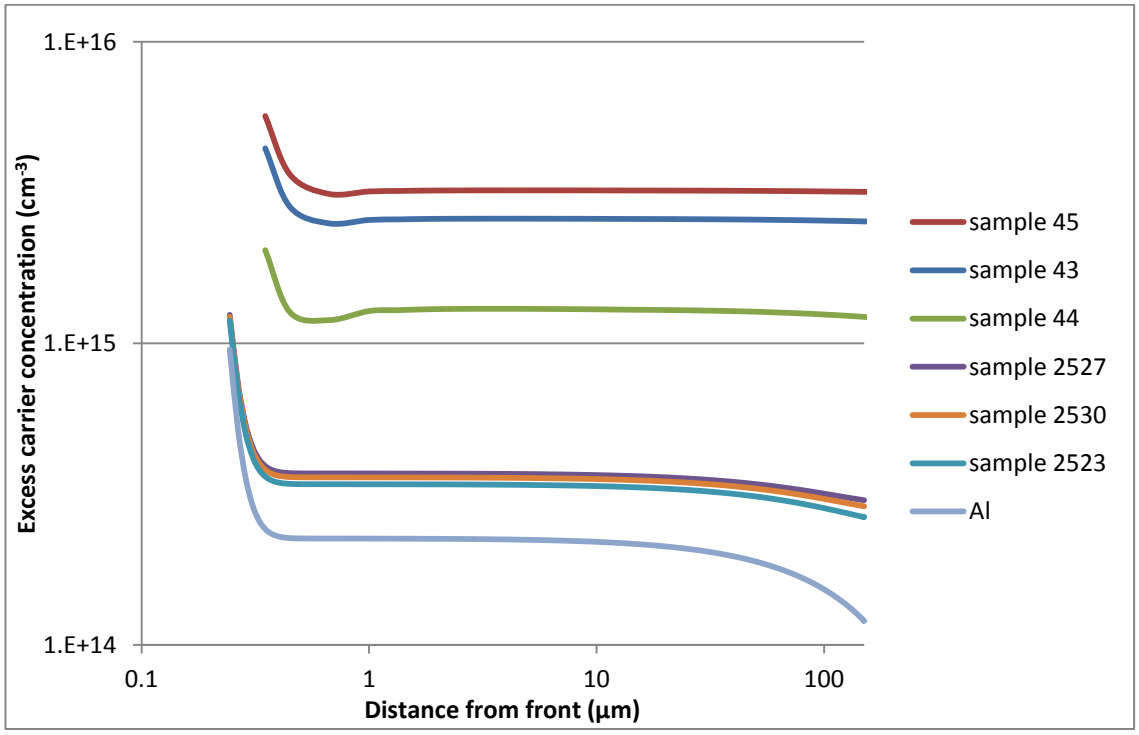

Figure 2.12 Excess carriers concentration versus distance from the front surface. Samples 43-45 are deposited on FZ 8000 ohm.cm wafers and samples 2523-2530 on Cz 1 ohm.cm wafers. For instance the curve corresponding to sample 43 is the results of PC1D-5 simulation with bulk wafer corresponding to Fz 8000 ohm.cm and a SRV corresponding to sample 43.

i) ***Efficiency***

Figure 2.13 presents the results of the simulations for a Cz 1 ohm.cm wafer. Simulations have been done with the parameters given in 2.4.2 for different SRV values. It has also to be noted that the simulation does not take in account the effect of passivation degradation after Al coating for electric contact [2.19]

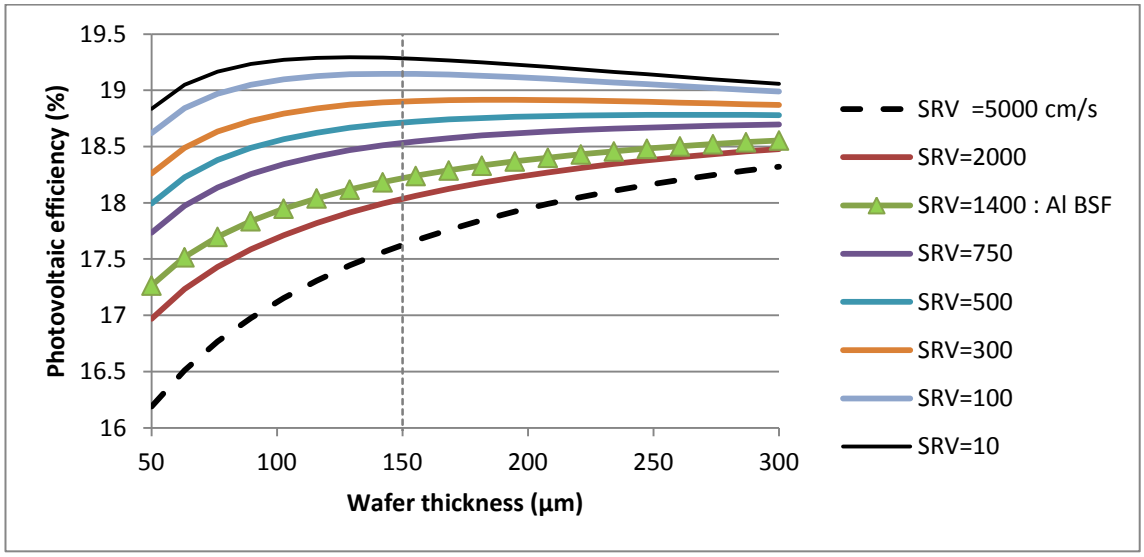

Figure 2.13 Efficiency of a Cz 1ohm.cm wafer versus thickness for various SRV (cm/s). The parameters used for the simulation are given on figure 2.11. When the SRV is below 300 cm/s, the efficiency for 150 µm thick wafer is around 19%

The evolution of the efficiency versus thickness at different SRV shows two tendencies. For very low SRV, the efficiency is maximum at the optimum thickness of 150 µm. Beyond this thickness, the efficiency increases slowly and below this thickness the reduction of efficiency is stronger. For high SRV, the efficiency decreases with thickness. Between these two tendencies, there is a range where the SRV is constant until 150 µm and decreases below this value. This explains the choice of this optimal thickness. This can be explained as follows; when the thickness of the cell decreases, the ratio of the diffusion length and the thickness of the wafer increases, i.e., the probability of carriers to meet the electrical contacts is higher. Nevertheless, the bulk of the wafer having a long lifetime, the diffusion length is high compare to the thickness of the cell. This explains the weak influence of the thickness decrease until the optimum value. When this thickness is reached, the gain ratio of diffusion length versus thickness is balanced by the loss due to the contribution of recombination surfaces which becomes more significant as the thickness decreases. Indeed, the recombination is much larger at

the surface than in the bulk and obviously, surface effects become important as the volume decreases. This also explains why the efficiency decreases more rapidly when the SRV is high. Indeed, the SRV is so important that it exceeds the gain of the ratio of diffusion length versus thickness for thicknesses less than 300µm. The SRV of the rear surface of LGBC solar cells passivated with Al-BSF, have been estimated to be 1400 cm/s by NaREC by fitting the evolution of the experimental efficiency versus wafer thickness with PC1D5 simulation [1.3]. Figures 2.13 and 2.14 show that for having the same efficiency as 300 µm thick LGBC solar cells with a thickness of 150 µm, the SRV has to be below 300 cm/s for Cz 1 ohm.cm wafer.

2.5 Conclusion

The main contribution highlighted on this chapter is a method for substituting the effective SRV -including fixed charge density and defect density- to the SRV at high injection level. Substituting effective SRV is very important in the case of SiN_x film deposition where fixed charge can increase the SRV higher than one order of magnitude.

Simulation has been done for Cz 1 ohm.cm after having replaced in the PC1D-5 parameters the high injection level SRV by the effective SRV value. The necessity of having a SRV below 300 cm/s has been deduced from these results. In chapter 3, the dependence of the SRV to injection level, particularly due to the influence of fixed charge density will be described and explain in detail. This will allow understanding the importance of using effective SRV instead of high injection level SRV value in PC1D-5 simulation.

BIBLIOGRAPHY OF CHAPTER 2

[2.1] A.H. Wilson, The Theory of Electronic Semi-Conductor, Proc. R. Soc. Lond. A 133-822, 458-491 (1931)

[2.2] P.J. Collings *et al.*, Simple Measurement of the band gap in silicon and Germanium, Am. J. Phys. 48(3), 197-199 (1980)

[2.3] S.M. Sze, Physics of Semiconductor Devices 2^{d} Edition, Willey-Interscience publication (1981)

[2.4] M.A. Green, Solar Cells Operating Principles Technology and System Applications, University of New South Wales, 1998.

[2.5] U.A. Elani, The effective carrier lifetime measurement in silicon: The conductivity modulation method, J.King Saud University-Science 22(1) 9-13 (2010)

[2.6] W.Shockley *et al.*, Detailed balance limit of efficiency of P-N junction solar cells, J.Appl.Phys. 12(3), 510-519 (1961)

[2.7] S.R. Wenham, Australia Patent 570309 Buried Contact Solar Cell

[2.8] M. Hofmann *et al.*, PECVD-ONO: A New Deposited Firing Stable Rear Surface Passivation Layer System for Crystalline Silicon Solar Cells , Hindawi Publishing Corporation Advances in OptoElectronics Volume 2008, Article ID 485467, 10 pages

[2.9] D.A. Clugston *et al.*, PC1D version 5: 32-bit solar cell modeling on personal computers, 26th IEEE Photovoltaic Specialists Conf., October 1997.

[2.10] D.T. Rover *et al.*, Solar cell modeling on personal computers, 18th IEEE PVSC, 703-709 (1995).

[2.11] G.A.M. hurkx *et al.*, A new analytical diode model including tunneling and avalanche breakdown, IEE transaction on electron devices 39 (9),2090-2098 (1992)

[2.12] N.Benahmed-benabdallah, Propriétés physiques des semi-conducteurs (Si monocristallin et Ge) et Simulation des cellules solaires à base de Si et SiGe, thèse en magister chapter 4 (2006)

[2.13] S.Sepeai *et al.*, Design Optimization of Bifacial Solar Cell by PC1D Simulation, Journal of Energy Technologies and Policy 3(5) 1-11 (2013)

[2.14] P.Song and Ch. Jiang, Modeling of wavelength down conversion based on the Nd^{3+}–$Yb3^{+}$ system for improving c-Si solar cell performance, J. Opt. 15 025002-8 (2013)

[2.15] G. Claudio *et al.*,Surface passivation by silicon nitride in Laser Grooved Buried Contact (LGBC) silicon solar cells, Superlattices and Microstructures 45, 234-239(2009)

[2.16] M. Burgelman *et al.*,Modeling polycrystalline semiconductor solar cells, Thin Solid Films 361-362 ,527-532(2000)

[2.17] M. Burgelman *et al.*, Modeling Thin-film PV Devices, Prog . Photovolt: Res. Appl. 11, 1–11(2003).

[2.18] C. Voz *et al.*, Surface passivation of crystalline silicon by Cat-CVD amorphous and nanocrystalline thin silicon films, Thin Solid Films 430 , 270–273(2003)

[2.19] J. Dupuis, Rear passivation schemes for industrial silicon solar cells,

Chapter 3

<SURFACE RECOMBINATION VELOCITY (SRV)>

Recombination process is a very important notion for understanding the loss of charge carriers which results in a decreasing of photovoltaic efficiency. 3 regions can be distinguished regarding recombination process. Indeed recombination occurs in the bulk and the two surfaces of the solar cell: the front and the rear surfaces. This work is focused on rear surface because the design of the front surface is already set. Rear surface recombination is limited by passivating layer deposition. It has to be recalled that silicon is a semiconductor with indirect bandgap and thus recombination between electron and hole occurs via defects inducing energy levels inside the bandgap. In the bulk recombination occurs via discrete energy levels whereas it occurs via energy level density. The passivation consists to reduce this defect density and thus the recombination at the surface. The surface recombination velocity (SRV) is a parameter for quantifying the passivation quality.

3.1 Recombination processes

Recombination between electrons and holes occurs by three mechanisms which are radiative, Auger recombination and recombination via defects. This latter will be explained in section 3.2.

3.1.1 Radiative recombination

Radiative recombination [3.1-3.3] is a direct process where electrons from the conduction band loss its energy by emitting a photon with energy equal to the bandgap and fall at an energy level corresponding to the valence band limit where it recombines with a hole. This process is driven by mass action law weighted by the probability coefficient B which depends on the material, particularly its band structure. Relation between recombination rate and injection level Δn (assuming that $\Delta n = \Delta p$) is given by equation 3.1. In the presence of a light source, the generation rate G_{rad} equal to $B.n_i^2$ has to be subtracted in order to have the net recombination rate. This leads to equation 3.2 [3.2].

$$U_{rad} = B.n.p \tag{3.1}$$

$$U_{rad} = B.(n.p - n_i^2) \tag{3.2}$$

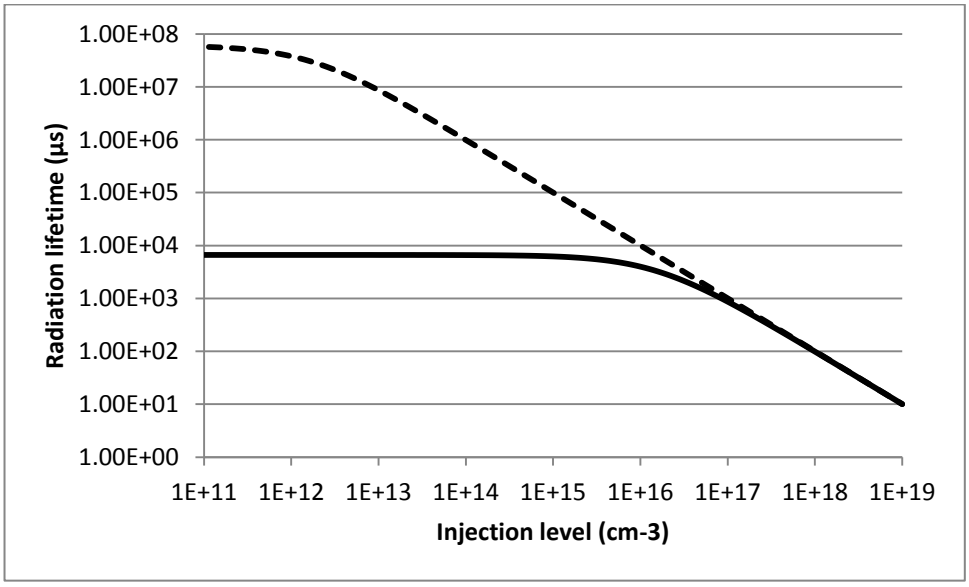

Figure 3.1 Radiation lifetime versus injection level with doping $2.6x10^{11}$ cm^{-3} (dash), $1.5x10^{16}$ cm^{-3}(plain). Since injection level is below $1x10^{16}$ cm^{-3}, the lifetime does not decrease below 10 ms due to radiative recombination. Since lifetime in this work is below 1ms, radiative recombination can be neglected.

For semiconductors with direct band gap such as GaAs, the value of B is much higher than for semiconductors with indirect bandgap such as Si ($B=3.10^{-10}$ $cm^3.s^{-1}$ for GaAs and $B=1.10^{-14}$ $cm^3.s^{-1}$ for Si at room temperature [3.4]). As can be seen in figure 3.1, radiative process can be neglected in the range of our investigation. Indeed it can be seen for both curves that when increasing injection level or doping concentration, lifetime remains constant until a threshold and then decreases rapidly. The lifetime degradation due to radiative recombination starts to be consequent beyond an injection level of 10^{17} cm^{-3} while injection level for solar cells remains in the range 10^{14}-10^{15} cm^{-3} and does not exceed 10^{16} cm^{-3} in our lifetime measurement.

3.1.2 Auger recombination

In Auger recombination process, an electron in conduction band loses its energy excess by transferring it to another particle i.e., an electron or a hole. It is a three particle process which requires energy and momentum conservation and therefore the Auger recombination occur probability is very low. This explains why the effect of Auger does not contribute significantly to a decrease in lifetime except at very high injection level as can be seen in figure 3.2. Considering that recombination only occurs by Auger process, the lifetime of excess carrier is given by equation 3.3.

$$\tau_{CE-Auger} = \frac{n - n_0}{C_n{}^*.(n^2p - n_0{}^2p_0) + C_p{}^*.(np^2 - n_0p_0{}^2)} \tag{3.3}$$

$$C_n{}^* = 2.8.10^{-31}.g_{eeh}.\left(\frac{n_0}{n_0 + \Delta n}\right) + \frac{1.66.10^{30}}{2}\left(\frac{\Delta n}{n_0 + \Delta n}\right) \tag{3.4}$$

$$C_p{}^* = 9.9.10^{-32}.g_{ehh}.\left(\frac{p_0}{p_0 + \Delta p}\right) + \frac{1.66.10^{30}}{2}\left(\frac{\Delta p}{p_0 + \Delta p}\right) \tag{3.5}$$

$$g_{eeh} = 1 + 44\left\{1 - \tanh\left[\left(\frac{Nd}{5.10^{16}}\right)^{0.34}\right]\right\} \tag{3.6}$$

$$g_{ehh} = 1 + 44\left\{1 - \tanh\left[\left(\frac{Na}{5.10^{16}}\right)^{0.29}\right]\right\} \tag{3.7}$$

The graph of figure 3.2 can be drawn from equations 3.3-3.7 [3.2]. It highlights that for silicon doping below $1.5.10^{16}$ cm^{-3} and for low injection level below 1.10^{17} cm^{-3}, Auger recombination is low enough to be neglected. The maximum minority carrier injection under AM1.5 illumination is around $1x10^{14}$ cm^{-3} and $1x10^{15}$ cm^{-3} for very high efficiency solar cells depending on the minority carrier lifetime as will be seen in

chapter 2. Auger recombination does not decrease the lifetime below 1 ms which is a high enough value for our purpose.

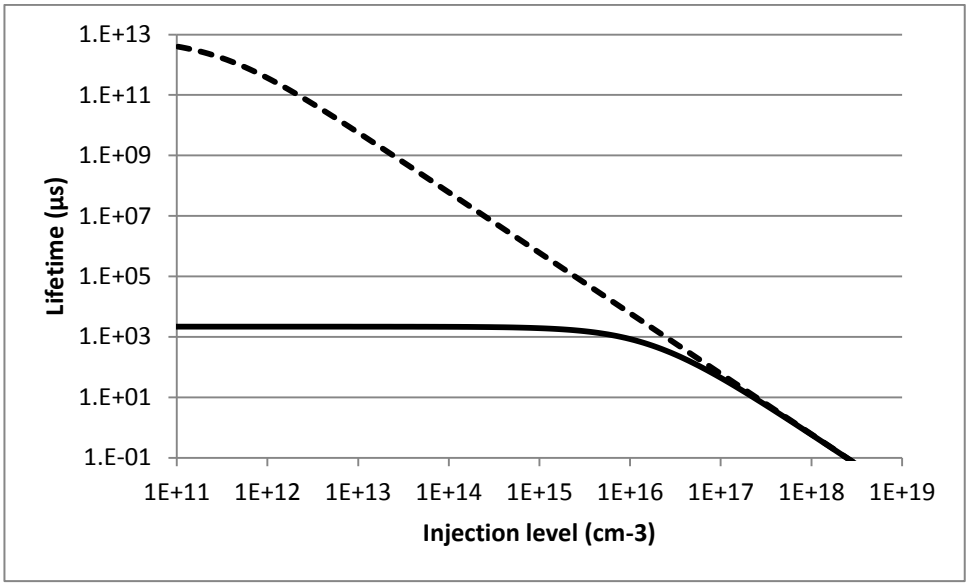

Figure 3.2 Auger lifetime versus injection level with doping $2.6x10^{11}$ cm^{-3} (dash), $1.5x10^{16}$ cm^{-3}(plain). Since lifetime in our samples is always below 1ms, Auger recombination can be neglected.

Similarly to radiative recombination Auger process can be neglected for lifetime determination in the range of our measurement. Therefore the only recombination process which has to be taken in account is recombination via defect.

3.2 Shockley-Read-Hall (SRH) theory

3.2.1 Condition of validity for SRH theory [3.5]

- The defect concentration is very small compared to the doping density.
- The electron and hole distribution is given by Fermi-Dirac statistic
- The semiconductor material is not degenerate. A semiconductor is degenerate for very high doping when electron and hole concentrations are so high that exclusion principle of Pauli has to be taken in account. For our purpose, the doping is lower or equal to $1.5x10^{16}$ cm^{-3} which corresponds to a non-degenerate semiconductor.

- The energy level of a defect is the same when it is occupied by an electron or not. This latter property is assumed to simplify the calculation of the electrons and holes transition rates during capture and emission (section 3.2.4).
- The relaxation time of charge carrier is very low compared to the time between two emissions of electron and hole (section 3.2.4).
- There is no transition occurring from a defect to another.

3.2.2 Direct and indirect band-gap semiconductor

A semiconductor with a direct bandgap is a semiconductor where the minimum difference between the edge of the conduction band and the edge of the valence band in the momentum space, corresponds to the same value of the momentum. On the other hand for an indirect semiconductor, the higher point of the valence band edge and the lower point of the conduction band edge correspond to two different values of the momentum. [3.6]. Recombination process, requires both energy and momentum conservation. The former condition is manifested by photon emission during recombination by radiation process. The energy of this latter is the difference between electron and hole energy. Regarding momentum conservation, two cases have to be considered. If the semiconductor is a direct bandgap semiconductor, then, by definition, the total momentum is conserved after recombination. If the semiconductor is an indirect bandgap one, the total momentum before and after recombination would be different (and consequently not be possible), unless a third term is involved in a way that it balances this difference of momentum.

3.2.3 Recombination rate for direct bandgap semiconductor

- **Calculation of recombination rate**

Recombination rate for a direct bandgap semiconductor can be established by considering the interacting volume described by the electrons during one second. The number of holes in this volume is calculated. This number is also the number of holes encounters per second by the electrons.

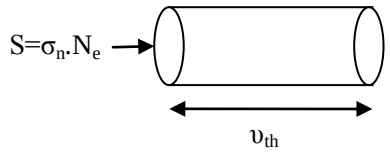

Figure 3.3 Volume of interaction occupied by N_e electron per second. v_{th} is the electron velocity corresponding to thermal excitation. σ_n is electron-hole recombination cross section and S the section corresponding to the volume of interaction.

Since carrier disappears in pairs by recombination, the recombination rate is given by:

$$R_{rate} = \frac{dn}{dt} = \frac{dp}{dt} \tag{3.8}$$

For calculation of R_{rate} let us first consider the interaction volume of an electron moving with the speed v_{th} due to thermal agitation. If the electron is assumed to be a sphere of section S, the electron describes a volume V during the interval of time t:

$$V = S.v_{th}.t \tag{3.9}$$

Actually due to the fact that interaction with electrons does not occur via contact force but coulomb interaction which is a long range force, the electron cannot be considered as a sphere of section S during the interaction but as a particle with an interaction cross section σ_n. Then equation 3.9 becomes:

$$V = \sigma_n.v_{th}.t \tag{3.10}$$

Therefore the interaction volume V_{int} per second (t=1s) of N_e electrons is

$$V_{int} = N_e \sigma_n . v_{th} \tag{3.11}$$

This volume contains the number of hole N_p:

$$N_p = p . V_{int} = p . N_e \sigma_n . v_{th} \tag{3.12}$$

N_p is then the number of holes "encounters" by electrons per second. If the semiconductor has a direct bandgap, every time an electron and a hole interact with each other, there is a recombination and therefore N_p is also the recombination number per second. Recombination rate is usually express as recombination rate per unit of volume. Dividing the second term of equation 3.12 by the volume, N_e becomes n and recombination rate by volume unit R_{rate} is obtained:

$$R_{rate} = \sigma_n . v_{th} . n . p \tag{3.13}$$

It can be remarked that σ_n value is about 10^{-16}-10^{-15} cm^2 [3.1], therefore if electron was consider as a sphere its radius would be in the order of the 0.1 nm which is the scale of the atom. This result is due to the fact that interaction is electromagnetic and not due to physical contact.

- **Net recombination rate**

In the previous section, recombination rate has been calculated in the theoretical case where no electron-hole pairs are generated. Actually, electron-pair are generated due to thermal effect. By definition, at equilibrium, generation rate G_{eq} and recombination rate R_{eq} are balanced:

$$G_{eq} = R_{rate-eq} \tag{3.14}$$

Since $n.p=n_i^2$ at equilibrium, equation 3.14 becomes:

$$G_{eq} = \sigma_n . v_{th} . n_i^2 \tag{3.15}$$

At non equilibrium the net rate of recombination U which is the difference between the recombination rate and the generation rate due to thermal effect is not equal to zero anymore and the combination of equations 3.13 and 3.15 gives:

$$U = R_{rate} - G_{eq} = \sigma_n . v_{th} (n. p. - n_i^2) \tag{3.16}$$

It can be noted that the quantity q.U (where q is the absolute value of the electron charge), represents the net current flowing from the conduction band to the valence band.

- **Approximation of charge carrier lifetime at low injection level**

Equation 3.16 gives equation 3.17 after simplification when considering a small deviation of equilibrium with $n = n_0 + \Delta n$ and $p_0 = p + \Delta p$ with $\Delta n = \Delta p$. This latter condition $\Delta n = \Delta p$ is respected if the impurity concentration is small compared to the doping and if the time of relaxation of the carrier captured by defect are very small compared to their reemission times.

$$U = \sigma_n . v_{th} \left[\left(n_0 + p_0 + (\Delta n) \right) . (\Delta n) \right] \tag{3.17}$$

For low injection condition, if the semiconductor is p-type, then $p_0 >> n_0$ and $p_0 >> \Delta n$, then $p_0 \# p$:

$$U = \sigma_n . v_{th} . p . \Delta n \tag{3.18}$$

By definition:

$$U = -\frac{dn}{dt} = -\frac{d(n_0 + \Delta n)}{dt} \tag{3.19}$$

U=0 at equilibrium therefore:

$$U_{eq} = -\frac{dn_0}{dt} = 0 \tag{3.20}$$

$$U = -\frac{d\Delta n}{dt} = \sigma_n . v_{th} . p . \Delta n \tag{3.21}$$

Equation 3.21 is a first order differential equation and its resolution gives for Δn:

$$\Delta n = \Delta n_0 . e^{-\sigma_n . v_{th} . p . t} \tag{3.22}$$

This can be rewritten with τ given by equation 3.24

$$\Delta n = \Delta n_0 . e^{-.\frac{t}{\tau}} \tag{3.23}$$

$$\tau = \frac{1}{\sigma_n . v_{th} . p} \tag{3.24}$$

For a n-type n and n_0 should be substituted to p and p_0 in equations 3.17-3.23. Introducing τ in equation 3.21 gives:

$$\Delta U = \frac{\Delta n}{\tau} \tag{3.25}$$

3.2.4 Net recombination rate for a semiconductor with indirect bandgap

For an indirect band gap semiconductor like silicon for instance, momentum conservation during recombination requires a third term involved in recombination. It has been seen previously that Auger recombination process has very low probability; therefore almost the totality of recombination occurs via recombination centre or defect which induces intermediate energy levels in the forbidden bandgap. These defects are due to impurity or crystallographic imperfections which act as a trap [3.5] and recombination center [3.7] for charge carrier .Because of this intermediate energy level E_d four transitions rates (figure 3.4) have to be considered: transition of electron from conduction band to the defect or in other words electron capture $U_{ec,}$ emission of electron from the defect to the conduction band U_{ee} , valence band hole capture by a defect U_{hc} and hole emission from a defect to the valence band U_{eh} [3.5, 3.8]. Electron capture by a defect is equivalent to the transition from a state where the defect is empty of electron to a state where the defect is occupied by one electron assuming for simplicity reasons that there are only two possible states for the defect that is to be occupied by an electron or empty (non degenerate semiconductor [3.5]). Regarding hole the former is equivalent to a defect occupied with a hole and the latter to a defect free of hole. For determining these transition rates, the same method as in paragraph on direct band gap is used but now interaction between electron in conduction band and hole in valence band is replaced by interaction between electron with defect free of electron (or hole in defect) and hole with defect occupied by an electron (or empty of hole). In the following sections, the defect number free of electrons is noted N_d^0 and the number of defect occupied by an electron N_d^e and the term empty and occupied defect will designate respectively empty and occupy in regard with electron. It is assumed that the defect energy level is not affected when occupied or empty (cf condition of validity of SRH in 3.2.1).

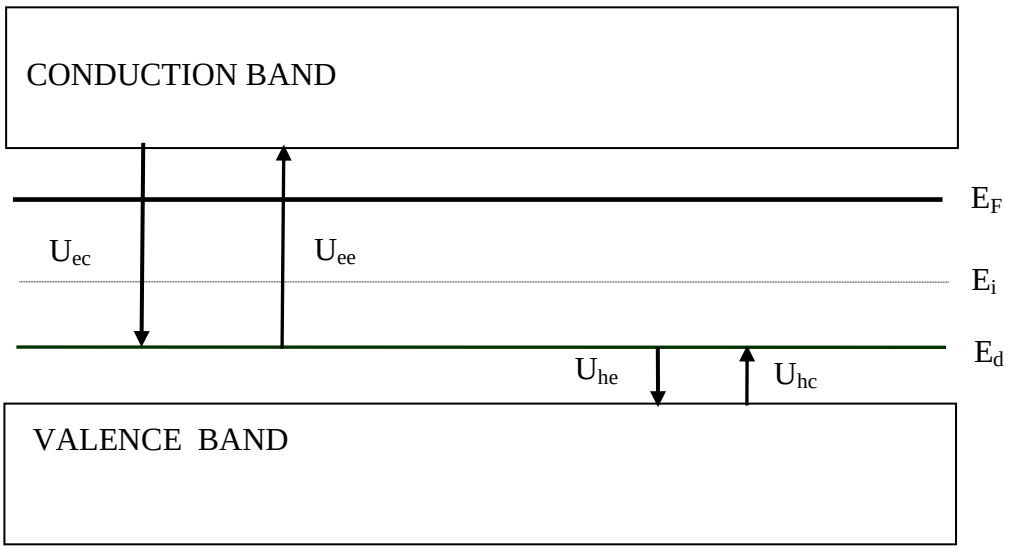

Figure 3.4 Transition modes involved in SRH recombination for a defect with a single energy level E_d. Electron (hole) can be emitted from the defect level toward the conduction (valence) band with an electron (hole) emission rate U_{ee} (U_{he}) and electron in the conduction (valence) band can be captured by the defect with a capture rate U_{ec} (U_{hc}).

- Calculation of electron capture and hole capture transition rate

The expression of the number of empty defects can be deduced by following the same way which had led to equation 3.11,

$$N_d^0 = n_d^0 . V_{int} = n_d^0 . N_e \sigma_n . v_{th} \tag{3.26}$$

The density n_d^e of occupied defects is equal to the density of defect N_d time the probability of occupation. This latter is given by Fermi statistic $f(E_d, T)$.

$$f(E,T) = \frac{1}{1 + e^{\frac{(E_d - E_F)}{K.T}}} \tag{3.27}$$

For simplicity f (E, T) will be noted f. The density of empty defect is then the difference between the defect density and the occupy defects density:

$$n_d^0 = N_d(1 - f) \tag{3.28}$$

After substituting equation 3.28 in equation 3.26 and dividing by the volume, electron capture transition rate U_{ec} is:

$$U_{ec} = \sigma_n . v_{th} . n . N_d (1 - f) \tag{3.29}$$

For calculating hole capture transition rate U_{hc}, the same way drives to a similar relation as equation 3.29 expect that hole cross section σ_p is substituted to σ_n in the calculation of interaction volume, n is replaced by the hole density p, and the density of defect empty of electron n^0_t is substituted by density of defect occupied by one electron n^e_t. The density of defect occupy by an electron is N_d.f.

$$U_{hc} = \sigma_p . v_{th} . p . N_d . f \tag{3.30}$$

- **Calculation of electron emission and hole emission transition rate**

Electron emission density from a defect to the conduction band is proportional to the density of defect occupy by an electron N_d.f. The proportionality coefficient is the electron emission probability [3.5, 3.9] e_n.

$$U_{ee} = e_n . N_d . f \tag{3.31}$$

For having a local equilibrium between the electron capture and electron emission, U_{ec} and U_{ee} should be balanced. After equaling the second terms of equation 3.29 and 3.31 it becomes:

$$e_n = \frac{\sigma_n . v_{th} . n(1 - f)}{f} \tag{3.32}$$

Hole emission density from a defect to the conduction band is proportional to the density of defect free of electron (or in other point of view: occupy by a hole). The proportionality coefficient is the hole emission probability e_p.

$$U_{he} = e_p . N_d . (1 - f) \tag{3.33}$$

$$e_p = \frac{\sigma_p . v_{th} . p . f}{1 - f} \tag{3.34}$$

Using the expression of Fermi statistic (equation 3.27) it comes:

$$\frac{1 - f(E_d , T)}{f(E_d , T)} = e^{\frac{(E_d - E_F)}{k.T}} \tag{3.35}$$

Therefore:

$$e_n = \sigma_n . v_{th} . n . e^{\frac{(E_d - E_F)}{k.T}} = \sigma_n . v_{th} . n_i e^{\frac{(E_d - E_i)}{k.T}} = \sigma_n . v_{th} . n_1 \tag{3.36}$$

$$n_1 = n_i e^{\frac{(E_d - E_i)}{k.T}} \tag{3.37}$$

The term n_1 is the density of electron in the conduction band issue from the energy level E_d due to thermal agitation in agreement with Boltzmann statistic. Similarly if we call p_1 the hole density in the valence band issue from the defect E_d:

$$e_p = \sigma_p . v_{th} . p . e^{-\frac{(E_d - E_F)}{k.T}} = \sigma_p . v_{th} . n_i e^{-\frac{(E_d - E_i)}{k.T}} = \sigma_p . v_{th} . p_1 \tag{3.38}$$

$$p_1 = n_i . e^{\frac{-(E_d - E_i)}{k.T}} \tag{3.39}$$

Net recombination of electrons U_e and net recombination of hole U_h is given respectively by equations 3.40 and 3.41.

$$U_e=U_{ec}-U_{ee}=\sigma_n.v_{th}.N_d[n.(1-f)-n_1.f)] \tag{3.40}$$

$$U_h = U_{hc} - U_{he} = \sigma_p.v_{th}.N_d[p.f - p_1(1-f)] \tag{3.41}$$

Under steady state condition (this condition will have to be considered for SRV measurement described in section 3.5.1), a local equilibrium is reached between the electrons and the holes current. Therefore, U_e and U_h are balanced and equal to the net recombination rate. This latter can be determined either from equations 3.40 or 3.41 .However in order to include the steady state condition i.e., $U_e = U_h = U$, the defect occupation probability f of an electron is extracted from the resolution of equation $U_e = U_h$ .This gives the following relation:

$$f = \frac{\sigma_n.n + \sigma_p.p_1}{\sigma_n(n+n_1) + \sigma_p(p+p_1)} \tag{3.42}$$

It can be noted that equation 3.42 is actually the Fermi level determination. Substituting equation 3.42 into equation 3.40 (or 3.41) gives after simplification the net recombination rate U:

$$U = \frac{N_d.v_{th}(n.p - n_i^2)}{\frac{(n+n_1)}{\sigma_p} + \frac{(p+p_1)}{\sigma_n}} \tag{3.43}$$

This relation can be extended to a quasi-continuum distribution of energy level in the bandgap [3.1] and gives the extended SRH:

$$U = v_{th}(n.p - n_i^2).\int_{E_v}^{E_c} \frac{D(E)}{\frac{(n + n_1(E))}{\sigma_p(E)} + \frac{(p + p_1(E))}{\sigma_n(E)}}\, dE \tag{3.44}$$

In summary, recombination rate is obtained by resolving 3 relations of local equilibrium: the balance of electrons capture and the electrons emission between the defect energy level and the conduction band, the holes capture and emission between the defect and the valence band and a dynamic equilibrium between the net recombination electrons and holes currents. This third condition corresponds to the Fermi level determination. The final expression of U is therefore the synthesis of these 3 relations. Thus in order to interpret the result for different cases, it is easier to analyse these relations separately.

- **Lifetime approximation**

Considering a small deviation of equilibrium with $n = n_{eq} + \Delta n$ and $p_{eq} = p + \Delta p$ with $\Delta n = \Delta p$, equation 3.43 gives after simplification:

$$U = \frac{N_d.v_{th}.[(n_0 + p_0 + (\Delta n)).(\Delta n)]}{\frac{(n_0 + \Delta n + n_1)}{\sigma_p} + \frac{(p_0 + \Delta n + p_1)}{\sigma_n}} \tag{3.45}$$

In the case of p-type semiconductor and defect around mid-gap (deep level), $n_1 \# p_1 \# n_i$ $n_i << p$. At low injection, $p >> \Delta n$ therefore $p_{eq} \# p$. Equation 3.45 becomes after approximation:

$$U = \frac{N_d.v_{th}.p.\Delta n}{\frac{n_0}{\sigma_p} + \frac{p}{\sigma_n}} \tag{3.46}$$

Since $n/\sigma_p << p/\sigma_n$:

$$U = \sigma_n . v_{th} . N_d . \Delta n \tag{3.47}$$

Using the same considerations as equations 3.18-3.20, a differential equation similar as equation 3.21 appears where N_d is substituted to p. This drives to the minority carrier or excess charge carrier lifetime:

$$\Delta n = \Delta n_0 . e^{-.\frac{t}{\tau}} \tag{3.48}$$

$$\tau_{n0} = \frac{1}{\sigma_n . v_{th} . N_d} \tag{3.49}$$

For an n-type:

$$\tau_{p0} = \frac{1}{\sigma_p . v_{th} . N_d} \tag{3.50}$$

Therefore lifetime can be written as in equation 3.25:

$$U = \frac{\Delta n}{\tau} \tag{3.51}$$

- Effect of defects energy level

In equation 3.43, n_1 and p_1 depend on the energy level E_d of the defect,

$$n_1 = n . e^{\frac{(E_d - E_i)}{k.T}} \tag{3.52}$$

$$p_1 = n_i . e^{\frac{-(E_d - E_i)}{k.T}} \tag{3.53}$$

Figure 3.5 represents the ratio between the lifetime τ and τ_{n0} where τ_{n0} is the lifetime given in equation 3.49, for a defect in the mid-gap versus the defect position inside the band gap ($E_d = E_v+0.6$ eV). On this figure, the ratio of σ_n to σ_p is 0.145. This ratio has been chosen because it corresponds to the mean value of the ratio σ_n to σ_p integrated on the energy level of the defect used for SRV calculation as will be seen further. However, the result is similar if $\sigma_n = \sigma_p$ except that the curve is perfectly symmetric [3.1]. If σ_n is higher than σ_p, the lifetime is higher for defect near the conduction band. It can be seen on figure 3.5 that the lifetime decreases by several orders of magnitude when the defect position approaches the mid-gap and then there is an interval where the lifetime is equal to τ_{n0}. The broadness of this interval where lifetime remains at a minimum increases with the doping: For a high doping of 10^{18} cm^{-3}, the lifetime is equal to τ_{n0} almost all along the band gap expect near the edge where it becomes about 10 times higher near the conduction band and 100 times higher near the valence band. On the other hand for a doping of $1.7x10^{12}$ cm^{-3} corresponding to the 8000 ohm.cm FZ wafer, the minimum is much localized and at the edge the lifetime increases strongly.

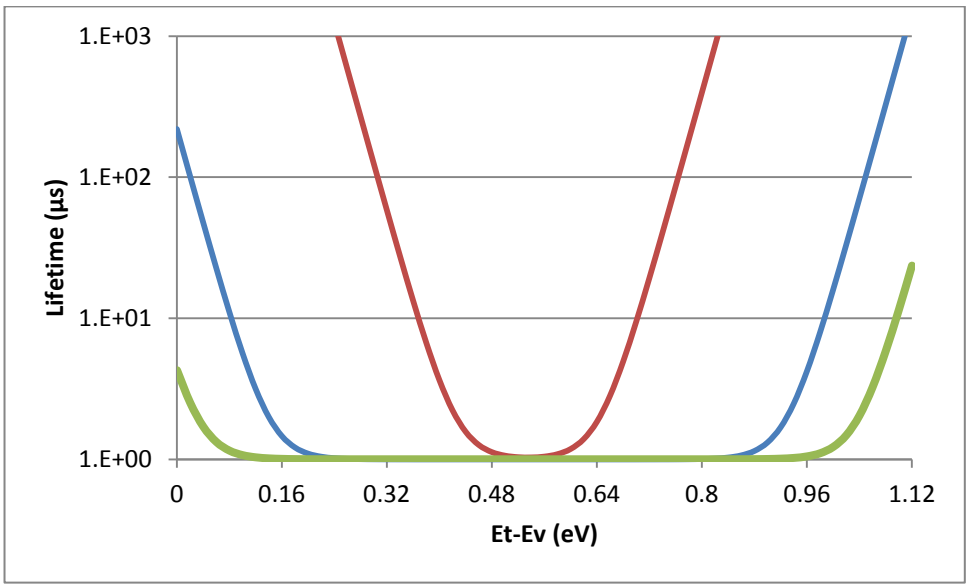

Figure 3.5 Variation of lifetime versus energy position for a single defect energy level Na=10^{18} (green), $1.5x10^{16}$ (blue) and $2.6x10^{11}$ cm^{-3} (red). The lifetime is higher for defect near the conduction band (E_t-E_v > 0.6) because electron capture cross section is lower on this example than hole capture cross section.

The effect of defect could be further studied with the 3 local equilibriums of section 3.2.4 from which recombination rate and SRV are deduced. For instance if the defect level E_d is closer to the conduction band E_c, n_1 increases (equation 3.52) resulting in an increase of the Fermi level E_F. When E_F is higher, the defect occupation probability $f(E_d, T)$ is lower and electron capture increases. Eventually it has to be added that a there is a critical density value N_{crit} which is strongly dependent on the defect energy position and which reaches a maximum for mid-gap defect. If the number of defects is very higher than N_{crit} thus the SRH theory is not valid anymore [3.10]. N_{crit} is given for a mid-gap defect by

$$N_{crit} = N_A . \frac{\sigma_p}{\sigma_n} \tag{3.54}$$

However, the defect density for a passivating film is around 1.10^{11} and the σ_p to σ_n ratio is equal to 10, thus for the lower doping density that we use in this study ($2.6x10^{11}$ cm^{-3}), N_{crit} is $2.6x10^{12}$ cm^{-3}. Therefore the SRH theory can be applied with our samples.

3.3 Extended SRH and surface recombination velocity (SRV).

SRV [3.11, 3.12] is a parameter used for characterising the recombination rate U_s at the surface. For a better understanding it has to be recalled that the surface is not a real surface (in the mathematical signification) but a very thin volume. Therefore surface recombination rate and the bulk recombination rate have qualitatively the same meaning. Their difference comes from the fact that at this very thin volume near the surface, the recombination rate is higher. SRV is expressed in cm/s and its relation with U_s, Δn and the wafer thickness is

$$U_S = \frac{S . \Delta n}{W} \tag{3.55}$$

By comparison of equations 3.54 and 3.51, a lifetime at the surface can be deduced:

$$\tau_S = \frac{W}{S} \tag{3.56}$$

SRV only depends on the surface quality of the wafer whereas the lifetime at the surface also depends on the wafer thickness: when the thickness of the wafer decreases the lifetime decreases. Therefore although less intuitive than surface lifetime, SRV is used for characterising the quality of the surface. The reason of the higher rate at the surface for a non passivated surface is the higher density of defect inducing energy level inside the bandgap. Indeed due to the asymmetry of the surface, defects induced a continuum of energy levels in the band gap mostly originated from silicon dangling bond as will be seen in chapter 5. Passivation decreases the defect density but does not remove this continuum. Therefore the determination of the recombination rate at the surface has to be integrated on this energy interval with the expression of the extended SRV given in equation 3.44. Another effect of passivation under Si substrate is the trapping of charge generally positive which repel the holes and attract the electron [3.13]. Therefore the equality between electrons in the conduction band and holes in the valence band is broken and has to be determined in order to calculate the surface recombination rate. The effect of fixed charge on passivation is either to increases or decreases the SRV depending on the fixed charge density, the excess carrier injection level and the wafer doping as will be seen further.

3.3.1 Effect of defects energy level distribution

The effect of the position of a defect has been seen section 3.2.4. A defect can induce energy levels in the bandgap. This level distribution is around a maximum value. The broadness of a mid-gap defect is expected to have a great impact for the high doped wafer, since the minimum value of the lifetime has a great extension as seen in figure 3.6. On the other hand, the broadness of level distribution is not important for a mid-gap defect on a low doped wafer.

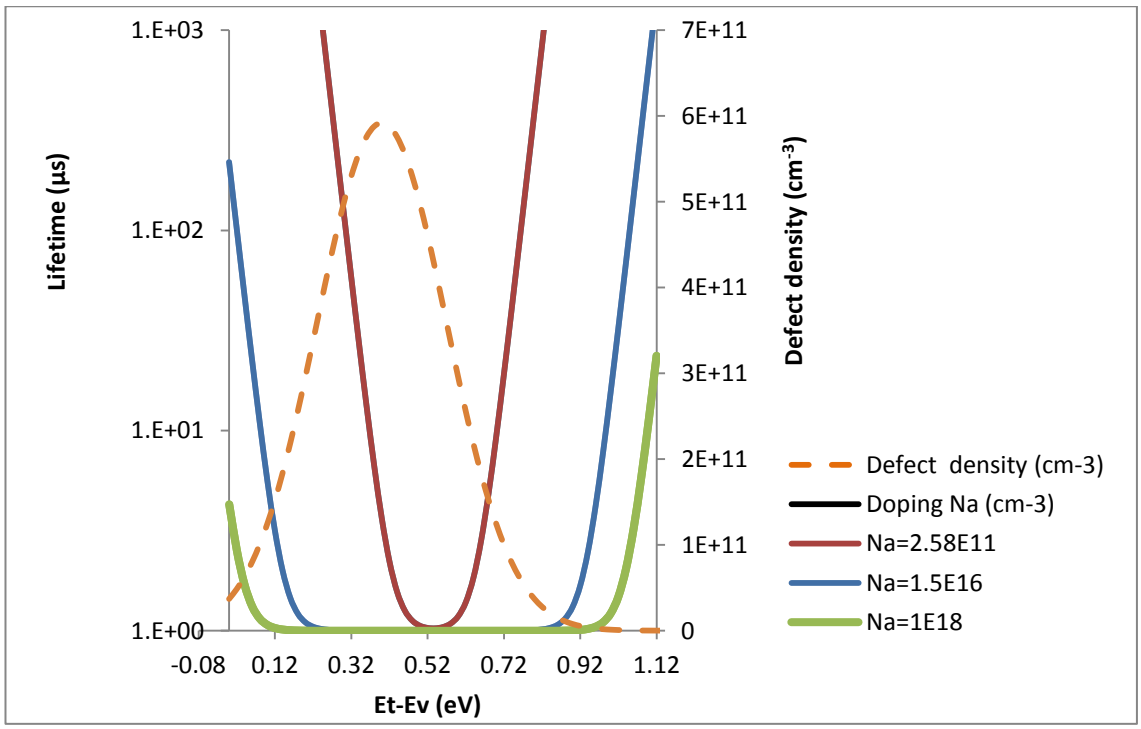

Figure 3.6 Lifetime and Gaussian defect density versus energy position of a defect energy level density centered 0.4 eV above the valence band with a FWHM equal to 0.115 eV and a maximal defect energy density of 5.9×10^{11} $cm^{-2}.eV^{-1}$. On this example, it can be seen that for the higher doping, the peak corresponds to the lifetime value of mid-gap defect where as it varies for more than 2 orders of magnitude for a doping of 2.58×10^{11} cm^{-3}.

3.3.2 Effect of fixed trapped charge at the interface

- **Effect of fixed charge at the silicon-insulator interface**

Considering that n_s and p_s are respectively the electrons and holes concentration at the surface and N_{sd} the number of defects at this surface equation 4.43 can be rewritten

$$U_s = \frac{N_{sd}.v_{th}(n_s.p_s - n_i^2)}{\frac{(n_s + n_1)}{\sigma_p} + \frac{(p_s + p_1)}{\sigma_n}} \tag{3.57}$$

$$S_{eff} = \frac{U_s}{\Delta n} \tag{3.58}$$

The effective SRV S_{eff} is given by equation 3.58. The effect of fixed charge at the insulator-silicon interface is to induce an electric-field that breaks the equality between

electrons excess and holes excess i.e., Δp is not equal anymore to Δn and both depend on the difference between the potential at the semiconductor-insulator interface and the potential in the semiconductor beyond the depletion region .Therefore this difference of potential has to be known in order to determine n_s and p_s. If the potential at the edge of depletion is taken as a reference and the potential at the surface is ψ_s, Boltzmann statistic gives the relation between carrier concentration at the surface and ψ_s [3.1]:

$$n_s = n_d . e^{\frac{q.\psi_s}{k.T}} \tag{3.59}$$

$$p_s = p_d . e^{\frac{-q.\psi_s}{k.T}} \tag{3.60}$$

With n_d and p_d being respectively the carrier concentration at the edge of the depletion region. At the edge of the depletion region and beyond it, the effect of the fixed charge is negligible and the excess concentration of holes and electrons are equal: $\Delta p = \Delta n$. Therefore considering a p-type semiconductor, if the charge carrier concentration of electrons and holes beyond the depletion region are respectively n_{p0} and p_{p0}:

$$n_d = n_{p0} + \Delta n \tag{3.61}$$

$$p_d = p_{P0} + \Delta n \tag{3.62}$$

The relation between excess carrier and the quasi-Fermi levels of electrons Φ_n and hole Φ_p are obtained [3.1] from Boltzmann statistic:

$$n_d = n_i . e^{\frac{-q.\phi_n}{k.T}} \tag{3.63}$$

$$p_d = n_i . e^{\frac{+q.\phi_n}{k.T}} \tag{3.64}$$

- **Relation between fixed charge and the potential at the surface**

Charge neutrality of the system semiconductor/insulator implies that $Q_{si} + Q_{it} + Q_f = 0$ where Q_{Si} is the charge density induced into the silicon substrate by the electric field E_S resulting from the fixed charge Q_f within the native oxide at the interface and Q_{it} is the trap charged density in the defects. For calculation simplicity we assume that there is no charge due to defects $Q_{it}=0$ [3.14] therefore:

$$Q_f = Q_{Si} \tag{3.65}$$

The dielectric constant of Si being ε_{si}, it results from Gauss law:

$$Q_{Si} = -\varepsilon_{Si} \, . \, E_S \tag{3.66}$$

- Model abrupt junction: calculation of the surface potential

The calculation of the surface potential as a function of the fixed charge Q_f has been obtained by adapting the calculation of Sze [2.3] p 367 which gives a demonstration of the relation between the surface potential, the fixed charge and the electric field when there is no excess carrier that is when $\Delta n = 0$. When the wafer is illuminated, the injection level has to be integrated in this relation. In order to include the effect of illumination, the relation 3.63 and 3.64 between quasi-fermi levels of electrons and holes with respectively electrons and holes excess given by Aberle in reference [3.1] have been integrated in the calculation of Sze. In this calculation, N_a and N_d are respectively the acceptors and the donor concentration and p_p and n_p are respectively the holes and the electrons concentration. E is the electric field induced by the fixed charge density.

Maxwell equation gives:

$$\frac{dE}{dx} = -\frac{q}{\varepsilon_{si}}\left(N_a - N_d + p_p - n_p\right)\Big) \tag{3.67}$$

The expression of n_p and p_p are obtained by the substitution of the expression of n_d and p_d from respectively equations 3.63 and 3.64 respectively in equations 3.59 and 3.60:

$$n_p = n_i . e^{\frac{q(\psi - \Phi_n)}{k.T}} \tag{3.68}$$

$$p_p = n_i . e^{\frac{-q(\psi - \Phi_p)}{k.T}} \tag{3.69}$$

Equation 3.67 becomes:

$$\frac{dE}{dx} = -\frac{q}{\varepsilon_{si}} . n_i . \left(\frac{N_A - N_D}{n_i} + e^{\frac{-q.(\psi - \Phi_p)}{k.T}} - e^{\frac{q.(\psi - \Phi_n)}{k.T}} \right) \tag{3.70}$$

By definition:

$$E = -\frac{d\psi}{dx} \tag{3.71}$$

Therefore:

$$\frac{d^2\psi}{dx^2} = -\frac{q}{\varepsilon_{si}} . n_i . \left(\frac{Na - Nd}{n_i} + e^{\frac{-q.(\psi - \Phi_p)}{k.T}} - e^{\frac{q.(\psi - \Phi_n)}{k.T}} \right) \tag{3.72}$$

$$\int_0^{\psi} \left(\frac{d^2\psi}{dx^2}\right) d\psi = \int_0^{\psi} \left(\frac{d^2\psi}{dx . dx}\right) d\psi = \int_0^{d\psi/dx} \left(\frac{\partial\psi}{\partial x}\right) d\left(\frac{\partial\psi}{\partial x}\right) \tag{3.73}$$

$$\int_0^{\psi} \left(\frac{d^2\psi}{dx^2}\right) d\psi = \int_0^{d\psi/dx} \left(\frac{d\psi}{dx}\right) d\left(\frac{d\psi}{dx}\right) = \int_0^{-E} -E \, dE = \frac{1}{2} \; E^2 \tag{3.74}$$

Substituting the second term of equation 3.72 in the first term of equation 3.74:

$$E^2 = -2 . \frac{q}{\varepsilon_{si}} . n_i . \int_0^{\psi} \left(\frac{Na - Nd}{n_i} + e^{\frac{-q.(\psi - \Phi_p)}{k.T}} - e^{\frac{q.(\psi - \Phi_n)}{k.T}} \right) d\psi \tag{3.75}$$

$$E^2 = \frac{2.n_i.k.T}{\varepsilon_{si}}\left(\frac{Na-Nd}{k.T.n_i}q.\psi + e^{\frac{-q.(\psi-\Phi_p)}{k.T}} - e^{\frac{q.\Phi_p}{k.T}} + e^{\frac{q.(\psi-\Phi_n)}{k.T}} + -e^{\frac{-q.\Phi_n}{k.T}}\right) \quad (3.76)$$

$$E = \pm\sqrt{\frac{2.k.T.n_i}{\varepsilon_{si}}F(\psi,\Phi_n,\Phi_p)} \quad 3.76\ b)$$

With k.T. expressed in Joule

$$F(\psi,\Phi_n,\Phi_p) = \frac{Na-Nd}{k.T.n_i}q.\psi + e^{\frac{-q.(\psi-\Phi_p)}{k.T}} - e^{\frac{q.\Phi_p}{k.T}} + e^{\frac{q.(\psi-\Phi_n)}{k.T}} + -e^{\frac{-q.\Phi_n}{k.T}} \quad (3.77)$$

Therefore using equation 3.76 b:

$$Q_{Si} = -\varepsilon_{Si}.E_S = \mp\sqrt{2.k.T.n_i.\varepsilon_{si}.F(\psi_s,\Phi_n,\Phi_p)} \quad (3.78)$$

$Q_{si} > 0$ if $\psi_s < 0$ and $Q_{si} < 0$ if $\psi_s > 0$.

3.4 Implementation of SRV at a given Q_f

It has to be recalled that the aims of the implementation is to determine ψ_s in order to solve equations 3.59 and 3.60 which give the negative and positive charge carriers respectively n_s and p_s at the surface for a given fixed charge Q_f. However if Q_f can be calculated from equation 3.78 knowing ψ_s, Φ_n and Φ_p, ψ_s cannot be directly extracted from equation 3.78 which is self consistent since E_s is also connected to ψ_s. Therefore an arbitrary value of ψ_s is chosen at a given carrier injection level and Q_{si} is calculated with equation 3.78. This calculated value is compare to the fixed charge. If the relative error is higher than 1/1000, another value of ψ_s is chosen using dichotomy method for approaching Q_f. When this value is reached, the values of n_s and p_s are calculated with equations 3.59 and 3.60 and S_{eff} is determined by equations 3.57 and 3.58. This operation is repeated for each level of injection and therefore S_{eff} can be expressed as a

function of injection level for a given fixed charge. The following figures used a defect with a Gaussian energy distribution with a maximum at $3.5x10^{10}$ $cm^{-2}.eV^{-1}$, a broadness of 0.577 eV and hole and electron capture cross section respectively σ_p and σ_n given further . Figure 3.7 is for a doping of $1.5x10^{16}cm^{-3}$ which corresponds to a wafer with a resistivity of 1ohm.cm). For studying the effect of the doping on the SRV at a given value of Q_{Si}, ψ_s versus the injection level is determined with the previous implementation for different doping. The corresponding curve is represented in figure 3.8 for a fixed charge density equal to $1x10^{11}$ cm^{-2}.

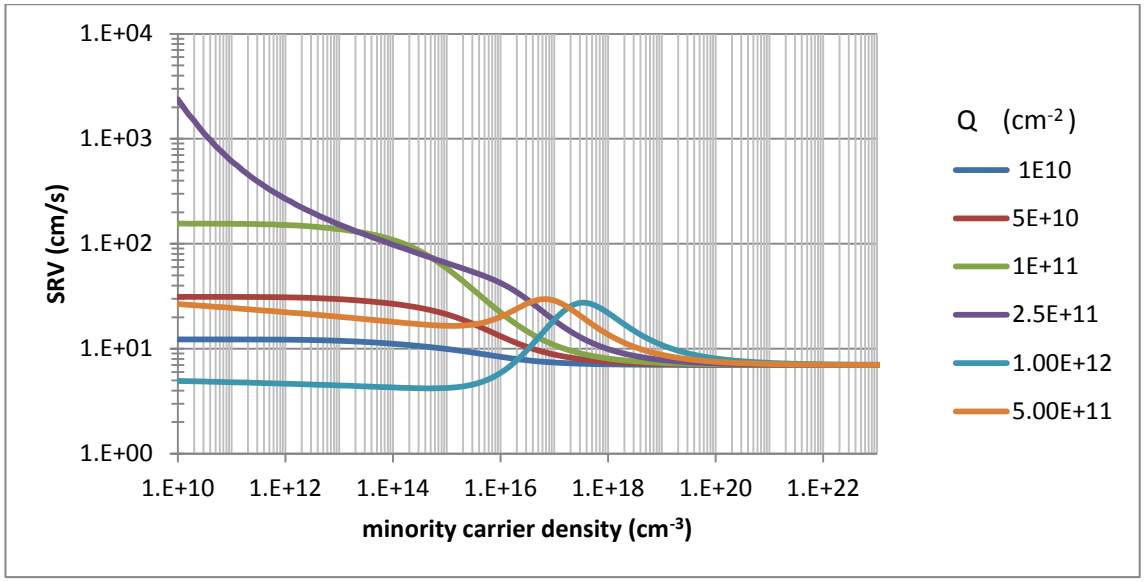

Figure 3.7 Evolution of the SRV versus injection level for different fixed charge density Q_f. The doping of the wafer is $1.5x10^{16}$ cm^{-3}. The defect Gaussian energy level density is centered at 0.4 eV above the valence band with a maximum equal to $3.5x10^{10}$ $cm^{-2}.eV^{-1}$ and a FWHM of 0.115 eV. At low injection levels 3 regimes can be distinguished depending on the range of Q_f. When Q_f increases from $1x10^{10}$ to $1x10^{11}$ cm^{-3}, electron concentration is very below hole concentration at the surface and the SRV increases with Q_f because recombination is limited by electron concentration which increases with Q_f. Then for Q_f above $5x10^{11}$ cm^{-3}, the SRV decreases with Q_f because of the strong inversion: hole concentration is very below electron concentration and recombination is limited by hole concentration which decreases with Q_f. Between this 2 regime, there is a range where electron and hole concentration have the same order of magnitude. Recombination is then very high. The curve with Q_f=$2.5x10^{11}$ cm^{-2} is in this intermediate regime.

The effect of the surface charge is to break the balance between the electrons density Δn_s and the holes density Δp_s at the surface. The extremes cases are when Δn_s is very lower than Δp_s and when Δn_s is very higher than Δp_s. For understanding figure 3.7 the

occupation state of the defects energy level versus injection level has to be analysed. It is given by the Fermi-statistic f (E_d, T). For simplification a defect with a single energy level at mid-gap can be considered ($E_d = E_i$).

$$f(E,T) = \frac{1}{1 + e^{\frac{E_d - E_F}{k.T}}} \tag{3.79}$$

For a small injection that is $\Delta n << p_0$, the Fermi level EF is closed to the valence band and thus $E_i - E_F >> kT$, therefore f (E_i, T) $\rightarrow$0.Therefore all of the defects are almost free of electron (or in other sight of view occupied by a hole) and the recombination process occurs by electrons capture. When Δn increases E_F increases toward E_i , and f(E,T) increases (cf. equation 3.79) .However, the electron capture remains predominant until E_i-E_F is close to kT (0.026eV at 300K). At high injection when $\Delta n >> p_0$, the hole and electron concentration at the surface respectively ns and ps becomes almost equal and E_i # E_F, f$\rightarrow$0.5 thus, the electron and hole capture becomes equivalent if the electron and hole capture cross sections are equals. Otherwise, the electron to hole capture ratio is equivalent to the electron to hole capture cross section ratio. The effect of the fixed charge Q_f is to attract the electron at the surface and then $n_s >> \Delta n$. If Q_f is low, $n_s << p_s$. In this low Q_f range, the increase of Q_f resulting in an increase of ns and a decrease of p_s induces an increase of the SRV since increasing n_s is equivalent to increase the electrons capture. This explains why the SRV increases from $Q_f = 1x10^{10}$ to $Q_f = 2.5x10^{11}$cm-2. On the other hand, when the charge becomes high enough for having $n_s >> p_s$ even at small injection, E_F is then closer to the conduction band, $E_i - E_F << kT$ and f $\rightarrow$ 1, which means that the defects are saturated by electrons. Thus the recombination process can only occurs by holes capture. Since p_s is very lower than the injection level Δn, the SRV is strongly reduced. With a further increase of Q_f, p_s becomes further lower and the SRV is further reduced. This explains why the SRV is lower at $Q_f = 1x10^{12}$ cm^{-2} than $5x10^{11}$ cm^{-2}. When the injection level increases, E_F decreases toward E_i and the situation is the same as for low charge. This explains why at very high injection the SRV has the same value whatever is Q_f. In the case of SiN_x, defects induce an energy level distribution centred between the mid-gap and the valence band (more precisely 0.4 eV above the valence band). If the doping is high enough to ensure that E_F is closer to E_V than E_d, the situation at low injection and in the low Q_f range, is the same as for mid-gap defect except that the electrons capture and electron

capture becomes equivalent when E_F # E_d .Since $E_F - E_d < E_F - E_i$, this situation occurs for a lower injection level than mid-gap defect because (for application, cf section 4.2.2 with $Q_f = 0$). Furthermore when p_s and n_s becomes almost equal, that is at high injection, $E_F = E_i$ and then f (E, T) → 1, the recombination is thus dominated by hole capture. In the case of a low doping E_F is further closer to E_d and a lower Q_f than in the case of high doping is enough for having $n_s >> p_s$. For high injection, f (E, T) → 1 as has seen for the previous case.

- **Effect of the doping to the SRV**

The doping concentration of majority carrier is the reference for the range of injection level (low, intermediate or high). The explanation of section 3.2.4 can be taken for different doping. From $p_0 = 1x10^{15}$ to $1.5x10^{16}cm^{-3}$, the SRV behaviour corresponds to the low Q_f because $n_s << p_s$. On the other hand for $p_0 = 2.6x10^{11}cm^{-3}$,the situation corresponds to high since $n_s >> p_s$ (cf section 4.1.4 for the value of n_s and p_s)

$$n_s = (n_0 + \Delta n).e^{\frac{q.\psi_s}{k.T}} \quad (3.80)$$

$$p_s = (p_0 + \Delta n).e^{\frac{-q.\psi_s}{k.T}} \quad (3.81)$$

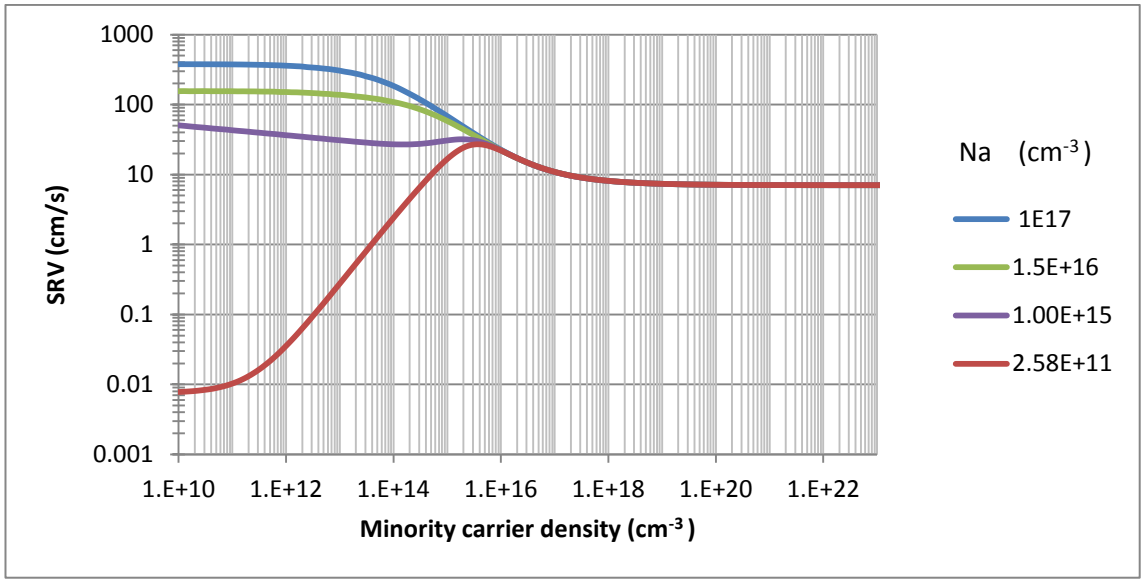

Figure 3.8 Evolution of the SRV versus injection level for different doping level for a fixed charge density Q_f equal to $1x10^{11}$ cm^{-2}. The defect Gaussian energy level density is centered at 0.4 eV above the valence band with a maximum equal to $3.5x10^{10}$ $cm^{-2}.eV^{-1}$ and a FWHM of 0.115 eV. The curve with $Na=1.5x10^{16}$ corresponds to figure 3.7 ($Q_f=1x10^{11}$ cm^{-2}). It can be seen that the regime of Q_f depends on the doping. For $Q_f=1x10^{11}$ cm^{-2} is in the range of the low Q_f for high doping, intermediate Q_f for $Na=1x10^{15}$ cm^{-3} and the regime of high Q_f for low doping ($2.58x10^{11}$ cm^{-3}) where strong inversion occurs.

3.5 Application to silicon wafer passivated with silicon nitride films (SiN_x)

3.5.1 Simulation of recombination rate

Recombination rate is calculated with equation 3.44. The variation of energy level density D(E), hole and electron capture cross sections σ_n and σ_p and p_1 and n_1 with energy requires determining these profiles. On the other hand n_s which does not depend on energy level is the only parameter which depends on the fixed charge Q_f. Therefore energy dependence and charge dependence can be treated separately.

3.5.2 Energy density of defects in silicon wafer passivated with SiN_x film

Schmidt has reported that three major defects which he has labeled A, B and C in SiN_x films that induce energy levels with gauss distributions. However σ_p to σ_n ratio is 10^4 for the defect A, 10 for the defect B and below 1 for C [3.14]. Therefore as explained in section 3.6 the effect on SRV of defect A and B can be neglected in regard with defect C.

$$D(E) = D(E_0).\, e^{-\frac{(E-E_0)^2}{2.\sigma^2}} \tag{3.82}$$

Three parameters are enough for determining one function which are the maximum $D(E_0)$, around 1-10x10^{11} $eV^{-1}.cm^{-2}$ [3.15] which correspond to a defect density in the range 10^{15}-10^{17} cm^{-3} [3.16, 3.17], the most probable energy E_0 and the width of the gauss peak at mid length σ. These parameters were determined from the shape of the curves figure 5.34 in reference [3.1] and the correction used for fit in figure 5.34 in the same reference. Figure 3.9 shows the distribution of three defects. The defect number 3 corresponds to the major defect determined by Aberle in reference [3.1]. Defects 1 and 2 have the same parameters except that defect 1 is centered at 0.6 eV from the valence band which corresponds to mid-gap and defect 2 is centered at 0.8 eV whereas defect 3 is centered at 0.4 eV. Defects 1 and 2 are chosen for illustrating the effect of the defect position. It has to be recalled that the configuration of defects and the capture cross sections of electrons and holes are not always the same for different samples [3.1, 3.18, and 3.19]. Furthermore, the defect 3 corresponds to SiN_x film and in this work a-Si:H has also been deposited, therefore the defects are not expected to be the same nor the

energy level distributions induced by these defects. Although energy level distribution is the result of the individual defect summation, this latter can be modeled by a single Gaussian distribution in the scope of this study. The results of simulations with defect centered at mid-gap and near the conduction band are presented in order to give indications for fitting the results. Regarding capture cross sections of electrons and holes, the case with maximum hole to electron capture cross section corresponds to the case of the defect C. The other cases, which either have equal maximum electron and hole capture cross sections or have maximum hole capture below the electron capture cross section are used to illustrate the effect of electron to hole capture cross section ratio.

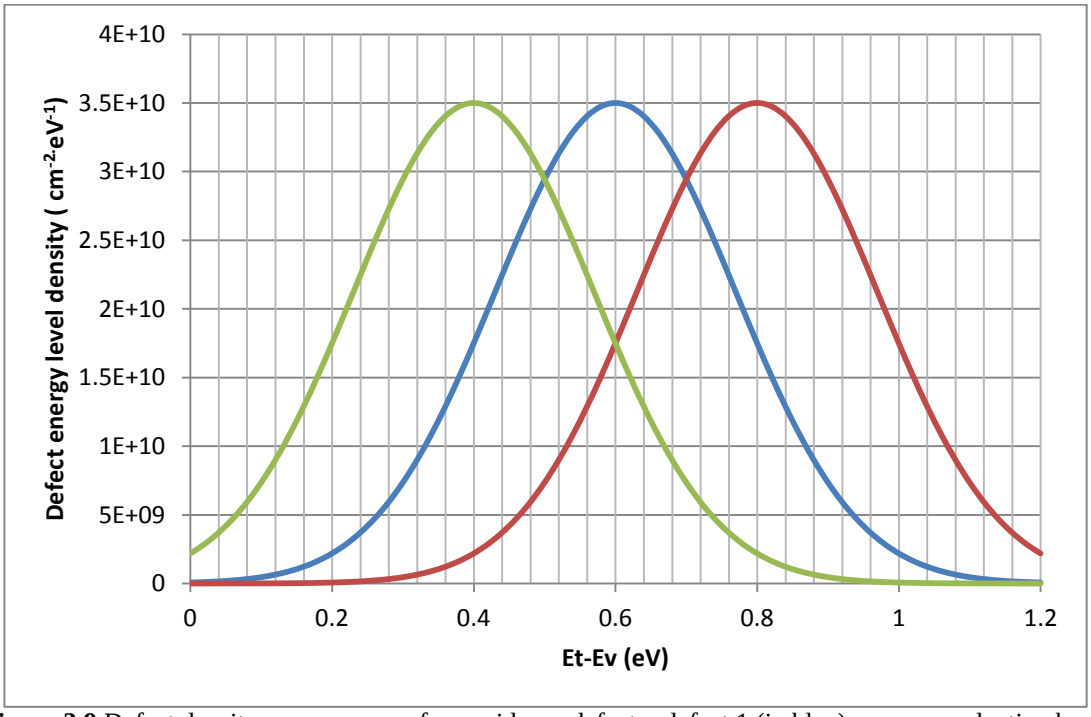

Figure 3.9 Defect density versus energy for a mid-gap defect: defect 1 (in blue), a near conduction band defect : defect 2 (in red) and a near valence band defect: defect 3 (in green). The defect density is a Gauss function with a maximum equal to 3.5×10^{10} $cm^{-2}.eV^{-1}$, a FWHM of 0.115 eV and centred at 0.6 eV for defect 1, 0.8 eV for defect 2 and 0.4 eV for defect 3.

3.5.3 Hole and electron capture cross section

It is assumed that the function of σ_n and σ_p follows the law:

$$\sigma(E) = \sigma_0 . e^{\alpha(E_d - Ev)} \quad (3.83)$$

α and σ_0 were determined from the shape of the curves figure 5.34 in reference [3.1]. Figures 3.10-3.12 represent the electrons and holes capture cross sections versus energy level. The energy level densities of 3 defects are also represented. It can be seen that when the energy level distribution is centered near the valence band (defect 3), the holes capture is higher than the electrons capture and reversely for a defect centered near the conduction band (defect 1). For the defect 3, the mean electron capture is 1.45 much higher than the hole capture if the maxima of σ_n and σ_p are the same (case 2).

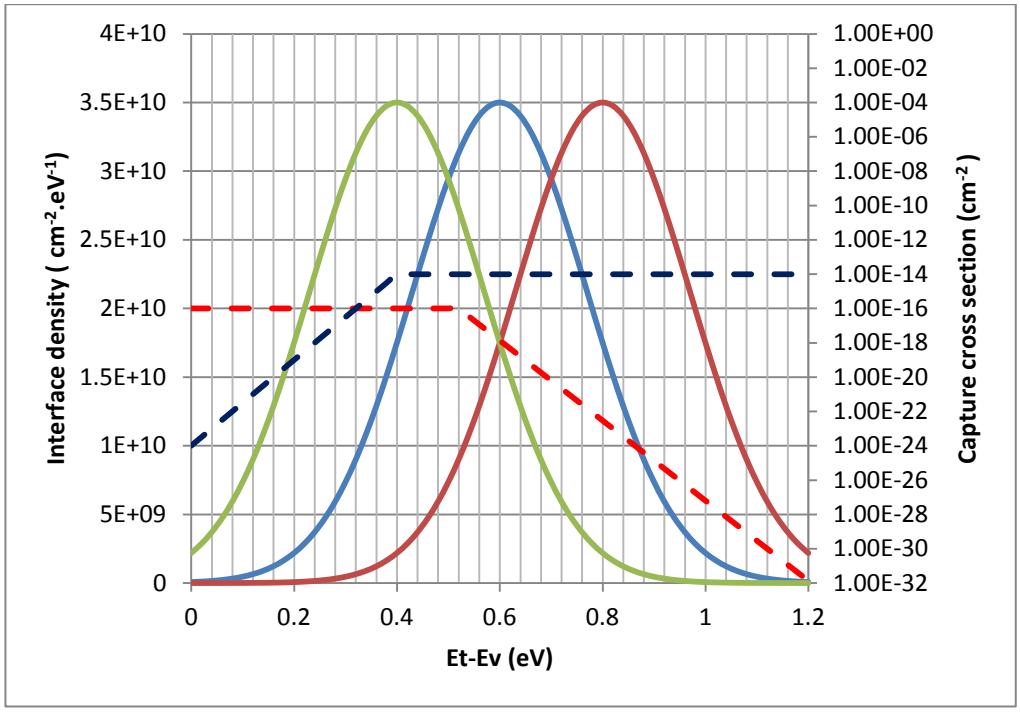

Figure 3.10 Defect density, electron (dashed curve in red) and hole capture cross section (dashed curve in blue) versus energy for a mid-gap defect: defect 1 (in blue), a near conduction band defect :defect 2 (in red) and a near valence band defect: defect 3 (in green). The defect density is a Gauss function with a maximum equal to $3.5x10^{10}$ $cm^{-2}.eV^{-1}$, a FWHM of 0.115 eV and centered at 0.6 eV for defect 1, 0.8 eV for defect 2 and 0.4 eV for defect 3. In this figure $<\sigma_n>/<\sigma_p>=0.0145$ (case 1) for defect 3.

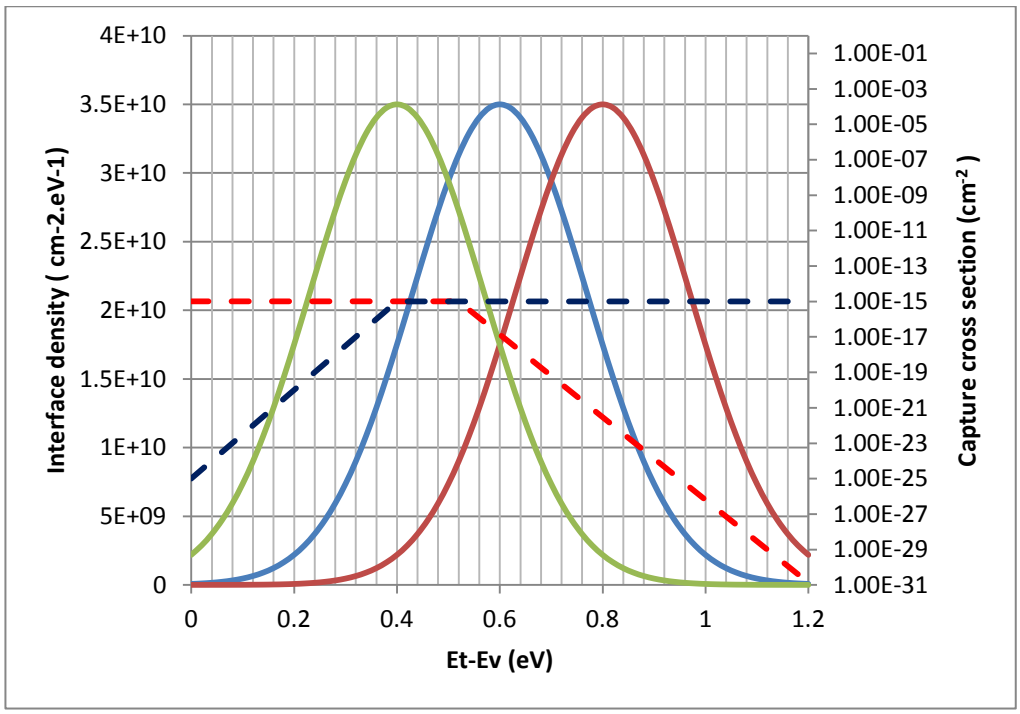

Figure 3.11 Defect density, electron (dashed curve in red) and hole capture cross section (dashed curve in blue) versus energy for a mid-gap defect (cf. figure 3.10).In this figure $\langle\sigma_n\rangle/\langle\sigma_p\rangle=1.45$ (case 2) for defect 3.

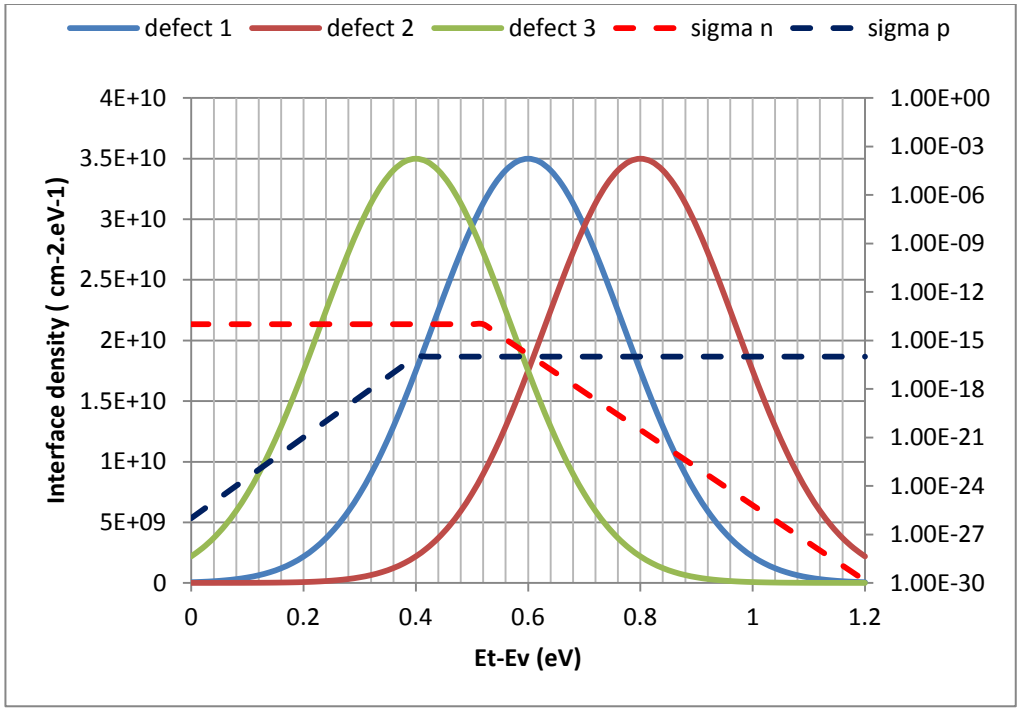

Figure 3.12 Defect density, electron (dashed curve in red) and hole capture cross section (dashed curve in blue) versus energy for a mid-gap defect (cf. figure 3.10).In this figure $\langle\sigma_n\rangle/\langle\sigma_p\rangle=145$ (case 3) for defect 3.

On figures 3.10-3.12, the electron and hole capture cross section respectively σ_n and σ_p used for the defects are represented as a function of energy E. The ratio of the mean electron to mean hole cross section has been calculated via equation 3.84.

$$\frac{<\sigma_n>}{<\sigma_p>} = \frac{\int \sigma_n . D(E) . dE}{\int \sigma_p . D(E) . dE} \tag{3.84}$$

3.5.4 Implementation of recombination rate

In a first step, the differential recombination rate dU/dE is calculated for each value of E = (E_d – E_v) at a given value of n_s. This latter is determined both by the injection level and the fixed charge Q_f with the implementation of section 3.4.

$$\frac{dU}{dE} = v_{th}(n_S . p_s - n_i^2) . \frac{D(E)}{\frac{(n_s + n_1(E))}{\sigma_p(E)} + \frac{(p_s + p_1(E))}{\sigma_n(E)}} \tag{3.85}$$

The second step consists of integrating dU/dE between Ev and Ec which gives the recombination rate at a given injection level Δn and fixed charge Q_f.

$$[U(\Delta n)]_{Qf} = v_{th}(n . p - n_i^2) . \int_{E_v}^{E_c} \frac{D(E)}{\frac{(n + n_1(E))}{\sigma_p(E)} + \frac{(p + p_1(E))}{\sigma_n(E)}} \, dE \tag{3.86}$$

This operation is repeated for each level of injection. As has been seen in section 3.4, recombination rate depends on doping. Simulations are presented for p-type doping Na=1.5x10^{16} cm^{-3} (resistivity 1 ohm.cm) and Na=2.6x10^{11} cm^{-3} (resistivity 8000 ohm.cm). In order to understand SRV versus injection, the relation linking SRV and injection is analysed in the following section.

3.5.5 Study of the effective SRV (S) versus injection

Figures 3.13 and 3.14 represent the SRV and the net recombination rate versus minority to majority carrier densities ratio. The recombination rate is interesting because it allow following the evolution of recombination with both injection level and minority carrier ratio. On figure 3.14 representing recombination rate versus carrier ratio, the increasing of injection level Δn is indicated by the arrows. In flat band case, where there is no fixed charge, injection level is the same for both minority and majority carrier densities.

The effect of fixed charge is to break this equality. Whatever is the value of Q_f, the function tends toward the same value at high injection level where the minority to majority carrier density ratio is almost equal to 1. Indeed at high injection, the effect of Q_f becomes negligible, the situation is the same as $Q_f = 0$ and the photo-induced carrier density is very much higher than the doping. One obvious effect of the fixed charge is to attract electrons at the surface and repel the holes.

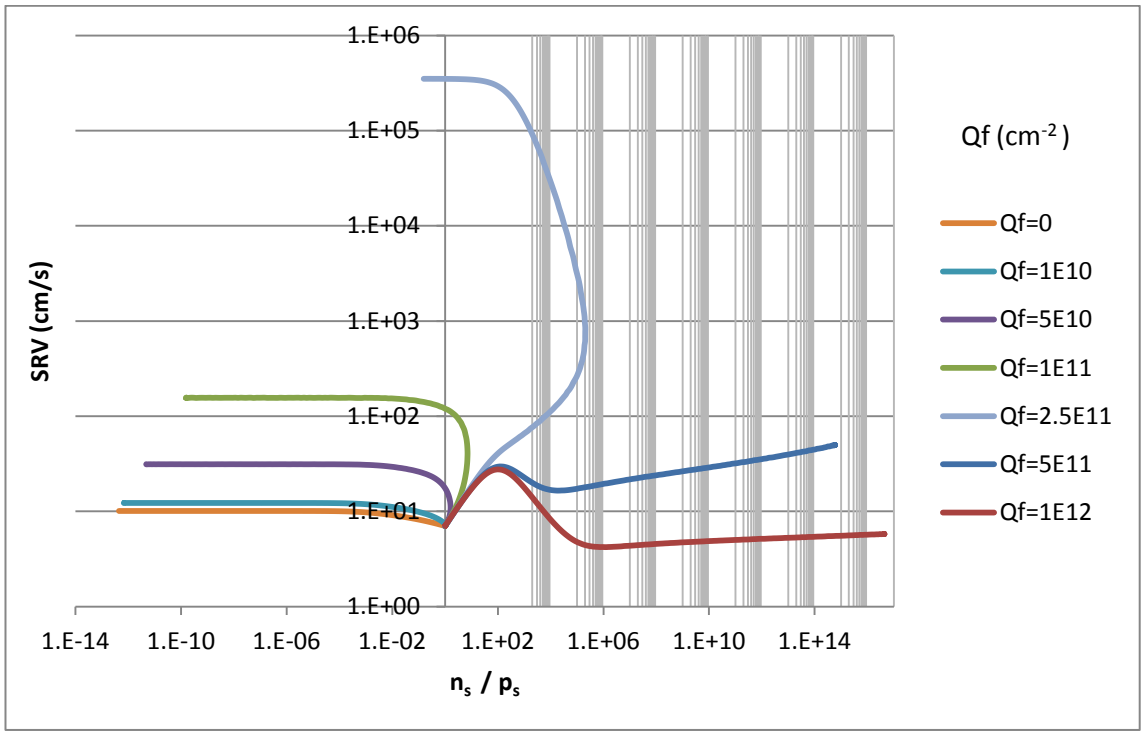

Figure 3.13 Evolution of the SRV versus electron concentration (n_s) to hole concentration at the surface (p_s) ratio at different fixed charge density Q_f (cm^{-2}). This graph presents another view of the 3 regimes of Q_f. The doping is $1.5x10^{16}$ cm^{-3} and the defect has the same characteristic as for figure 3.7. All the curves converge toward a point where $n_s=p_s$ and where $n_s=n_p$ and the SRV remains at the same value. This point corresponds with high injection level.

In figure 3.13, the injection level increases from the extremities, toward a single point where all the curves converge. At low injection and for low Q_f, (0 to $1x10^{11}$ cm^{-2}), electron concentration is very far below hole concentration at the surface and thus recombination rate is limited by the electron (cf figure 3.15-16). This ratio increases with Q_f and consequently the SRV increases because more electrons are available for recombination contribution. On this regime, when the injection level becomes higher than the doping (acceptor concentration), the inversion occurs if Q_f is high enough to have a strong influence on n_s and p_s. This explain why the curve reach a first point where $n_s=p_s$ and when injection level increases $n_s > p_s$. This inversion is stronger as Q_f

is high but since the influence of Q_f is weak, n_s and p_s have the same order of magnitude and the SRV is close to its maximum. Is the injection level is further increased, the effect of Q_f decreases and becomes negligible at high injection. For the regime of high Q_f, the strong inversion already occurs at low injection (cf. figure 3.18). Since the holes concentration is very low, the recombination is limited by the hole concentration. If Q_f is higher the holes are further repels and their concentration decrease resulting in a lower SRV. For a given high Q_f, when the injection level increases, the effect of Q_f is balanced by the charge density due to the electron concentration and becomes negligible at high injection. However a maximum SRV is reached before the equality between electron and hole concentration because, electron capture cross section is below hole capture cross section and therefore the maximum contribution of electron and hole is reach when electron concentration is higher than hole concentration. The curve where $Q_f = 2.5 \times 10^{15}$ corresponds to intermediate regime. At low injection level, the electron concentration is almost equal to hole concentration (cf. figure 3.17) and thus the SRV is very high because of high recombination rate compare to injection level (cf. figure 3.14). When the injection level increases, the n_s to p_s ratio reach a maximum because of high enough injection level combine with a strong influence of Q_f. Then if the injection level is further increased, the influence of Q_f is lower until becoming negligible at the convergence point.

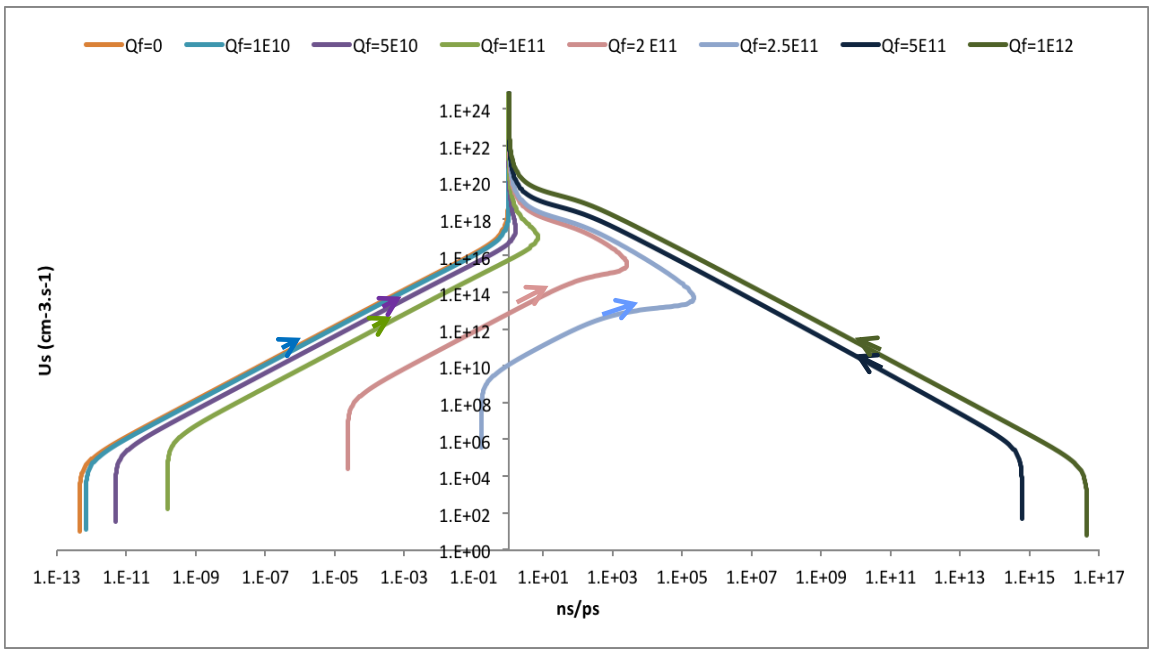

Figure 3.14 Evolution of surface recombination rate versus n_s to p_s ratio (Q_f is expressed in cm^{-2}). This figure allows highlighting figure 3.13. On this figure, the arrows indicate the increase of the injection level. The portion of the curve where $n_s=p_s$ and where all the curves converge corresponds with the common point of figure 3.13 that is with high injection level. The vertical shape of the curves on the bottom is due to the fact that, n_s/p_s is almost constant until injection level becomes higher than equilibrium electron concentration. The important point which can be noted is that the highest recombination rate at low injection level corresponds with the highest SRV on figure 3.13.

- **Evolution of the surface charge carriers for substrate with resistivity 1 ohm.cm (p_0=1.5x10^{16}cm^{-3})**

Figures 3.15-3.18 represent the evolution of the electrons and holes concentration at the surface as a function of the injection level Δn when the fixed charge is from figures 3.15 to 3.18 respectively 1x10^{10}, 1x10^{11}, 2.5x10^{11} and 1x10^{12} cm^{-2}.

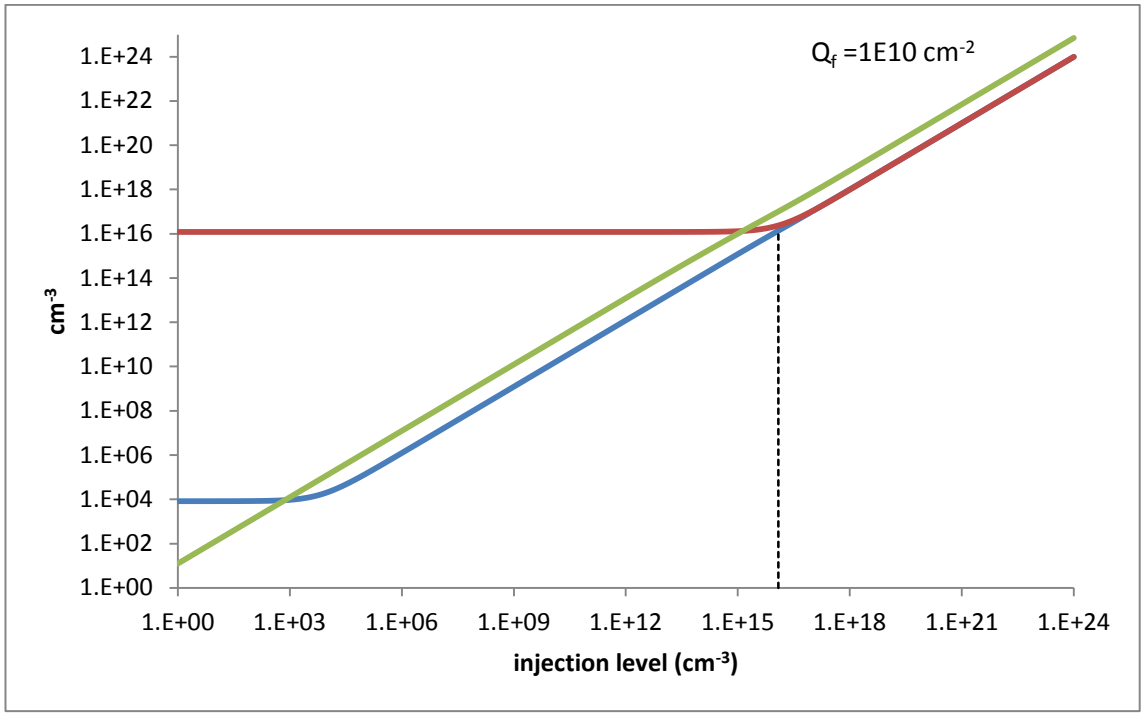

Figure 3.15 Evolution of the surface carriers versus injection level (Q_f = 10^{10} cm^{-2}). Electron concentration (in blue), hole concentration (in red) and recombination rate (in green) are represented. The recombination rate follows the lowest carrier concentration.

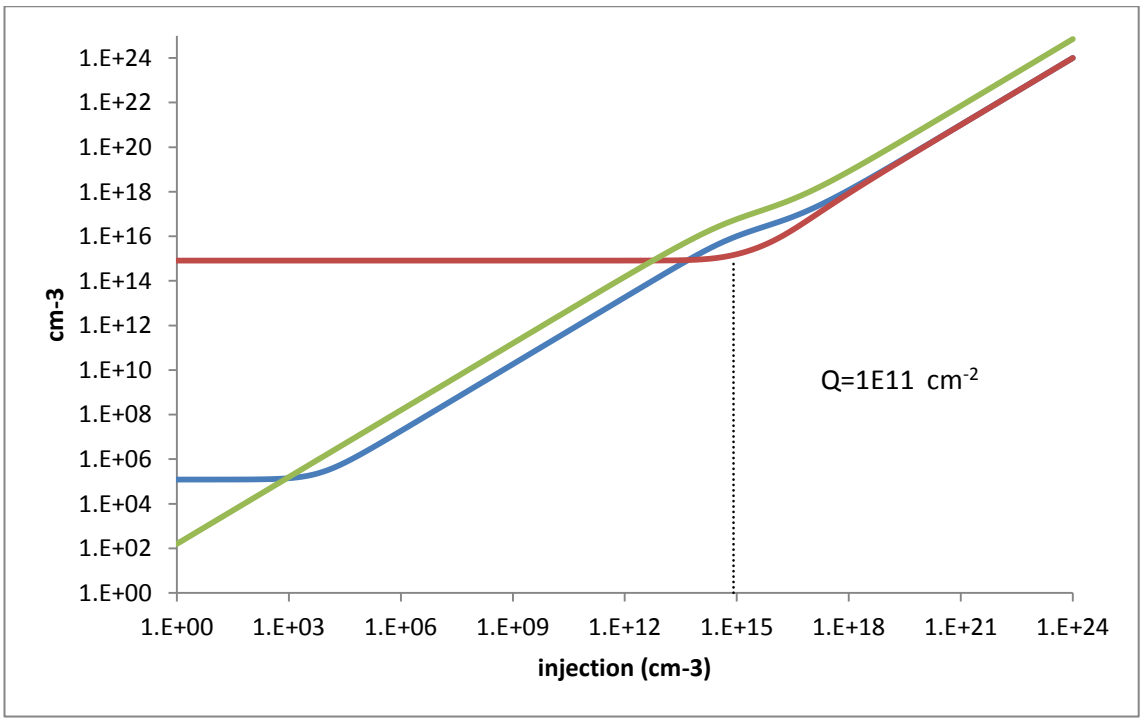

Figure 3.16 Evolution of the surface carriers versus injection level (Q_f = 10^{11} cm^{-2}). Electron concentration (in blue), hole concentration (in red) and recombination rate (in green) are represented. The recombination rate follows the lowest carrier concentration if electron and hole capture cross section are equal. Here electron capture cross section is almost 2 orders of magnitude lower and thus the recombination rate is still limited by electron even when its concentration is one order of magnitude higher.

Firstly it has to be said that when $\Delta n << n0$, U_s should be constant. If it is not the case in all the figures of this section, this is due to the fact that we wrote the simulation code for an injection level starting at Δn $1x10^{10}cm^{-3}$ which corresponds to $\Delta n >> n_0$. Thus, the injection level is approximated to Δn instead of n which is equal to $n_0+\Delta n$. Therefore the minimum injection level for the curve U_s is actually n_0 not 1 .It can be seen on figure 3.16 that the recombination rate follows the variation of n_s until the injection level reach$10^{18}cm^{-3}$ (that is $\Delta n >> n_0$) because the capture of electrons is then predominant. In all of the simulation of this section $\sigma_n/ \sigma_p=0.0145$, therefore even when the occupation of the defect is equal for electron and hole, electron capture is almost 100 times lower and limit the recombination process.

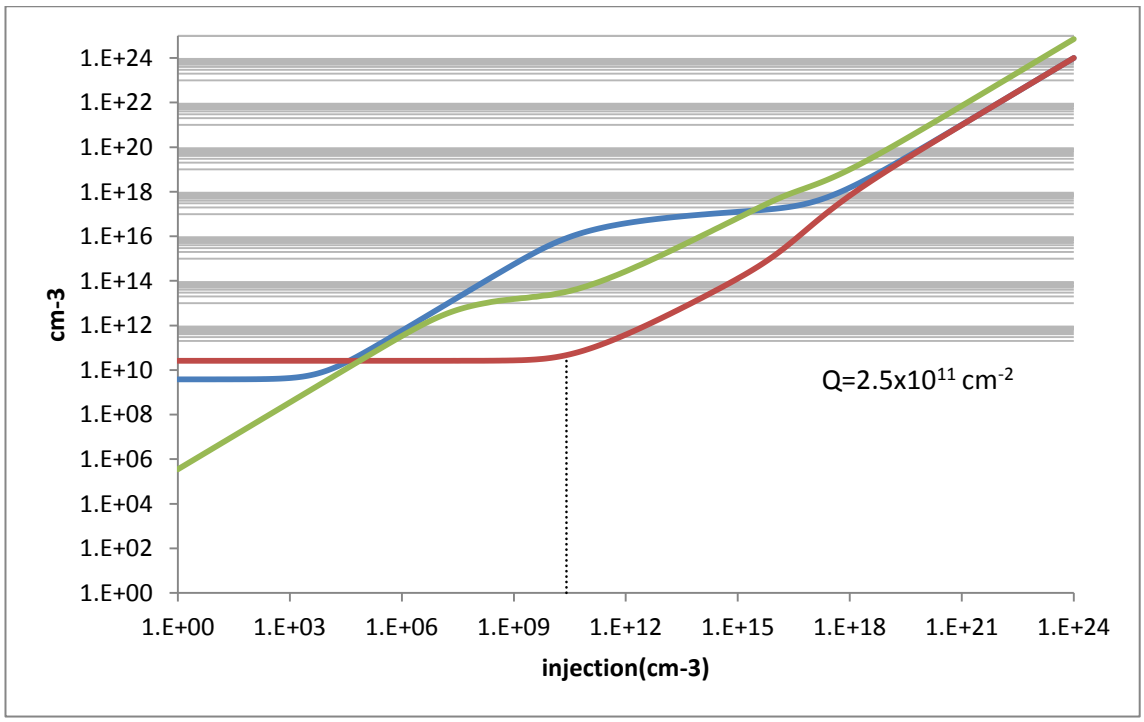

Figure 3.17 Evolution of the surface carriers versus injection level (Q_f = 2.5x10^{11} cm^{-2}). Electron concentration (in blue), hole concentration (in red) and recombination rate (in green) are represented. The recombination rate follows the lowest carrier concentration if electron and hole capture cross section are equal. Electron capture cross section is almost 2 orders of magnitude lower. Since Q_f is high enough to have a strong influence even above low injection level, when the injection level becomes high enough, electron concentration is more than 2 orders of magnitude higher than the hole concentration and the recombination rate is limited by the hole concentration.

On figure 3.17 the hole capture becomes the dominant process when n_s = 1.72x10^{12}cm^{-3} and p_s = 2.5x10^{10}cm^{-3}. This situation corresponds to n_s / p_s= 68.8 and it can be remarked that σ_p / σ_n= 1/0.0145 (= 68.9). In other this n_s to p_s ratio correspond to the situation where the number of captured holes becomes equal to the captured electrons.

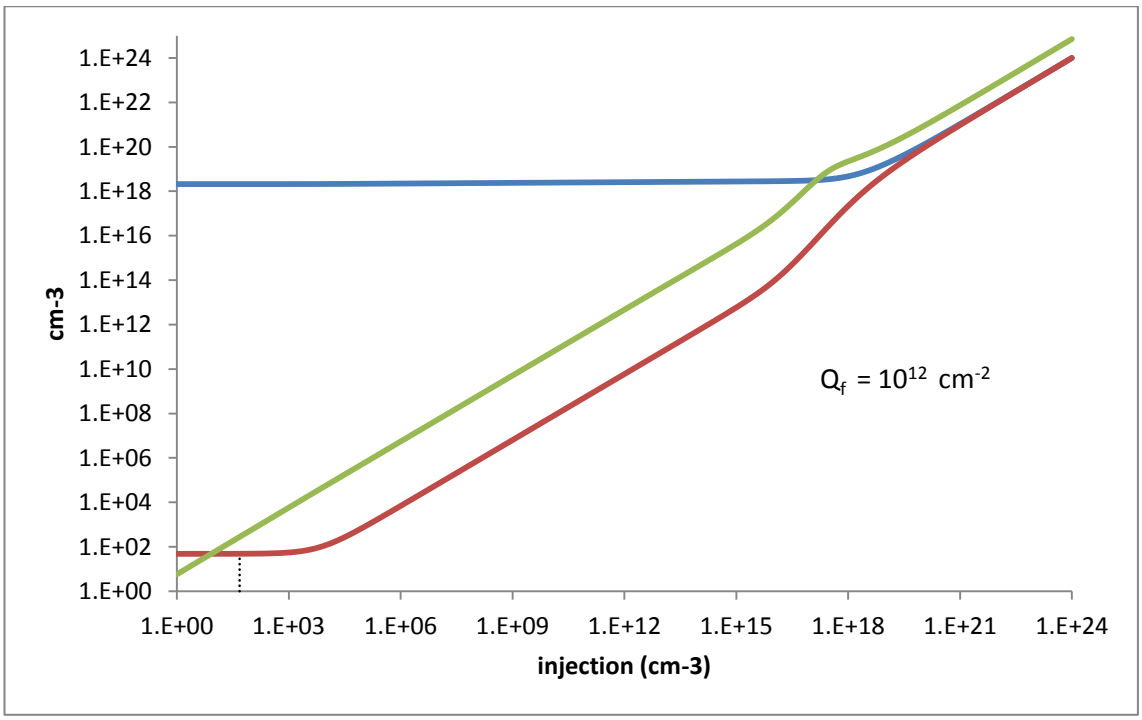

Figure 3.18 Evolution of the surface carriers versus injection level (Q_f = 10^{12} cm^{-2}). Electron concentration (in blue), hole concentration (in red) and recombination rate (in green) are represented. The recombination rate follows the lowest carrier concentration if electron and hole capture cross section are equal. Here electron capture cross section is only 2 orders of magnitude lower and the hole concentration is very below electron concentration (strong inversion) due to the high Q_f which strongly repels the holes and attract electrons. The recombination rate is limited by the hole concentration.

Figure 3.18 corresponds to the high fixed charge behavior, $n_s >> p_s$. Due to the repelling of the positive fixed charge, the hole concentration at the surface becomes very low and the number of electrons which recombined with hole via defects is neglected in regards with electrons concentration at the surface until reaching high injection level. When the fixed charge induces this behavior, the recombination rate is drastically reduced at low injection level and consequently the SRV is also reduced.

- **Evolution of the surface charge carriers for substrate with resistivity 8000 ohm.cm (p_0=2.6x10^{11} cm^{-3})**

Figures 3.19 and 3.20 represent the evolution of the electrons and holes concentration at the surface of a 8000 ohm.cm wafer as a function of the injection level Δn when the fixed charge is from figures 3.19 and 3.20 respectively 3.10^8 and 1.10^9 cm^{-2}. For this latter value of fixed charge, the high charge behavior is already reached because of the lower doping.

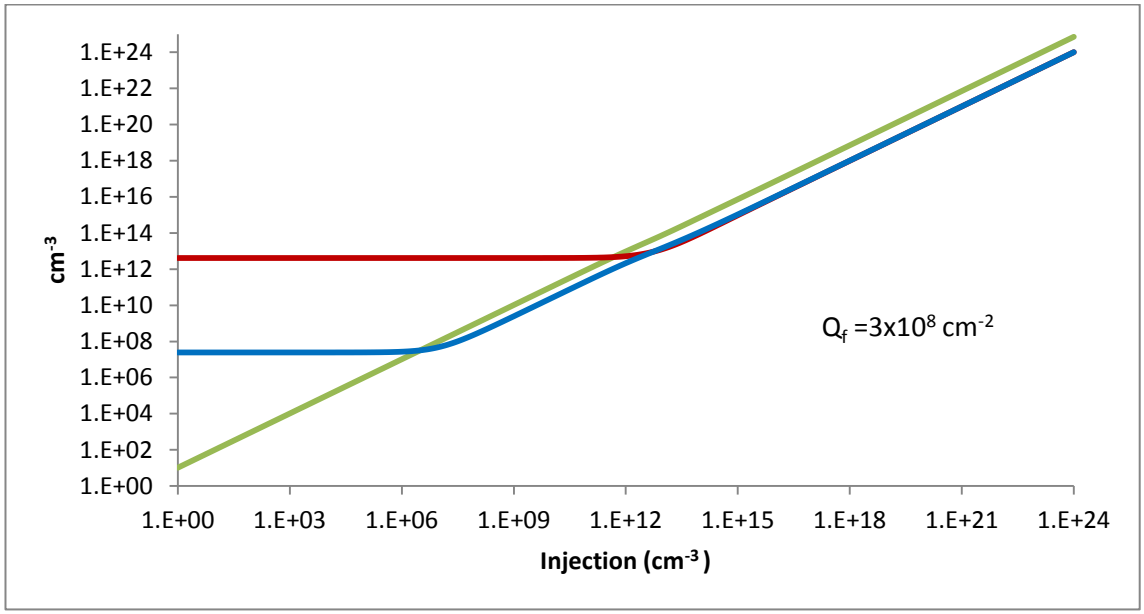

Figure 3.19 Evolution of the surface carriers versus injection level (Q_f = 3x10^8 cm^{-2}). Electron concentration (in blue), hole concentration (in red) and recombination rate (in green) are represented. The situation is similar as in figure 3.15.

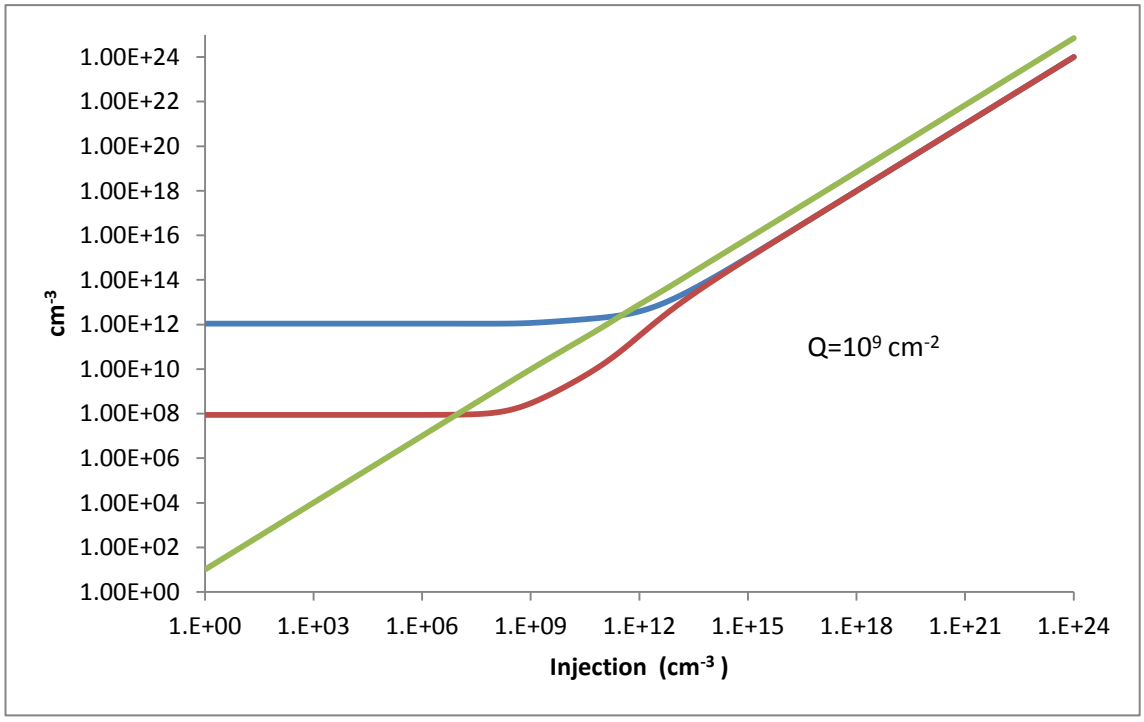

Figure 3.20 Evolution of the surface carriers versus injection level (Q_f = 10^9 cm^{-2}). Electron concentration (in blue), hole concentration (in red) and recombination rate (in green) are represented. The situation is similar as in figure 3.18. The regime corresponds to high value of Q_f where strong inversion occurs because the acceptors concentration is several order lower than previously (figure 3.15-18). A lower value of Q_f is thus enough to inverse the electron to hole concentration ratio.

Since the doping is very low for the 1ohm.cm wafer, a lower fixed charge is required to induce a consequent diminution of hole concentration at the surface relative to its concentration when there is no fixed charge. Thus from a fixed charge as low as 10^9 cm^2 $n_{s\ >}$ ps. The situation of figure 3.20 corresponds to the high fixed charge behavior whereas figure 3.19 corresponds to the low charge behavior. As will be seen in the experimental part of this chapter, the fixed charge in our samples both for 1 and 8000 ohm.cm is around 10^{11} cm. Therefore, it is expected that Q_f will result in an increasing of the SRV for 1 ohm.cm wafers and a decreasing for 8000 ohm.cm wafers.

3.6 Results of the simulation

On these simulations defects 1, 2 and 3 correspond to Gaussian energy levels distribution centered respectively at 0.6 eV, 0.8 eV and 0.4 eV above the valence band. The FWHM and the maximum density are the same for the 3 defects (cf. figure 3.9). defects 1 and 2 are theoretical and correspond to a shift of defect 3. In other words, defect 1 is below the mid-gap, defect 2 is at mid-gap and defect 3 is above the mid-gap. Case 1, 2 and 3 correspond respectively to the values 0.01, 1 and 100 for the maximum of the electron capture cross section to the maximum of the hole capture cross section ratio ($\sigma_{n,\ max}$ / $\sigma_{p,\ max}$). Table 3.1 gives the value of $<\sigma_n>/<\sigma_p>$

Defect type	$<\sigma_n>/<\sigma_p>$		
	Case 1	Case 2	Case 3
Defect 3	$1.45 .10^{-2}$	1.45	145
Defect 1	$4.05 .10^{-3}$	0.405	40.5
Defect 2	$6.54 .10^{-4}$	$6.54.10^{-2}$	6.54

Table 3.1 The estimated mean values of σ_n to σ_p ratio for a ratio $_{\sigma n}$ max to $_{\sigma p\ max}$ equal respectively to 0.01, 0.1 and 1

Some general observations can be made regarding figures 3.21-3.29 and 3.30-3.39 whatever is the wafer resistivity. A very important point is the fact that the SRV is proportional to the σ_p to σ_n ratio. From case 1 to 3 as this ratio increases, the curve is shifted of 2 orders (multiply by 10 from case 1 to 2 and by 10 from case 2 to 3). This point explains why defects A and B can be neglected in regard with defect C (cf.

section3.52). Regarding the fixed charge density Q_f, its 3 regimes appears clearly. When Q_f is very low in regard with doping level, its increasing induces an increasing of the SRV at low injection, as Q_f is further increased, the SRV increases and its influence extents to a higher injection level as intuitively expected. Finally if Q_f reaches a critical value, the minority and majority carrier concentration at the surface is reversed and if Q_f is further increased, the SRV decreases from several orders. The influence of doping can be clearly observed by comparing figures 3.21-3.29 with figures 3.30-3.39. Indeed the charge Q_f effect on SRV at low injection is several orders for 8000.ohm.cm than for 1ohm.cm wafer.

In a first approximation, the contribution of electron(hole) in the conduction band (valence band) due to emission from a defect energy level can be neglected if the electron concentration n_1 (hole concentration p_1) is very low compare to electron concentration n_s (hole concentration p_s) at the surface. Although this approximation is not always correct, n_1 and p_1 can be neglected in most of the case as can be seen on figure 3.21-29 and 3.30-3.39. Under these condition and when $\Delta n >> n_0$ (p_0), the evolution of the SRV with the injection level can be described and understood easily by introducing a new quantity relative to the electron capture and to hole capture. This quantity is the product $\sigma_n.n_s/\Delta n$ ($\sigma_p.p_s/\Delta n$) is related to the electron (hole) capture probability by a defect and can be defined as a dynamic electron (hole) capture probability section. Similarly, the SRV can be understood as the recombination rate per excess charge carriers. Since electron-hole recombination occurs via capture by defect, electron (hole) limits the recombination if the electron capture probability section (hole) is below hole (electron) capture probability section. For a p-type wafer, at low injection when there is no fixed charge, ns is almost equal to Δn and $\sigma_n.n_s/\Delta n << \sigma_p.p_s/\Delta n$ .Thus, the recombination is limited by electron and more precisely varies as the electron probability capture. When injection level Δn increases, n_s increases proportionally to Δn, the electron, capture probability section $\sigma_n.n_s/\Delta n$ is constant and thus the SRV is constant. On the other hand when $\Delta n << p_0$, ps is almost equal to p_0 and the hole capture probability section $\sigma_p.p_s/\Delta n$ decreases with Δn. When Δn is increased until $\sigma_n.n_s/\Delta n$ becomes close to $\sigma_p.p_s/\Delta n$, the SRV varies both with the increase of electron capture probability section and the hole decrease probability thus the recombination rate varies slower than Δn and the SRV decreases until the high injection level where $\Delta n >> p_0$. Then the hole capture and electron capture probability section are constant and thus the SRV is constant. Regarding positive fixed charge density, its effect at low injection

level is to attract electrons and to repel holes at the surface, in other words, n_s is higher and p_s is lower when Q_f is higher.. When Q_f increases, the electron capture probability section $\sigma_n.n_s/\Delta n$ increases and the hole capture probability section $\sigma_p.p_s/\Delta n$ decreases. . For a given Q_f in the low range, $\sigma_n.n_s/\Delta n$ is almost constant since $n_s$is almost proportional to Δn and thus SRV is constant. Higher is Q_f, higher is $\sigma_n.n_s/\Delta$ n and lower the injection level where $\sigma_n.n_s/\Delta n$ reaches $\sigma_p.p_s/\Delta n$ .However, when the injection level is high enough the fixed charge effect starts to decrease and $\sigma_n.n_s/\Delta n$ decreases. If Qf is low, the decrease of electron probability starts before $\sigma_n.n_s/\Delta n$ reaches $\sigma_p.p_s/\Delta n$ and the SRV always follow electron capture probability section. SRV decreases with $\sigma_p.p_s/\Delta n$ and when an injection level is high enough that the effect of Q_f is negligible, $\sigma_p.p_s/\Delta n$ is constant and thus SRV. This corresponds to the low range for Q_f.

In the case where Q_f is high enough to allow having $\sigma_n.n_s/\Delta n$ beyond $\sigma_p.p_s/\Delta n$, the SRV follows the hole capture probability section when Δn increases and thus the SRV decreases. However, when the influence of Q_f starts to decrease, the electron probability $\sigma_n.n_s/\Delta n$ decreases and one the other hand the decrease of the hole probability $\sigma_p.p_s/\Delta n$ is slower. Therefore when the injection level is high enough, the electron capture probability section becomes lower than the hole capture probability section and the SRV decreases as $\sigma_n.n_s/\Delta n$. Then if injection level is further increased, Q_f effect becomes negligible and both electron and hole capture probabilities are constant and thus the SRV. This regime corresponds to the intermediate range of Q_f.

The last case corresponds to the case where Q_f is high enough for having $\sigma_n.n_s/\Delta n$ higher than $\sigma_p.p_s/\Delta n$ even at low injection level. At low injection level and from a threshold Q_f corresponding to $\sigma_n.n_s/\Delta n= \sigma_p.p_s/\Delta n$ the SRV reaches a maximum, and then if Q_f is increased, the SRV decreases. On this range, for a given Q_f, SRV decreases slowly following the hole capture probability section $\sigma_p.p_s/\Delta n$. Indeed hole capture probability section decreases slowly with injection level because the influence of Q_f on hole attraction decreases slightly more rapidly that $1/\Delta n$ On the other hand, electron capture probability section decreases rapidly until $\sigma_n.n_s/\Delta n= \sigma_p.p_s/\Delta n$ which correspond to a local minimum of the SRV. Then the SRV continues to decrease with Δn but even more slowly following the evolution of the electron probability until it remains constant.

3.6.1 Simulation results for 8000 Ohm.cm wafers

- **Case 1 $<\sigma_n>$ / $<\sigma_p>$= {0.0145, 4.05x10^{-3}, 6.54x10^{-4}} respectively for defect {3, 1, 2}.**

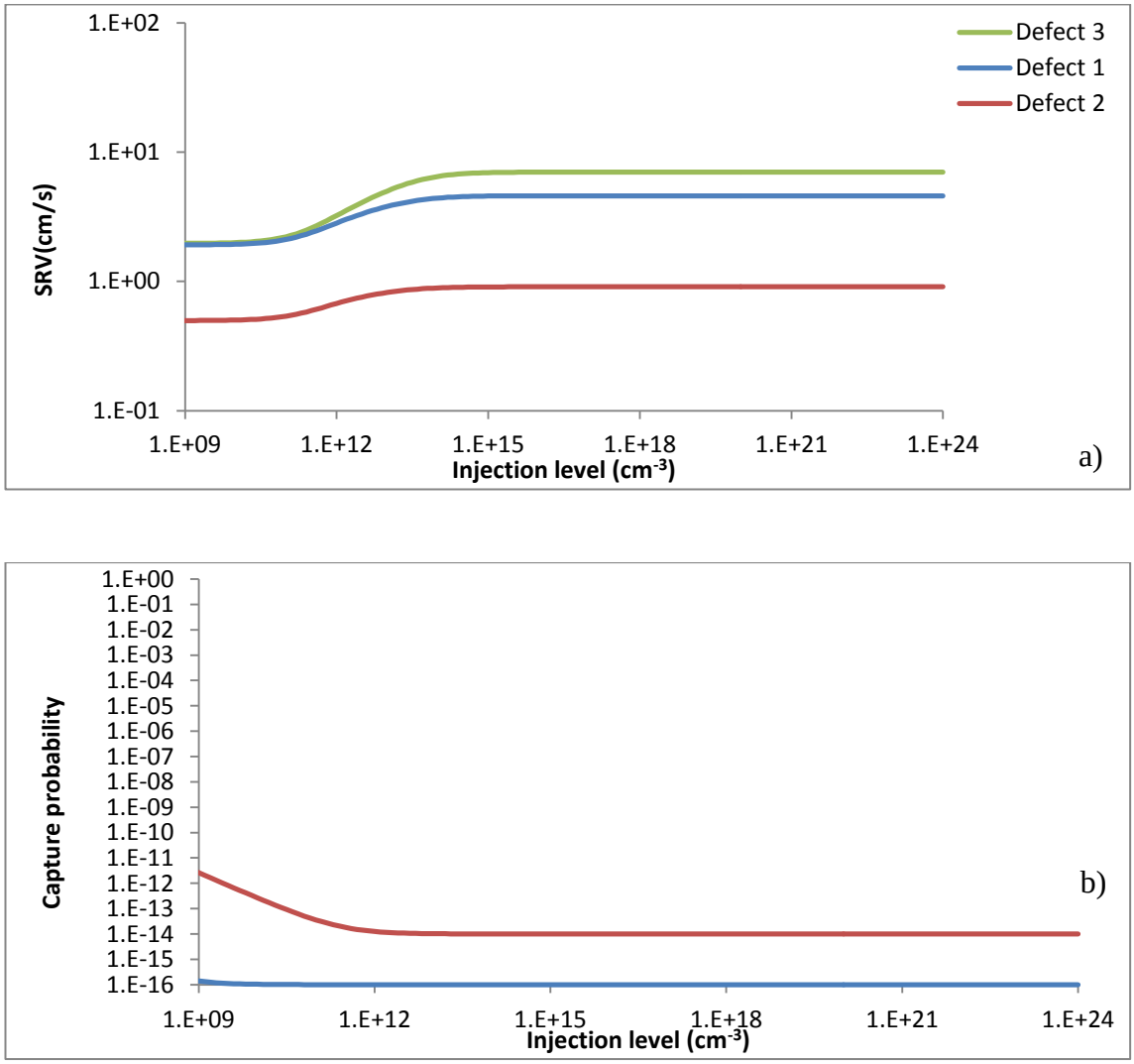

Figure 3.21 a) Evolution of the SRV versus injection level Δn when Q_f=0. Defects 1 to 3 follow the same Gaussian function with the same parameters except that defect 1, 2 and 3 are centered respectively 0.8, 0.6 and 0.4 eV above the valence band. (cf. figure 3.9). **b)** Electron (in blue) and hole (in red) capture probabilities: respectively $\sigma_n.n_s/\Delta n$ and $\sigma_p.n_s/\Delta n$. Since electron-hole recombination occurs via capture by defect, electron (hole) limits the recombination in the case where the electron capture probability section (hole) is below hole (electron) capture probability section. The decrease of hole capture probability section until $\Delta n=p_0$ is due to the fact that for Q_f=0 $ps/\Delta n= (1+p_0/\Delta n)$. For high injection level $\Delta n >> p_0$ and thus $p_s/\Delta n=1$. If the SRV is lower at low injection level it is due to the contribution of the hole emission process: the hole concentration p_1 in the valence band from coming from defect becomes negligible when Δn is around 1x10^{14} cm^{-3}. The different values of electron to hole capture probability section: $<\sigma_n>$ / $<\sigma_p>$={0.0145, 4.05x10^{-3} , 6.54x10^{-4} } respectively for defect {3, 1, 2 }, explain why SRV is limited by electron capture probability section at high injection level and why the lowest SRV value is for defect 2 following by defect 1 and 3.

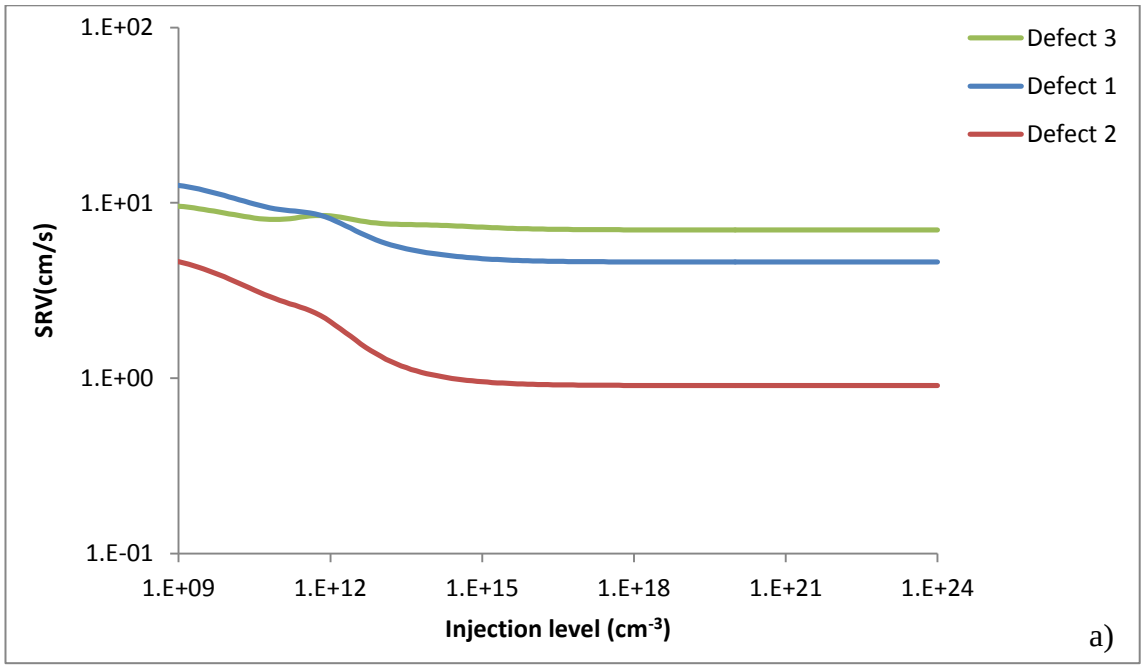

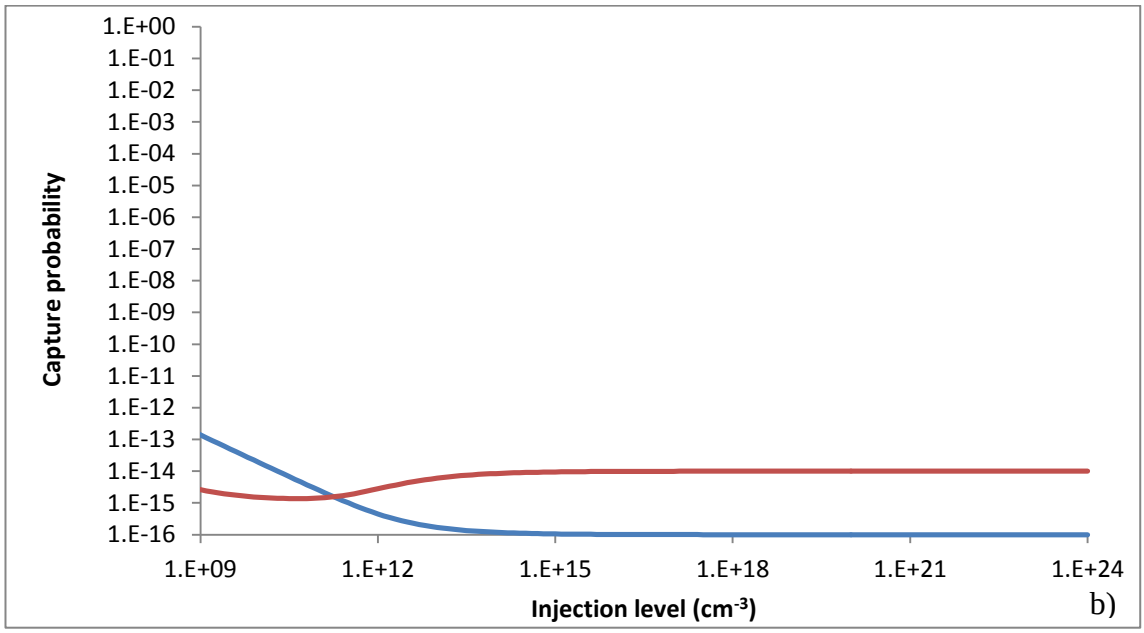

Figure 3.22 a) Evolution of the SRV versus injection level Δn when the fixed charge density $Q_f=10^9$ cm^{-2}. Defects 1 to 3 follow the same Gaussian function with the same parameters except that defect 1, 2 and 3 are centered respectively 0.8, 0.6 and 0.4 eV above the valence band. (cf. figure 3.9). **b)** Electron (in blue) and hole (in red) capture probabilities: respectively $\sigma_n.n_s/\Delta n$ and $\sigma_p.n_s/\Delta n$.

Since electron-hole recombination occurs via capture by defect, electron (hole) limits the recombination in the case where the electron capture probability section (hole) is below hole (electron) capture probability section. For a wafer with a doping $2.6x10^{11}$ cm^{-3}, Q_f is in the high range at 10^9 cm^{-2}: the SRV follows the evolution of hole capture probability section (which is below electron capture probability section) at low injection level.

In figure, 3.22, the SRV follows the evolution of hole capture probability section (which is below electron capture probability section) at low injection level. This is due to the fact that the positive charge density Q_f attracts the electron at the surface whereas the holes are repelled. Electron capture probability section decreases with Δn because electron concentration starts to balance the effect of Q_f which results in a decrease of the surface potential ψ_s. Since $n_s/\Delta n \sim e^{q\psi s/kT}$, the electron capture probability section decreases until the effect of Q_f is negligible (that is $\psi_s \sim 0$). Reciprocally, the hole capture probability section increases since $p_s/\Delta n \sim e^{-q\psi s/kT}$. Since $\sigma_n/\sigma_p=1/100$, the SRV is limited by electron at high injection level. On figure 3.22 a), the SRV corresponding to defect 3 decreases below the SRV of defect 1 below $\Delta n=5x10^{10}$ cm^{-3}. This is due to the fact that σ_n/σ_p is very lower for defect 2 and 1 than for defect 3. In addition, for defect 3 the curve of defect 3 does not follow the electron capture probability section as well than for defects 1 and 3 due to the process of hole emission from the defect toward the valence band. Since defect 2 and 3 are centered respectively 0.6 and 0.4 eV above the valence band, the hole emission is higher (and thus p_1) for defect 3 which enhanced further the reduction of the SRV.

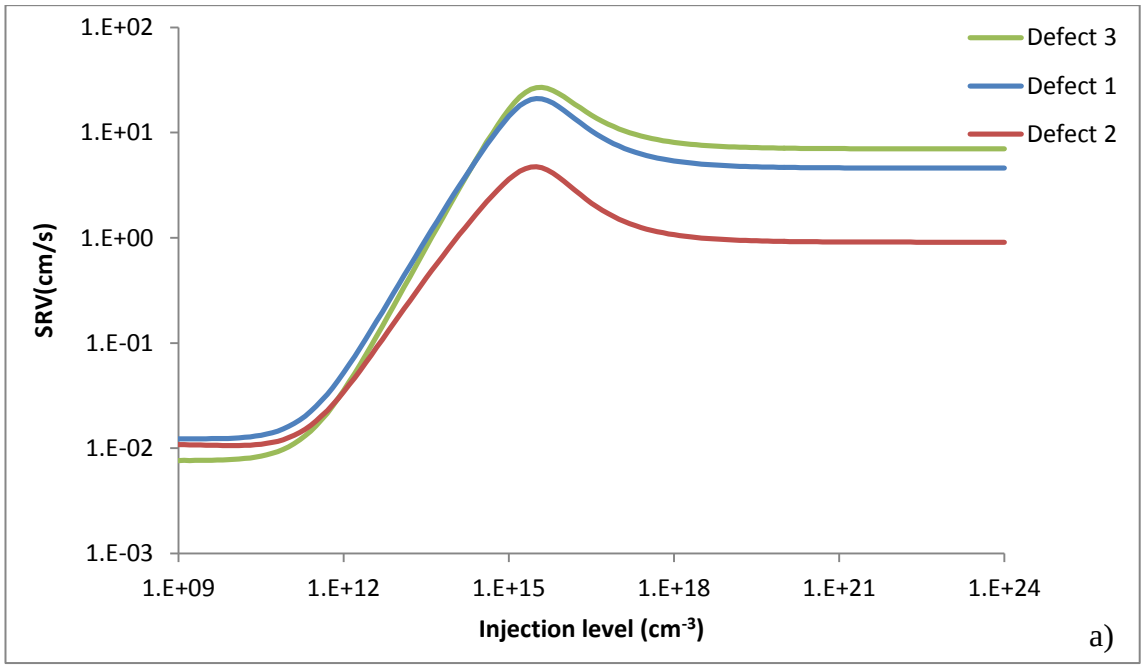

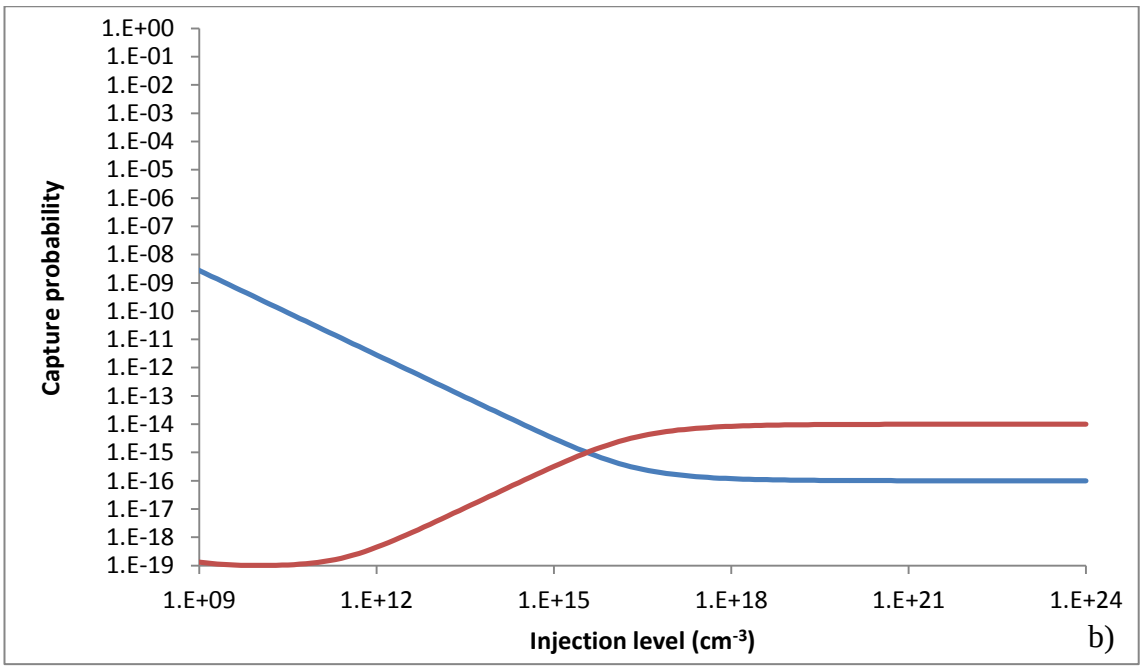

Figure 3.23 a) Evolution of the SRV versus injection level Δn when the fixed charge density $Q_f=10^{11}$ cm^{-2}. Defects 1 to 3 follow the same Gaussian function with the same parameters except that defect 1, 2 and 3 are centered respectively 0.8, 0.6 and 0.4 eV above the valence band. (cf. figure 3.9). **b)** Electron (in blue) and hole (in red) capture probabilities: respectively $\sigma_n.n_s/\Delta n$ and $\sigma_p.n_s/\Delta n$.

Since electron-hole recombination occurs via capture by defect, electron (hole) limits the recombination in the case where the electron capture probability section (hole) is below hole (electron) capture probability section. At low injection, SRV evolution with Δn follows hole capture probability section which explains that it increases (cf. caption on figure 3.22).

It can be seen in figure 3.23 that SRV reached a maximum when electron and hole capture probability section are equal. When injection level is further increased, electron capture probability section decreases below hole capture probability section and the SRV decreases until a minimum which corresponds to the limit of Q_f influence (cf . caption on figure 3.22). Since Q_f is higher than on figure 3.22, the effect of Q_f extends for higher Δn. A last remark has to be made regarding the value of the SRV for defect 3 which is the lowest at low injection. It is not due as on figure 3.22 to the hole emission process but actually to the value of $<\sigma_n>$ / $<\sigma_p>$= {0.0145, $4.05x10^{-3}$, $6.54x10^{-4}$} respectively for defect {3, 1, 2}. Since SRV is limited by hole capture at low injection, SRV is lower for defect 3 where the hole capture to electron capture ratio is higher. Similarly the hole to electron capture ratio also explains why the SRV corresponding to defect 1 is so close to the SRV corresponding to defect 2 (although this latter is still lower).

Case 2 $<\sigma_n>$ / $<\sigma_p>$= {1.45, 0.405, 6.54x10^{-2}} respectively for defect {3, 1, 2}.

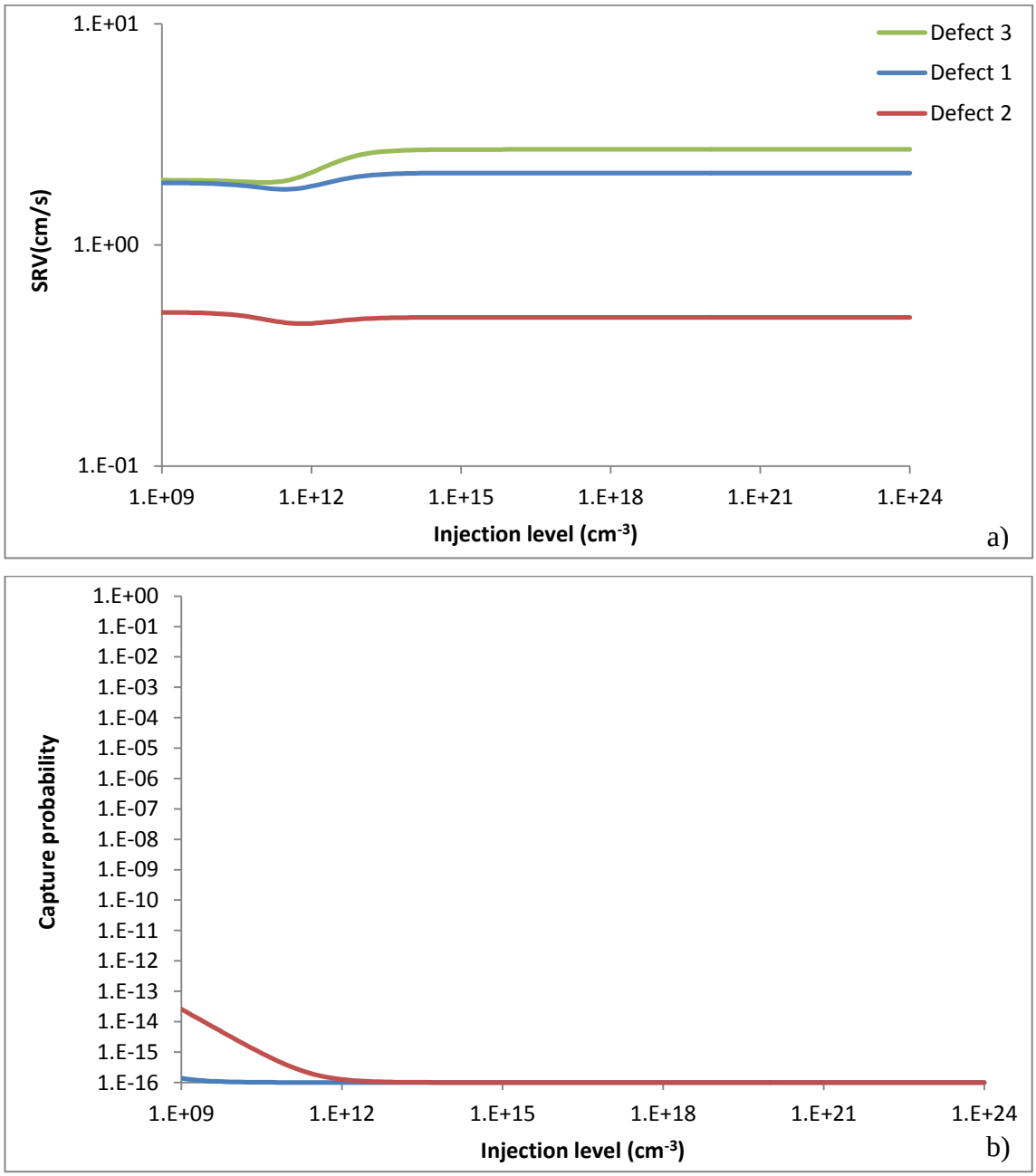

Figure 3.24 a) Evolution of the SRV versus injection level Δn when Q_f=0. Defects 1 to 3 follow the same Gaussian function with the same parameters except that defect 1, 2 and 3 are centered respectively 0.8, 0.6 and 0.4 eV above the valence band. (cf. figure 3.9). **b)** Electron (in blue) and hole (in red) capture probabilities: respectively $\sigma_n.n_s/\Delta n$ and $\sigma_p.n_s/\Delta n$. Since electron-hole recombination occurs via capture by defect, electron (hole) limits the recombination in the case where the electron capture probability section (hole) is below hole (electron) capture probability section. The graph can be explained in the same way as figure 2.1 except that at high injection, SRV is limited both by electron and hole capture since electron and hole capture cross section are of the same order of magnitude. The decrease of the SRV due to hole emission is reduced compared with figure 2.1 because, hole emission is proportional to σ_p (cf. equation 3.38) which is 100 times lower in this case.

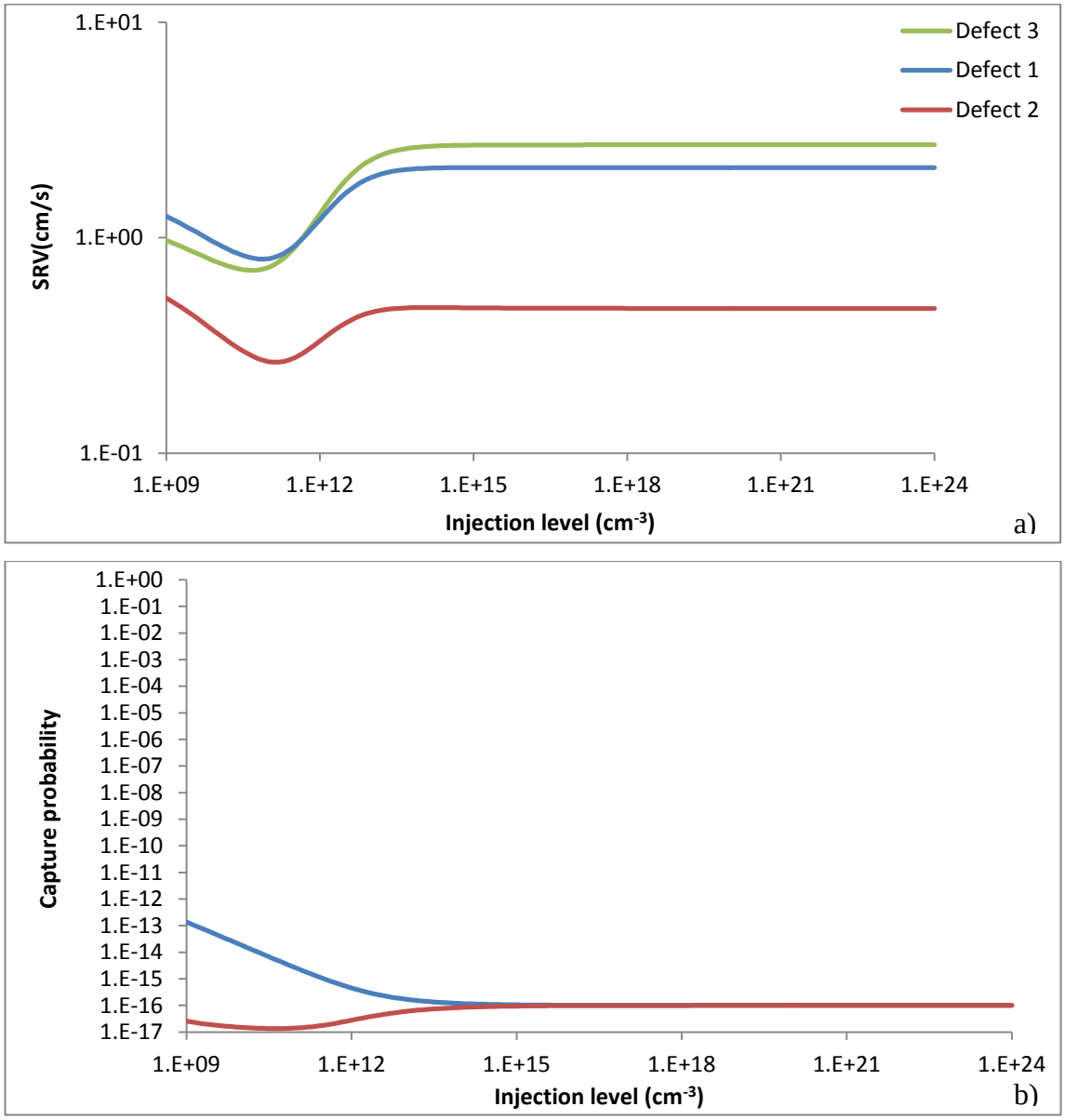

Figure 3.25 a) Evolution of the SRV versus injection level Δn when the fixed charge density $Q_f=10^9$ cm^{-2}. Defects 1 to 3 follow the same Gaussian function with the same parameters except that defect 1, 2 and 3 are centered respectively 0.8, 0.6 and 0.4 eV above the valence band. (cf. figure 3.9). **b)** Electron (in blue) and hole (in red) capture probabilities: respectively $\sigma_n.n_s/\Delta n$ and $\sigma_p.n_s/\Delta n$. Since electron-hole recombination occurs via capture by defect, electron (hole) limits the recombination in the case where the electron capture probability section (hole) is below hole (electron) capture probability section. Although the shape of the SRV is very different than on figure 3.22, the curve can be described in the same way except that the SRV curve on figure 3.25 always follow the evolution of the hole capture probability section with Δn because electron capture probability section does not decrease below hole capture probability section since σ_n and σ_p .

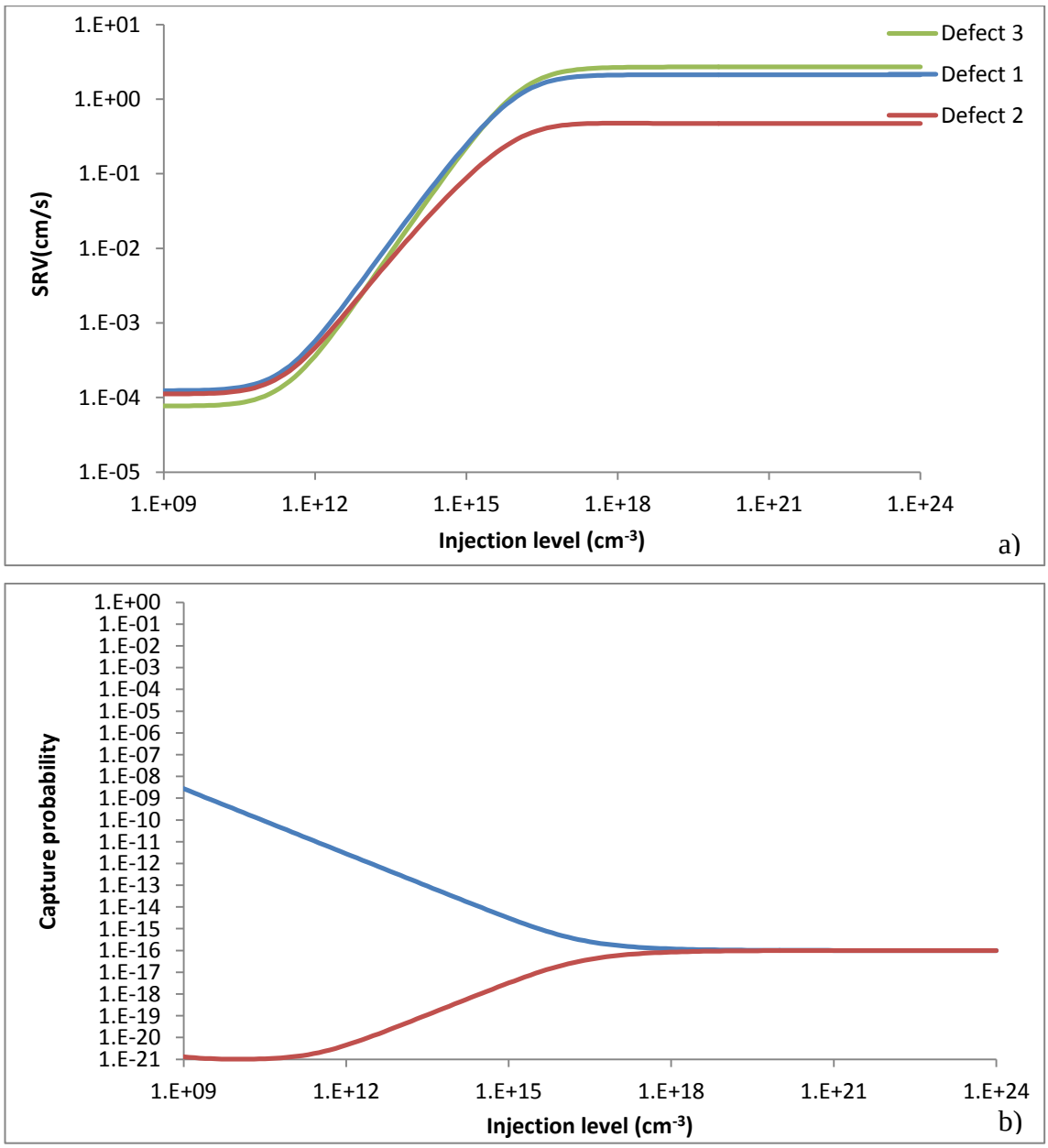

Figure 3.26 a) Evolution of the SRV versus injection level Δn when the fixed charge density $Q_f=10^{11}$ cm^{-2}. Defects 1 to 3 follow the same Gaussian function with the same parameters except that defect 1, 2 and 3 are centered respectively 0.8, 0.6 and 0.4 eV above the valence band. (cf. figure 3.9). **b)** Electron (in blue) and hole (in red) capture probabilities: respectively $\sigma_n.n_s/\Delta n$ and $\sigma_p.n_s/\Delta n$. Since electron-hole recombination occurs via capture by defect, electron (hole) limits the recombination in the case where the electron capture probability section (hole) is below hole (electron) capture probability section. The SRV curves can be described in the same way as on figure 3.23. However since SRV is limited by hole capture when injection level is not very high, the SRV at low injection is 100 times lower than on figure 3.23. The value of SRV at high injection is of same order of magnitude than on figure 3.23 due to the fact that on figure 3.23, the SRV is limited by the value of σ_n and on figure 3.26 to both σn and σ_p.

- **Case 3 $<\sigma_n>$ / $<\sigma_p>$= {145, 40.5, 6.54} respectively for defect {3, 1, 2}.**

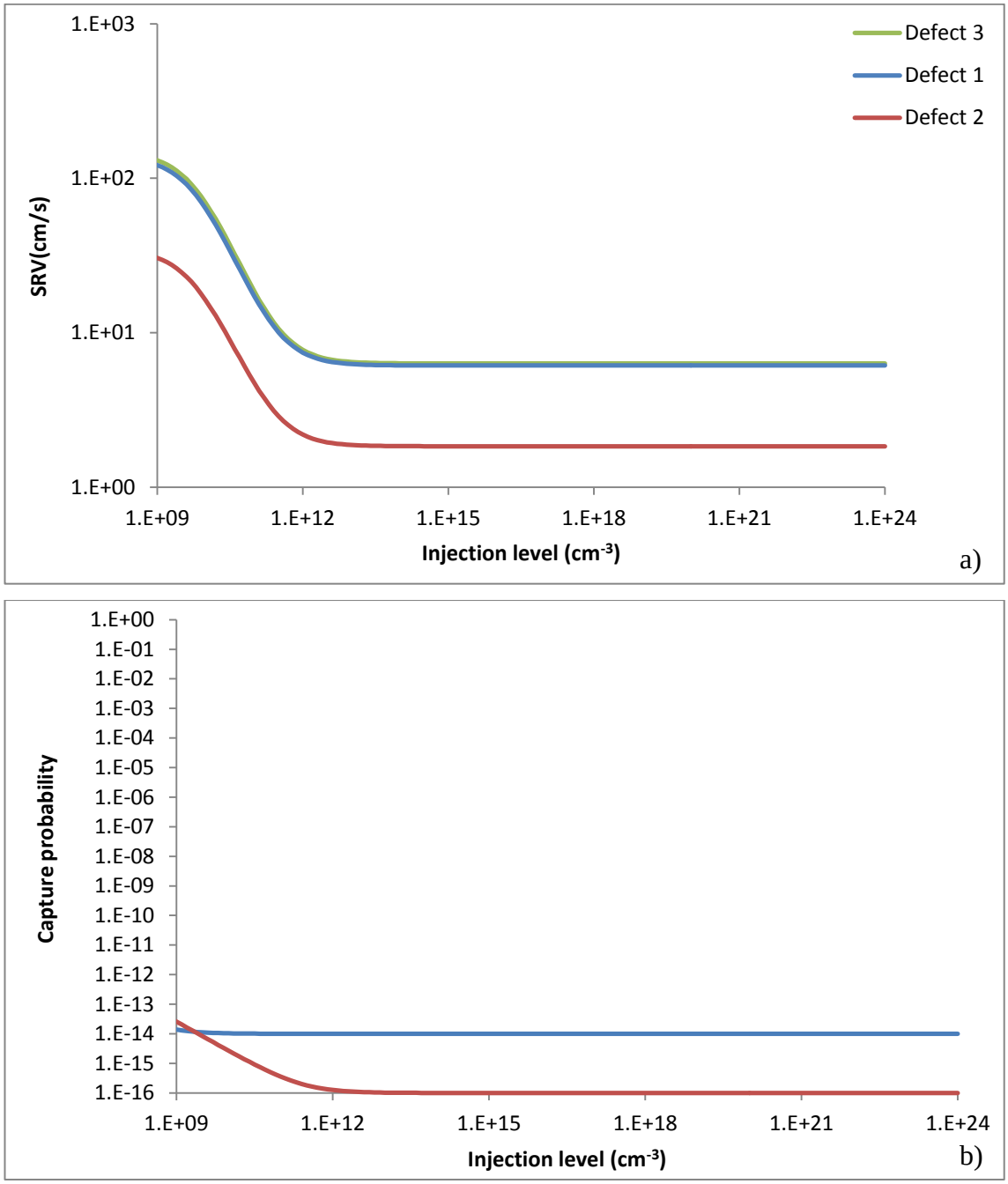

Figure 3.27 a) Evolution of the SRV versus injection level Δn when Q_f=0. Defects 1 to 3 follow the same Gaussian function with the same parameters except that defect 1, 2 and 3 are centered respectively 0.8, 0.6 and 0.4 eV above the valence band. (cf. figure 3.9). **b)** Electron (in blue) and hole (in red) capture probabilities: respectively $\sigma_n.n_s/\Delta n$ and $\sigma_p.n_s/\Delta n$. Since electron-hole recombination occurs via capture by defect, electron (hole) limits the recombination in the case where the electron capture probability section (hole) is below hole (electron) capture probability section.

The difference with case 1 and 2 of figure 3.21 and 3.24 is that since σ_n is 100 times higher than σ_p, the electron capture probability section is almost below hole capture

probability section at low injection level. Therefore, SRV follow the decrease of the hole capture probability section explained whose origin is explained on figure 3.21. The SRV at high injection are higher than on figure 3.21 (and a fortiori figure 3.22) for defect 2and 1 and lower for defect 3 because $<\sigma_p>$ on figure 3.27 is higher than $<\sigma_n>$ on figure 3.21 as can be easily remarked by comparing the corresponding values of σ_n/σ_p.

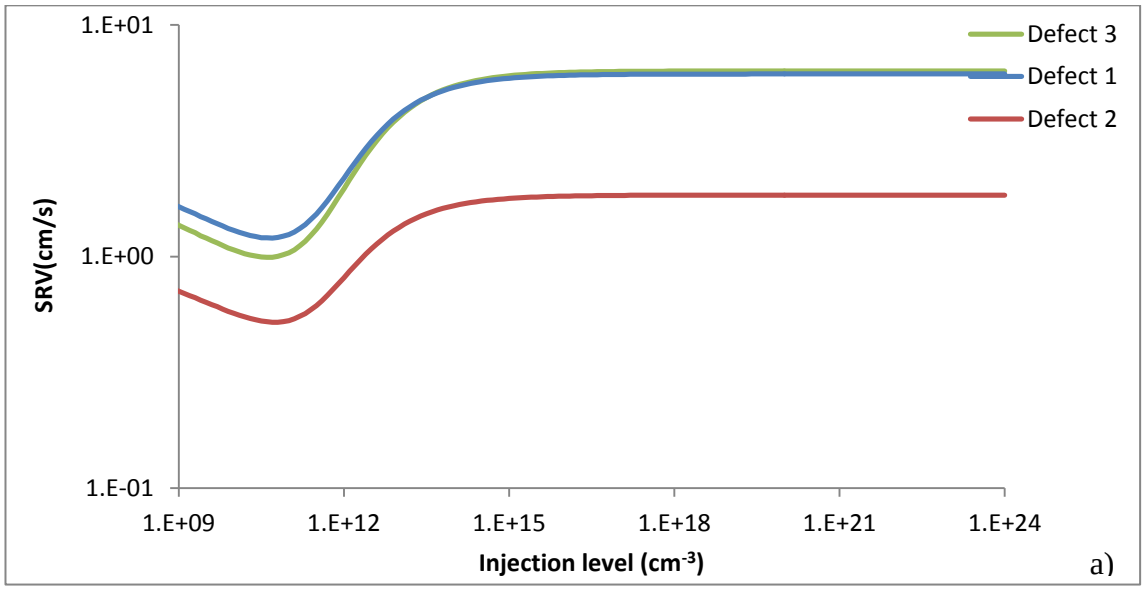

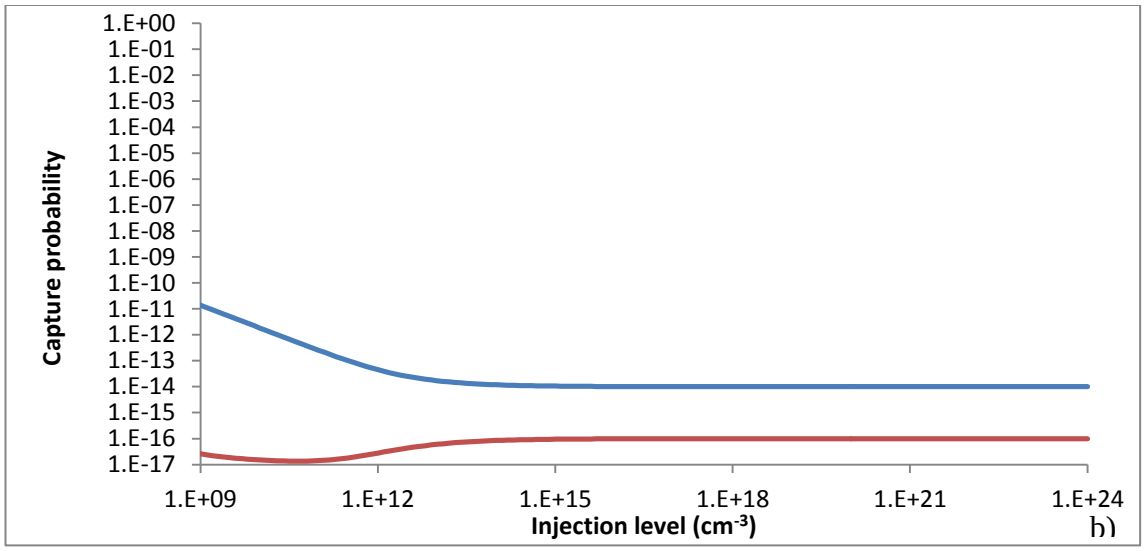

Figure 3.28 a) Evolution of the SRV versus injection level Δn when the fixed charge density $Q_f=10^9$ cm^{-2}. Defects 1 to 3 follow the same Gaussian function with the same parameters except that defect 1, 2 and 3 are centered respectively 0.8, 0.6 and 0.4 eV above the valence band. (cf. figure 3.9). **b)** Electron (in blue) and hole (in red) capture probabilities: respectively $\sigma_n.n_s/\Delta n$ and $\sigma_p.n_s/\Delta n$.

Since electron-hole recombination occurs via capture by defect, electron (hole) limits the recombination in the case where the electron capture probability section (hole) is below hole (electron) capture probability section. The only difference with figure 3.25 is the value at high injection level: the SRV is higher because it depends only on the value of σ_p on figure 3.28 whereas (σ_p/ (1+σ_p/σ_n) on figure 3.25.

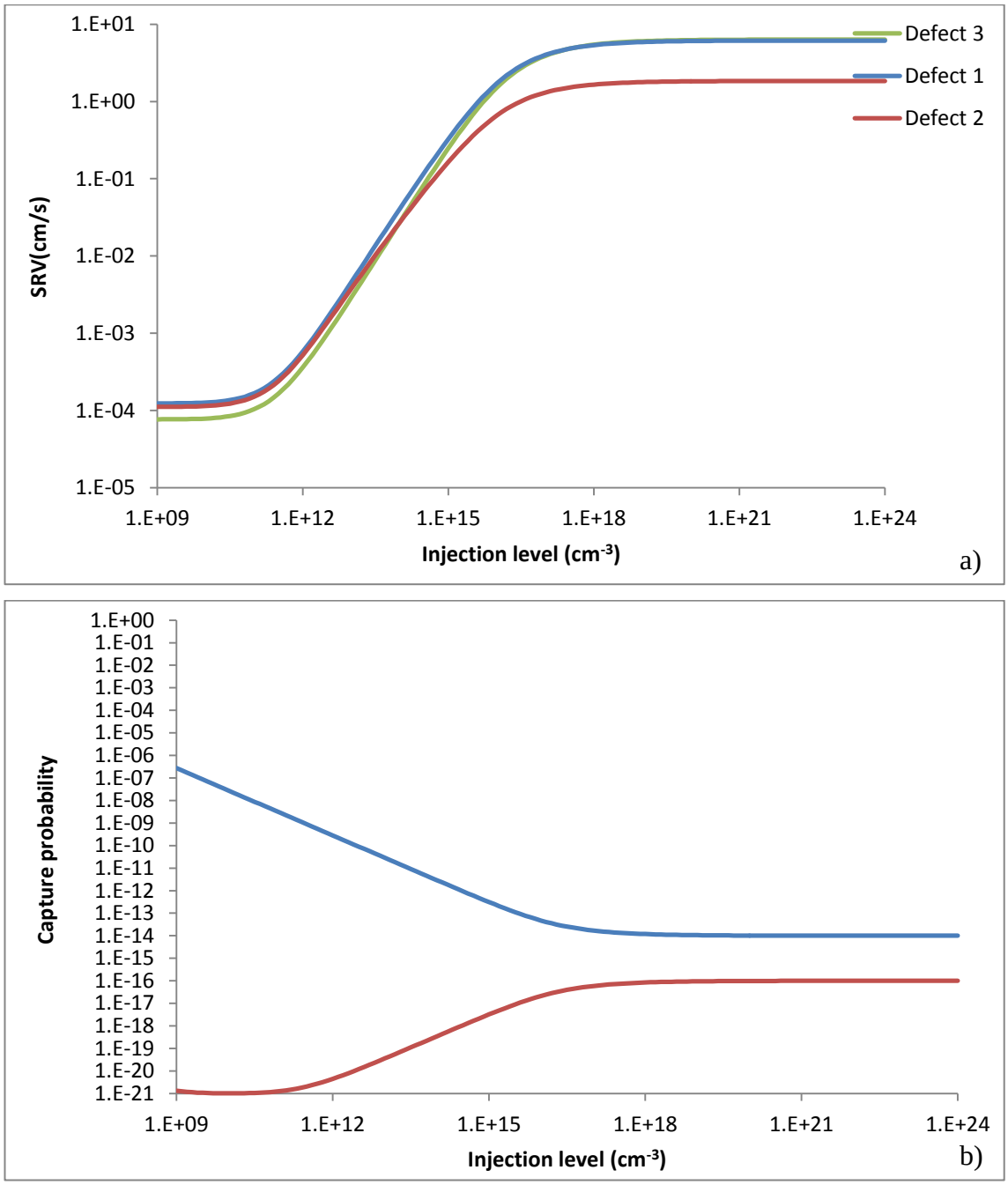

Figure 3.29 Evolution of the SRV versus injection level Δn when the fixed charge density $Q_f=10^{11}$ cm^{-2}. Defects 1 to 3 follow the same Gaussian function with the same parameters except that defect 1, 2 and 3 are centered respectively 0.8, 0.6 and 0.4 eV above the valence band. (cf. figure 3.9). **b)** Electron (in blue) and hole (in red) capture probabilities: respectively $\sigma_n.n_s/\Delta n$ and $\sigma_p.n_s/\Delta n$.

Since electron-hole recombination occurs via capture by defect, electron (hole) limits the recombination in the case where the electron capture probability section (hole) is below hole (electron) capture probability section. The only difference with figure 3.26 is

the value at high injection level: the SRV is higher because it depends only on the value of σ_p on figure 3.29 whereas (σ_p/ (1+σ_p/σ_n) on figure 3.26.

3.6.2 Simulation results for 1 Ohm.cm wafers

- **Case 1 <σ_n> / <σ_p>= {0.0145, 4.05x10^{-3}, 6.54x10^{-4}} respectively for defect {3, 1, 2}.**

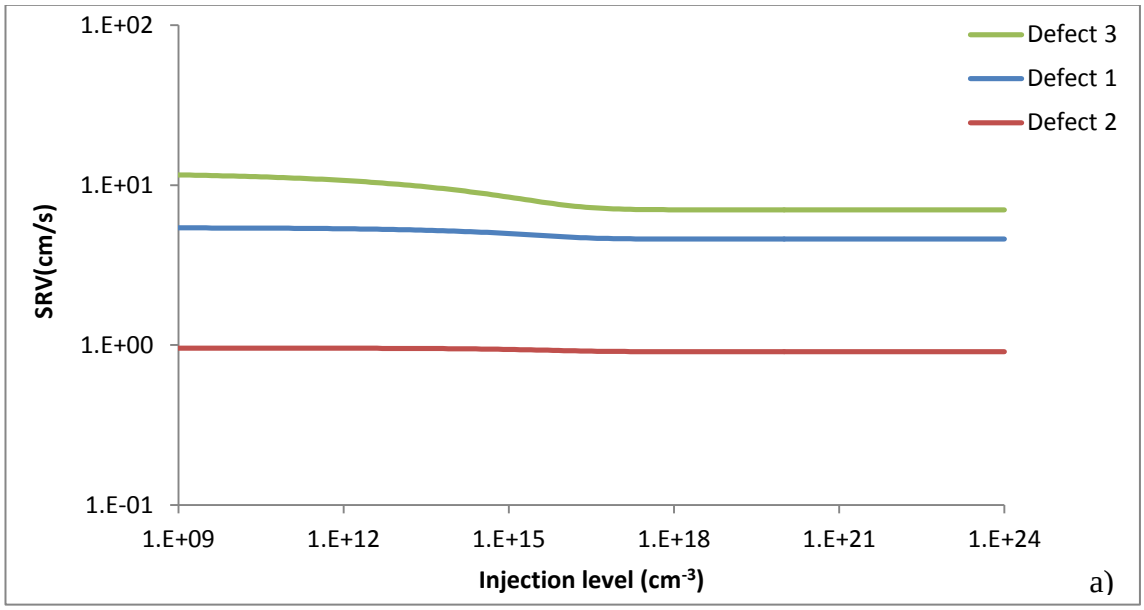

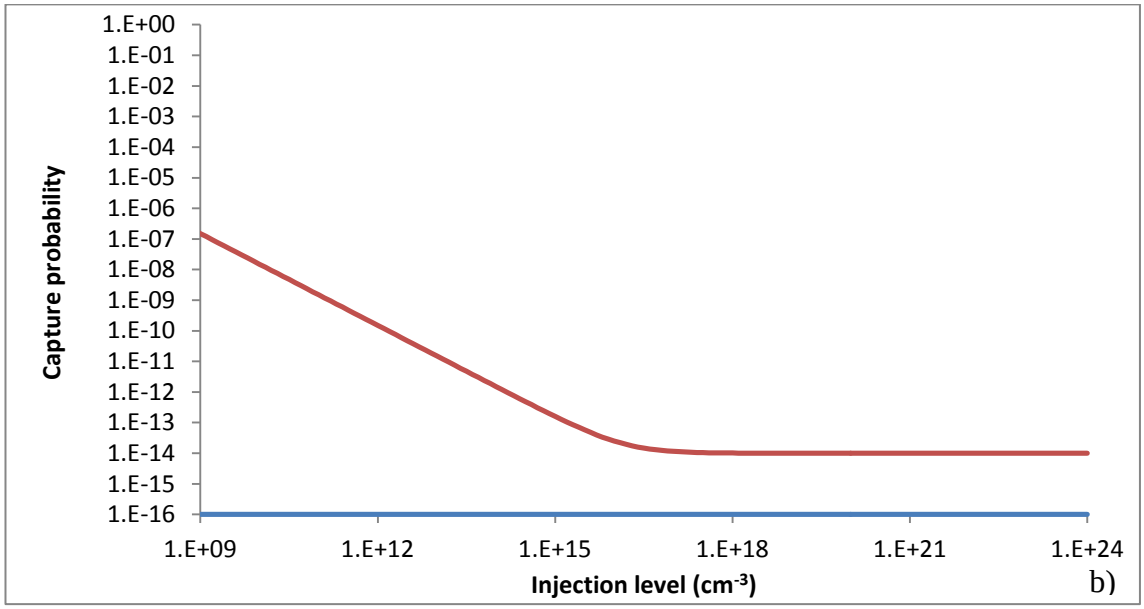

Figure 3.30 a) Evolution of the SRV versus injection level Δn when Q_f=0. Defects 1 to 3 follow the same Gaussian function with the same parameters except that defect 1, 2 and 3 are centered respectively 0.8, 0.6 and 0.4 eV above the valence band. (cf. figure 3.9). **b)** Electron (in blue) and hole (in red) capture probabilities: respectively $\sigma_n.n_s/\Delta n$ and $\sigma_p.n_s/\Delta n$. Since electron-hole recombination occurs via capture by defect, electron (hole) limits the recombination in the case where the electron capture probability section (hole) is below hole (electron) capture probability section.

As can be seen, the only difference with figure 3.21 is the fact that on figure 3.30 the effect of hole emission is negligible because the hole concentration p_1 in the valence band due to emission from defect is below the doping p_0 (cf. equation 3.45). The explanation of the shape of curve corresponding to defect 3 at low injection would require a complete analysis of the integration of the SRV function on the defect width which is beyond the scope of this study.

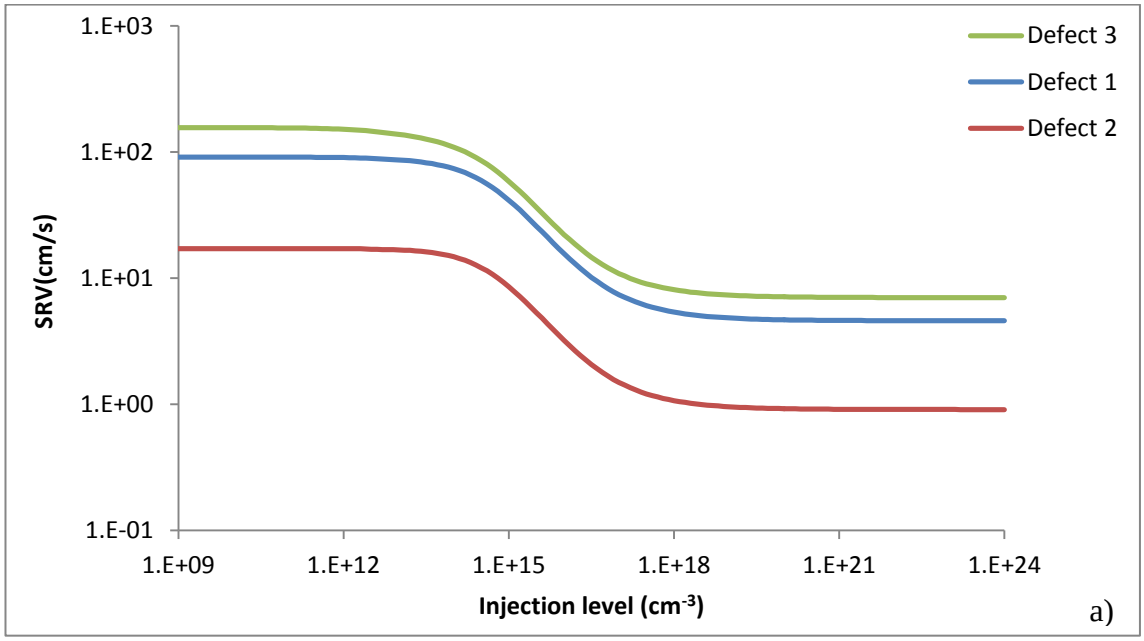

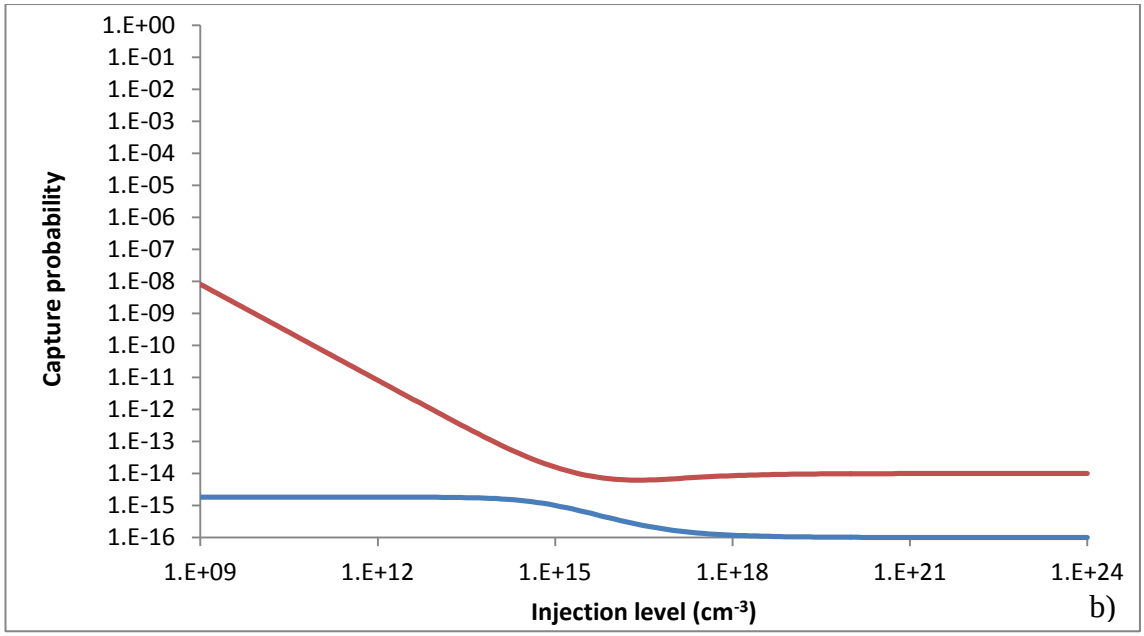

Figure 3.31 a) Evolution of the SRV versus injection level Δn when $Q_f=10^{11}$ cm^{-2}. Defects 1 to 3 follow the same Gaussian function with the same parameters except that defect 1, 2 and 3 are centered respectively 0.8, 0.6 and 0.4 eV above the valence band. (cf. figure 3.9). **b)** Electron (in blue) and hole (in red) capture probabilities: respectively $\sigma_n.n_s/\Delta n$ and $\sigma_p.n_s/\Delta n$. Since electron-hole recombination occurs via capture by defect, electron (hole) limits the recombination in the case where the electron capture probability section (hole) is below hole (electron) capture probability section.

The figure 3.31 describes the case where Q_f is in low range is illustrated. The interesting effect of Q_f regarding SRV is the surface potential generate by Q_f increases the electron concentration at the surface, but since is still p_s very beyond n_S the SRV follows the electron capture probability section which is higher due to the increase of n_s. Since the value of Q_f is relatively high here compare with the previous case of 8000 ohm.cm wafer and on the other hand because the electron concentration is not high enough to balance the effect of Q_f, the surface potential ψ_S ($n_s/\Delta n \sim e^{q\psi s/kT}$ in respect with equation 3.59) remains almost constant until a injection level around 10^{14} cm^{-3} where it decreases and (consequently n_s) until reaching a minimum where it remains constant. The SRV follows the evolution of electron capture probability section on the whole injection level range.

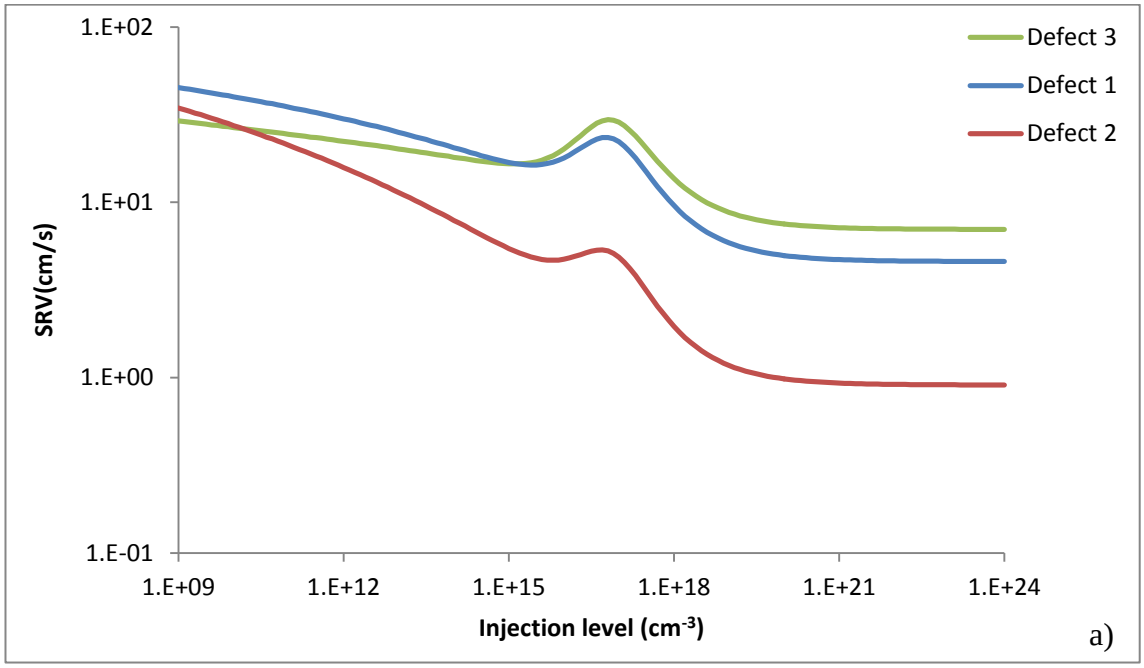

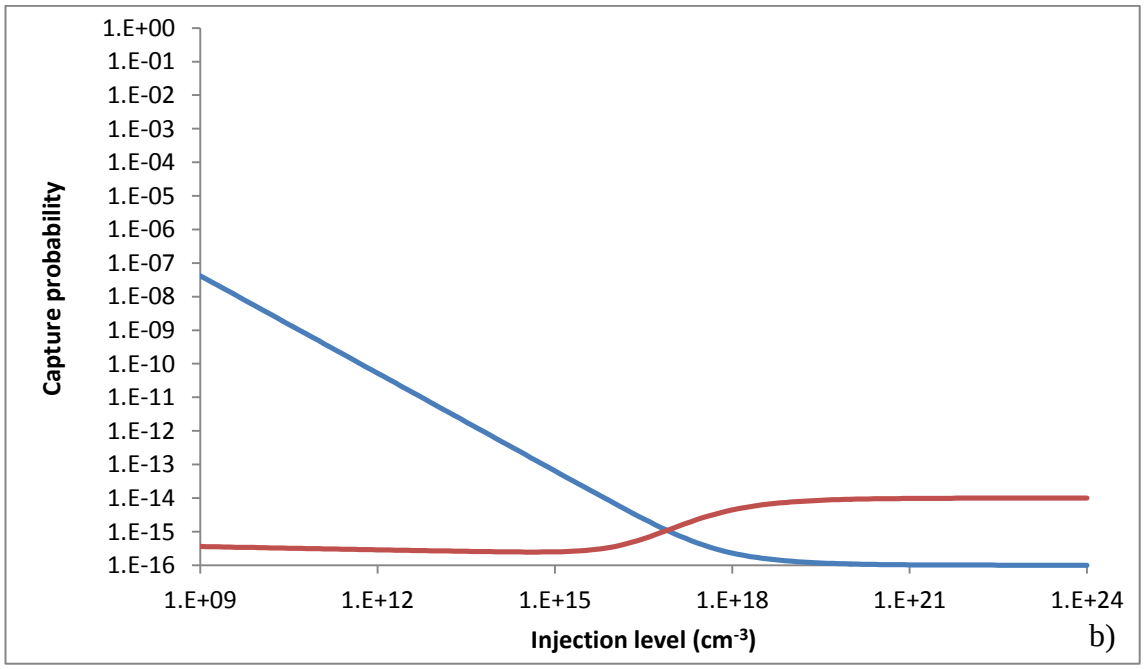

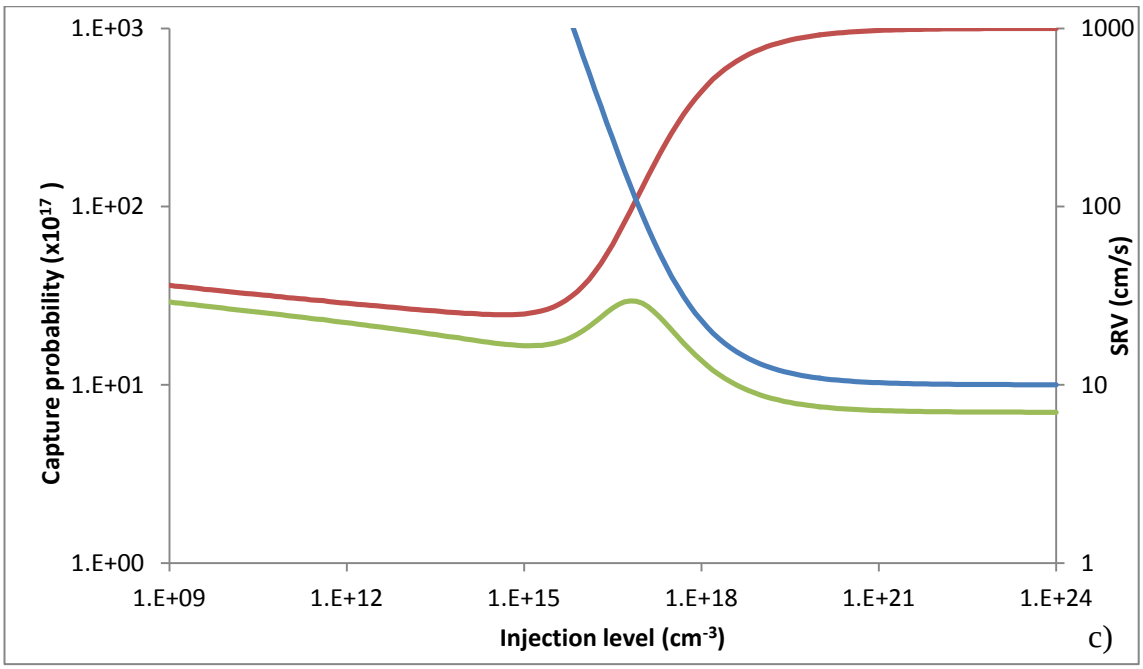

Figure 3.32 a) Evolution of the SRV versus injection level Δn when the fixed charge density Q_f=5x10^{11} cm^{-2}. Defects 1 to 3 follow the same Gaussian function with the same parameters except that defect 1, 2 and 3 are centered respectively 0.8, 0.6 and 0.4 eV above the valence band. (cf. figure 3.9). **b)** Electron (in blue) and hole (in red) capture probabilities: respectively $\sigma_n.n_s/\Delta n$ and $\sigma_p.n_s/\Delta n$. **c)** Electron (in blue) and hole (in red) capture probabilities and SRV (in green)**.** Since electron-hole recombination occurs via capture by defect, electron (hole) limits the recombination in the case where the electron capture probability section (hole) is below hole (electron) capture probability section.

The case of figure 3.32 (Q_f=5x10^{11} cm^{-2}) is similar to figure 3.22 (Q_f=10^9 cm^{-2}). However the major difference between the 2 figures appears for defect 3 near the low injection level range. This is due to the fact that the contribution p_1 of the hole emission from defect to valence band is negligible here compare with the doping p_0 whereas it is not the case on figure 3.22. Thus, as can be seen on figure 3.32 c, the SRV follow the evolution of the minimum between electron and hole capture probabilities for the 3 curves.

- **Case 2 $<\sigma_n>$ / $<\sigma_p>$= {1.45, 0.405, 6.54x10^{-2}} respectively for defect {3, 1, 2}.**

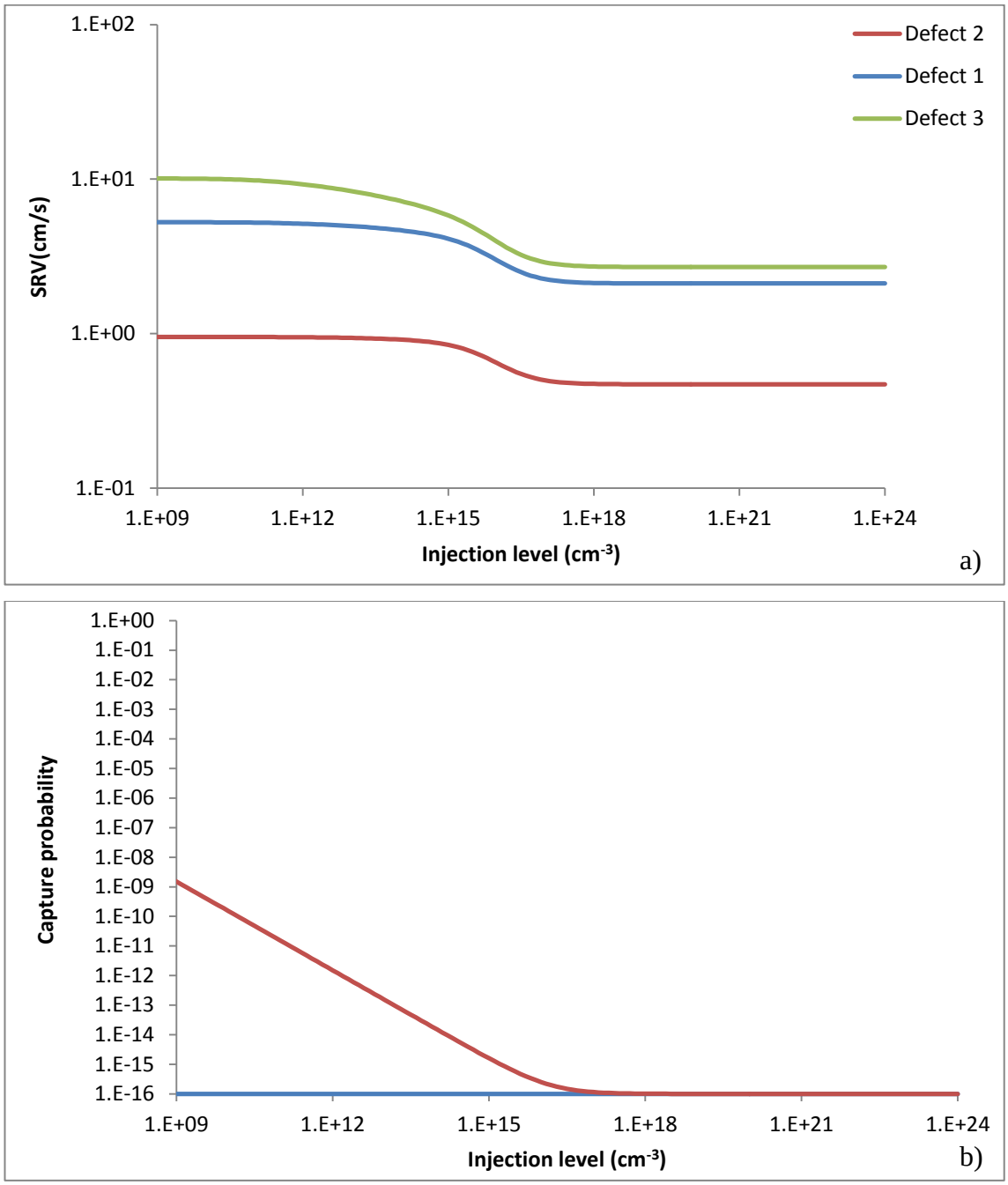

Figure 3.33 a) Evolution of the SRV versus injection level Δn when Q_f=0. Defects 1 to 3 follow the same Gaussian function with the same parameters except that defect 1, 2 and 3 are centered respectively 0.8, 0.6 and 0.4 eV above the valence band. (cf. figure 3.9). **b)** Electron (in blue) and hole (in red) capture probabilities: respectively $\sigma_n.n_s/\Delta n$ and $\sigma_p.n_s/\Delta n$.

Since electron-hole recombination occurs via capture by defect, electron (hole) limits the recombination in the case where the electron capture probability section (hole) is below hole (electron) capture probability section. The case described above in figure

3.33 is similar as figure 3.30, at low injection the SRV values are the same because SRV in only limited by electron capture probability section as in figure 3.30.Since σ_n and σ_p have the same order of magnitude electron and hole capture probabilities have also the same order of magnitude when $\Delta n > p_0$ as seen on figure 3.33 b. Then SRV is limited both by electron and hole capture an thus, SRV at high injection is lower.

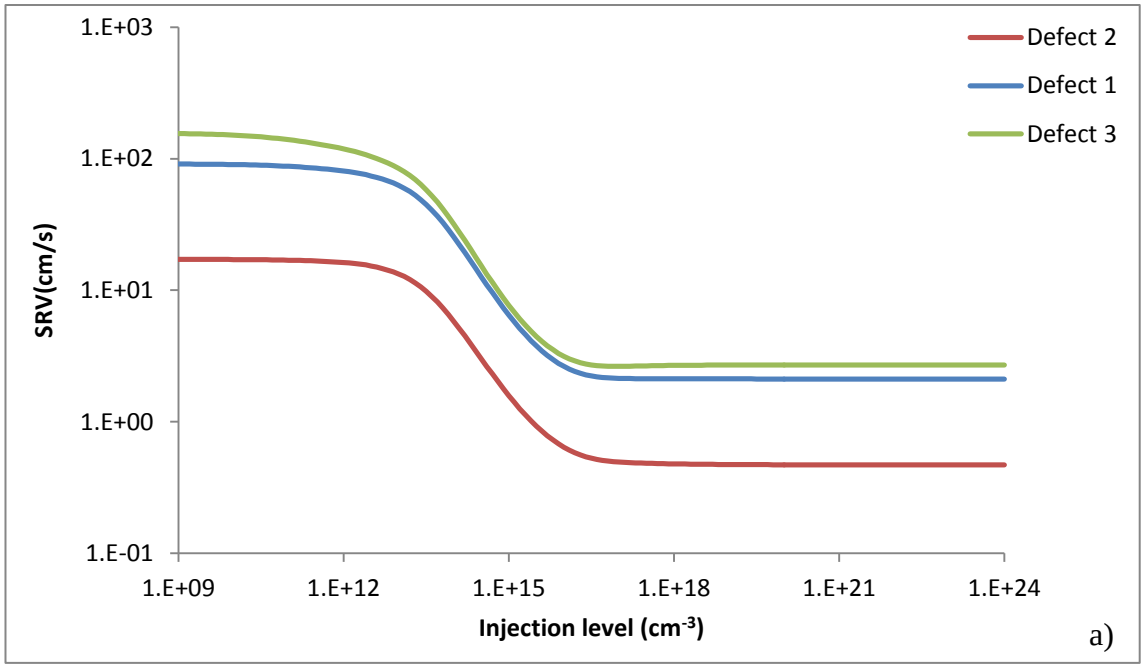

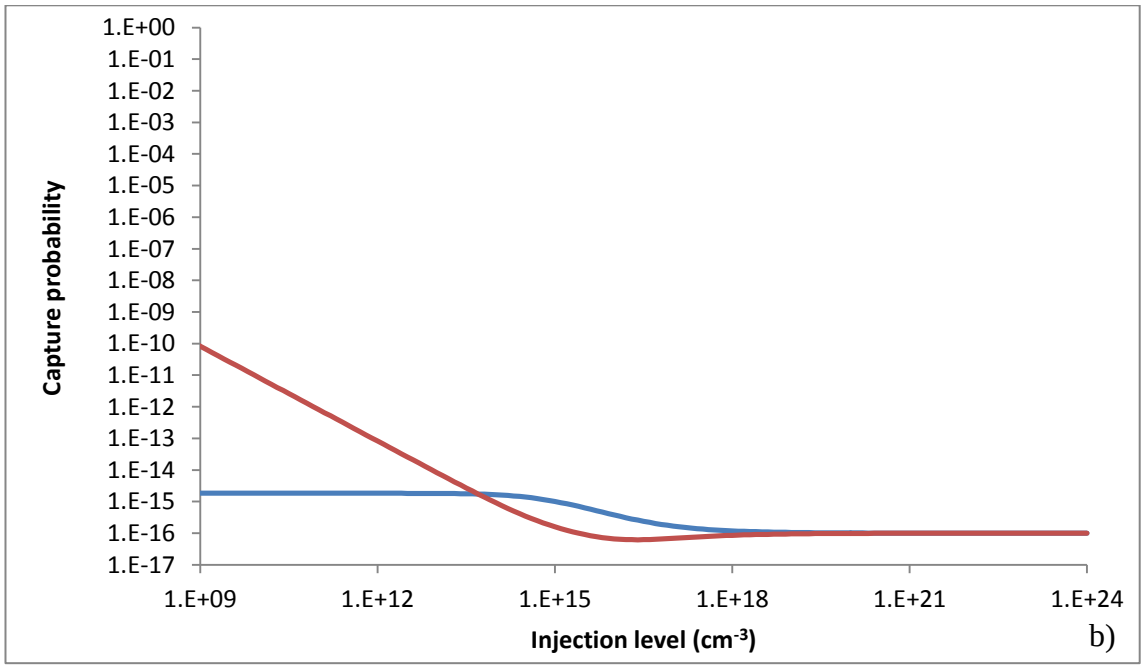

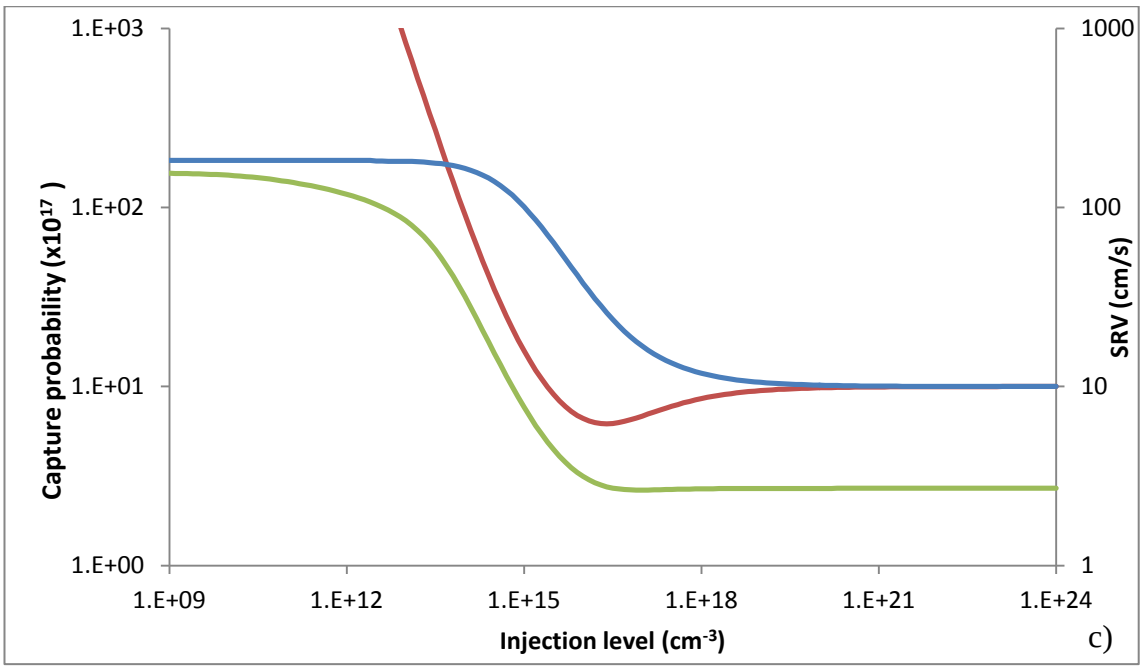

Figure 3.34 a) Evolution of the SRV versus injection level Δn when the fixed charge density Q_f=1x10^{11} cm^{-2}. Defects 1 to 3 follow the same Gaussian function with the same parameters except that defect 1, 2 and 3 are centered respectively 0.8, 0.6 and 0.4 eV above the valence band. (cf. figure 3.9). **b)** Electron (in blue) and hole (in red) capture probabilities: respectively $\sigma_n.n_s/\Delta n$ and $\sigma_p.n_s/\Delta n$. **c)** Electron (in blue) and hole (in red) capture probabilities and SRV (in green). The shape of the SRV curves is similar as SRV curves of figure 3.31 but since σ_p is 100 times lower than on figure 3.31, the hole capture probability section becomes lower than the electron capture probability section when Δn around 10^{14} cm^{-3} and since at this level, the decrease of capture probability section is higher for hole than for electron, the SRV decrease faster than on figure 3.31.

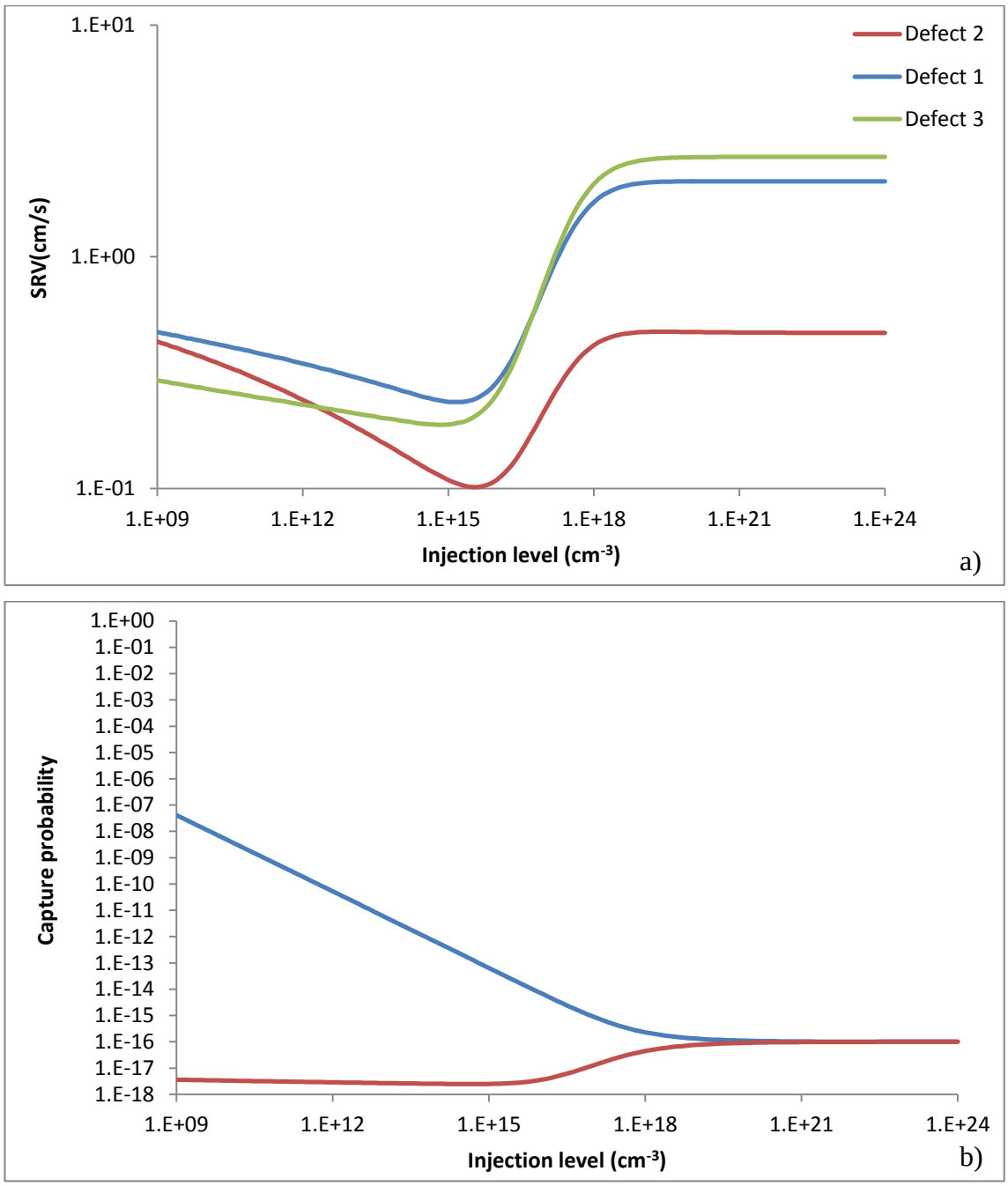

Figure 3.35 a) Evolution of the SRV versus injection level Δn when the fixed charge density Q_f=5x10^{11} cm^{-2}. Defects 1 to 3 follow the same Gaussian function with the same parameters except that defect 1, 2 and 3 are centered respectively 0.8, 0.6 and 0.4 eV above the valence band. (cf. figure 3.9). **b)** Electron (in blue) and hole (in red) capture probabilities: respectively $\sigma_n.n_s/\Delta n$ and $\sigma_p.n_s/\Delta n$. Since electron-hole recombination occurs via capture by defect, electron (hole) limits the recombination in the case where the electron capture probability section (hole) is below hole (electron) capture probability section.

In the figure 3.35 above, until Δn around 10^{16} cm^{-3}, the SRV follow the same evolution than on figure 3.32 because on both case but since $\sigma_n << \sigma_p$ for figure 3.32, the capture probability section becomes very lower for electron than for hole from Δn around 10^{17} cm^{-3} whereas on the figure 3.35, electron and hole capture probabilities become almost

equal and thus SRV follows the increase of the hole capture probably which is due to the decrease of the surface potential ψ. At high injection, SRV reaches a constant value independent of the fixed charge density.

- **Case 3 $<\sigma_n\ \sigma_n>$ / $<\sigma_p>$= {145, 40.5, 6.54} respectively for defect {3, 1, 2}.**

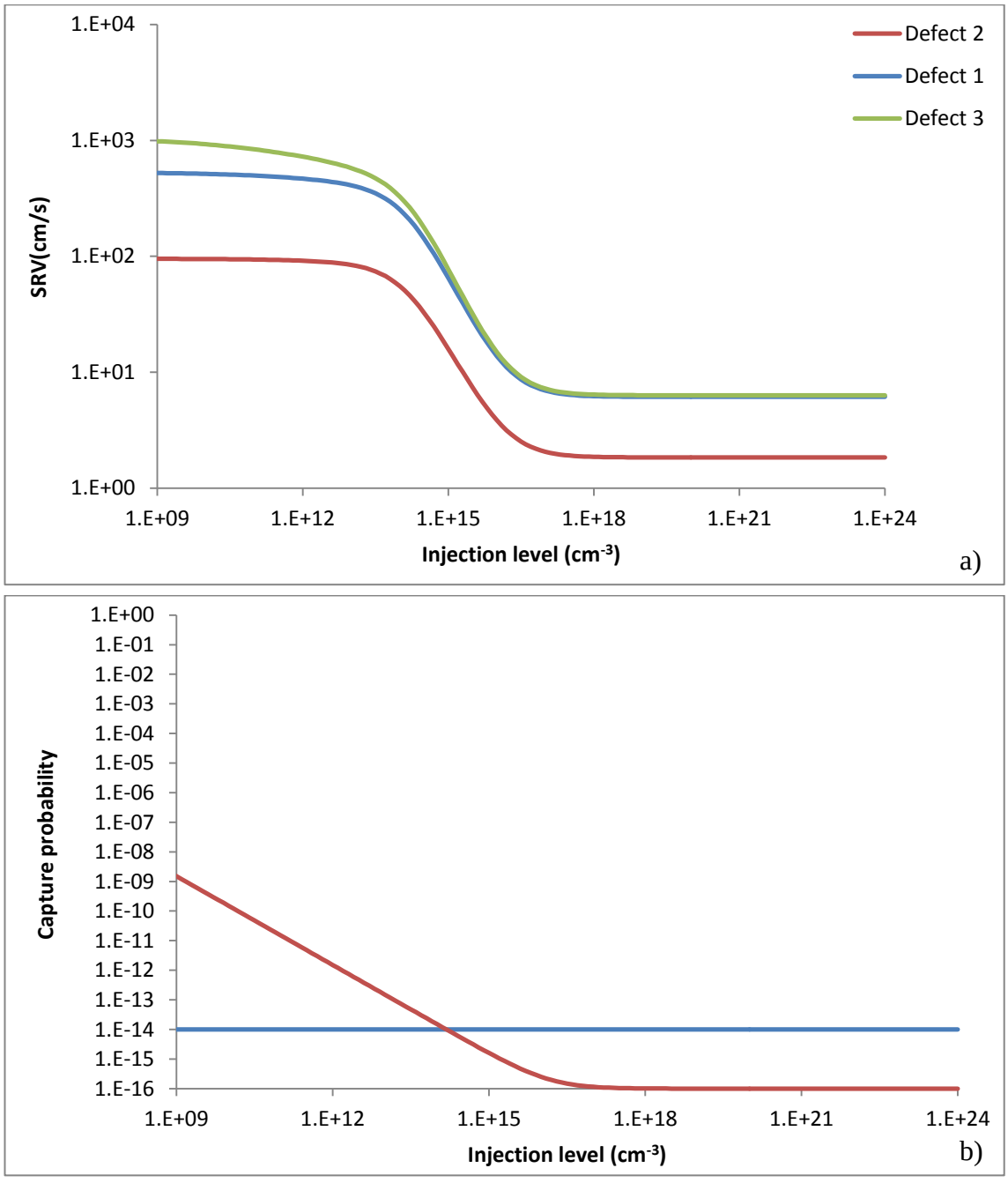

Figure 3.36 a) Evolution of the SRV versus injection level Δn when Q_f=0. Defects 1 to 3 follow the same Gaussian function with the same parameters except that defect 1, 2 and 3 are centered respectively 0.8, 0.6 and 0.4 eV above the valence band. (cf. figure 3.9). **b)** Electron (in blue)

and hole (in red) capture probabilities: respectively $\sigma_n.n_s/\Delta n$ and $\sigma_p.n_s/\Delta n$. Since electron-hole recombination occurs via capture by defect, electron (hole) limits the recombination in the case where the electron capture probability section (hole) is below hole (electron) capture probability section.

The case represented above in figure 3.36 is similar as figure 3.30, at low injection the SRV is 100 times higher because electron capture probability section is 100 times higher. Due to the decrease of the hole capture probability section, this latter goes below the electron capture probability section for an injection level around $\Delta n = 10^{14}$ cm^{-3} and at high injection level, SRV is only limited by hole capture which explain why SRV at high injection is higher for case 2 than for case 2.

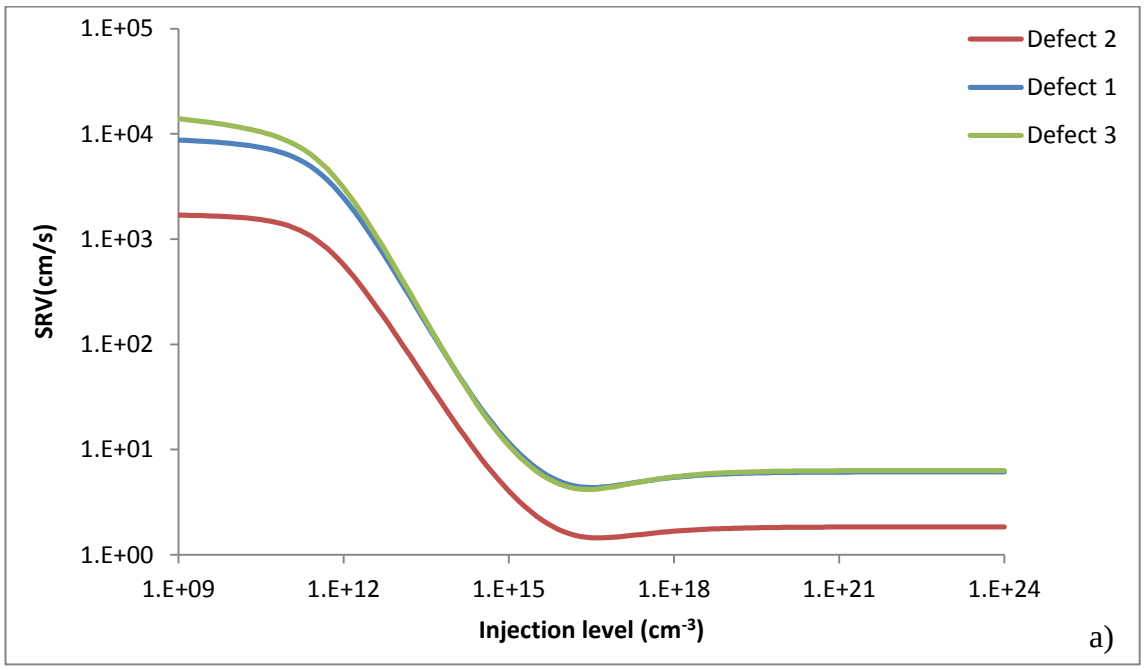

a)

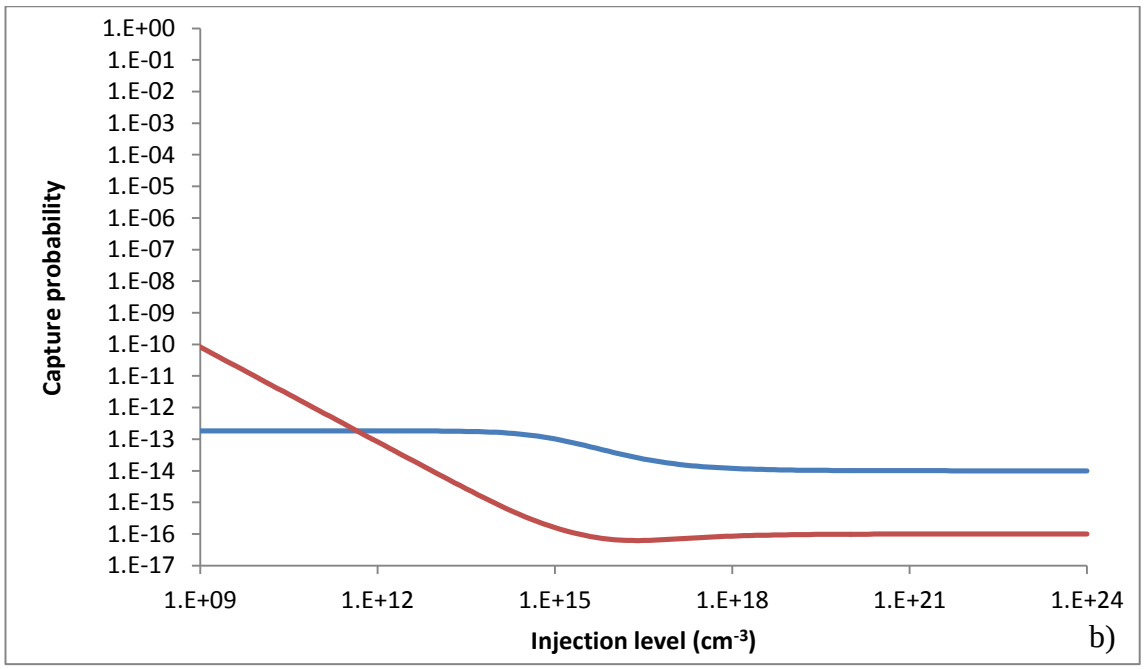

Figure 3.37 a) Evolution of the SRV versus injection level Δn when Q_f=0. Defects 1 to 3 follow the same Gaussian function with the same parameters except that defect 1, 2 and 3 are centered respectively 0.8, 0.6 and 0.4 eV above the valence band. (cf. figure 3.9). **b)** Electron (in blue) and hole (in red) capture probabilities: respectively $\sigma_n.n_s/\Delta n$ and $\sigma_p.n_s/\Delta n$. Since electron-hole recombination occurs via capture by defect, electron (hole) limits the recombination in the case where the electron capture probability section (hole) is below hole (electron) capture probability section. The SRV curve are shifted toward the high value compare with figure 3.36 because, the fixed charge attract electron and thus electron probability increases resulting in an increase of the SRV at low injection.

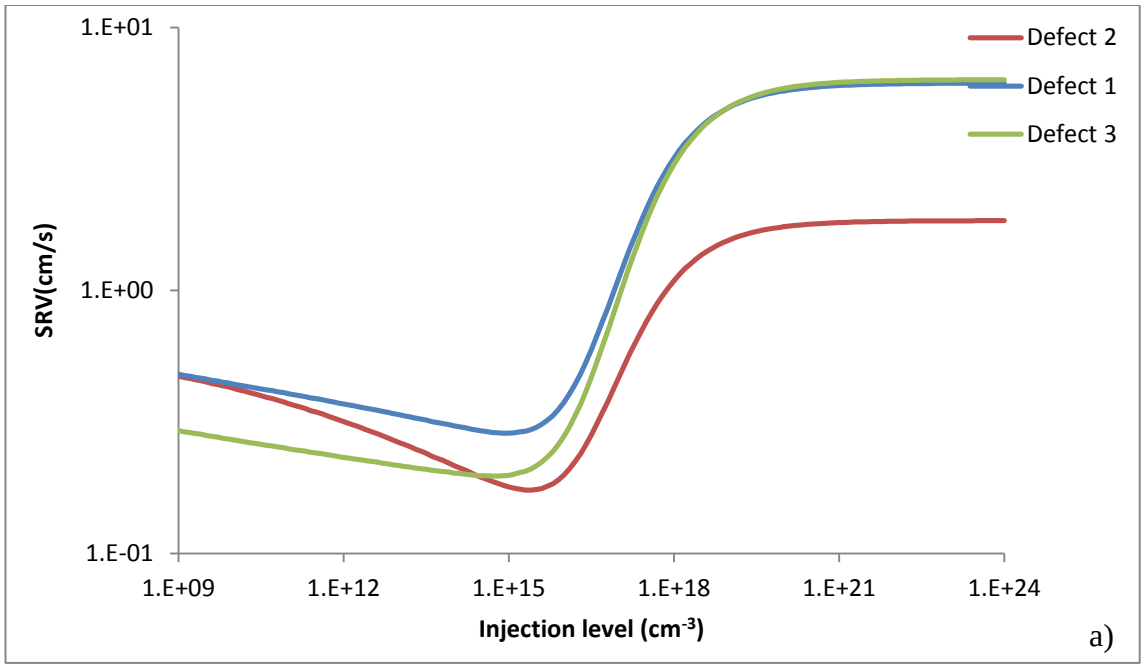

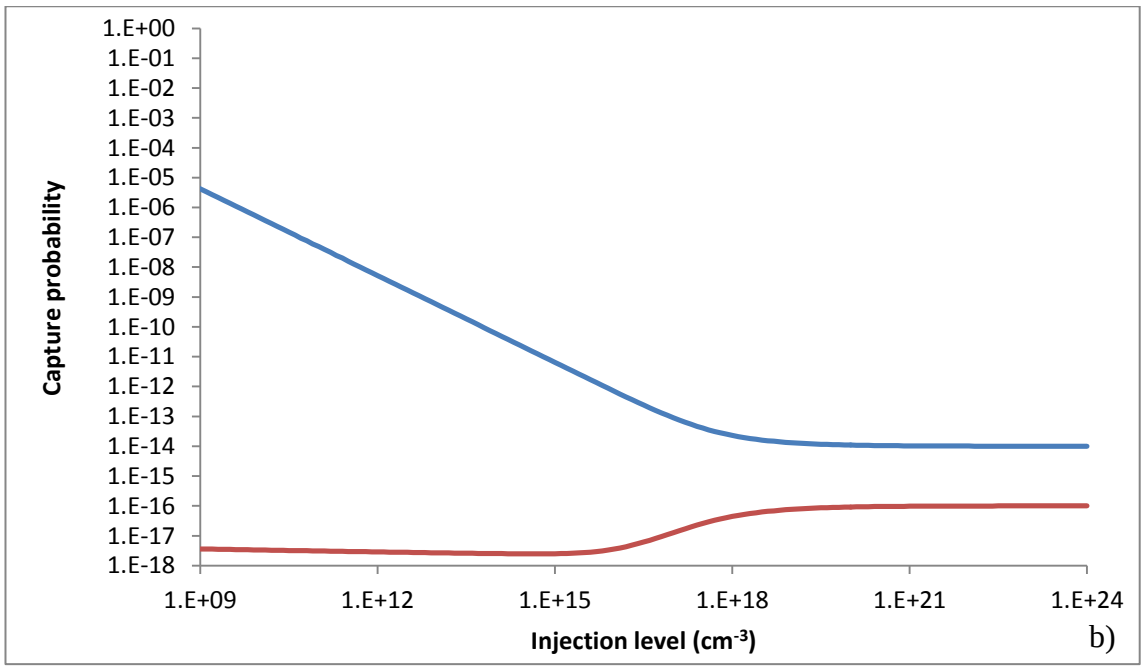

Figure 3.38 a) Evolution of the SRV versus injection level Δn when the fixed charge density Q_f=5x10^{11} cm^{-2}. Defects 1 to 3 follow the same Gaussian function with the same parameters except that defect 1, 2 and 3 are centered respectively 0.8, 0.6 and 0.4 eV above the valence band. (cf. figure 3.9). **b)** Electron (in blue) and hole (in red) capture probabilities: respectively $\sigma_n.n_s/\Delta n$ and $\sigma_p.n_s/\Delta n$.

In the figure 3.38 above, since electron-hole recombination occurs via capture by defect, electron (hole) limits the recombination in the case where the electron capture probability section (hole) is below hole (electron) capture probability section. The SRV follows the same evolution versus injection level as on figure 3.35 except that it is limited only by hole capture probability section even at high injection level because σ_n is 100 times higher than σ_p.

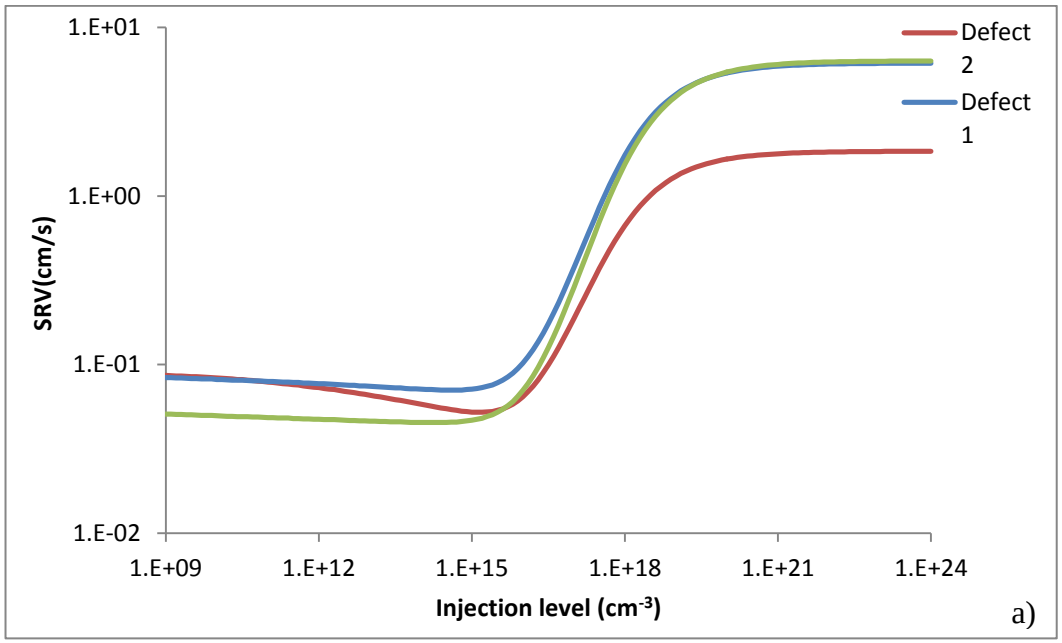

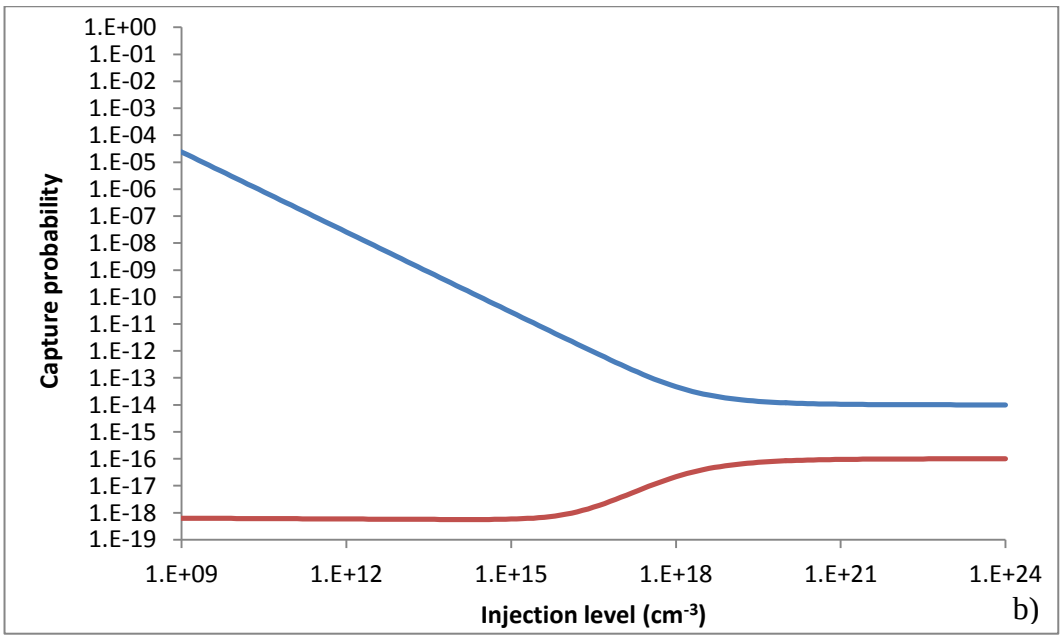

Figure 3.39 a) Evolution of the SRV versus injection level Δn when the fixed charge density $Q_f=10^{12}$ cm^{-2}. Defects 1 to 3 follow the same Gaussian function with the same parameters except that defect 1, 2 and 3 are centered respectively 0.8, 0.6 and 0.4 eV above the valence band. (cf. figure 3.9). **b)** Electron (in blue) and hole (in red) capture probabilities: respectively $\sigma_n.n_s/\Delta n$ and $\sigma_p.n_s/\Delta n$.

In the figure 3.39 above, since electron-hole recombination occurs via capture by defect, electron (hole) limits the recombination in the case where the electron capture probability section (hole) is below hole (electron) capture probability section. The difference with figure 3.38 is that due to the very high fixed charge density, p_s is almost equal to Δn even for Δn as low as 10^9 cm^{-3} which explains why hole capture probability section remains constant until the effect of Q_f becomes to reduce around $\Delta n=10^{15}$ cm^{-3}.

3.7 Comparison between experimental SRV and simulation

3.7.1 Measurement of SRV

- **Method**

Micro-wave photo carrier decay (MW-PCD) [3.20, 3.21] is usually used for measuring the minority carrier lifetime in the wafers. The relation between lifetime and recombination rate: $\tau = \Delta n / U$, has been established in section 2.3.4 only for low injection levels. Indeed the relation is an approximation where Δn and n_0 are neglected

before p_0. However, the SRV can be obtained directly from S= U / Δn because the net recombination rate U is:

$$U = G - \frac{dn}{dt} \tag{3.87}$$

The values of the generation rate G, dn/dt as well as Δn are registered (highlighted on figure 3.40) on the excel spreadsheet calculus of Sinton software. However, G is actually expressed in cm^{-2} on the spreadsheet (cf. equation 3.88) whereas G is expressed in cm^{-3} (cf. equation 3.89) in equation 3.87 thus, the registered G has to be divided by the wafer thickness W.

Results Ohms/sq requires special procedure. **Instrument Parameters**

Lifetime @ specified D carrier density (µs)	Maximum Apparent Carrier Density	Approx. Average 1/Tau	Ohms/sq	Ohm-cm	"Carrier density" at bias point	Traps (equiv e-h pairs)	Tau fit ((µs)) (intercept @ $-N_A$)	If h-l-i data, then Jo (A/cm2)	Ref wafer V/sun		Auger Coef. (Don't change)	
9.93	3.8E+15	8.3E+04	75.03478	1.50	0.0E+00	0.0E+00	-124.5	1.55E-12	8.33E-03		1.66E-30	
9.93	1.0E-04						90902	6.54E-12	-1.7E-05	0.032507	-0.63563602	Calibration aS²+bS+c

Carrier-Density Range	Generation (pairs/s)	TAU	1/tau - Auger term	Fit	Implied Voltage (25 C)	PCD with baseline shift.	Suns near bias point	density near bias point	Delta N	Implied V (w/o traps)	Minority Carrier Density	dn/dt
	5.32E+17			92851	0.6384	0.0446			2.98E+14	0.63841083	2.98E+14	
	7.19E+17	1.15E-05	87033	93606	0.6470	0.0619			4.13E+14	0.64702348	4.13E+14	
	9.35E+17	-6.54E-05	-15284	94462	0.6543	0.0814			5.44E+14	0.65430044	5.44E+14	5.51E+19
	1.15E+18	4.67E-04	2142	95368	0.6604	0.1020			6.82E+14	0.66035004	6.82E+14	5.61E+19
	1.35E+18	7.27E-05	13750	96295	0.6654	0.1230			8.24E+14	0.66542775	8.24E+14	5.60E+19
	1.53E+18	5.22E-05	19166	97097	0.6692	0.1411			9.47E+14	0.66918522	9.47E+14	5.82E+19

Figure 3.40 Picture of Sinton software interface: generation rate G, injection level Δn and dn/dt are highlighted in yellow. From these 3 quantities, the recombination rate U is calculated with equation 3.87 for each value of Δn then the SRV is obtained by U/Δn.

This method which is actually similar to the generalized analyses mode in MW-PCD [3.22-3.24] measurement presents the advantage of being the same both on transient or quasi-steady-state and does not require special condition as for instance transient method which requires having a neglected generation rate. However, this does not remove all of the constraint. It has been seen in section 3.24 that the net hole and electron recombination rate are balanced only under steady-state condition. Therefore, the short time duration when the flash light intensity increases has to be removed from the measurement since this duration correspond to a non steady-state. Figure 3.41 represents the evolution of the injection level Δn during the flash intensity which can be divided in two steps. The increasing of Δn corresponds to the time when the flash light intensity increases. After reaching a maximum, the light intensity decreases in an exponential way and so does Δn. The quasi-steady-state regime corresponds to the decreasing step. On figure 3.42, the measuring SRV is given when the measurement

includes the two steps. On the other hand, figure 3.43 and 3.44 represents the same measurement when the measurement of the increasing step has been removed. As can be seen, several SRV values correspond to the same Δn on figure 3.42. These values correspond to the non quasi steady-state regime and should be removed because SRH theory is not valid in this case.

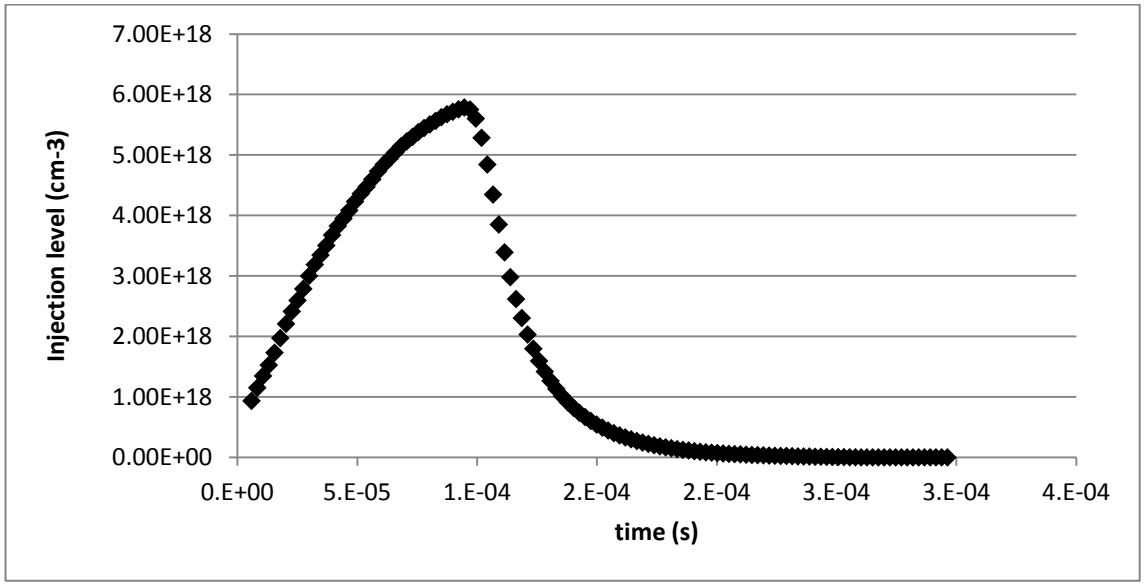

Figure 3.41 Evolution of the injection level Δn with time during the MW-PCD Sinton process. A flash light illuminates the measured sample and then the excess carrier concentration (or injection level) generated depends on the light intensity. The ascendant phase corresponds to the phase following the "switch on" of the light and the descendant phase to the phase following the "switch off" of the light. Lifetime or recombination cannot be determined during the ascendant phase because generation and recombination rate are not in quasi-equilibrium.

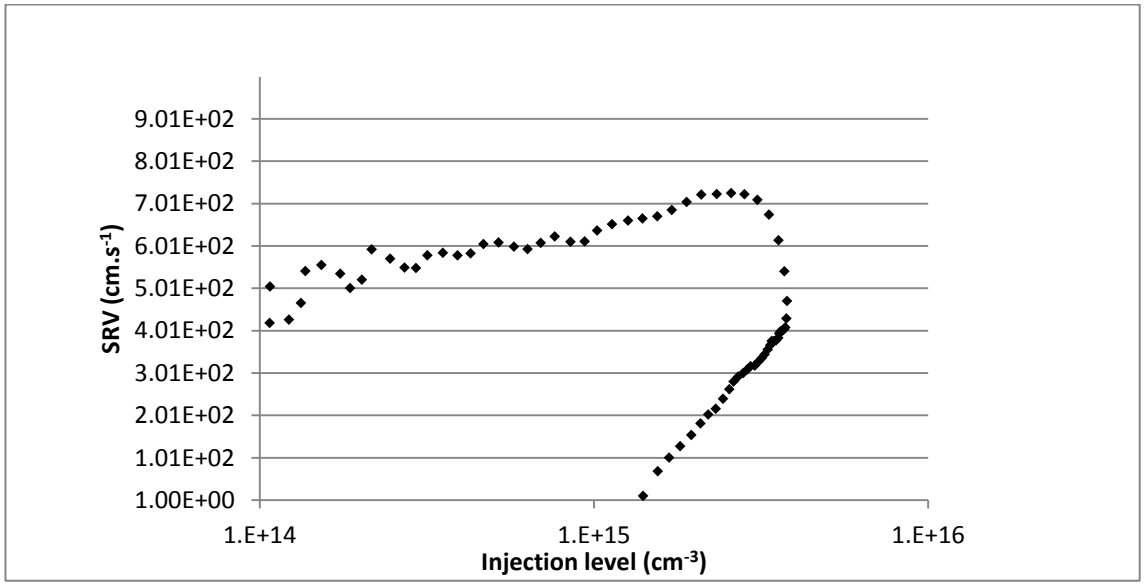

Figure 3.42 SRV as a function of the injection level Δn. The values of Δn correspond to figure 3.41. At higher injection level, there are two SRV values for one value of Δn because the SRV cannot be determined from the values of Δn related to the ascendant phase of the light (cf. figure 3.41).

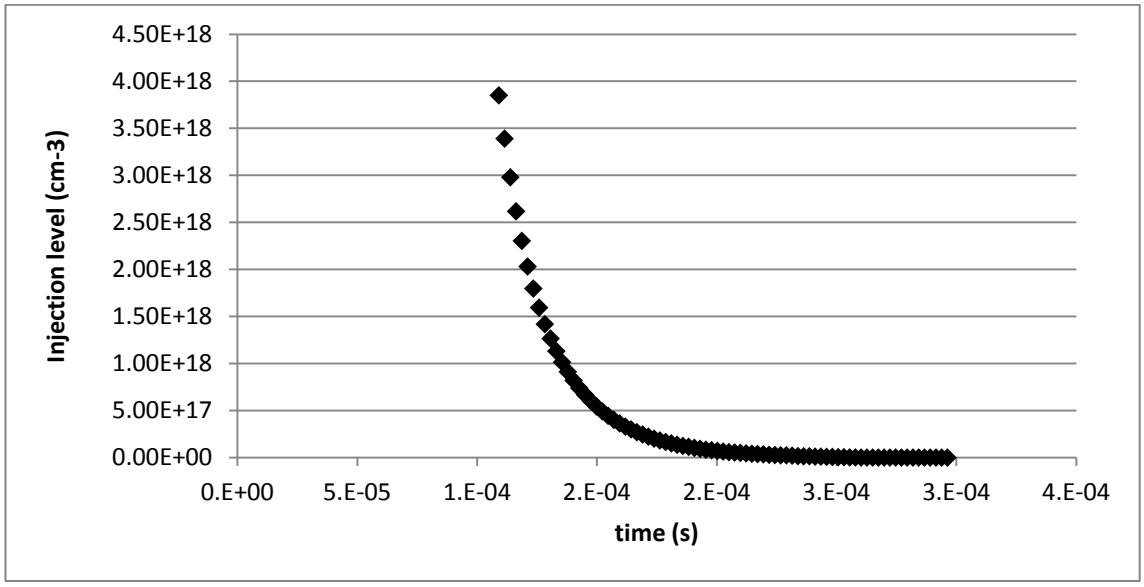

Figure 3.43 Evolution of the injection level Δn with time during the MW-PCD Sinton process. On this figure, the value of Δn corresponding to the phase where light is "switched on" have been removed (cf. figure 3.41)

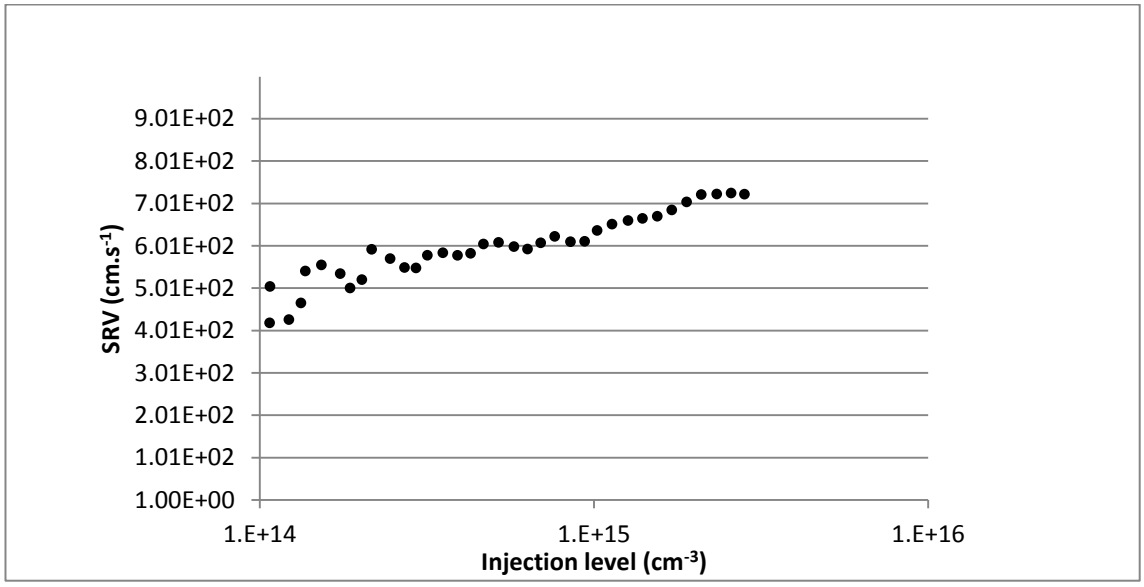

Figure 3.44 SRV as a function of the injection level Δn. The values of Δn correspond to figure 3.43 where the values of Δn corresponding to light "switched on" have been removed (cf. figure 3.41-42).

- **Instrumentation and measurement of parameters**

The generation rate is deduced from the light intensity and the sample absorption f_{abs}. This latter is measured by a light sensor and converted in sun unity. Knowing that the 1 sun induces a photogenerated charge of 0.038 $C.cm^{-2}.s^{-1}$ [3.25], the photogenerated carriers flux F is given by

$$F = \frac{0.038\ N_{ph}.f_{abs}}{1.6x10^{-19}} \tag{3.88}$$

The generation rate is:

$$G = \frac{F}{W} \tag{3.89}$$

The injection level Δn is deduced from the conductivity variation Δσ [3.26, 3.27]:

$$\Delta n = \frac{\Delta\sigma}{q.W(\mu_n - \mu_p)} \tag{3.90}$$

Conductivity variation is measured by a RF coil coupled to the sample. The variation dn/dt is calculated from the slope of Δn (t).

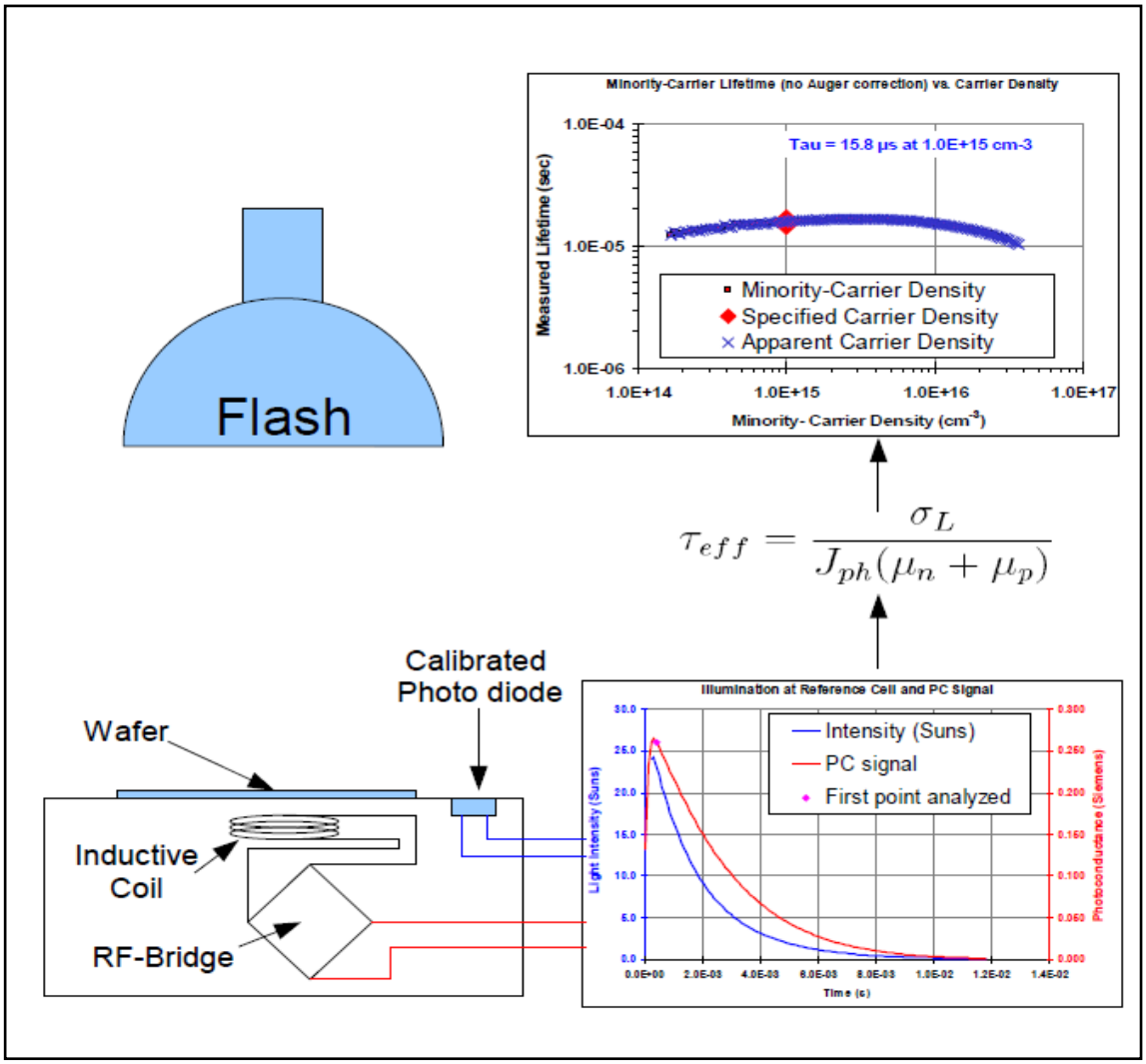

Figure 3.45 Schematic representation of the MW-PCD system [3.28]. A wafer is illuminated by a flash light: the light intensity increases during the phase where light is "switched on" and decreases after the light is "switched off". The light induced an excess of electron an hole resulting in a increasing σ_L of the wafer conductivity proportional to Δn (cf. equation 3.90). The Photoconductance σ_L is measured via an inductive coil and Δn then is deduced from equation 3.90. Then usually lifetime of the excess carrier is determined as shown on this figure but in this work recombination rate is determined with equation 3.87 and then SRV is deduced.

The relation between the SRV, the effective and the bulk lifetime has been developed by Luke and Cheng in 1987 [3.29]. Equation 3.91 [3.30] expresses the connection between the SRV S, the bulk lifetime τ_b and the wafer thickness W for a well passivated surface:

$$\frac{1}{\tau_{eff}} = \frac{1}{\tau_b} + \frac{2.S}{W} \qquad (3.91)$$

This correspond to the summation of bulk recombination rate U_b and the recombination rate at the rear and front surface of the wafer surface assuming that the passivation quality is the same for both faces of the sample.

$$S = \frac{1}{2}W\left(\frac{1}{\tau_{eff}}\right) - \frac{W}{2.\tau_b} \tag{3.92}$$

When the bulk lifetime is very high as for Fz-wafer of 8000 ohm.cm, the lifetime is equal to 1ms and the bulk recombination can be neglected. On the other hand for Cz wafer of 1 ohm.cm, the lifetime is 30µs and the bulk recombination has to be subtracted which correspond approximately to subtract 330 cm/s. The determination of the SRV in the previous relation is possible only if the bulk lifetime of the wafer is uniform. The uniformity of lifetime in the bulk can be checked by comparing transit time (second term of equation 3.93) with lifetime [3.31]. If the latter is higher than the former the lifetime can be consider as uniform.

$$\tau_b \; > \frac{W^2}{2D} \tag{3.93}$$

Table 3.2 shows that the bulk lifetime is uniform in the samples used for this work.

Parameters	**Type of wafers**	
	Cz 1ohm.cm	**FZ 8000 ohm.cm**
W (cm)	0.02	0.05
τ_b(s)	**$3.00x10^{-5}$**	**$1.00x\ 10^{-3}$**
D_n (cm^2/s)	31	37
Transit time(s)	$6.4x10^{-6}$	$3.4x10^{-5}$

Table 3.2 Bulk lifetime and transit time for 1 and 800 ohm.cm wafers (cf. equation 3.93). W is the wafer thickness, τ_b is the bulk lifetime and D_n the diffusion coefficient of electron. τ_b is higher than the transit time W^2/ (2D), the bulk lifetime can be consider to be uniform. This table shows that the bulk lifetime is uniform in the wafer used for this work.

.

- Difference of SRV measurements at relevant injection level for different doping

On figure 3.46, the effect of doping on SRV is highlighted for different doping level. The concentration N_a equal to $1.5x10^{16}$ and $2.6x10^{11}$ cm^{-3} correspond respectively to 1 and 8000.ohm.cm wafers. On this figure the fixed charge is 10^{11} cm^{-2}, $\sigma_n = 10^{-16}$, $\sigma_p=10^{-14}$, the defect is defect C (section 3.6) with a maximal density of $3.5.10^{10}$ $cm^{-2}.eV^{-1}$. Table 3.3 shows the 1 ohm.cm to 8000.ohm.cm SRV ratio R_{SRV} in the range of the injection level corresponding to an intensity one sun (cf. chapter 2).

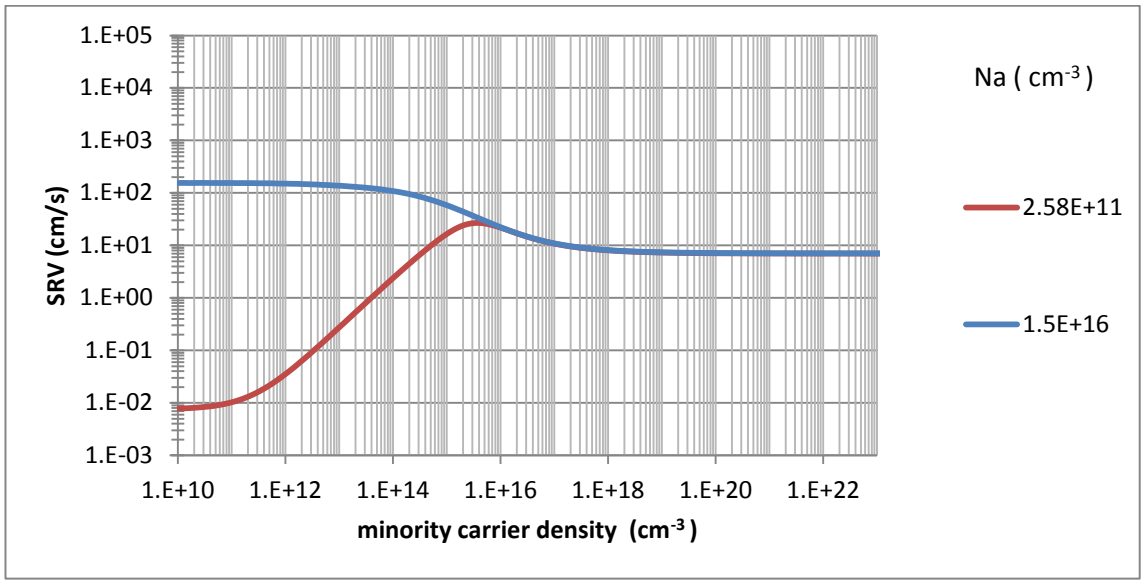

Figure 3.46 Evolution of the SRV versus injection level for different doping level for a fixed charge density Q_f equal to $1x10^{11}$ cm^{-2}. The defect Gaussian energy level density is centered at 0.4 eV above the valence band with a maximum equal to $3.5x10^{10}$ $cm^{-2}.eV^{-1}$ and a FWHM of 0.115 eV.

Injection (/cm^{-3})	10^{14}	$5x10^{14}$	10^{15}
R_{SRV}	45	8	4

Table 3.3 1 ohm.cm to 8000 ohm.cm SRV ratio at 3 injections levels for injection level in the range corresponding with an illumination of one sun intensity. The ratios are calculated with the values of figure 3.46. (It is recalled that $1.5x10^{16}$ cm^{-3} and $2.58x10^{11}$ cm^{-3} correspond respectively with resistivity 1 and 8000 ohm.cm)

1ohm.cm and 8000.ohm.cm wafer operated respectively around 10^{14} and 10^{15} cm^{-3} as seen in chapter 2. For the same film quality, it can be seen that the SRV is expected to be 45 times lower at $10^{14}cm^{-3}$ for the high resistivity wafer.

3.7.2 Experiments

In the following samples, both types of p-type silicon wafer have been used. Fz with a resistivity of 8000 ohm.cm corresponding to a doping of $2.6x10^{11}cm^{-3}$ and a Cz with a resistivity of 1ohm.cm corresponding to a doping around $1.5x10^{16}cm^{-3}$ .Measurements show that the shape of the function representing the SRV versus injection level starts to increase until a maximum and then decreases in a similar way for the simulated SRV (8000 ohm.cm). For the samples 43, 44 and 45 the maximum SRV measured by MW-PCD coincides with the maximum simulated SRV. The values of Q_f are between 1 - $2.5.10^{11}$ cm^{-2} whereas the most often reported values are around 10^{12} cm^{-3} as reported on several references [3.32, 3.33-3.36, and 3.37]. However this difference is explained by the measurement method used for Q_f determination [3.14]. The higher Q_f values (~10^{12} cm^{-2}) are obtained with C-V measurement in the dark [3.38], whereas the lower (~10^{11} cm^{-2}) are deduced from lifetime measurement. The fixed charge density is actually due to a defect known as K center which Schmidt identifies with a defect labeled D. This defect is 0.1 eV below the conduction band and captures electrons during illumination which results in a decreasing of the fixed charge from 1 order and indeed Schmidt reports values between 1 and 3.10^{11} cm^{-2} for Q_f which correspond remarkably with our own values. It has also to be noted that for almost all the sample covered both FZ 8000 ohm.cm and 1 ohm.cm, the value of the fixed charge Q_f is almost the same (1.3-$1.5x10^{11}$ cm^{-2}) with an exception for the sample 45 which has a fixed charge of $2.5x10^{11}$ cm^{-2}. This latter is also the one with the lowest SRV: 100 cm/s for its maximum value at an injection level of $1x10^{16}$ cm^{-3} and an expected value of 25 cm/s at very high injection. It is also the sample with the highest maximal injection level. Since every sample has been measured for the same flash intensity, it can be deduced that this lowest SRV sample corresponds to the best efficiency in term of photo-generated carrier. Sample 43 which has also a low SRV (180 cm/s), has also a high injection level (around $8x10^{15}$ cm^{-2}). One important remark has to be made about sample 43, this latter is covered with a-Si:H whereas all the other are covered with SiN_x. The fixed charge is exhaustively reported in literature for SiN_x film but we do not find this regarding a-Si:H film. However, it appears clearly is in this example and with other a-Si:H sample that we have grown but which are not presented here, that there is a fixed charge. Indeed fixed charge is the only parameter that can explain the flatness of the curve at low injection followed by an increase until high injection regime. Moreover, the origin of the fixed charge in SiN_x as well as SiO_2 films is explained by a transition layer of SiO_x between the Si bulk and the film due to the oxidation during the time when the sample

are loaded in the PECVD chamber [3.1]. Since the procedure is the same for growing a-Si:H, it seems coherent to have also fixed charge.

- **Fitting for 8000 ohm.cm wafers**

Figures 3.47-3.49 are the result of the fitting of SRV simulation presented in section 3.6 to 3 wafers with resistivity 8000 ohm.cm. The fitting have been done by using the values for σ_n and σ_p of figure 3.10. The amplitude of the defect density, the central value of the peak, its broadness and the fixed charge Q_f used in the SRV simulation have been optimized in order to fit with the experimental curve after the implementation of a code based on Levenberg-Marquardt algorithm for minimizing the mean-square error (MSE) between the simulated and the experimental curve adapted to this problem. However a more analytic way for determining parameters will be described at the end of this chapter.

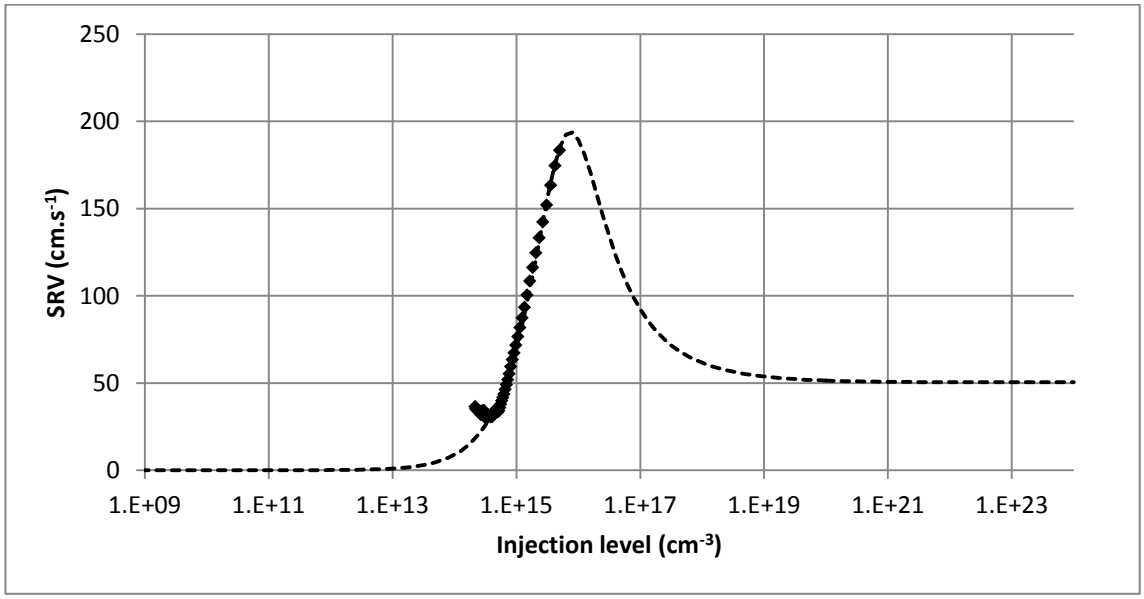

Figure 3.47 Fitting of the theoretical SRV (dashed line) with the experimental values of sample 43 (squares). The situation is the same as on figure 3.23. The values for σ_n and σ_p are respectively 10^{-16} and 10^{-14} cm^2, the width of the Gaussian defect is 0.0577 eV, the maximum density is $2.52x10^{11}$ $cm^{-2}.eV^{-1}$, and Qf is 1.41 cm^{-2}. The result of the fit gives a MSE of 9.8 with 40 points. The experimental points at lower injection level do not fit with the curve because defects generated by the PECVD deposition at the very beginning of the bulk wafer alter the bulk lifetime. When injection level is higher, this effect becomes negligible.

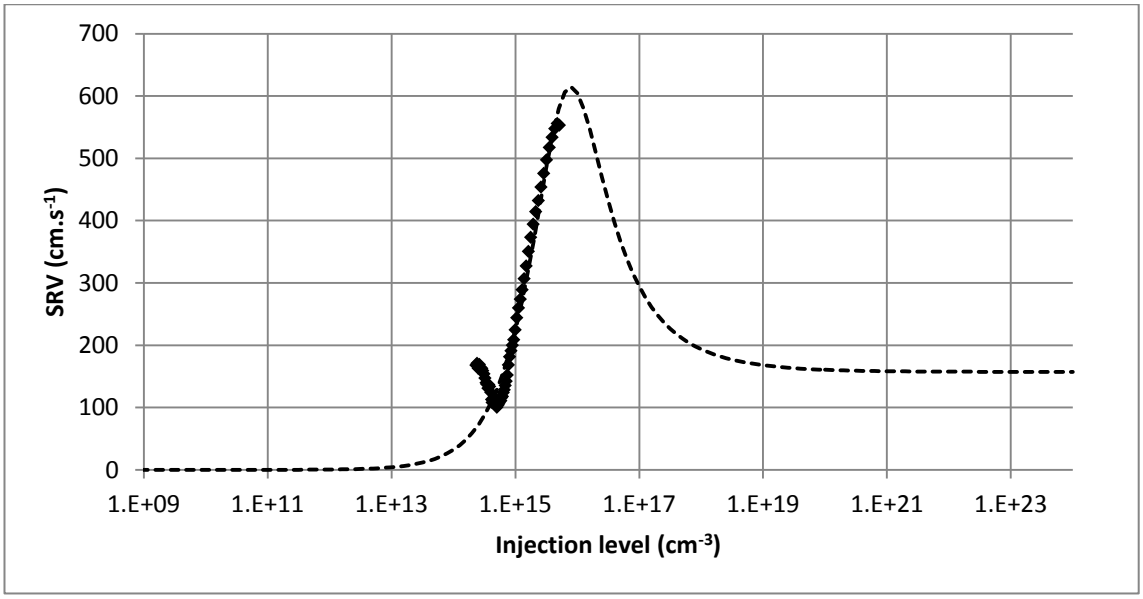

Figure 3.48 Fitting of the theoretical SRV (dashed line) with the experimental values of sample 44 (squares). The situation is the same as on figure 3.23. The values for σ_n and σ_p are respectively 10^{-16} and 10^{-14} cm^2, the width of the Gaussian defect is 0.0577 eV, the maximum density is $7.24x10^{11}$ $cm^{-2}.eV^{-1}$, Q_f is 1.48 cm^{-2}. The result of the fit gives a MSE of 527 with 40 points. The experimental points at lower injection level do not fit with the curve because defects generated by the PECVD deposition at the very beginning of the bulk wafer alter the bulk lifetime. When injection level is higher, this effect becomes negligible.

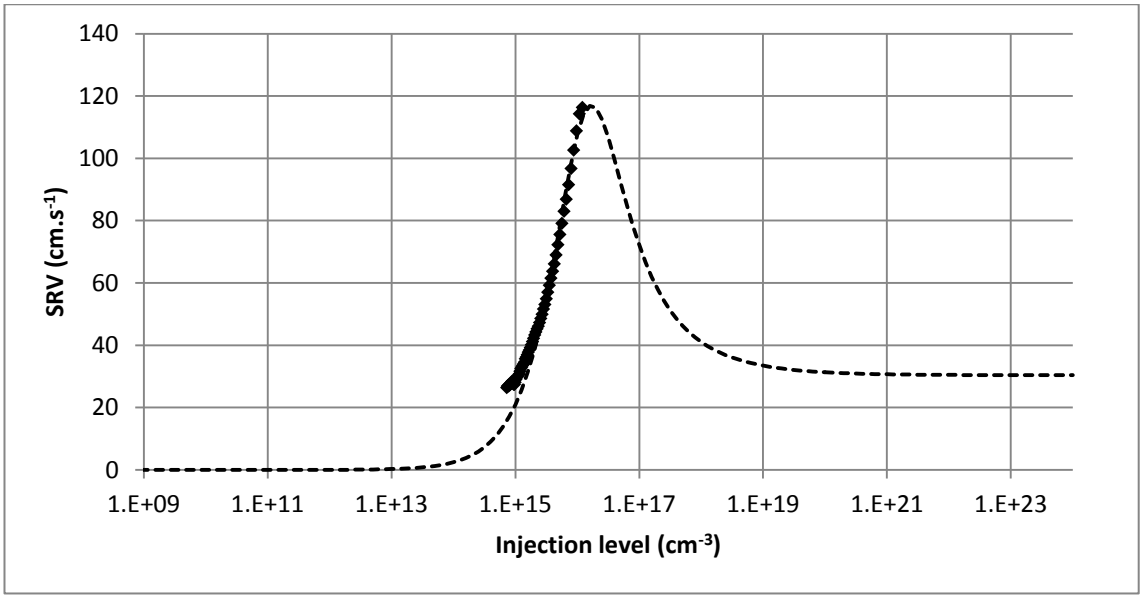

Figure 3.49 Fitting of the theoretical SRV (dashed line) with the experimental values of sample 45 (squares). The situation is the same as on figure 3.23. The values for σ_n and σ_p are respectively 10^{-16} and 10^{-14} cm^2, the width of the Gaussian defect is 0.0577 eV, the maximum density is $1.47x10^{11}$ $cm^{-2}.eV^{-1}$, Q_f is 2.01 cm^{-2}. The result of the fit gives a MSE of 14.2 with 40 points. The experimental points at lower injection level do not fit with the curve because defects generated by the PECVD deposition at the very beginning of the bulk wafer alter the bulk lifetime. When injection level is higher, this effect becomes negligible.

- **Fitting for 1 ohm.cm wafers**

Figures 3.50-3.52 are the result of the fitting of SRV simulation presented in section 3.6 to 3 wafers with resistivity 1ohm.cm. It can be seen that while the fixed charge has a positive effect on passivation (a strong decrease of the SRV) for the high resistivity wafers, it increases the SRV for the low resistivity wafer. This is due to the fact that as seen in section 3.6, the fixed charge is too low for inducing the inversion between majority and minority charge carrier but high enough to increases the recombination rate. A very important point regarding simulation is the fact that although the sample are supposed to be 1 ohm.cm wafer, the conformity of measurement with simulation show that the doping is $1x10^{15}$ cm^{-3} instead of $1.5x10^{16}$ cm^{-3}. Thus the corresponding resistivity is 13ohm.cm. For all the simulation with these Cz wafer, the fit agree with 13 ohm.cm instead of 1 ohm.cm.

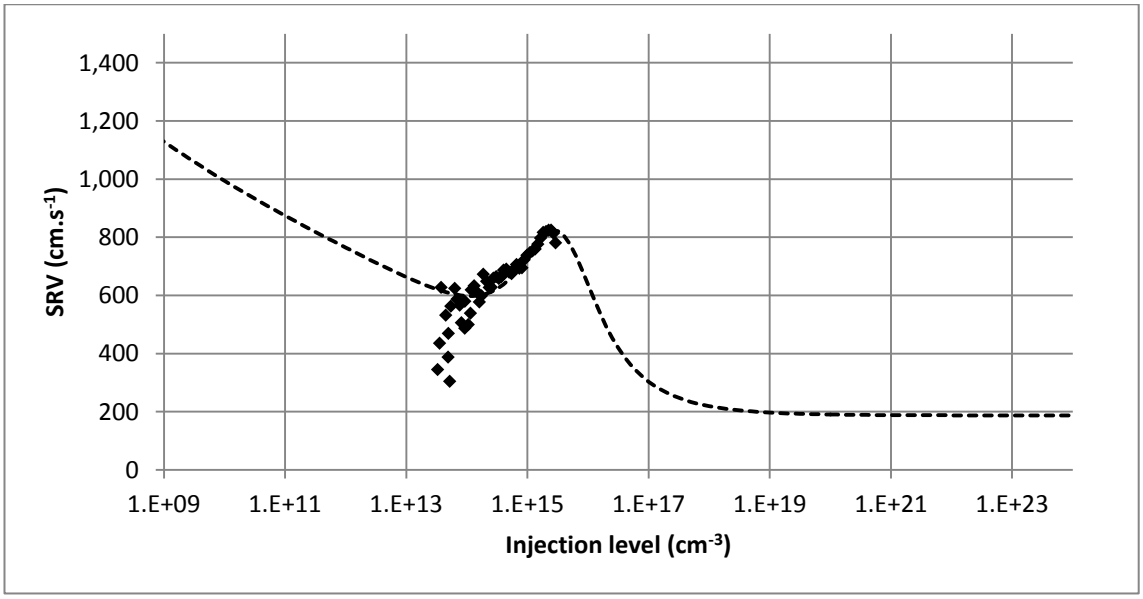

Figure 3.50 Fitting of the theoretical SRV (dashed line) with the experimental values of sample 2527 (squares). The situation is the similar as on figure 3.32 but the doping is 10^{15} cm^{-3} instead of $1.5x10^{16}$ cm^{-3} and Q_f if 5 times lower. .The values for σ_n and σ_p are respectively 10^{-16} and 10^{-14} cm^2, the width of the Gaussian defect is 0.0577 eV ,the maximum density is $9.07x10^{11}$ $cm^{-2}.eV^{-1}$, Q_f is 1.01 cm^{-2}. The result of the fit gives a MSE of 1500 with 40 points. The experimental points at lower injection level do not fit with the curve because defects generated by the PECVD deposition at the very beginning of the bulk wafer alter the bulk lifetime. When injection level is higher, this effect becomes negligible.

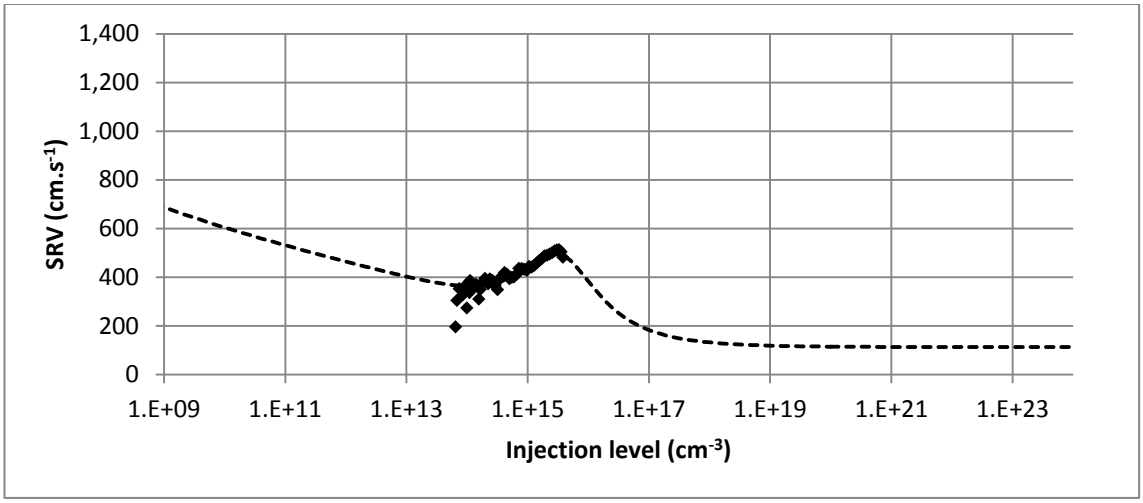

Figure 3.51 Fitting of the theoretical SRV (dashed line) with the experimental values of sample 2530 (squares). The situation is the similar as on figure 3.32 but the doping is 10^{15} cm^{-3} instead of $1.5x10^{16}$ cm^{-3} and Q_f if 5 times lower. .The values for σ_n and σ_p are respectively 10^{-16} and 10^{-14} cm^2, the width of the Gaussian defect is 0.0577 eV ,the maximum density is $5.66x10^{11}$ $cm^{-2}.eV^{-1}$, Q_f is 1.1 cm^{-2}. The result of the fit gives a MSE of 277 with 40 points. The experimental points at lower injection level do not fit with the curve because defects generated by the PECVD deposition at the very beginning of the bulk wafer alter the bulk lifetime. When injection level is higher, this effect becomes negligible

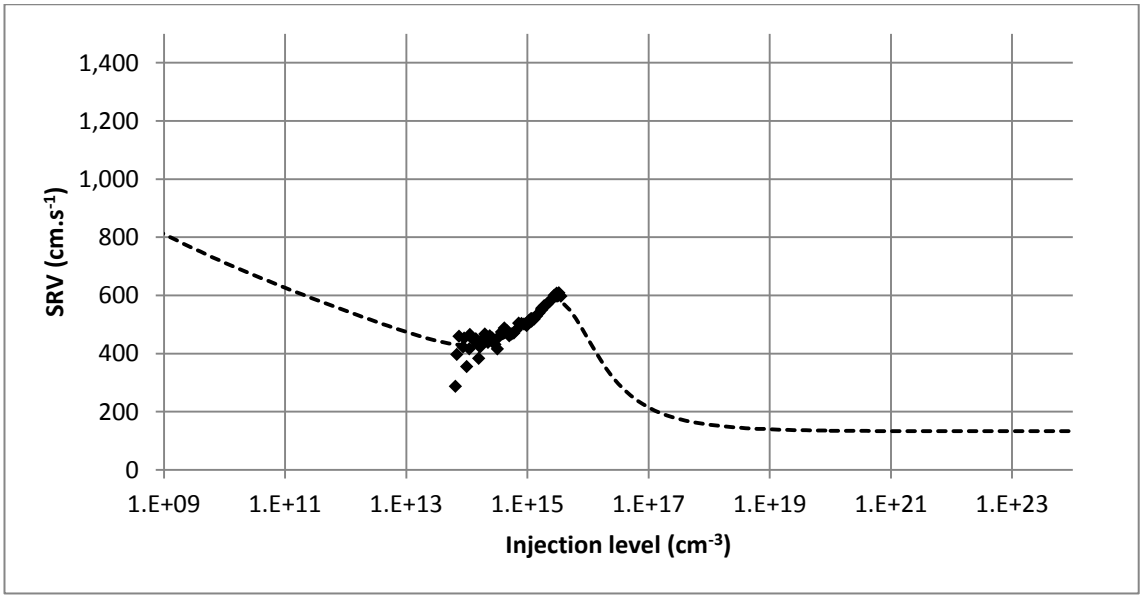

Figure 3.52 Fitting of the theoretical SRV (dashed line) with the experimental values of sample 2532 (squares). The situation is the similar as on figure 3.32 but the doping is 10^{15} cm^{-3} instead of $1.5x10^{16}$ cm^{-3} and Q_f if 5 times lower. .The values for σ_n and σ_p are respectively 10^{-16} and 10^{-14} cm^2, the width of the Gaussian defect is 0.0577 eV ,the maximum density is $6.63x10^{11}$ $cm^{-2}.eV^{-1}$, Q_f is 1.1 cm^{-2}. The result of the fit gives a MSE of 527 with 40 points. The experimental points at lower injection level do not fit with the curve because defects generated by the PECVD deposition at the very beginning of the bulk wafer alter the bulk lifetime. When injection level is higher, this effect becomes negligible

3

Figures 3.53 and 3.54 give the profile of the defect energy levels respectively for 13 and 8000 ohm.cm wafers resulting from the fitting. It can be remarked that for all the samples even for sample 43 which is passivated with a-Si:H film, the curve can be fitted by keeping the same values except for the defect density amplitude.

For the same passivating film parameters values, the SRV tends at high injection level toward a value which is the same whatever is the doping of the wafer and the fixed charge density at the interface (cf. figure 3.21-39). Therefore the film quality can only be compared at high injection level. The lowest SRV at high injection level is 25 cm/s and 120 cm/s for respectively 8000 and 13 ohm.cm wafers. The difference between both can only be due to worse PECVD conditions during the film deposition on 13 ohm.cm wafers. Therefore passivating film with SRV of 25 cm/s can be deposited on 13 ohm.cm wafer. Another condition to take in account is the effect of fixed charge density at the interface. As shown in chapter 2, a wafer illuminated with an intensity of one sun corresponds to injection levels of $3.5x10^{14}$ cm^{-3} and 10^{15} cm^{-3} respectively for 13

ohm.cm and 8000 ohm.cm wafer. For 13 and 8000 ohm.cm this gives a SRV of respectively 390 and 15 cm/s. This is due to the fact that the effect of fixed charge is to reduce the SRV for 8000 ohm.cm wafer and to increase SRV for 13 ohm.cm wafer. For a wafer 1 ohm.cm, the deposition of a film with the characteristic of sample 45 results in a SRV of 295 cm/s at one sun injection level ($3.5x10^{14}$ cm^{-3}).

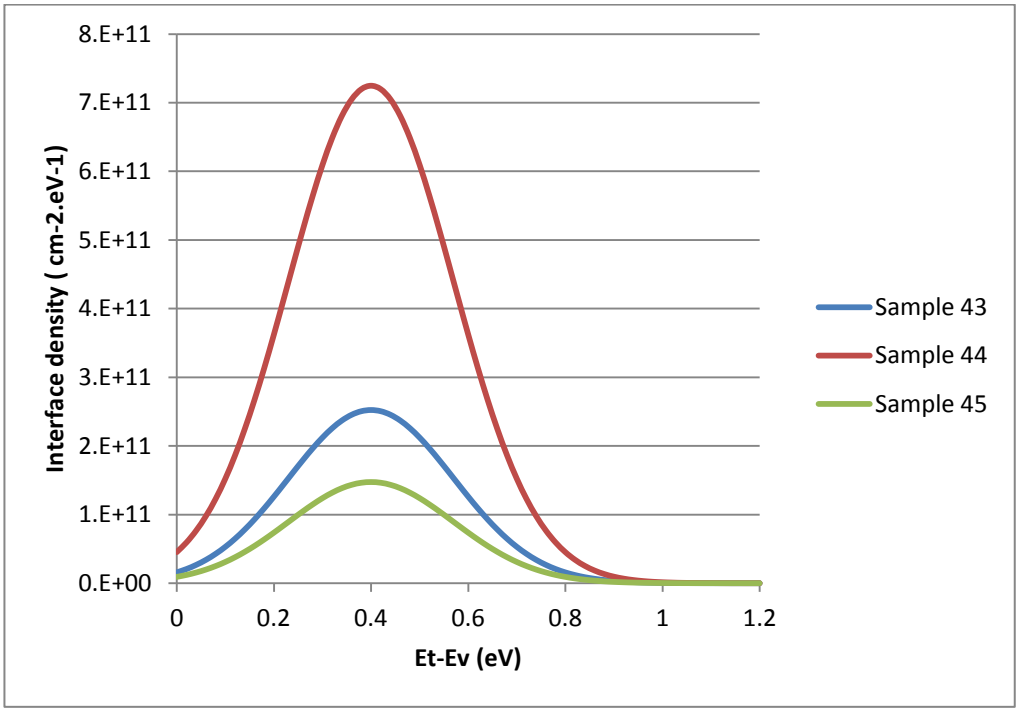

Figure 3.53 Energy levels distribution of defect for 8000 ohm.cm wafers. The width of the Gaussian defect is 0.0577 eV, the density is maximum when defect energy E_t is 0.4 eV.

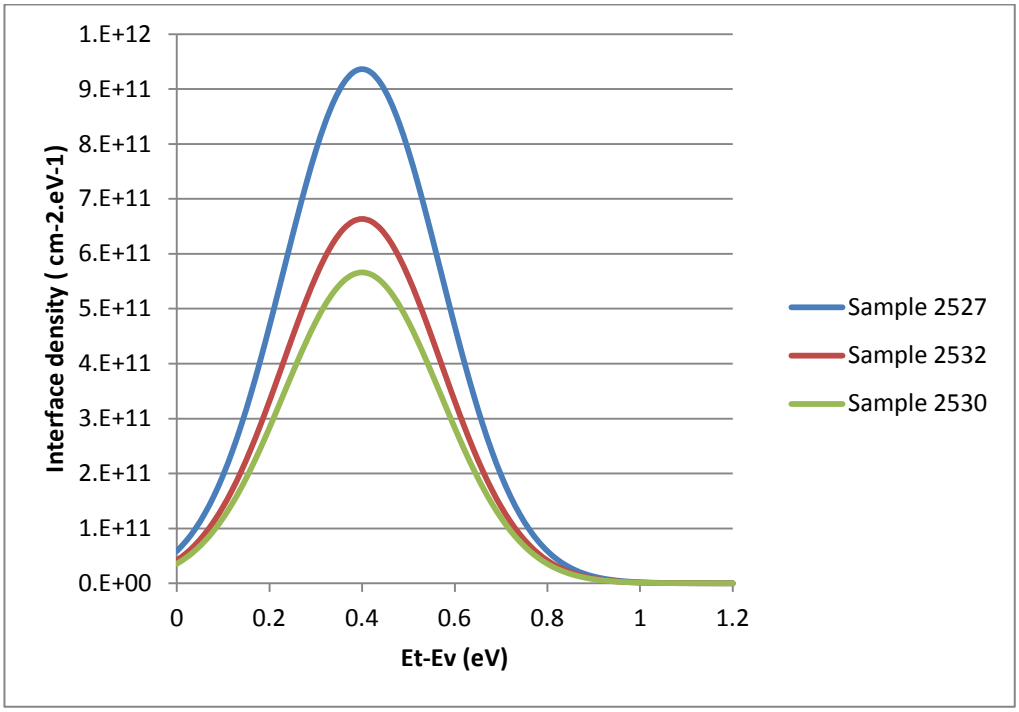

Figure 3.54 Energy levels distribution of defect for 1ohm.cm wafers. Energy levels distribution of defect for 8000 ohm.cm wafers. The width of the Gaussian defect is 0.0577 eV, the density is maximum when defect energy E_t is 0.4 eV.

3.8 Proposition of a method for the determination of the major parameters for passivating film quality.

Regarding passivating quality, the deposited film can be described by 4 parameters. These parameters are the fixed charge density at the interface between the substrate and the passivating film Q_f, the electron to hole capture cross section ratio σ_n/σ_p and the product of electron capture cross section σ_n and the integration from the valence band E_v to the conduction band E_c of defect level density D (E) given in equation 3.94 a (equation 3.94 b is similar with σ_p instead of σ_n).

$$10^7 x\, \sigma_n \int_{E_V}^{E_C} D(E)dE \qquad (3.94\ a)$$

$$10^7 x\, \sigma_p \int_{E_V}^{E_C} D(E)dE \qquad (3.94\ b)$$

Q_f can be determined when Q_f is in the low range that is when an increase of Q_f induces an increase of the SRV at low injection level. For this situation which corresponds for instance to figure 3.31 where the SRV follows on the all injection level range the evolution of the electron capture probability section ($\sigma_n.n_s/\Delta n$). Since $\sigma_n.n_s << \sigma_n.p_s$ It is easy to see that using equations 3.60 and 3.62 the expression SRV S given by the right hand term of equation 3.57 divided by the injection level Δn can be approximated if $p_s >> p_1$ by the equation 3.95:

$$S = 10^7 x\, \sigma_n \left(\int_{E_V}^{E_C} D(E)dE \right) \; e^{\frac{q\psi}{kT}} \qquad (3.95)$$

At high injection level, the effect of fixed charge is negligible and ψ is almost equal to 0 and thus the SRV is given by the right hand term of equation 3.95 divided by the exponential term. Therefore it is possible to determine the exponential term by a ratio of the SRV at an injection level where $p_s>>p1$ and the high injection SRV.

For instance on figure 3.31, S ($\Delta n=1x10^9$ cm^{-3}) =155.75 cm/s and S ($\Delta n=1x10^{24}$ cm^{-3}) =7.01 which gives a ratio of 22.21. The function of $e^{q\psi/kT}$ versus Q_f is represented on figure 3.55. The value 22.21 for $e^{q\psi/kT}$ corresponds to a Q_f equal to 10^{11} cm^{-2} which is the value of Q_f used for the simulation. We have checked the agreement of this method for several simulations providing that Q_f is in the low range and $p_s>>p_1$. However the experimental values presented on figure 3.47-52 do not correspond to this case because Q_f is too high compare with the doping. Using a very higher doped substrate (for instance $1x10^{18}$ cm^{-3}) would ensure that Q_f is in the low range. A test wafer with higher doping could be placed near the 1 ohm.cm wafer during PECVD which would ensure that the films are the same for both wafers and thus have the same Q_f. The test wafer would allow determining this value of Q_f.

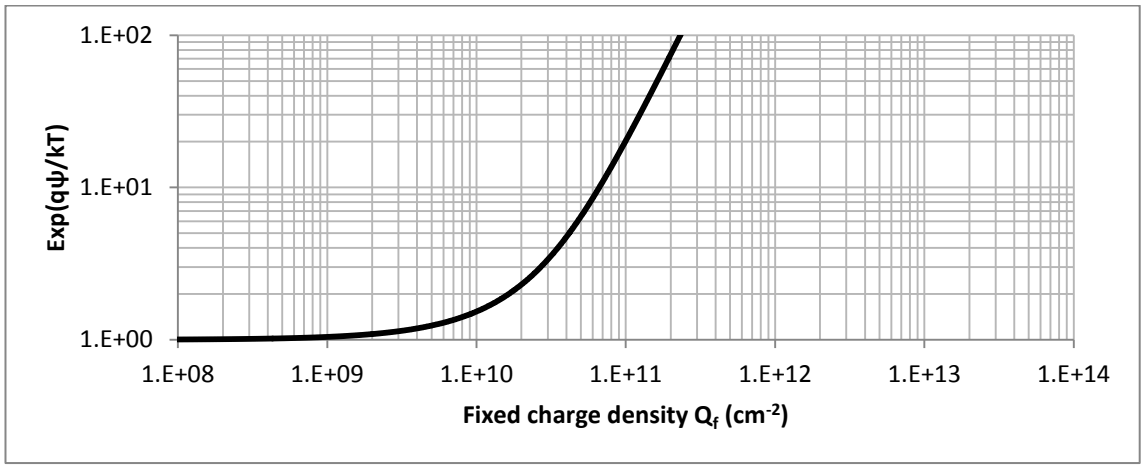

Figure 3.55 Evolution of exp (qψ/kT) versus fixed charge density Q_f for a 1 ohm.cm wafer at an injection level Δn equal to $1x10^9$ cm^{-3}. This injection level has been chosen in order to have $p_s >> p_1$ (cf. text of this section). Ψ is the surface potential generated by the presence of Q_f. This curve have been obtained with by varying Q_f instead of Δn in the code described in section 3.4 of this chapter and is used to determine Q_f.

If Q_f can be determined when the condition described at the beginning of section 3.8 are fulfilled.

When Q_f is in the high range compare with doping as it is the case on figure 3.47-49 where the doping is $2.58x10^{11}$ cm^{-3} , the SRV S at low injection is given by equation 3.96 which is obtained by using equations 3.59 and 3.61 .

$$S = 10^7 x\, \sigma_p \left(\int_{E_V}^{E_C} D(E)dE \right) \; e^{\frac{-q\psi}{kT}} \qquad (3.96)$$

and if Q_f is known the term given in equation 3.94 b can be determined. For instance on figure 3.48, S (Δn=$1.5x10^{15}$ cm^{-3}) =348 and $e^{q\psi/kT}$ is equal to 38 for Q_f=$1.4x10^{11}$ cm^{-2}, the integration of the defect density give a value of $3x10^{11}$ cm^{-3} and thus by using equation 3.96, the mean value of σ_p is $4.3x10^{15}$ cm^2 which is in agreement with a maximum value 10^{-14} cm^{-2} used for the fit.
Regarding

The problem here is the determination of Q_f since conditions required for its determination are not fulfilled. If a test wafer with high doping as previously described is placed near the 8000 ohm.cm wafer, Q_f can be determined from this test wafer.
It can also be seen that on this range of Q_f, the SRV reach a maximum before decreasing to its value at high injection level. This is the case for instance on figure 3.23 and this corresponds to a point where $\sigma_n.n_s = \sigma_p.p_s$ (cf. figure 3.23 b). It can also be noted that this is also the case for every knee-point of the SRV versus Δn as on figure 3.32 where Q_f is not in high range compare with doping. At these knee points where $\sigma_n.n_s = \sigma_p.p_s$, the σ_n to σ_p ratio can be determined by equation 3.97 is Q_f and thus ψ are known.

$$\frac{\sigma_n}{\sigma_p} = \frac{p_0 + \Delta n}{n_0 + \Delta n} \; e^{\frac{-2q\psi}{kT}} \qquad (3.97)$$

For instance on figure 3.44, S ($\Delta n=3.98x10^{15}$ cm^{-3}) =536 cm/s correspond to a single where the SRV is maximum. For $Q_f=1.4x10^{11}$ cm^{-2}, $e^{q\psi/kT}$ is equal to 16.3. This gives using equation 3.97 a σ_n to σ_p ratio of 0.017 which correspond to the ratio 0.0145 used for defect 3.

When σ_n to σ_p ratio has been determined, the term of equation 3.94 a can be deduced from equation 3.97 and 3.94 b.

In summary, the film parameters could be determined from the SRV value by the deposition of the film on 3 wafers at the same time. This will ensure that the film is the same on the 3 wafers and thus Q_f, σ_n, σ_p and the defect density D (E). The first wafer would have a high doping around 10^{18} cm^{-3} for the determination of Q_f. Knowing Q_f, the second wafer would have a low doping around $1x10^{12}$ cm^{-3} for allowing the determination of σ_n to σ_p ratio and the product of σ_p with the integration of the defect density. The third wafer would have an intermediate doping (for instance 10^{15}-10^{16} cm^{-3}) for the determination of Q_f. This method could be pushed further for the determination of the Gaussian parameters of the defect.

3.9 Conclusion

In this chapter, a method for measuring the SRV directly with Sinton MW-PCD without the mediation of the lifetime determination has been explained from the SRH theory. This method is available and the whole range of injection level used with Sinton whereas the usual method of lifetime determination from recombination rate is not available with 8000 ohm.cm wafer because the injection level range corresponds to high injection level with high resistivity wafers.

The most important contribution of this chapter is related to the description and understanding of the SRV evolution with the injection level. After several developments for understanding the variation of charge carrier at the film/substrate interface, the relation between the passivating film parameters (Q_f, $\sigma_n \int D(E)\, dE$, σ_n/σ_p), injection level and SRV have been explained by the introduction of two quantities: $\sigma_n.n_s/\Delta n$, $\sigma_n.n_s/\Delta n$ that we have called respectively electron and hole (dynamic) capture probability section.

A new method for determining the film parameters only from SRV evolution with injection level has been proposed in this chapter, whereas film parameters determination usually requires adding other technique as C-V measurement [3.38]. This would require

use PECVD on 3 wafers: the first with a low doping, the second with a high doping and the third with an intermediate doping. The film has to be deposited on the 3 wafers at the same time in order to have the same film on the 3 wafers. The high doping wafer is used to determine Q_f, the low one to determine, the ratio σ_n/σ_p and $\sigma_n \int D(E)\, dE$ (or $\sigma_p \int D(E)\, dE$). The low and high doping wafers are used only for the film parameters determination of the second wafer.

On this study, the film parameters have been determined by fitting the experimental values measured with Sinton MW-PCD with the theoretical SRV expected with SRH theory. This theoretical SRV has been obtained from code implemented for this work. The results have shown that although the parameters of the defect are taken from the known value of SiN_x, the same parameters can be used for simulating a-Si:H sample (cf. figure 3.47 with sample 43). However, the determination of the parameters could be improved by the method of the 3 wafers described below.

Regarding the aim of having a low SRV, the lowest SRV at high injection level is 25 cm/s which would correspond to an SRV of 295 cm/s for an illumination of one sun intensity. This chapter was primarily focused on the film characterization in regards with passivation quality, particularly defect characterization but does not give information about the film structure. In chapter 4 the determination of optic properties and film composition by ellipsometry and x-ray photospectroscopy will be described.

BIBLIOGRAPHIE CHAPTER 3

[3.1] A.G. Aberle, Crystalline silicon solar cells: advanced surface passivation and analyses (University of New South Wales, Centre for photovoltaic engineering, Sydney, 1999).

[3.2] S.Rein, Lifetime spectroscopy: A method of defect characterization in Silicon for Photovoltaic Applications, Springer Series in Materials Science, Vol 85 (2005)

[3.3] D. K. Schroder ,Carrier Lifetimes in Silicon, IEEE Transactions on Electron Devices 44(1), 160-170(1997)

[3.4] W. Gerlach et al., On the radiative recombination rate in silicon, Physica status solidi A, 13 (1) , 277-283 (1972).

[3.5] W. Shockley et al., Statistics of the recombinations of holes and electrons, Phys.Rev. 47 (5), 835-842 (1952).

[3.6] V.K. Khanna et al., Physical understanding and technological control of carrier lifetimes in semiconductor materials, Progress in Quantum Electronics And devices: Acritique of conceptual development, state of the art and applications 29 ,59–163(2005).

[3.7] R. N. Hall, Electron-Hole Recombination in Germanium, Physical Review, vol. 87, Issue 2, pp. 387-387 (1952)

[3.8] S. Olibet , Silicon Solar Cell Passivation using Heterostructures, PV-LAB-CONF-2007-013 (2007)

[3.9] S.J. Watts et al., A new model for generation-recombination in silicon depletion regions after neutron irradiation, IEEE transactions on nuclear science 43(6) 2587-2594 (1996)

[3.10] D. Macdonald et al.,Validity of simplified Shockley-Read-Hall statistics for modeling carrier lifetimes in crystalline silicon, PHYS. REV. B 67, 075203-1-7 (2003)

[3.11] A. B. Sproul et al. ,Dimensionless solution of the equation describing the effect of surface recombination on carrier decay in semiconductors, J. Appl. Phys. 76, 2851-2854 (1994)

[3.12] J. Mitchell et al., Surface passivation of n- and p-type crystalline silicon wafers by amorphous silicon films, Australian and Newzealand solar energy society conference (solar 2004), 1-4 (2004)

[3.13] C. Leguijt et al., Low temperature surface passivation for silicon solar cells, Solar energy materials and solar cells 40, 297-345 (1996)

[3.14] J.Schmidt et al., Carrier recombination at silicon–silicon nitride interfaces fabricated by plasma-enhanced chemical vapor deposition, J. Appl. Phys. 85, 3626-3633 (1999).

[3.15] Chuan Li et al., Surface and Bulk Passivation Layer of Silicon Nitride for Solar Cell Applications, Materials and processes (NREL), 15th workshop on crystalline silicon solar cells and modules, 153-157 (2005)

[3.16] K. Jarolimek et al., Amorphous semiconductors studied by first-principles simulations : structure and electronic properties, MRS proceedings 1153, A04-03 (2009)

[3.17] J.Mitchell et al., Plasma-Enhanced Chemical Vapour Deposition of a-Si:H to provide surface passivation of c-Si surfaces at low temperature, Proceeding of the 22nd European photovoltaic solar energy conference, Milan, Italy, 928-931,(2007).

[3.18] M. Lamers et al . Interface properties of a-SiNx:H/Si to improve surface passivation, Solar Energy Materials and Solar Cells 106, 17–21 (2012)

[3.19] S. Steingrube et al. ,Interpretation of recombination at c-Si/SiNx interfaces by surface damage J. Appl. Phys. 108, 014506 (2010)

[3.20] J. Schmidt et al., Accurate method for the determination of bulk minority-carrier lifetimes of mono- and multicrystalline silicon wafers. J. Appl. Phys. 81(9), (1997).

[3.21] R.A. Sinton et al., Contactless determination of current-voltage characteristics and minority-carrier lifetimes in semiconductors from quasi-steady-state Photoconductance data, Appl. Phys. Let. 69(17) ,2510-2512 (1996)

[3.22] M.J. Kerr et al, Generalized analysis of quasi-steady-state and transient decay open circuit voltage measurements, J.Appl. Phys. 91(1), 399-404 (2002)

[3.23] H.Nagel et al., Generalized analysis of quasi-steady-state and quasi-transient measurements of carrier lifetimes in semiconductors, J.Appl. Phys. 86(11), 6218-6221(1999)

[3.24] J. Schmidt et al., Measurement of Differential and Actual Recombination Parameters on Crystalline Silicon Wafers, IEEE Transactions on Electron Devices 46 (10), 2018-2025(1999)

[3.25] R.Sinton, WCT-120 Photoconductance Lifetime Tester and optional Suns-VOC Stage User Manual, Sinton Consulting, Inc. 2006

[3.26] U. A. Elani et al., A New Method for the Determination of Carrier Lifetime in Silicon Wafers from Conductivity Modulation Measurements, J. of Semiconductor Technology and Science, 8(4) , 311-317(2008)

[3.27] M. Lipiñski et al., Silicon nitride for photovoltaic application,Archives of materials science and engineering 46(2),69-87(2010)

[3.28] D.N. Wright,Optical and passivating properties of hydrogenated amorphous silicon nitride deposited by plasma enhanced chemical vapour deposition for application on silicon solar cells , PhD Thesis (2008)

[3.29] Keung L. Luke et al., Analysis of the interaction of a laser pulse with a silicon wafer: Determination of bulk lifetime and surface recombination velocity, J. Appl. Phys. 61, 2282-2293 (1987)

[3.30] M.J. Kerr et al.,Recombination at the interface between silicon and stoichiometric plasma, silicon nitride, Semicond. Sci. Technol. 17,166–172 (2002)

[3.31] M. D. Abbott et al., The effect of diffusion-limited lifetime on implied current voltage curves based on photoluminescence data, J. Appl. Phys. 102, 044502 (2007)

[3.32] J.R. Elmiger et al., Recombination at the silicon nitride/silicon interface, J.Vac.Technol.A15, 2418-2425 (1997)

[3.33] A. Cuevas et al., Passivation of Crystalline Silicon using Silicon Nitride , Third World Conference on Photovoltaic Solar Energy Conversion, Osaka, Japan, May 11-18, 2003.

[3.34] L.Zhong et al., Investigation of charge trapping centers in silicon nitride films with a laser-microwave photoconductive method, Appl.Phys.Lett. 62 (6), 615-617 (1992)

[3.35] S. V. Deshpande et al. ,Opticali properties of silicon nltride films deposited by hot filament chemical vapor deposition, J, Appl. Phys. 77 (12), 6534-6541 (1995)

[3.36] M. Lamers et al.,The interface of a-SiNx:H and Si: Linking the nano-scale structure to passivation quality, Solar Energy Materials and Solar Cells (2013)

[3.37] N. M. Nursam, Characterization of Boron Surface Doping effects on PECVD Silicon Nitride Passivation, PVSC 35th IEEE, 3214-3219 (2010)

[3.38] D.Jousse et al., Observation of multiple silicon dangling bond configurations in silicon nitride, Appl. Phys. Lett. 54 (11), 1043-1045 (1989)

Chapter 4

< Ellipsometry and XPS >

The determination of defect density, ratio between electron and hole capture cross section and fixed charge density at the interface would be enough regarding the estimation of passivation quality. It would allow knowing the photovoltaic efficiency that we can expect from the improvement providing by the deposition of this film on rear surface of the wafer. However it is difficult to understand PECVD conditions required for having a high passivating film without having information about the film structure and composition. Indeed film structure and composition directly depends on PECVD parameters and can be control by the optimisation of PECVD conditions. For instance it is easy to understand that if the PECVD conditions provide a high dissociation of NH_3 the N content of the SiN_x film will be higher. On the other hand it is difficult to deduce that this high dissociation of NH_3 results in lower defect density but a relation can be made between the low defect density and the N content in the film. Thus, a connection should be established between film structure and passivation quality and at the same time between film structure and PECVD conditions. Therefore the determination of film structure allows relating PECVD conditions and film quality. Chapter 4 is about ellipsometry and XPS which are two techniques for the determination of the film structure.

4.1 Principles of ellipsometry

This section is for a large part based on a book of Fujiwara [4.1] and the Handbook of ellipsometry [4.2]. Particularly figures 4.5, 4.7 and 4.9 have been reproduced from Fujiwara book. These figures in this chapter resulted from our simulation program and have been used as a check for its accuracy in its different steps of development: figure 4.5 has been used for checking the accuracy of the reflectance calculation in non absorbing material. Figure 4.7 has been used for an absorbing medium using complex refractive index. Figure 4.9 is the result of the first test of simulating the determination of the two values ψ and Δ (cf further) used in ellipsometry measurement for a c-Si substrate covered with a a-Si: H film. Eventually, in the book by Fujiwara, the equations for determination of ψ and Δ are given for a system composed with substrate, film and air. We have developed a code on Excel in VBA basic for extending this determination to N layers (N > 3) by a recurring relation. This Excel simulation program is given in

the annex CD of this thesis and the corresponding Macro can be read and further developed. Other methods for the determination of ψ and Δ can be used [4.3]

4.1.1 Aims of ellipsometry

Ellipsometry is a method for characterising a thin layer deposited on a substrate by the determination of the polarisation change which occurs when an electromagnetic wave is reflected by the material. Electromagnetic waves are altered by the medium that they cross. As will be seen in the following, this is due to the interaction between the permittivity of the crossed material and the electromagnetic wave: this induces a change in wave velocity and attenuation of the wave intensity. Actually both phenomena are correlated by a causality law described by Kramers-Kronig relation. The electromagnetic wave alteration at a boundary between two media can be determined by measuring the ratio between the electric field component parallel to the plane of incident and the component orthogonal to the incidence plan. This ratio between electric field components gives the Fresnel coefficients and is a measure of the electromagnetic wave polarity. These latter can be expressed as a function of two values ψ and Δ which are directly measured with an ellipsometer. Thus ellipsometry measurements are the measure of changes in the electromagnetic wave resulting from the permittivity of the material. Since permittivity is related to the composition of the material, ellipsometry gives information about composition and is a way to characterise a material. Another advantage of ellipsometry is that it uses the property of interference and the relation between phase difference and the penetration length in order to determine the thickness of a material as will be presented in the following. Understanding ellipsometry requires recall of what is an electromagnetic wave and how it interacts with the crossed material.

4.1.2 Modification of electromagnetic wave due to the refractive index of the medium

- **Electromagnetic wave**

An electromagnetic wave which propagates in a medium with a refractive index n_f, along an axis z can be expressed as follows:

$$k_z = \frac{2\pi . n_f}{\lambda_0} \quad (4.2)$$

It is important to notice that in equation 4.1, λ0 is the wave length in vacuum and not in the medium. This medium not only changes the velocity of the electromagnetic wave but can also be absorbent and lead to a diminution of the wave intensity. In order to include the absorption, n_f can be replaced by a complex refractive index N where n_f and k are the real and imaginary part respectively.

$$N = n_f - i.k \quad (4.3)$$

Therefore equation 4.1 becomes:

$$E(z,t) = E_0 . e^{i(\omega t - 2\pi . n_f . z/\lambda 0 .)} . e^{-2\pi . k . z/\lambda 0} \quad (4.4)$$

The influence of k is explicit in the expression of the intensity $I = E.E^*$.

$$I = I_0 e^{-4\pi . k . z/\lambda 0} \quad (4.5)$$

$$I = I_0 e^{-\alpha z} \quad (4.6) \quad (4.6)$$

$$\alpha = \frac{4\pi . k}{\lambda 0_0} \quad (4.7)$$

The absorption coefficient α describes the loss of intensity of the electromagnetic wave through an absorbent material. Intensity exponentially decreases as light goes deeper into an absorbent material. $L_\alpha = 1/\alpha$ represents the absorption length. These results can be applied to the magnetic induction. Indeed magnetic induction and electric field are related with the following relation:

$$\mathbf{B} = \frac{\mathbf{k} \times \mathbf{E}}{\omega} \quad (4.8)$$

Equation 4.8 shows that magnetic induction is orthogonal to the plane formed by **E** and **k** and results in

$$B = \frac{c}{n_f}.E \tag{4.9}$$

It is therefore obvious that the previous equations on electric field can be applied to the magnetic induction. Thus, knowing the refractive index n_f, the electromagnetic wave can be described only by its electric field and wave vector **k**. The polarity is measured by the ratio of the electric field components by the way of Fresnel coefficient.

- **Determination of Fresnel coefficients**

Ellipsometry is based on the determination of Fresnel coefficients. The 4 Fresnel coefficients are expressed by equations 4.10a, 4.10b and 4.11a, 4.11b. In these equations, E_{pr} and E_{pi} are the parallel components to the incident plane of respectively the reflected and incident electric field, E_{tr} and E_{ti} are the parallel components to the incident plane of respectively the transmitted and incident electric field. E_{sr} and E_{si} are the orthogonal components to the incident plane of respectively the transmitted and incident electric field, E_{tr} and E_{ti} are the orthogonal components to the incident plane of respectively the transmitted and incident electric field.

$$r_p = \frac{Ep_r}{Ep_i} \qquad (4.10a) \qquad t_p = \frac{Ep_t}{Ep_i} \qquad (4.10b)$$

$$r_s = \frac{Es_r}{Es_i} \qquad (4.11a) \qquad t_p = \frac{Es_t}{Es_i} \qquad (4.11b)$$

$$\rho = \frac{r_p}{r_s} \tag{4.12}$$

The relation 4.12 describes the polarisation of the electromagnetic wave. The relations between the components of incident, reflected and transmitted electric fields are issued from the law of electric field and magnetic induction continuation between two media with different refractive indices. When an electromagnetic wave is reflected on an interface which separates two media, the angle of incidence is equal to the angle of reflection whereas the angle of transmission is determined by Snell-Descartes law. This law can be extended to complex refractive index if angles with a real and imaginary part are introduced. In this case, the effect of attenuation due to absorption is included for absorbent material.

$$\theta_i = \theta_r = \theta_0 \tag{4.13}$$

$$N_0 . \sin(\theta_0) = N_1 . \sin(\theta_1) \tag{4.14}$$

Figure 4.1 and 4.2 show the p-component and s-component respectively. By definition, E_p and B_p are the projection of **E** and **B** on the plane of incidence and E_s is the component of **E** orthogonal to the incidence plane. Therefore the component E_s is parallel to the interface plane and from equation 4.8, $\mathbf{B_p}$ is also parallel to the interface whereas B_s is orthogonal to the interface (B_s is parallel to the incidence plane).

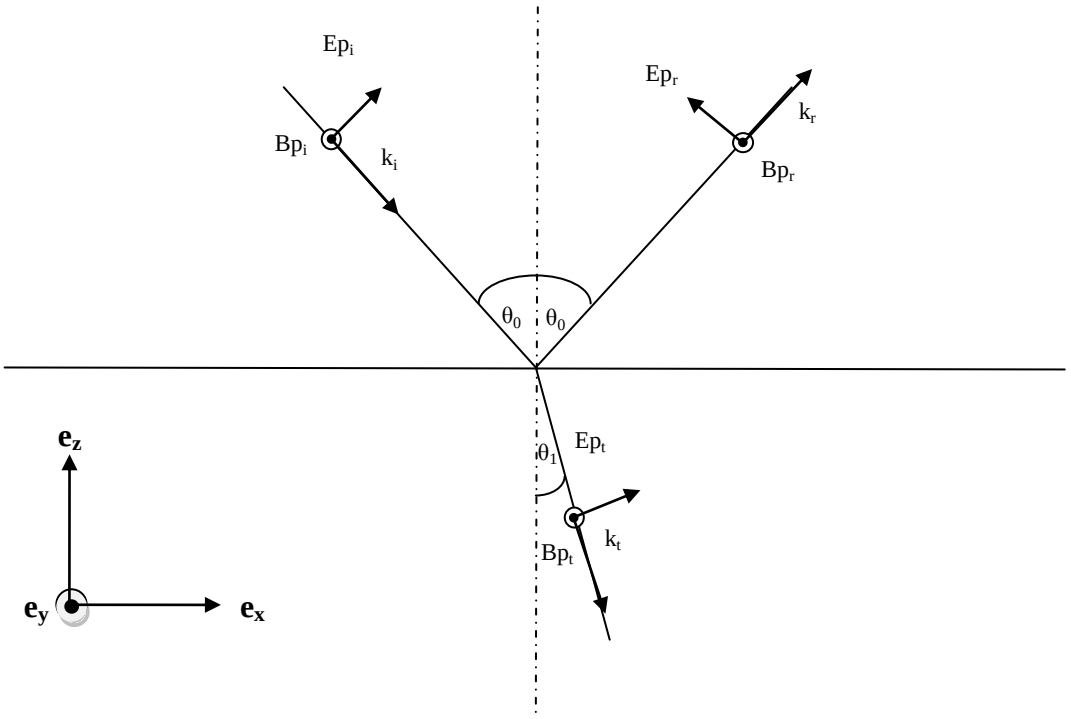

Figure 4.1 Electric field **E** and magnetic induction **B** for a p-polarisation. E_{pi} ($E_{pr,}$ E_{pt}), B_{pi} ($B_{pr,}$ B_{pt}) and k_i ($k_{r,}$ k_t) are respectively the incidence (reflected, transmitted) electric field, magnetic induction and wave vector.

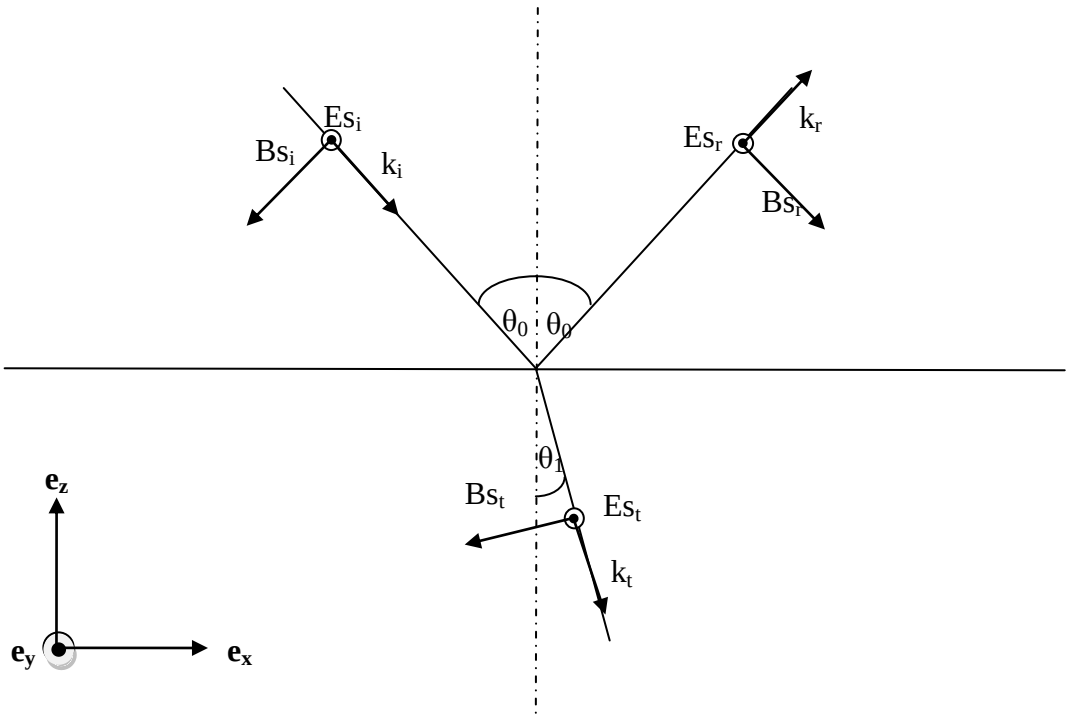

Figure 4.2 Electric field **E** and magnetic induction **B** for a s-polarization. E_{si} ($E_{sr,}$ E_{st}), B_{si} ($B_{sr,}$ B_{st}) and k_i ($k_{r,}$ k_t) are respectively the incidence (reflected, transmitted) electric field, magnetic induction and wave vector.

In agreement with boundary conditions, the parallel component of the electric field **E** on the first medium and the transmission medium are equal. The same continuity condition applies on the magnetic induction **B** at both sides. By projection of p-component and s-component of **E** and **B**, the following equations result:

$$\mathrm{Ep_i}.\cos(\theta_0) - \mathrm{Ep_r}.\cos(\theta_0) = \mathrm{Ep_t}.\cos(\theta_1) \tag{4.15}$$

$$\mathrm{Bp_i} + \mathrm{Bp_r} = \mathrm{Bp_t} \tag{4.16}$$

$$\mathrm{Es_i} + \mathrm{Es_r} = \mathrm{Es_t} \tag{4.17}$$

$$-\mathrm{Bs_i}.\cos(\theta_0) + \mathrm{Bs_r}\cos(\theta_0) = -\mathrm{Bs_t}.\cos(\theta_1) \tag{4.18}$$

Equation 4.9 combines with equations 4.16 and 4.18 lead to

$$\frac{1}{\mathrm{N_0}}(\mathrm{Ep_i} + \mathrm{Ep_r}) = \frac{1}{\mathrm{N_1}}\mathrm{Ep_t} \tag{4.19}$$

$$\frac{1}{\mathrm{N_0}}(-\mathrm{Es_i}.\cos(\theta_0) + \mathrm{Es_r}\cos(\theta_0)) = -\frac{1}{\mathrm{N_1}}.\mathrm{Es_t}.\cos(\theta_1) \tag{4.20}$$

Fresnel coefficients of reflection for p-polarisation are calculated by resolving the system of equation 4.19 and equation 4.15 and the system of equation 4.20 and equation 4.17.

$$r_{p(01)} = \frac{N_1.\cos(\theta_0) - N_0.\cos(\theta_1)}{N_1.\cos(\theta_0) + N_0.\cos(\theta_1)} \tag{4.21}$$

$$r_{s(01)} = \frac{N_0.\cos(\theta_0) - N_1.\cos(\theta_1)}{N_0.\cos(\theta_0) + N_1.\cos(\theta_1)} \tag{4.22}$$

The couple of indexes (01) mean that the reflection occurs at interface between medium 0 and medium 1. In the following the indexes (i,j,k...) will mean that the media from i to k,... go from the more external (ambient) to the more internal (substrate).

- **Measuring the polarisation: ψ and Δ**

When an electromagnetic wave propagates along an axis z, the vector which represents the electric field **E** of intensity E_0 is orthogonal to z. With δ_p and δ_s being the initial phases of the components E_p and E_s along the axes parallel to $\mathbf{E_p}$ and $\mathbf{E_s}$ (respectively p and s axes), the expression of E_p and E_s are given by:

$$E = \begin{bmatrix} E_p \\ E_s \end{bmatrix} = \begin{bmatrix} E_{p0}.\, e^{-i(\omega t - kz + \delta_p)} \\ E_{s0}.\, e^{-i(\omega t - kz + \delta_s)} \end{bmatrix} \tag{4.23}$$

By taking the real part of the upper relation one can deduce the following relation which is an ellipse equation:

$$E_{0s}^2.E_p^2 + E_{0p}^2.E_s^2 - 2.E_{0p}.E_{0s}.E_p.E_s.\cos(\delta_p - \delta_s) = E_{0p}^2.E_{0s}^2.\sin^2(\delta_p - \delta_s) \tag{4.24}$$

The value ψ in equation 4.25 represents the angle between the s axis and the electric field **E** when it is at its maximum intensity E_0 in the first quadrant, which is equivalent to:

$$\tan\phi = \frac{E_{0p}}{E_{0s}}, \psi\epsilon \left[0, \frac{\pi}{2}\right] \quad (4.25)$$

By introducing $\Delta = (\delta_p - \delta_s)$ the phase difference between the x and y components of the electric field the ellipse equation can be written:

$$\frac{E_p^2}{E_0^2} + \tan^2\psi . \frac{E_s^2}{E_0^2} - 2 . \tan\psi . \frac{E_p . E_s}{E_0^2} . \cos\Delta = \sin^2\psi . \sin^2\Delta \quad (4.26)$$

The introduction of the couple (ψ, Δ) presents the advantage of being both measurable and bringing information about polarization. Indeed the two phases δ_p and δ_s of respectively E_p and E_s cannot be observed due to a too short period (around 10^{-14}-10^{-15} s in the range 200-2000 nm) and only the phase difference Δ can be determined. In the same way, the p and s components of **E** are not directly accessible and information about polarization is only known by their ratio (i.e. $\tan\psi$). Ψ is represented on figure 4.3.

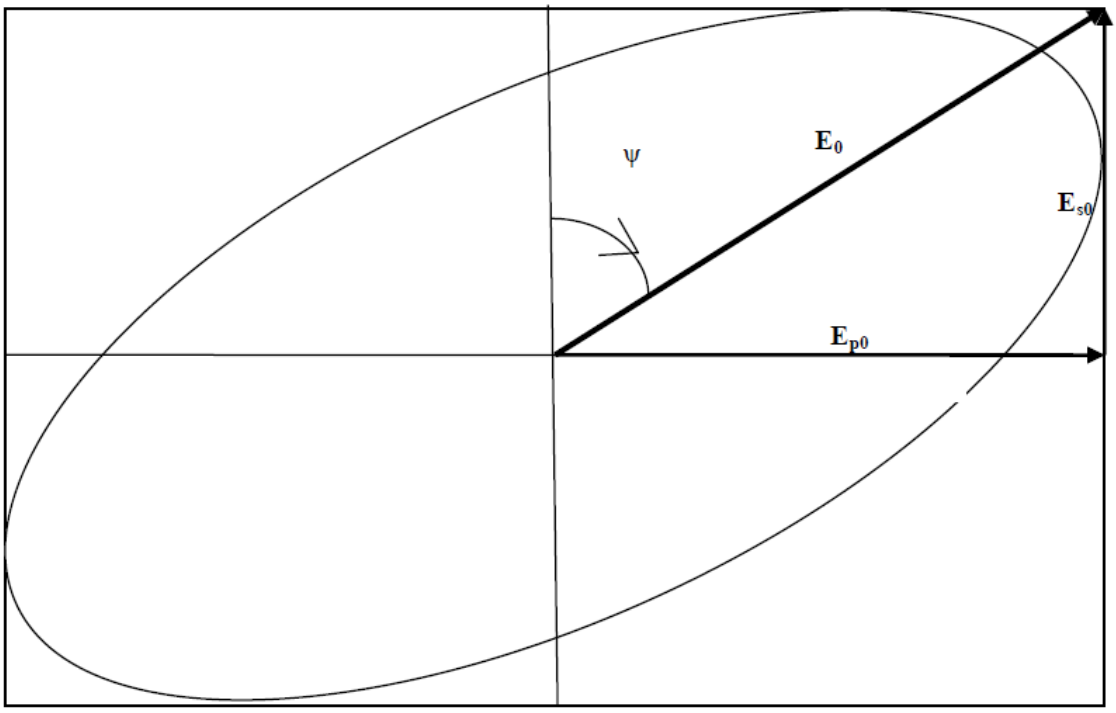

Figure 4.3 Representation of the elliptical polarization, E_{p0} and E_{s0} represents the component of the electric field $\mathbf{E_0}$ which is the maximum of the electric field **E.** The ellipse describes the periodical evolution of **E** intensity.

The important point is that measurement of ψ and Δ is a way to measure the rapport between the p-polarisation and s-polarisation after reflection and therefore a way to characterise the material on which reflection occurs. Indeed it has been seen that ellipsometry is based on the measurement of ρ which is the s-polarisation to p-polarisation ratio of the reflected electromagnetic wave. Knowing the values of ψ and Δ, ρ can be calculated by the means of equation 4.27 as will be explained in the next section:

$$\rho = \tan\psi . \cos\Delta \tag{4.27}$$

- **Representation of observables by Jones Matrix**

The electric field can be expressed as follows by obvious factorisation:

$$E = e^{-i(\omega t - kz)} \begin{bmatrix} E_{p0} . e^{i\Delta} \\ E_{s0} \end{bmatrix} \tag{4.28}$$

It has been seen in the previous section that the polarisation of an electromagnetic wave depends only on the electric field component along the p axis relative to its component along s axis and does not depend on the absolute value of E_p and E_s. The representation of Jones is obtained by normalising the intensity to 1, this leads to $E_{0p}^2+E_{0s}^2=1$. Since $E_{0s}= E_{0p}$ .tan ψ

$$E = \frac{1}{\sqrt{1 + \tan^2\psi}} \begin{bmatrix} e^{i\Delta} \\ \tan\psi \end{bmatrix} \tag{4.29}$$

For instance, for an electromagnetic wave polarised along the p axis, $E_s=0$ and for a right-circular polarisation, $E_p = E_s$ ($\tan\psi = 1$) the phase difference Δ is equal to $-\pi/2$.

$$E_{lp} = \begin{bmatrix} 1 \\ 0 \end{bmatrix} \qquad E_{RC} = \frac{1}{\sqrt{2}} . \begin{bmatrix} 1 \\ i \end{bmatrix} \tag{4.30}$$

4.1.3 Instrumentation

Schematically, the process of ellipsometry measurement is the following: an incident electromagnetic wave which is not polarised propagates along a z-axis, the first device placed on this axis is a polariser which gives a linear polarisation to the wave, the wave is reflected by the sample to be analysed and encounters an analyser at the end of the optic axis. These different devices are described in the following section

- **Polariser and analyser**

Polariser and analyser are actually similar devices and are only different because of their respective functions. Both play the role of selecting a single component of the electric field. The polariser which is placed just after the laser which generates the electromagnetic wave converts this incident radiation initially non- polarised into a linearly polarised wave. The analyser, just as the polariser, selects a single component of the electric field and is positioned after the reflected wave. The polarisation is measured from the rotation angles of the analyser and the polariser. The possibility for the polariser to select a single component of the electric vector is due to the birefringence property of the material inside, for instance crystal of $CaCO_3$. An anisotropic material has the particularity of having a refractive index depending on the light direction. Polarisers use material with two orthogonal optical axes along which the refractive index is different. Since the wave propagation velocity in a material of index n_f is equal to c/n_f, the velocity is slower along the axis where the refractive index is higher and then one is called the fast axis whereas the other is the slow axis. By playing with the reflective properties it is possible to eliminate the electromagnetic wave in the direction of one axis by a total reflection. Since the electric field can be expressed as a function of its component along the two orthogonal optical axes of the polariser, by eliminating the component along one axis, the transmitted electric field has a single component and therefore the light is linearly polarised. This axis is called the transmission axis.

- **Compensator or retarder**

A compensator uses also the birefringence property but it is used for transforming a linear polarisation into a circular polarisation. While a polariser eliminates a component

of the electric vector, a compensator transmits both components but with a phase difference δ due to velocity difference between the slow and the fast axes. If the axes system of the compensator has a rotation of 45° relative to the electric field vector, therefore the components of this latter along the two axes are equal. Furthermore, if $\delta = \pi/2$, the polarisation is circular.

- **Sample**

The sample reflects the incident electromagnetic wave as has been seen previously:

$$E_{rp} = r_p . E_{ip} \tag{4.31}$$

$$E_{sp} = r_s . E_{is} \tag{4.32}$$

This can be written with the following matrix expression:

$$\begin{bmatrix} E_{rp} \\ E_{sp} \end{bmatrix} = \begin{bmatrix} r_p & 0 \\ 0 & r_s \end{bmatrix} . \begin{bmatrix} E_{ip} \\ E_{is} \end{bmatrix} \quad (4.33) \tag{4.33}$$

The operator S representing the sample is

$$S = \begin{bmatrix} r_p & 0 \\ 0 & r_s \end{bmatrix} \tag{4.34}$$

Similarly the operators P or A representing the polariser (or analyser) and C representing the compensator are

$$P = A = \begin{bmatrix} 1 & 0 \\ 0 & 0 \end{bmatrix} \tag{4.35}$$

$$C = \begin{bmatrix} 1 & 0 \\ 0 & e^{-i\delta} \end{bmatrix} \tag{4.36}$$

Since there is a change in reference axis when passing through the different optical devices, a rotation operator has to be added: the passage from a reference axes system x-y to x'-y' with a relative angle α is expressed by the rotation operator R (α):

$$R(\alpha) = \begin{bmatrix} \cos\alpha & \sin\alpha \\ -\sin\alpha & \cos\alpha \end{bmatrix} \tag{4.37}$$

- **Ellipsometer**

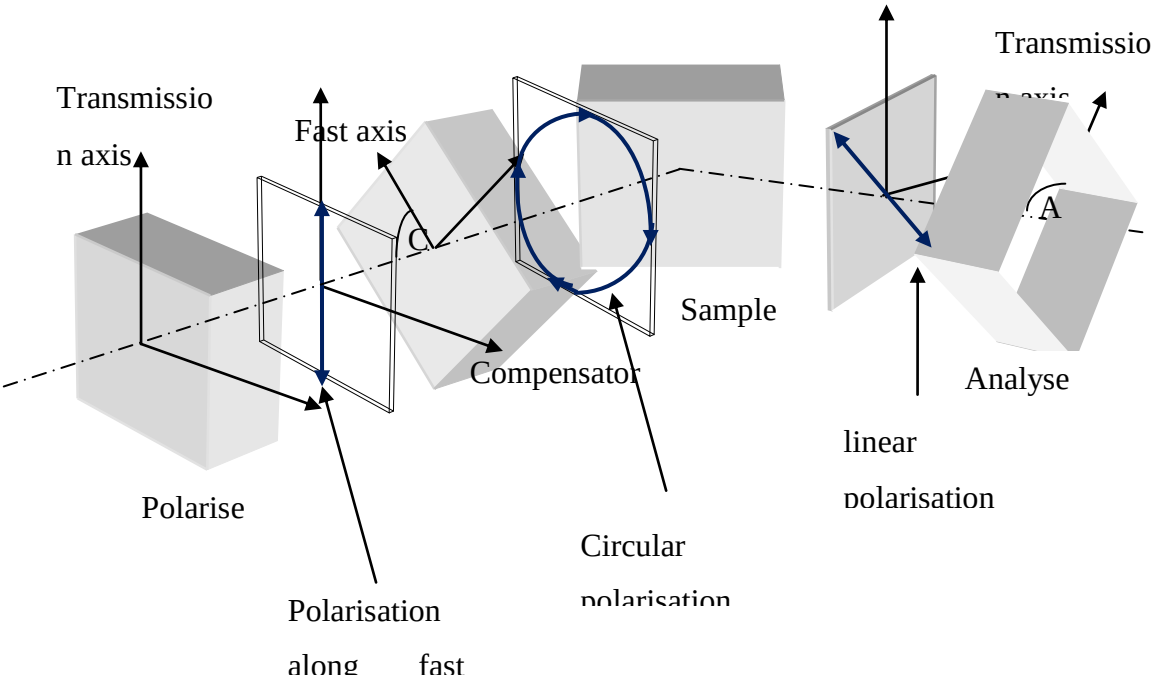

Figure 4.4 Representation of ellipsometry measurement system. After having adjusted the polarizer and analyzer angles a non-polarized monochromatic becomes circularly polarised by a combination of a polariser following with a compensator. Then this light is reflected by the sample surface which gives a linear polarization to the light. This linear polarization is measured by an analyzer at the end of.

On figure 4.4, Initial randomize polarisation of light becomes linear after going through the polariser with fast axis x, E = E_x, then the light is modified by the compensator. Since this latter has a fast axis oriented with an angle C equal to 45°Crelative to the light polarisation, the reference axes (x, y) are rotated by the same angle and at the same time the birefringence of the compensator induces a phase difference of 90° between the

two equal intensity components of the projected polarisation on the new base from which result a circular polarisation. The circular polarisation is converted to a linear polarisation after reflection by the sample. This is due to the orientation of the polariser. The angle of this later is set in order to have linear polarisation after reflection. In other word, the polariser angle is rotated and adjusted until polarisation after sample reflection becomes linear.

4.1.4 Reflectance and Brewster angle θ_B

Reflectance R_p (R_s) is the link between the electromagnetic intensity of the reflected electromagnetic wave and the incident wave:

$$R_p = \left(\frac{|E_{pr}|}{|E_{pi}|}\right)^2 \tag{4.38}$$

$$R_S = \left(\frac{|E_{sr}|}{|E_{si}|}\right)^2 \tag{4.39}$$

The variation of reflectance as a function of the incidence angle θ_0 is represented on figures 4.5-4.6 while figure 4.7 represents the ratio between s-reflectance and p-reflectance. Since ellipsometry is based on the measurement of this ratio, this figure also highlights the variation of measurement sensitivity versus incidence angle. This sensitivity is much higher around a value of the incidence angle (around 75° for air/c-Si interface at λ=630 nm) which is known as the Brewster angle θ_B. Therefore in order to optimise the measurement, values around the Brewster angle are chosen when processing. For an absorbing material on the medium of transmission - which is expressed by a non null imaginary part in the complex refractive index- there is no Brewster angle but R_p passes through a minimum value. The incidence angle corresponding to this minimum is called the pseudo-Brewster angle θ'_B.

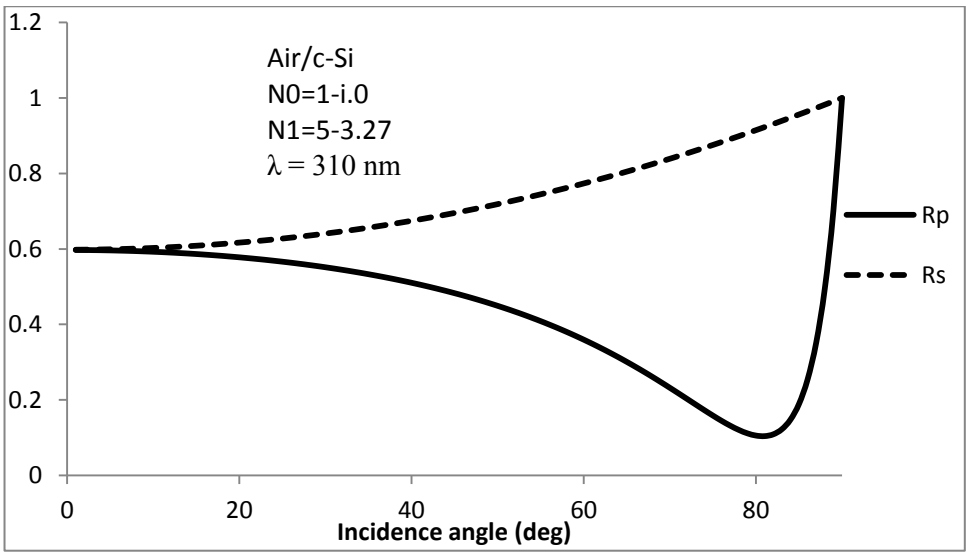

Figure 4.5 Reflectance for p and s components for an interface Air/c-Si for a wavelength λ=310 nm. The complex refractive index $N_1 = n_1 - ik_1$ with t n_1 =5 and k=3.27 [4.1].

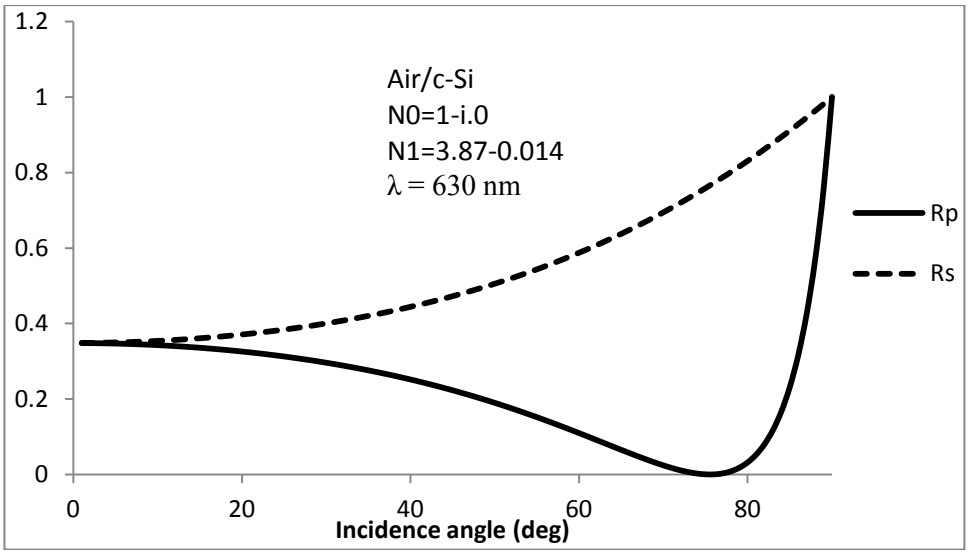

Figure 4.6 Reflectance for p and s components for an interface Air/c-Si for a wavelength λ=630nm. The complex refractive index $N_1 = n_1 - ik_1$ with t n_1 =3.87 and k=0.014.

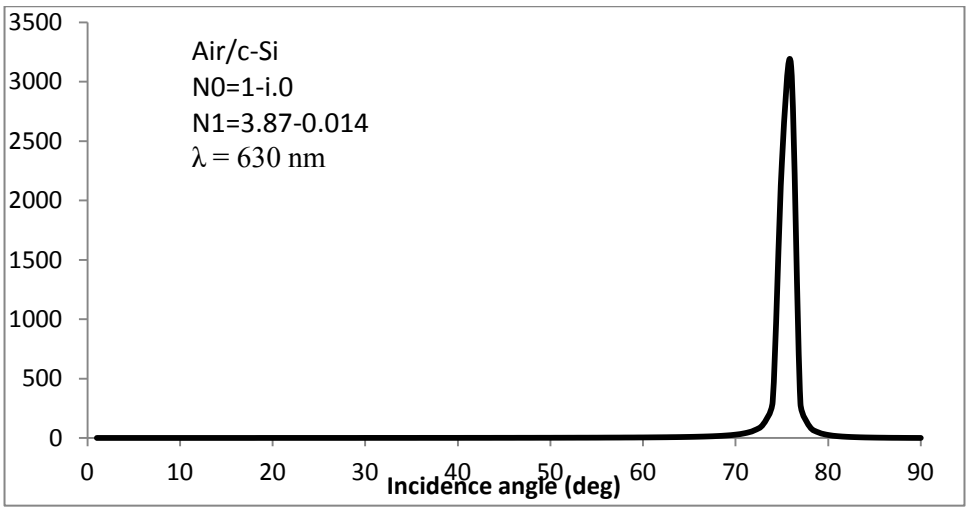

Figure 4.7 Ratio R_s/R_p between the s-component to p-component reflectance for an interface Air/c-Si for a wavelength λ=630nm. The complex refractive index $N_1 = n_1 - ik_1$ with t n_1 =3.87 and k=0.014. Since ellipsometry is based in the value of R_s/R_p, this figure shows that the sensitivity is maximal for an incidence angle around 75° for the ellipsometry measurement.

4.2 Effect of thickness and refractive index

On figure 4.8, the lines labelled 1, 2 and 3 represents the 1st, 2nd and 3rd order of reflected electromagnetic wave. There are noted respectively E_{r1}, E_{r2} ... E_{rn} in the following. The same notation used for equations 4.21 and 4.22 is kept for indexing the media.

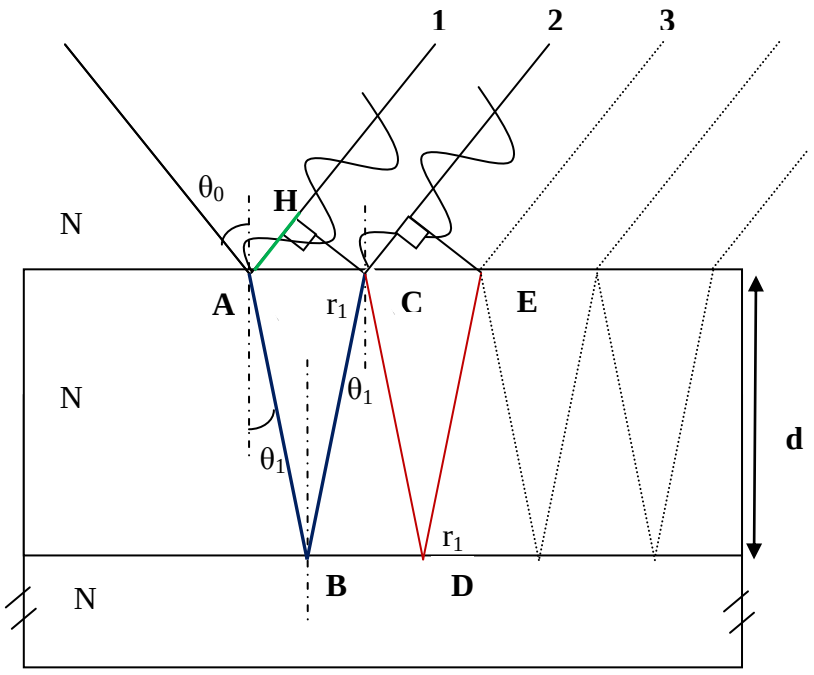

Figure 4.8 Optical path difference between incident and reflected waves. N_0 is refractive index of air, N_1 and N_2 are respectively the complexes refractive index (N=n-ik) of the film with a thickness d and the substrate.

$$E_{r1}(z,t) = r_{(01)}.E_{0}.e^{i(\omega t - 2\pi.N_0.z/\lambda_0)} \quad (4.40)$$

$$E_{r2}(z,t) = t_{(01)}.r_{(12)}.t_{(10)}.E_{0}.e^{i(\omega t - 2\pi.N_0.\frac{z}{\lambda_0} - \varphi)} \quad (4.41)$$

The phase difference φ is proportional to the optical path difference δ:

$$\varphi = 2\pi/\lambda_0.\ \delta \quad (4.42)$$

Figure 4.8 shows this path difference. On this figure, the optical path of the incident wave appears in green while the optical path of the reflective wave appears in blue:

$$\delta = N_1(AB + BC) - N_0.AH \quad (4.43)$$

$$\delta = N_1\ \frac{2d}{\cos(\theta_1)} - N_0.2d.\tan(\theta_1).\sin(\theta_0) \quad (4.44)$$

By rearranging tan (θ_1) and using $N_1 \sin\theta_1 = N_0 \sin\theta_0$:

$$\delta = N_1\ \frac{2d}{\cos(\theta_1)} - N_1.2d.\frac{\sin^2(\theta_1)}{\cos(\theta_0)} \quad (4.45)$$

$$\delta = N_1.2d.\cos(\theta_1) \quad (4.46)$$

$$\varphi = \frac{4\pi.d.N_1}{\lambda_0}.\cos(\theta_1) \quad (4.47)$$

As can be seen in figure 4.8 the difference between the wave labeled 3 and the wave labeled 2 is a reflection ($r_{(10)}$) in the medium 1 at the interface separating the media 0 and 1, a reflection ($r_{(12)}$) in the medium 1 at the interface separating the media 1 and 2 and the optical path difference δ. The same relation applies for calculating the difference between the waves n and (n-1). Therefore for n≥2, one can write equations 4.48 and 4.49 :

$$E_{rn}(z,t) = t_{(01)}.r_{(12)}.t_{10}.E_{r(n-1)}(z,t).e^{-i\varphi}.\left[r_{(10)}.r_{(12)}.e^{-i\varphi}\right] \qquad (4.48)$$

$$E_{rn}(z,t) = t_{(01)}.r_{(12)}.t_{10}.E_{0}(z,t).e^{-i\varphi}.[r_{(10)}.r_{(12)}.e^{-i\varphi}]^{n-2} \qquad (4.49)$$

The resulting wave which is the sum of reflected waves for each order is

$$E_r(z,t) = E_0(z,t).\left\{r_{(01)} + t_{(01)}.r_{(12)}.t_{(10)}.e^{-i\varphi}.\sum_{n=2}^{+\infty}[r_{(10)}.r_{(12)}.e^{-i\varphi}]^{n-2}\right\} \qquad (4.50)$$

After noticing that the term with sum is a geometric series

a

$$E_r(z,t) = E_0(z,t).\left\{r_{(01)} + t_{(01)}.r_{(12)}.t_{(10)}.e^{-i\varphi}.\frac{1}{1 - r_{(10)}.r_{(12)}.e^{-i\varphi}}\right\} \qquad (4.51)$$

Since

$$r_{(ij)}=-r_{(ij)} \text{ and } t_{(01)}.t_{(10)}=1-(r_{(01)})^2 \quad (4.52)$$

$$E_r(z,t) = E_0(z,t).\left\{\frac{r_{(01)} + r_{(12)}).e^{-i\varphi}}{1 - r_{(10)}.r_{(12)}.e^{-i\varphi}}\right\} \quad (4.53)$$

If we divide by E_0, the reflection coefficient for 3 layers $r_{(012)}$ is obtained.

$$r_{(012)} = \frac{r_{(01)} + r_{(12)}).e^{-i\varphi}}{1 - r_{(10)}.r_{(12)}.e^{-i\varphi}} \quad (4.54)$$

$$\varphi = \frac{4\pi.d.N_1}{\lambda_0}.\cos(\theta_1) \quad (4.55)$$

Fresnel coefficients are obtained by measuring the connection between the component p of $r_{(012)}$: $r_{p(012)}$ which is calculated by replacing the terms $r_{(ij)}$ by $r_{p(ij)}$ and the component s of $r_{(012)}$: $r_{s(012)}$ which is determined by replacing the terms $r_{(ij)}$ by $r_{s(ij)}$. The effect of thickness for a thin film of amorphous silicon a-Si:H deposited on a c-Si substrate can be seen on the figure 4.9 where the thickness d of the a-Si:H film is varied from 0 to 400 nm for an incident wave length of 630.2 nm (At 630.2 Nm: $Nc\text{-}_{Si}$=3.87-i0014, $N_{a\text{-}Si}$ =4.21-i0.43)

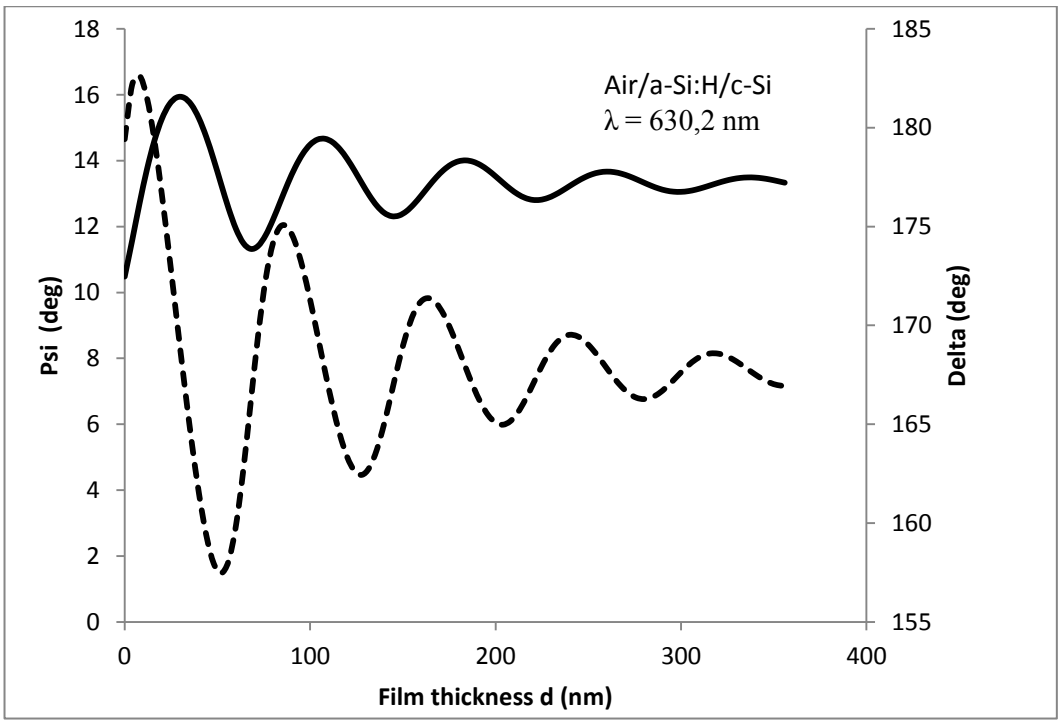

Figure 4.9 Variation of the two ellipsometry parameters ψ (plain) and Δnd in) as a function of the film thickness [4.1]. These curves have been obtained with a code that simulates the process of light reflection with a system with 3 media: air, a-Si film with thickness d and a substrate c-Si. The results of the simulation have been compared with reference [4.1] for checking the validity of the code.

4.3 Multilayers

When the sample is covered by several layers, Fresnel coefficients are calculated with the same method as a single layer (air/film/substrate) by iteration. Considering a number of layers k, the system of successive layers is reduced to 3 layers which are air, first layer and a layer N_{k-3} equivalent to the k-3 last layers.

$$r_{(01N_{k-3})} = \frac{r_{(01)} + r_{(1N_{k-3})}.e^{-i\varphi_1}}{1 - r_{(01)}.r_{(1N_{k-3})}.e^{-i\varphi_1}} \tag{4.56}$$

The coefficient $r_{(1N_{k-3})}$ is also equivalent to $r_{(12N_{k-4})}$ where the layer N_{k-4} is the layer equivalent to the k-4 last layers. There the reflection coefficient $r_{(1N_{k-3})}$ is calculated by considering the same system except that the air is removed, the k-4 last layers are equivalent to a layer N_{k-4}.

$$r_{(1N_{k-3})} = r_{(12N_{k-4})} = \frac{r_{(12)} + r_{(2N_{k-4})}.\, e^{-i\varphi_2}}{1 - r_{(12)}.\, r_{(2N_{k-4})}.\, e^{-i\varphi_2}} \tag{4.57}$$

The coefficient $r_{(2N_{k-3})}$ is also equivalent to $r_{(23N_{k-5})}$ where the layer N_{k-5} is the layer equivalent to the k-5 last layers.

There the reflection coefficient $r_{(2N_{k-4})}$ is calculated by removing the first layer, the k-5 last layers are equivalent to a layer N_{k-5}.

$$r_{(2N_{k-4})} = r_{(23N_{k-5})} = \frac{r_{(23)} + r_{(3N_{k-5})}.\, e^{-i\varphi_3}}{1 - r_{(23)}.\, r_{(2N_{k-5})}.\, e^{-i\varphi_3}} \tag{4.58}$$

This operation is reiterated until only the 3 last layers remain:

$$r_{(2N_{k-4})} = r_{(k-2,k-1,k)} = \frac{r_{(k-2,k-1)} + r_{(k-1,k)}.\, e^{-i\varphi_{k-1}}}{1 - r_{(k-2,k-1)}.\, r_{(k-1,k)}.\, e^{-i\varphi_{k-1}}} \tag{4.59}$$

(4.59)

In these equations, the optical path φ_i depends on the thickness d_i, the complex refractive index N_i and the complex incidence angle θ_i of the layer i. It has to be recalled that the imaginary part of θ_i is related to the absorption of the layer i. Therefore the absorption of the film is included in this calculation.

$$\varphi_i = \frac{4\pi.\, d_i.\, N_i}{\lambda_0}.\cos(\theta_i) \tag{4.60}$$

For the calculation, $r_{(k-2,k-1,k)}$ is calculated with the relation described in the previous section and by recurrence $r_{(01N_{k-3})}$ is deduced. These relations show clearly that the parameters involved in the determination of polarization are the layers' thicknesses and their complex refractive indices. There is no determined analytical expression of the

refractive index as a function of the wave length and it has to be deduced from dielectric function model.

4.4 Dielectric function model

The refractive index n_f is a quantity for representing the ratio of the light velocity in a given material and in the vacuum. This change of velocity is actually a consequence of dielectric constant of the material. The relation between refractive index and dielectric constant is expressed in equation 4.61

$$\varepsilon_1 = n_f{}^2 - k^2 \tag{4.61}$$

$$\varepsilon_2 = n_f . k \tag{4.62}$$

$$\varepsilon = \varepsilon_1 - i\varepsilon_2 \tag{4.63}$$

It has to be noted that there is a negative sign before ε_2 in equation 4.63, in another convention this sign is positive and therefore the relations which are deduced from equation 4.63 have to be adapted.

4.4.1 Interaction of light with the matter

- **Dielectric polarisation and dielectric constant**

The dielectric constant ε of a material describes the global effect induced by an electric field in this material. When an electric field **E** is applied to a dielectric material, spatial distribution of the charge is modified since positive charges move toward the direction of **E** while negative charges move toward the opposite direction. In a dielectric, positive and negative charges are strongly enough bonded for not being totally separated by the applied electric field (in the range of photon energy of our investigation). For an atom the barycentre of the positive charge and the negative charge does not coincide anymore and it results in the generation of a dipole whose momentum is expressed by:

$$\boldsymbol{\mu} = q . \mathbf{L} \tag{4.64}$$

where **L** is the distance between the barycentre of the positive charge and the barycentre of the negative charge (cf. figure 4.10).

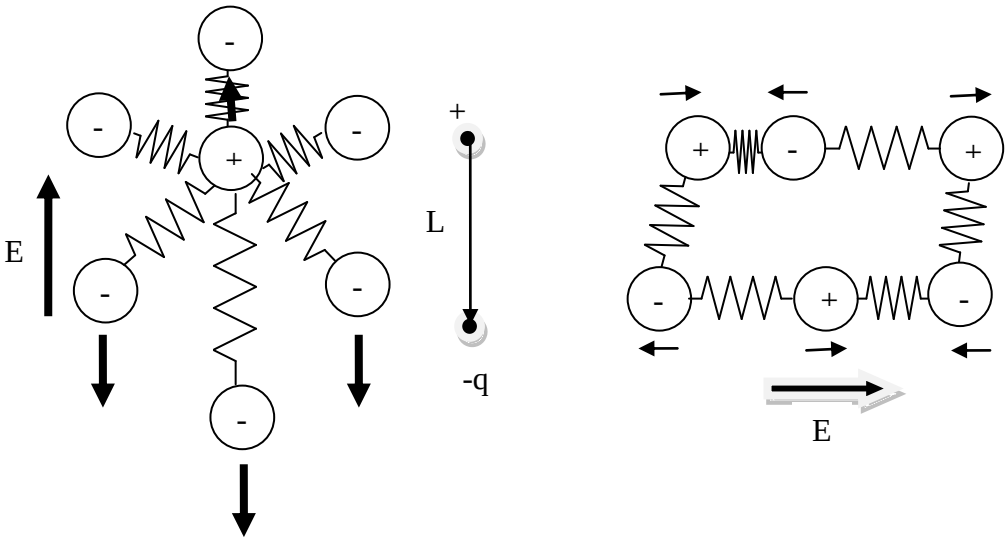

Figure 4.10 On the left, dielectric polarization with equivalent dipole, on the right, atomic polarization. The refractive index and dielectric permittivity describes the dielectric polarization resulting from an applied electric field E. (Adapted from [4.1])

This phenomenon is described by the polarisability **P** which represents the sum of the dipole moments by unit of volume in the material.

$$\mathbf{P} = -q.N.\mathbf{L} \tag{4.65}$$

However the response of the material or its capability to be polarised depends on its characteristic in regard to electromagnetic matter interaction. This latter is quantified by a constant known as dielectric permittivity. In other words, dielectric permittivity characterises the polarisation response to the applied electric field. From the above relation, it can be deduced that for a same electric field, the higher is the charge number and the distance between the two poles of the dipoles, the higher is the dielectric constant. It has to be noted that in the same way as the refractive index, the dielectric constant can be extended by complex notation in which the imaginary part represents the absorption. There is actually a strong correlation between the real part and the complex part of the dielectric permittivity. Dielectric permittivity is given by:

$$\varepsilon = 1 + \frac{P}{\varepsilon_0 E} \tag{4.66}$$

During ellipsometry measurement, the electric field of the electromagnetic wave generates electric dipoles in the investigated material. Since the applied electric field oscillates at a given frequency, the positive charges move alternatively forwards and backwards in the direction of the field and in the opposite way for the negative charges, consequently the generated dipoles oscillate at the same frequency as the incident electromagnetic wave and generate waves at this frequency. This phenomenon of dipole radiation is also known as the Huygens principle. Therefore the transmitted and reflected wave is the result of the constructive interference of this dipole radiation. Thus the significance of refractive index appears more clearly. The wave velocity decreases for a material of high refractive index because the higher the index, the higher is the sequential generation of electric dipoles, a phenomenon which slows the light propagation. Resonance for atomic polarisation occurs for electromagnetic waves in the infrared range whereas dielectric polarisation resonance occurs in ultraviolet region. When the electromagnetic field frequency is much lower than the resonance frequency of the oscillators, dielectric constant remains at a constant value ε_S and the behaviour of oscillations is the same as if the field was static. The same applies for dielectric polarisation. Thus for frequency much lower than atomic frequency (and a fortiori dielectric frequency), the permittivity is the sum of the static values for both atomic and dielectric polarisation. When the frequency increases around resonance, oscillations of bonded atoms follow the variation of the field until a critical frequency that oscillations cannot follow. At this point dielectric permittivity reaches a constant value ε_∞ which is the static value of electric permittivity for dielectric polarisation. If frequency is increased until reaching the value for dielectric polarisation resonance, dipole oscillation occurs until frequency becomes much higher than resonance, then dielectric permittivity remains at the constant value of 1. This process is illustrated in figure 4.11, although electric permittivity should appear constant for frequency both far beyond atomic polarisation range and far below dielectric polarisation. It is not the case on the figure because the frequency scale is compressed on this graph and is not represented on a logarithmic scale.

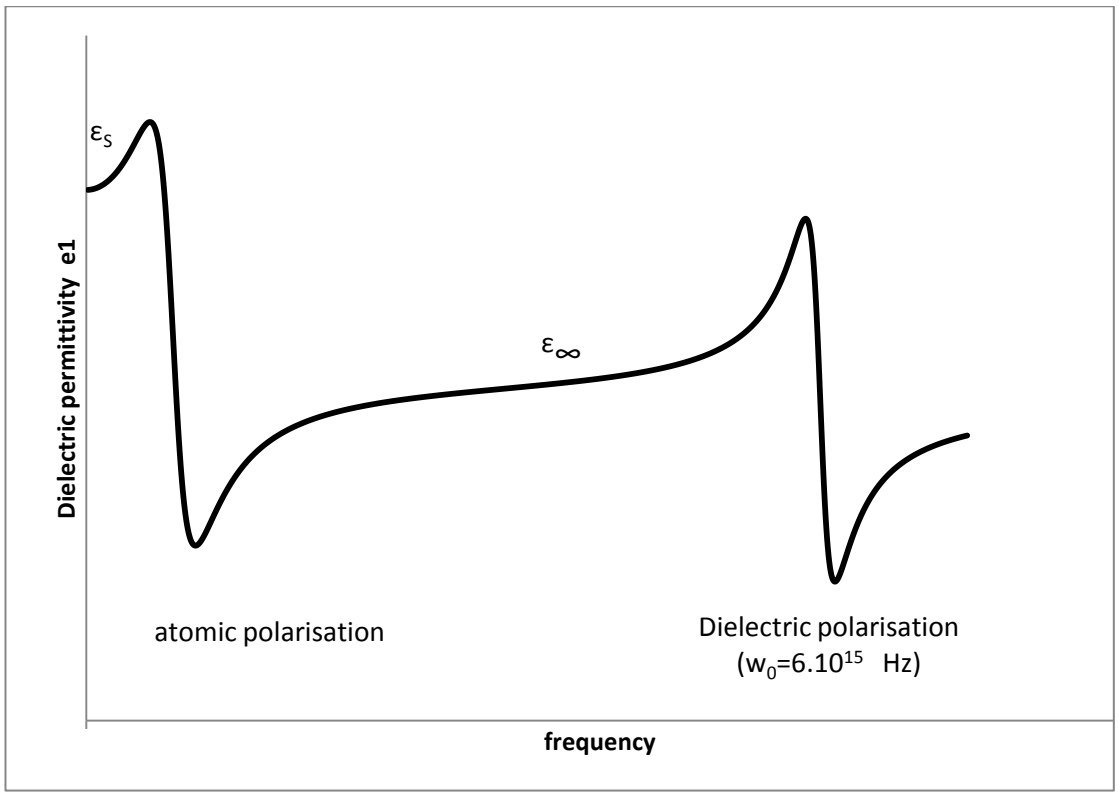

Figure 4.11 Electric permittivity versus frequency (adapted from [4.1]). When the electromagnetic field frequency is much lower than the resonance frequency of the atomic polarization, dielectric permittivity has a constant value ε_S. After atomic resonance, when the frequency increases around resonance, oscillations of bonded atoms follow the variation of the field until a critical frequency that oscillations cannot follow. At this point dielectric permittivity reaches a constant value ε_∞ which is the static value of electric permittivity for dielectric polarisation. Dielectric resonance occurs around a frequency $\nu=3x10^{14}$ - 10^{15} Hz corresponding with the range (200-1000 nm).

- **Relation between refractive index and absorption index (real and imaginary part) :Kramers-Kronig relation**

The Kramers-Kronig relation [4.1, 4.2, and 4.4] is the expression of the connection between the response of a physical quantity to a perturbation. In the case of the dielectric susceptibility, the response to the perturbation due to the applied electric field is the polarisation. It can be demonstrated that the real part of the dielectric function is the causal response to the imaginary part and they are connected with a Kramers-Kronig relation which is expressed in this case by equation 4.67

$$\varepsilon_1(\omega) = 1 + \frac{1}{\pi} \lim_{\varepsilon \to 0^+} \left(\int_{-\infty}^{-\varepsilon} \frac{\varepsilon_2(\omega')}{\omega' - \omega} d\omega' + \int_{+\varepsilon}^{+\infty} \frac{\varepsilon_2(\omega')}{\omega' - \omega} d\omega' \right) \qquad (4.67)$$

This relation can be discretised on an interval $[-\omega_1, \omega_1]$ and becomes:

$$\varepsilon_1(\omega) = 1 + \sum_{k=-\infty}^{+\infty} p_k \exp\left(\frac{ik\pi\,\omega}{\omega_1}\right) \tag{4.68}$$

The details of this numeric method and the calculation of Fourier coefficients p_k are given in reference [4.4]. This method has been used for the calculation of ε_1 in our simulation when Cody-Lorentz was applied since the analytic expression of ε_1 is very complicated. The imaginary part ε_2 can reciprocally be determined by Kramers-Kronig relation but it is not the case in practice since the expression of ε_2 is trivial in regard with the expression of ε_1. It has also to be noted that sometimes the analytical calculation of ε_1 is impossible and ε_1 can only be determined by using Kramers-Kronig relation.

4.4.2 Models

Electric permittivity is determined from equation 4.69

$$\varepsilon = 1 + \frac{P}{\varepsilon_0 E} \tag{4.69}$$

Where $\mathbf{P}$=-q.N_e.$\mathbf{l}$, l**,** is the vector between the positive and negative poles of the dipole.

- **Lorentz**

Lorentz model [4.1, 4.6] is a classic description. Electric permittivity is determined by modelling electromagnetic wave and medium interaction by an oscillating spring excited by an alternating electric field in a viscous environment. If x (t) represents the oscillator motion, x (t) also corresponds to the oscillating length of the dipole, therefore:

$$P = -q.N_e.|x(t)| \tag{4.70}$$

The forces which are applied on the spring are the electrostatic force (–q**E**), Hook reaction force (–k_H**x**), and viscous forces(-m.Γ_v.**dx/dt),** related to the acceleration by the fundamental principle of dynamics:

$$m\frac{d^2x}{dt^2} = -m.\Gamma_V.\frac{dx}{dt} - m{\omega_0}^2.x - q.E \tag{4.71}$$

$$\omega_0 = \sqrt{\frac{k_H}{m}} \tag{4.72}$$

$$E = E_0.e^{i\omega t} \tag{4.73}$$

The elongation x(t) is therefore proportional to $e^{i\omega t}$:

$$x(t) = C.e^{i\omega t} \tag{4.74}$$

The constant C is determined by substituting x(t) by its expression in equation 4.71

$$C = -\frac{qE_0}{m}.\frac{1}{({\omega_0}^2 - \omega^2) + i\Gamma_v\omega} \tag{4.75}$$

$$P(\omega) = \frac{q^2.N_e.E_0}{m}.\frac{1}{({\omega_0}^2 - \omega^2) + i\Gamma_v\omega} \tag{4.76}$$

$$\varepsilon(\omega) = 1 + \frac{q^2.N_e}{m.\varepsilon_0}.\frac{1}{({\omega_0}^2 - \omega^2) + i\Gamma_v\omega} \tag{4.77}$$

Since $\varepsilon=\varepsilon_1 - i\varepsilon_2$:

$$\varepsilon_1(\omega) = 1 + \frac{q^2.N_e}{m.\varepsilon_0}.\frac{({\omega_0}^2 - \omega^2)}{[({\omega_0}^2 - \omega^2)]^2 + (\Gamma_v\omega)^2} \tag{4.78}$$

$$\varepsilon_2(\omega) = -\frac{q^2.N_e}{m.\varepsilon_0}.\frac{\Gamma_v\omega}{[({\omega_0}^2 - \omega^2)]^2 + (\Gamma_v\omega)^2} \tag{4.79}$$

It can be noticed that $\varepsilon_1(\omega)$ can be calculated from $\varepsilon_2(\omega)$ with Kramers-Kronig relation and reciprocally. Lorentz oscillations are represented by the change in dielectric permittivity as a function of electromagnetic field energy on figure 4.12. This latter is related to the frequency via Planck relation: $E=h\upsilon$.

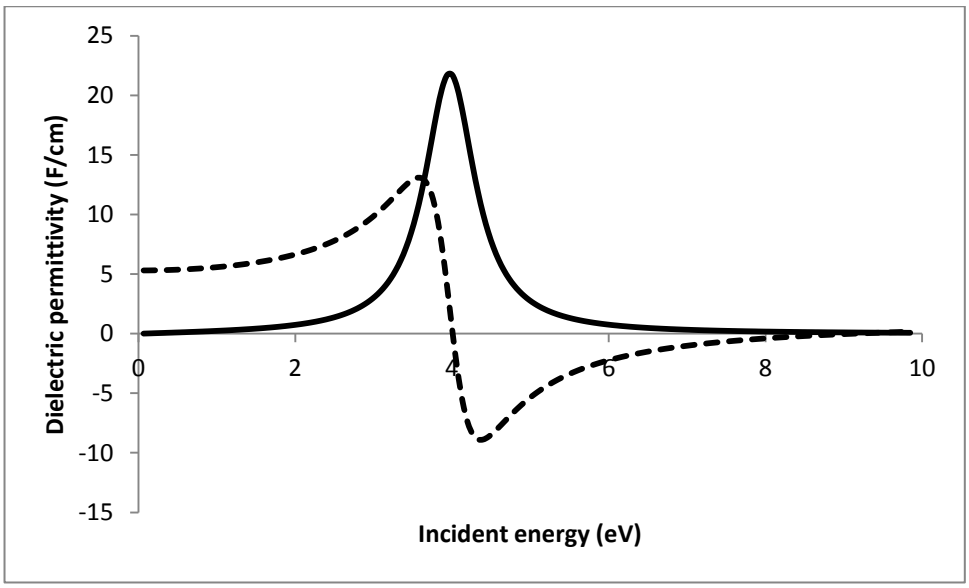

Figure 4.12 Dielectric permittivity $\varepsilon = \varepsilon_1 - i\varepsilon_2$ of a Lorentz oscillator: ε_1 (dash), ε_2 (plain). Deposited film complex refractive index function is determined with dielectric permittivity.

- **Sellmeier and Cauchy**

For transparent material or for frequencies far below resonance frequency of the material or for photon energy below energy band gap, ε_2 can be assumed to be null (thus $\varepsilon = \varepsilon 1 = n^2_f$). Using Lorentz model with $\Gamma \rightarrow 0$, and using $\omega/c = 2\pi/\lambda$:

$$\varepsilon_1(\lambda) = 1 + \frac{q^2.N_e}{m.\varepsilon_0(2\pi c^2)}.\frac{(\lambda.\lambda_0)^2}{\lambda^2 - {\lambda_0}^2} \tag{4.80}$$

This latter relation can be written for several oscillators with adjustable parameters A and B_j:

$$\varepsilon_1(\lambda) = A + \sum_j \frac{B_j.\lambda^2}{\lambda^2 - {\lambda_{0j}}^2} \quad ; \quad \varepsilon_2 = 0 \tag{4.81}$$

Cauchy's equation is an approximation of equation 4.81, after series development:

$$n_f(\lambda) = A + \frac{B}{\lambda^2} + \frac{C}{\lambda^4} + \cdots ; \quad k = 0 \tag{4.82}$$

For instance if a material has an energy band gap beyond 5 eV which corresponds to wave length of 248.0 nm, it can be modelled on the range of investigation 300 to 1000 nm with Cauchy approximation. The Sellmeier equation is a further development of this model with a more accurate representation of the refractive index across a wider frequency range.

- **Tauc-Lorentz**

Before modelling of a-Si:H by Tauc-Lorentz function several approaches have been investigated [4.7, 4.8]. In the Lorentz oscillator, absorption versus frequency represented by the imaginary part ε_2 of dielectric function is symmetric. Indeed absorption increases in a continuous way until resonance and decreases continuously for higher frequency. On the other hand, for amorphous semiconductors, absorption only occurs for energy beyond energy band gap. Therefore photon absorption does not occur until photon energy (or corresponding frequency) is at least equal to the energy band gap. In Tauc-Lorentz model, ε_2 [4.1, 4.9-4.12] is calculated taking into account the energy band gap E_g where for $En \leq Eg$, $\varepsilon 2 = 0$. This model is a mixed Lorentz model and Tauc-Gap relation. The Tauc-Gap relation [4.13, 4.14] is expressed by

$$\varepsilon_2(E_n) = A_{Tauc}.\frac{(E_n - E_g)^2}{E_n^2} \tag{4.83}$$

For En>Eg:

$$\varepsilon_2(E_n) = \frac{A.En_0.C(E_n - E_g)^2}{({E_n}^2 - En_0^2)^2 + (C.En)^2} .\frac{1}{En} \tag{4.84}$$

The real part of the dielectric permittivity ε_1 is determined with Kramers-Kronig relation. It has to be noted that C is the broadness as Γ_v in equation (4.79). Figure 4.13 represents the results of the real and imaginary parts of Tauc-Lorentz function.

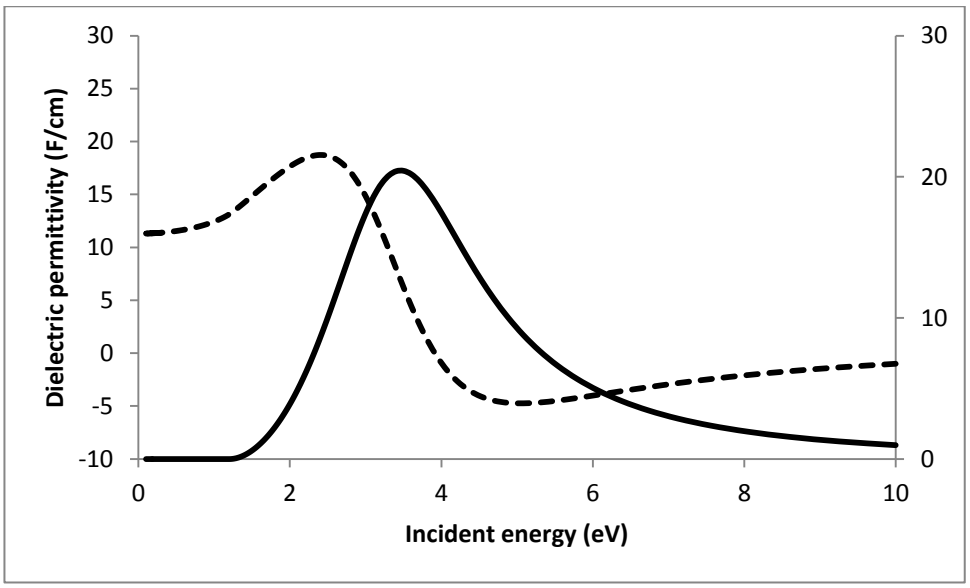

Figure 4.13 Dielectric permittivity of a Tauc-Lorentz oscillator: ε_1 (dash), ε_2 (plain). Tauc-Lorentz oscillator is used for representing the dielectric function of amorphous film particularly SiN_x films.

Similarly to Tauc-Lorentz, Cody-Lorentz model [4.15, 4.16], is based on Lorentz model and the Cody gap. This latter [4.17] is given by:

$$\varepsilon_2(\mathrm{E_n}) = \mathrm{A_{Tauc}}.(\mathrm{E_n} - \mathrm{E_g})^2 \tag{4.85}$$

$$\varepsilon_2(\mathrm{E_n}) = \frac{(\mathrm{E_n} - \mathrm{E_g})^2}{(\mathrm{E_n} - \mathrm{E_g})^2 + \mathrm{E_p^2}} \frac{\mathrm{A}.\mathrm{En_0}.\mathrm{C}(\mathrm{E_n} - \mathrm{E_g})^2}{(\mathrm{E_n}^2 - \mathrm{En_0^2})^2 + (\mathrm{C}.\mathrm{En})^2} \frac{1}{\mathrm{En}} \; ; \; \mathrm{E_n} > \mathrm{E_t} \quad (4.86) \tag{4.86}$$

$$\varepsilon_2(\mathrm{E_n}) = \frac{\mathrm{E_1}}{\mathrm{E_n}} \exp\left(\frac{\mathrm{E_n} - \mathrm{E_t}}{\mathrm{E_u}}\right); \; 0 < E_\mathrm{n} < \mathrm{E_t} \tag{4.87}$$

E_t is the transition energy between the so called Urbach tail regime (equation 4.87) determined by E_u which is the Urbach energy and is the width of the tail states in the bandgap and the Cody-Lorentz regime. The Cody-Lorentz regime is itself demarked by

E_p between the absorption onset behaviour and the Lorentz oscillator behaviour [4.13, 4.15, and 4.16]. One important point in equation 4.86 compared with equation 4.84 is the fact that the amplitude A is not the same as the amplitude in Tauc Lorentz. E_1 is determined by the continuity condition between the two regimes.

- **Effective medium approximation (EMA)**

EMA is used to calculate refractive index of a material composed with two phases with different dielectric permittivities. An equation describes a material composed of phases A and B with dielectric permittivities respectively ε_a and ε_b. The fractions of phase A and B in the material are respectively f_a and f_b. The screening factor q is equal to 1/3 for spherical symmetry. In EMA q is assumed to be 1/3.

$$\varepsilon = \frac{\varepsilon_a . \varepsilon_b + \kappa . \varepsilon (f_a . \varepsilon_a + f_b . \varepsilon_b)}{\kappa . \varepsilon + (f_a \varepsilon_b + f_b \varepsilon_a)} \tag{4.88}$$

$$\kappa = \frac{1 - q}{q} \tag{4.89}$$

EMA also known as Brugemann EMA [4.18] is a usual method for modelling the roughness of a material [4.19]. In this case, the first phase is the material on the top and the second material is the void. Their respective percentages are 50%. The roughness in our simulations has been modelled as a layer on the top of the film by an EMA function with 50% of void.

4.5 Simulations

In order to extract accurate information on the deposited film (a-Si:H or SiN_x) from the experimental data, a model is built consisting of several successive layers. Each layer, represented on figure 4.14, is described by its thickness and its complex refractive index at each wavelength of investigation. The substrate constitutes the first layer because the recurrence relation described in section 4.3 starts with the last layer encountered by the electromagnetic wave. However in the equation the substrate is the last layer (cf. equation 4.21 and 4.22 for instance). In this study the substrate is crystalline silicon and there is no need to give its thickness except that it should be very high. It can also be noted that the substrate type (FZ, Cz.), its doping, or its crystalline orientation are not involved. The simplest model consists of three layers which are the substrate, the film

and the ambient medium (air). For more complex models, a very thin interface layer can be added between the substrate and the film which can be SiO_2 or an EMA layer composed of 50% of the material of the substrate and 50% of the film for instance, or/and a SiO_2 native layer on the film surface and roughness. Roughness layer has been described with EMA method. The values ψ and Δ are calculated from the recurrence relation described in section 4.3.

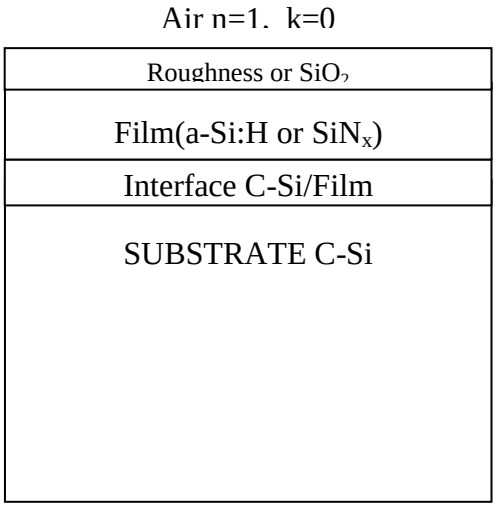

Figure 4.14 Representation of the sample modeling used in the simulations for the present work. Tauc-Lorentz dielectric and Cody-Lorentz dielectric functions has been used respectively for SiNx and a-Si films. The SiNx interface c-Si/Film layer has been tested but since it does not bring a great improvement of the modeling, this layer has been omitted for the major part of the samples.

Finding accurate parameters for semiconductors is not obvious. The Tauc-Lorentz function is described by 4 parameters whereas the Cody-Lorentz function which is an enhancement of the former needs 7 parameters. Furthermore several of these parameters are strongly correlated together which forbids doing an optimisation for each parameter as can be seen on figures 4.15 and 4.16 where the values of ψ versus wavelength are represented for different values of A (respectively E_g) in the Tauc-Lorentz function whereas the other parameters are settled at fixed values on figure 4.15 (respectively figure 4.16)

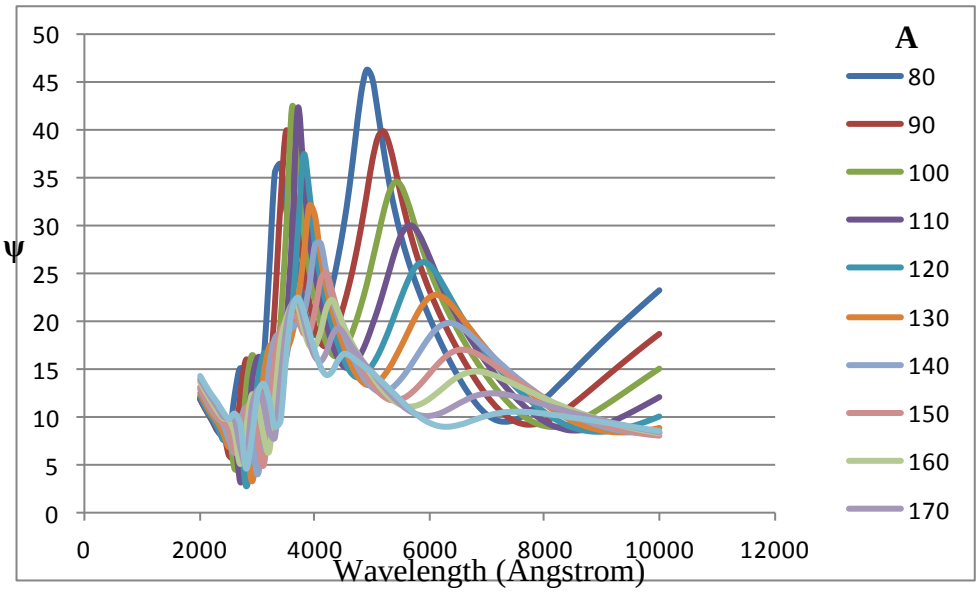

Figure 4.15 influence of the parameter A of Tauc-Lorentz function (cf. equation 4.84) on ψ. Figure 4.15 and 4.16 illustrate the difficulty for fitting the parameters separately. Wavelength is expressed in angstrom (1 angstrom=0.1 nm).

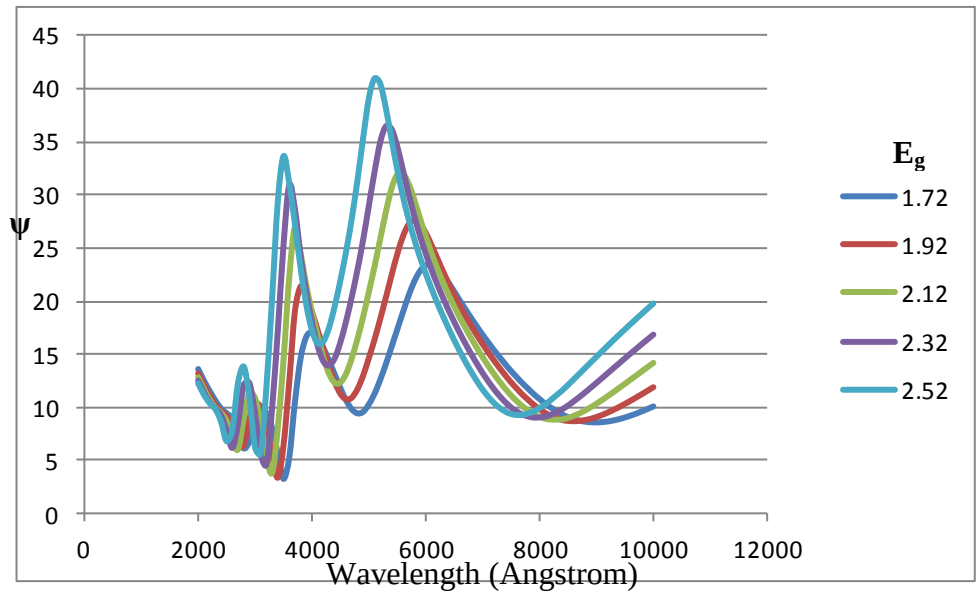

Figure 4.16 influence of the bandgap E_g of Tauc-Lorentz function (cf. equation 4.84) on ψ. Figure 4.15 and 4.16 illustrate the difficulty for fitting the parameters separately. Wavelength is expressed in angstrom (1 angstrom=0.1 nm)

Figure 4.15 and 4.16, which represent the value ψ for a Tauc-Lorentz film on a c-Si substrate are used for illustrating the difficulty that can generate the correlation between parameters. On the figure 4.15, the parameter A which is the amplitude of the imaginary part ε_2 of the dielectric permittivity is changed from 80 to 170 by step of 10. A clear

tendency can be deduced from this example: the shift of the second peak toward the high wavelength whereas the amplitude of this latter decreases and its breadth increases. Regarding the first peak, when A increases from 80 to 110 it increases and when A increases further, it decreases and at the same time a new peak and then another one appears in the low wavelength region. On the other hand on the figure 4.16, the second peak shifts toward the low wavelength and the amplitude of the peak increases when the gap E_g increases, the first peak follows qualitatively, this is the opposite effect of the increasing of A. On this example, we tried to adjust the value of ψ obtained by using a Tauc-Lorentz layer for the values of sample 44 (cf.table 4.2) by setting properly the 4 parameters. The problem is the following; the thickness has been adjusted and the curve fits quite well except for the low wavelengths where the experimental curve has fewer peaks. The higher number and the lower amplitude show that the film is more absorbent at high energies than the model and is an approximated indication of the energy gap. Therefore it seems that the energy gap chosen for Tauc-Lorentz model needs to be decreased. On the other hand the peak in high wavelength of Tauc-Lorentz model fits well and a decreasing of the gap leads to diminution of the second peak amplitude in high wavelength. Therefore the correction cannot be realised only by varying the energy gap. Thus we can try to decrease E_g and decrease A at the same time for balancing the diminution of the second peak but in parallel with the increasing of the second peak, the first peak also increases and neutralises the effect of decreasing E_g. Similar processes happened with other parameters which imply that the fit cannot be performed unless all the parameters are similarly adjusted. This required a numerical method. The numerical method for adjusting parameters for fitting to the experimental values of ψ and Δ has not been implemented in our simulation. Actually, for each sample, the fit has been firstly done using the software CompleteEASE developed by J.A Woolam Co. This software use a Levenberg-Marquardt algorithm [4.20, 4.21] in order to determine the values of the parameters which minimise the mean square error (MSE) [4.22] between the theoretical values of ψ and Δ of the simulation and the experimental values of ψ and Δ. In a second step the values of these parameters have been then used in our own implemented simulation and further manually adjusting when it was possible. The advantage of using our own code is that although less powerful it allows controlling every step of the simulation process. Figures 4.17 and 4.18 show the interfaces of our code for respectively, Tauc-Lorentz and Cody-Lorentz functions. In figure 4.17, the values of the Tauc-Lorentz function parameters have to be completed by the operator as well as the film thickness and the rough layer thickness. For each wavelength, the real

and imaginary part of the refractive index respectively n_{f3} and k_3 of the substrate are registered. In the case of silicon the values are extracted from reference [4.23]. The values of the complex refractive index of the film n_{f2} and k_2 are calculated by using equations 4.84, 4.61, 4.62 and the analytic expression of n_{f2} resulting from Kramers-Kroning relation. The roughness is then calculated with equations 4.86 and 4.87 using the values of n_{f2} and k_2 and the values of the void (n_f=1, k=0). The calculation of ψ and Δ is done by using the recurrence relation for the determination of the reflection coefficient when the sample is constituted by several layers (section 4.3). Figure 4.18 is a picture of the interface for a film with a Cody-Lorentz dielectric function. On this picture in addition with the 3 parameters of Cody-Lorentz, E_p, E_u and E_t, there are two supplementary columns which are labelled "A graded %" and "E_g graded %". These values are used when the film is graded. The values of the amplitude at the top and at the bottom of the film are given by equations 4.88 and 4.89 where p_A is the percentage of the parameter gradation thorough the film and similarly for other parameters. Graded layers have been added for Cody-Lorentz because this latter is used for a-Si:H film which present graded layers as will be seen in the following.

$$A_{top} = A + \frac{p_A}{100} \times \frac{A}{2} \tag{4.90}$$

$$A_{bottom} = A - \frac{p_A}{100} \times \frac{A}{2} \tag{4.91}$$

In the case of Cody-Lorentz, the real part of the dielectric function is determined by an algorithm using the numerical expression of Kramers-Kronig relation. Since this method required energy interval, ε_1 and ε_2 are calculated as a function of energy instead of wave length. Then in a second time, ε (E) as to be expressed as a function of the wavelength since the values of the substrate are only given at given wavelength. The missing values of ε (λ) are then interpolated.

A	Eg	B0 ou E0	C ou Br	eps_inf	Rough (A)	Film thickness (A)
76.263	4.814	8.344	0.715	1.658	33	2421.17
rough layer		Film		Substrate Si		
n1	k1	n2	k2	n3	k3	
1.59705666	0.01422086	2.27069789	0.03129194	1.8494544	3.3914855	
1.55935604	0.00778225	2.18782403	0.0170917	1.809784	3.3952696	
1.53115935	0.00404077	2.12594991	0.00885988	1.7699952	3.3994505	
1.50934645	0.00186224	2.07815675	0.00407739	1.7300982	3.4040365	
1.49205061	0.00066113	2.04031034	0.00144578	1.7367569	3.4259138	
1.47809966	0.00010918	2.00981768	0.00023852	1.737776	3.6659937	
1.46677262	0	1.98508414	0	1.8443866	4.0755596	
1.45754347	0	1.96494816	0	2.1565452	4.680853	
1.44982656	0	1.94812345	0	3.07231	5.2367334	
1.44327077	0	1.93383902	0	4.451619	5.129278	
1.43763468	0	1.92156512	0	5.055332	4.0981617	
1.4327417	0	1.91091456	0	5.068048	3.5344853	
1.42845842	0	1.90159506	0	5.088787	3.2508204	
1.42468176	0	1.89338093	0	5.1725454	3.0655696	
1.42133058	0	1.88609467	0	5.2874928	2.9364038	
1.41834013	0	1.87959467	0	5.4788957	2.8840601	
1.41565799	0	1.87376643	0	6.0025477	2.8804665	
1.41324135	0	1.8685164	0	6.8356614	2.066696	
1.41105481	0	1.86376735	0	6.54083	0.8987011	
1.40906892	0	1.85945497	0	5.9692945	0.47322795	
1.40725893	0	1.85552533	0	5.5856557	0.3075308	
1.40560393	0	1.85193279	0	5.302205	0.22232093	
1.40408611	0	1.84863857	0	5.088955	0.17220172	

CLICK here to RUN TAUC-LORENTZ

lamba (A)	PSI	DELTA
2000	95.515865	24.9461776
2100	98.4733846	29.3334745
2200	63.5375034	40.9055286
2300	134.926544	30.7858039
2400	127.208599	32.4414756
2500	93.9275163	50.5427581
2600	72.5697511	45.9597056
2700	93.9149181	38.3751513
2800	145.979446	34.3681044
2900	152.159674	32.0479136
3000	107.182851	33.2104173
3100	84.3527432	38.908862
3200	79.2641281	56.707631
3300	67.0717334	73.4191855
3400	70.6769406	46.0033573
3500	77.3040583	37.6841279
3600	91.7905822	33.8580378
3700	114.546349	30.2294856
3800	141.307008	25.3488307
3900	169.222152	21.6526198
4000	162.167346	20.2067833
4100	136.310959	20.6696304
4200	115.474371	22.3665946
4300	99.4877112	24.6714829
4400	87.303591	27.2976116
4500	77.8051783	30.2622573

Figure 4.17 Interface for running simulation of a wafer covered with Tauc-Lorentz film and roughness. On second first line the 5 parameters of the Tauc-Lorentz function and the thicknesses of the roughness and the film are input. On the right appear the resulting values PSI and DELTA of the simulation with the input values for Tauc-Lorentz function.

A	Eg	B0 ou E0	C ou Br	Ep	Et	Eu	Film thickness (A)	Rough (A)	A_Graded %	Eg_Graded %	E(Ev)	PSI	DELTA
585.00	1.18	3.62	2.11	9.63	0.00	0.50	1853.40	109.40	112.87	178.96	6.20	39.81	74.27
rough layer		Film		Substrate Si			Number of layers				5.90	39.30	75.82
n1	k1	n2	k2	n3	k3		11.00				5.64	38.68	77.44
1.30	-0.25	1.14	-1.86	1.85	3.39		Current layer				5.39	37.96	79.03
1.32	-0.24	1.24	-1.95	1.81	3.40		11.00				5.17	37.12	80.47
1.34	-0.23	1.35	-2.05	1.77	3.40						4.96	35.77	81.65
1.37	-0.22	1.47	-2.14	1.73	3.40						4.77	34.34	84.17
1.40	-0.21	1.60	-2.22	1.74	3.43						4.59	33.06	87.03
1.43	-0.16	1.75	-2.30	1.74	3.67						4.43	31.83	90.04
1.42	-0.12	1.91	-2.36	1.84	4.08						4.28	30.67	92.99
1.41	-0.09	2.08	-2.41	2.16	4.68						4.13	29.52	95.92
1.39	-0.07	2.26	-2.45	3.07	5.24						4.00	28.36	98.79
1.38	-0.05	2.45	-2.46	4.45	5.13						3.88	27.26	101.41
1.37	-0.04	2.65	-2.44	5.06	4.10						3.76	26.10	104.01
1.36	-0.04	2.85	-2.39	5.07	3.53						3.65	24.97	106.43
1.35	-0.03	3.03	-2.33	5.09	3.25						3.54	23.86	108.63
1.35	-0.02	3.21	-2.23	5.17	3.07						3.44	22.81	110.61
1.34	-0.02	3.36	-2.10	5.29	2.94						3.35	21.75	112.47
1.33	-0.02	3.48	-1.97	5.48	2.88						3.26	20.76	114.11
1.33	-0.02	3.58	-1.83	6.00	2.88						3.18	19.84	115.52

CLICK here to RUN CODY-LORENTZ

Figure 4. 18 Interface for running simulation of a wafer covered with Cody-Lorentz film and roughness. On second first line the 7 parameters of the Cody-Lorentz function and the thicknesses of the roughness and the film are input. On the right appear the resulting values PSI and DELTA of the simulation with the input values for Cody-Lorentz function.

4.6 Measurements

On the following figures, ψ is represented as a function of the wavelength. These curves present some oscillations due to interferences whose origin is the phase factor (equation 4.55 and reference [4.24]). It has to be recalled that two factors have a great influence on the pattern of this oscillation. These factors are the film thickness and the film refractive index. The number of oscillation peaks increases as one or both of these parameters increases. More precisely this number increases with the optical path which is proportional to the film thickness and its refractive index. It has also to be recalled that the amplitude of oscillations decreases in an absorbent material (k>0) in an exponential way with the optical path (or in other word with the real part of the

refractive index and the thickness of the layer). Thus the presence of oscillations in a wavelength interval shows that the film is transparent to wavelengths included in this interval. Conversely the attenuation of the oscillation signals that the material becomes absorbent. This is particularly important for semiconductors or insulators with low gap since they have both a transparent and absorbent region in the wave length range used in UV ellipsometry (200-1000nm). Since the number of peaks mainly depends on real part of the refractive index and film thickness, in a first step, the film is analysed in the transparent region in order to determine the thickness and have a first approximation of the refractive index. For this aim, the fitted curve has only to have the same number of peaks and then a simple Cauchy model is enough although far from describing the real complex refractive index. When thickness is determined, this latter is used as a fixed parameter and the film can be modeled by a Tauc-Lorentz or a Cody-Lorentz layer. As explicit by comparing equations 4.84 and 4.86, the amplitude A_{TL} of Tauc-Lorentz and Cody-Lorentz A_{CL} are related by equation 4.92:

$$\frac{A_{TL}}{A_{CL}} = \frac{1}{(E_n - E_g)^2 + E_p^2} \tag{4.92}$$

Since this A_{TL}/A_{CL} is a function of E_n, there is no trivial way for converting a Tauc-Lorentz function to a Cody-Lorentz function.

4.6.1 Ellipsometry measurement of SiN_x films

The first line of table 4.1 contains the values of the amplitude A, the Tauc-gap E_g, the resonance energy E_0 the broadness C and ε_∞ corresponding to Si_3N_4 when this material is parameterized with Tauc-Lorentz. These values are extracted from the model used in CompleteEase software. On several lines the same sample appears with different fitting values. Indeed the method used for fitting the sample was in a first approach a simultaneous fitting of the 4 parameters after having determined the thickness of the film. However during the fitting of the samples it appeared that the films which correspond to the lowest MSE have values closer to the values of Si_3N_4. Furthermore, the SiN_x samples with the lowest SRV also correspond to Tauc-Lorentz values close to Si_3N_4 in agreement with literature (cf. chapter 5). Therefore in a second time the values were fitted by keeping the Si_3N_4 values for E_g, E_0 and ε_{inf} and when it was possible for the broadness C. In the particular case of sample 16 and 16B, the value of A was so

close to Si_3N_4 that the fitting has been done with all the values of Si_3N_4 and indeed the fit has been improved. These two films have been deposited with MW PECVD with the same conditions. Another remarkable point is the fact that almost all the samples have a value for this amplitude A between 80 and 90. We can thus guess that these films have a similar structure. Figure 4.19 shows the linear relation between the refractive index and the amplitude A when all the other parameters of Tauc-Lorentz function have the values of Si_3N_4 figuring in the first line of table 4.1. The Tauc-Lorentz function of Si_3N_4 can be found in reference [4.25]

SAMPLE	A	Eg	E0	C	ε_∞	Roughness (A)	Film thickness (A)	MSE
Si3N4	131.636	4.814	8.334	2.787	1.658	X	X	X
16	129.802	4.814	8.334	2.787	1.658	51.9	115.2	1.721
16	131.636	4.814	8.334	2.787	1.658	53.6	114.5	1.717
19	80.405	4.814	8.334	2.787	1.658	10.5	137.5	0.967
20	86.383	4.814	8.334	2.787	1.658	54.9	435.4	5.962
21	82.858	4.814	8.334	2.787	1.658	36.4	1018.4	4.245
22	81.494	4.814	8.334	2.787	1.658	47.3	1575.8	13.189
23	89.871	4.814	8.334	2.787	1.658	30.3	886.3	2.128
23	89.771	4.814	8.334	2.787	1.658	27.6	886.4	3.877
44	70.669	4.814	8.334	0.695	1.658	39.4	2776.5	14.171
44	82.974	4.814	8.334	2.787	1.658	39.9	2772.2	16.762
45	83.364	4.814	8.334	0.041	1.658	31.2	995.6	2.263
45	102.265	4.814	8.334	2.787	1.658	48.2	996.8	4.048
46	76.263	4.814	8.334	0.715	1.658	33	2421.7	7.532
46	89.355	4.814	8.334	2.787	1.658	19.6	2419.5	13.526
16 B	123.855	4.814	8.334	2.787	1.658	30.9	45.9	1.174
16 B	131.636	4.814	8.334	2.787	1.658	33.7	44.5	1.153

Table 4.1 Results of ellipsometry fitting for SiN_xfilms.

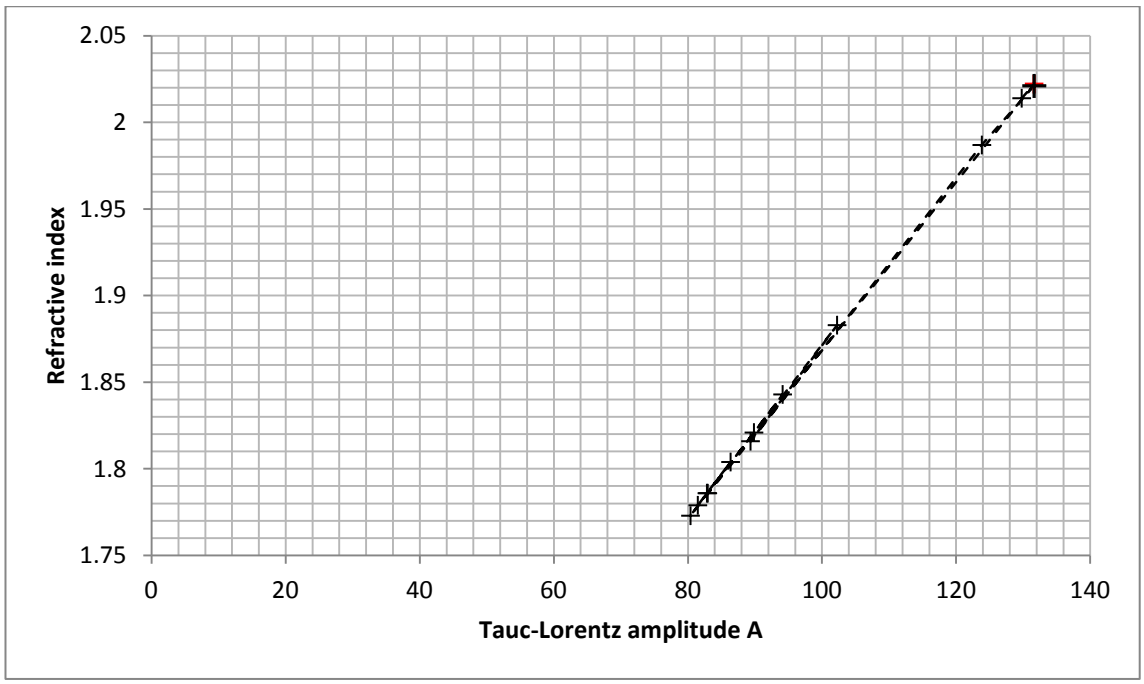

Figure 4.19 Refractive index versus amplitude A at fixed values for other Tauc-Lorentz parameters. For a given set of the 4 parameters, the refractive index is proportional to the amplitude A. This curve is used for the comparison between SiN_x films and Si_3N_4. All the parameters are set to the value of Si_3N_4 except the amplitude A.

Figures 4.20-4.22 represent the results of the fitting of ψ and Δ for respectively samples 44 to 46. Figure 4.23 represents the absorption coefficient k and the refractive index n_f of these samples. Higher refractive indices values were expected as explained in chapter 5. The refractive index of a SiN_x films decreases when x content increases from 0 to 1.33 from 3.4 to about 1.9 for Si_3N_4. The refractive index can further decrease when Si-N bond are replaced by N-N or N-H bonds but these low values can also be due to porosity. The porosity is confirmed by the results of XPS presented in the next section.

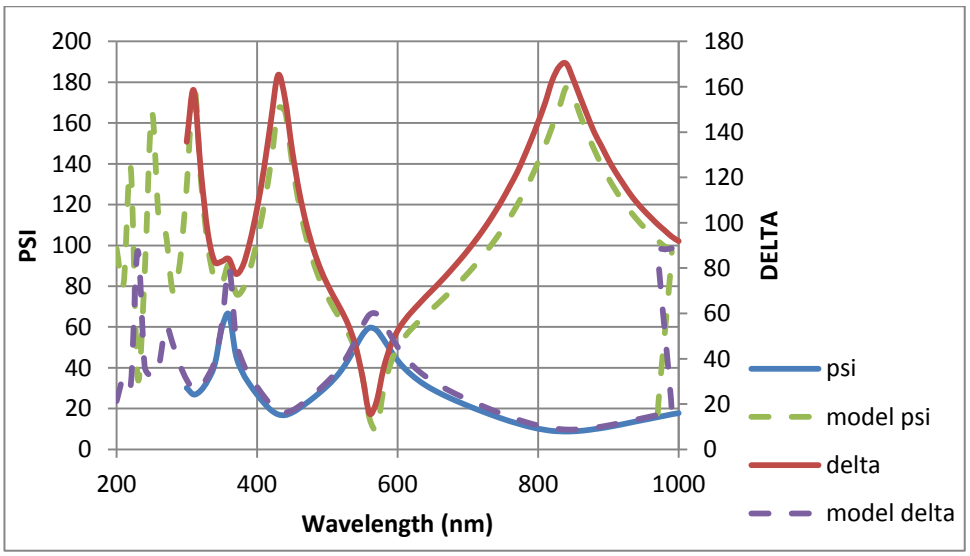

Figure 4.20 PSI and DELTA versus wavelength (sample 44). The dash curves correspond to the values from simulation and the plain curve to the experimental values. It has to be recalled that PSI and DELTA values measured the change of polarization after light reflection by the sample.PSI and DELTA include the whole multilayer system. The fitting between the theoretical curve of PSI and DELTA and the experimental values of PSI and DELTA is done by adjusting the parameters of the dielectric film function, the film thickness and the thickness of the roughness. When these parameters correspond to the film, theoretical and experimental values of PSI and DELTA are equal.

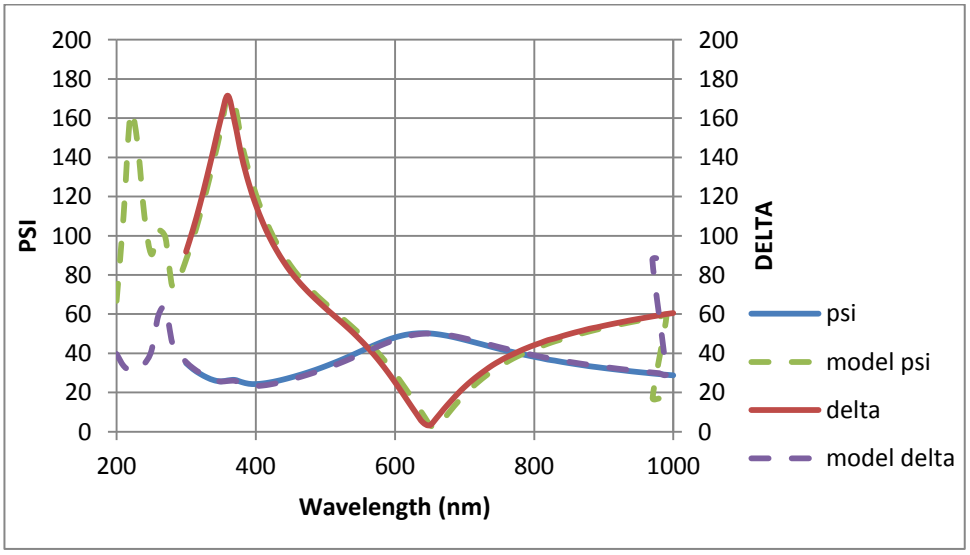

Figure 4.21 PSI and DELTA versus wavelength (sample 45). The dash curves correspond to the values from simulation and the plain curve to the experimental values (cf. figure 4.20 for explanations)

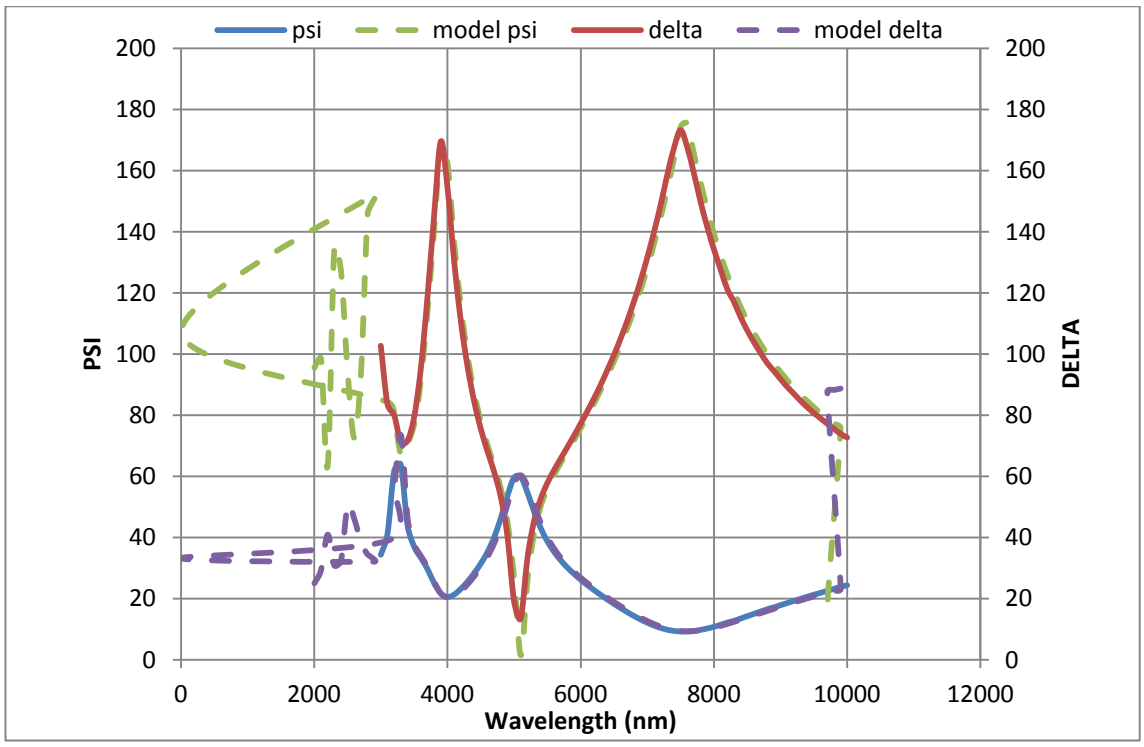

Figure 4.22 PSI and DELTA versus wavelength (sample 46). The dash curves correspond to the values from simulation and the plain curve to the experimental values (cf. figure 4.20 for explanations)

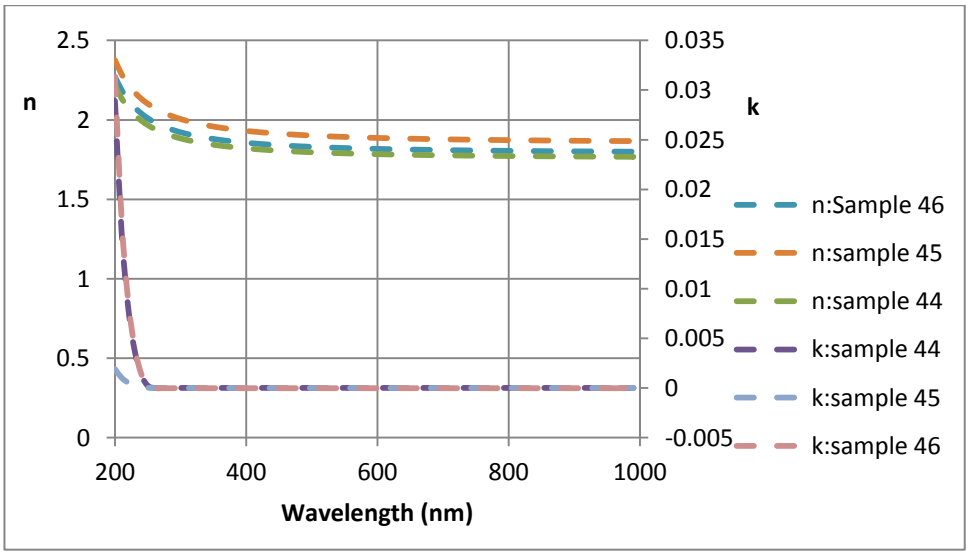

Figure 4.23 Real and imaginary parts of the complex refractive index versus wavelength. The values of n and k are deduced with equations 4.61-63 from the complex dielectric function ε that of the film that correspond to the fit of PSI and DELTA on figures 4.20-22.

4.6.2 Ellipsometry measurement of a-Si: H films

The a-Si: H films are more difficult to model than SiN_x films. For these latter as seen in previous section we have started from the Tauc-Lorentz function of Si_3N_4 and then we have adjusted the four parameters of the function. The usual dielectric function for a-Si: H in CompleteEase software is a Cody-Lorentz model with 7 parameters. Furthermore, due to a higher temperature drop the film structure changes from the beginning of the deposition to the end. As explained in section 5.3 of chapter 5, the film structure is strongly dependent on temperature around 400°C where hydrogen desorption occurs. In order to include this change of structure, a model of graded layer has been used. For instance sample 23 has been divided in 5 layers with two parameters being linearly graded with a fitted percentage. The two extremes values of A respectively on the top and on the film bottom are related to the parameter by equations 4.90 and 4.91. A similar relation is used for the other parameters. If we call the number of layers N, the first layer being the top layer and the graded parameter P, the value of P at the layer n_L is:

$$P(n_L) = P_{top} - (P_{top} - P_{bottom}) \times \frac{n_L - 1}{N} \tag{4.93}$$

Sample	A	Eg	B0 ou E0	C ou Br	Ep	Et	Eu	Film thickness (A)	Rough (A)
7	221.7	2.181	2.691	14.243	2.111	0.332	0.106	1570.3	14.24
9	55.061	2.389	3.713	5.54	0.305	0.439	0.455	667.5	220.5
43	156.529	2.148	3.441	3.203	1.75	0	0.5	1825.8	61.8

Table 4.2 Results of ellipsometry fitting for SiN_xfilms deposited on c-Si.

Sample	A_Graded %	Eg_Graded %	E0 graded %	C graded %	Ep graded %	Et graded %	Eu graded %	nf	MSE
7	149.32	-63.77	-129.6	-75.89	147.08	332.89	1000	3.193	5.284
9	-67.28	-43.65	0	0	0	0	0	3.229	5.455
43	128.22	57.59	0	0	0	0	0	3.685	8.129

Table 4.3 Results of ellipsometry fitting for SiN_xfilms deposited on c-Si (gradation, refractive index and MSE).

Each a-Si:H sample is graded. For samples 9 and 43, only two parameters need to be graded in order to have a correct fit. Sample 7 requires the gradation of the 7 parameters on 5 layers. The fitting result of sample 43 is given in figure 4.24.

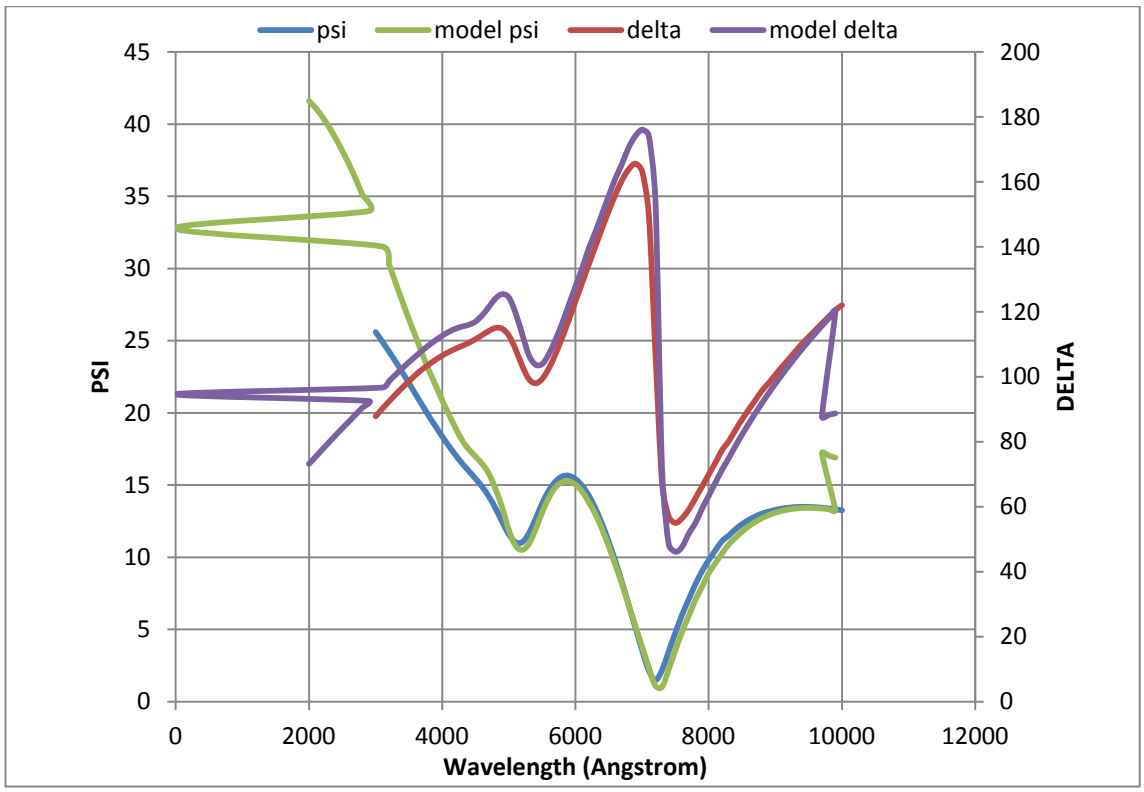

Figure 4.24 PSI and DELTA versus wavelength (sample 43). The dash curves correspond to the values from simulation and the plain curve to the experimental values (cf. figure 4.20 for explanations). a-Si film has been deposited on sample 43 whereas it SiNx films on samples 44-46. Therefore as seen in the text, Cody-Lorentz function is used for simulating the film. In addition, the dielectric function parameters vary with the depth of the film and require a graded layer. For these reason the curve does not fit as it does with SiN_x films.

4.7 Conclusion

SiN_x films present several advantages in regard to characterization by ellipsometry. These films can be modeled by a Tauc-Lorentz dielectric function which requires 4 parameters whereas a-Si:H films have to be modeled by a Cody-Lorentz function which required 7 parameters. Furthermore for most of our SiN_x, all the parameters can be settled to the values of Si_3N_4 and only the amplitude A needs to be fitted. On the other hand for a-Si:H sample, the 7 parameters have different values for each film. Eventually, the a-Si:H film is graded and has to be divided in several layers with different parameters values. However, it has to be noted that even for Tauc-Lorentz function, the parameters are correlated as was seen in section 4.5.1 and a simple look at equation 4.84 enables to understand this correlation. Thus similar values of the Tauc-Lorentz function can be obtained by changing several parameters and indeed the bandgap increases with x in SiN_x while the refractive index decreases. Thus although

refractive index of the layer is enough accurate, the values of the bandgap E_g, the broadness C and E_0 probably do not correspond to the real values. A more precise investigation for finding the correct values of the Tauc-Lorentz parameters will enable us to determine more precisely the film composition. It is reported for instance that the bandgap increases with the hydrogen content when N-H increases [4.4]. The broadness C is probably related to the disorder in the SiN_x film. By disorder we mean that the film is a randomized combination of the 5 bonding possibilities between a Si atom and its first neighbors as shown by Kärcher [4.26]. A study of Sancho-Parramon has established an expression of the dielectric function ε_2 (ω) for SiN_x films where there is a connection between the resonance energy and the absorption of the different bonds in the infrared region [4.27]. We have not found a similar study in the UV range but it would be interesting to know this connection. However it is interesting to note that for most of our films the amplitude A is around 80 when the other parameters are settled to Si_3N_4 values. Eventually 2 samples: samples 16 and 16B can be accurately fitted with amplitude corresponding to the value of Si_3N_4. Therefore these films should be very close to Si_3N_4. of Vetter [1.6] and Jan Schmidt [1.11] who have established a relation with the N content of SiN_x film, the refractive index at 630.2 nm and the bandgap energy, showing that the highest quality passivating films approach to Si_3N_4 structure.
The rigorous determination of dielectric function parameters would require using other measurement techniques like absorption measurement for bandgap determination. However since we already know that the optimal structure is Si_3N_4, we have chosen a simple method for comparing the dielectric function of the deposited film with the Si_3N_4 dielectric function. This method consist of setting all the dielectric function parameters with the Si_3N_4 except for the amplitude A which is thus the only parameter to fit. For Si_3N_4, A is 131.636. Therefore we can deduce that closer A is from 131.636 closer is the film structure from Si_3N_4.

4.8 X-ray photoelectron spectroscopy (XPS)

4.8.1 System

XPS is based on the photoemission after irradiation of a material by a monochromatic x-ray source. Consequently to the x-ray absorption by electron, these latter are ejected from the atoms with a kinetic energy equal to the difference between the x-ray energy and electron bonding energy. Kinetic energy is measured by the analyser and bonding

energy which is like a finger print of an element is calculated by subtracting the x-ray photon energy:

$$E_B = h\nu - E_K \quad (4.94)$$

It has to be noted that only the electronic bonds with energy lower than the x-ray are broken. Furthermore, energy bonding of a given element is slightly shifted when the element is surrounding by a different element which allow determining the molecule from which participated this atom. Since electron's kinetic energy is lost in an exponential way when traveling inside the matter, only the electrons at the surface of the material are collected by the analyser. It can be shown than 98% of the electrons contributing to the signal are extracted in a depth d below the escape depth $3.\lambda_{mfp}.\sin\theta$ where θ is the incident angle and λ_{mfp} the mean free path of electron. This mean free path varies linearly with the kinetic energy of the electrons. The 2% remaining are electrons with very low bonding energy reaching the analyser after losing kinetic energy. Therefore the bonding energy of these latter cannot be determined and they are the reason for the background of the XPS spectra. The electrons extracted from deeper depth are stopped before reaching the analyser. The XPS spectrometer used was an ESCA300 using a K_α Al x-ray of 1486, 6eV and FWHM (Full Width at Half Maximum) equal to 0.26eV. Since bonding energy of Si 2p is about 100 eV and bonding energy of N1s is around 400 eV, the kinetic energy of an electron extracted from Si 2p is roughly1.5 keV and from N1s, 1 keV. Thus, the mean free path [4.28] of electrons in Si is roughly 2 nm for electrons extracted from N1s and 3nm for electrons extracted from Si2p. Therefore the maximum escape depth (for θ=90°) is between 6 and 9 nm.

4.8.2 Electronegativity

It is known that the chemical elements react in a way to complete their external electron shell that is the one where the distance to the positive nucleus is the highest. The periodical table of chemical elements is organised in a way to highlight the filling level of their last layer. In the last column on the right are registered the elements with complete external shells. The first column on the left after this last right column contains element with only one electron missing for completing their last shell, then are registered the element with 2 electrons missing etc… Since they have their external

layer completed, the elements of the last right column do not react, and thus remain mono-atomic, they are known as inert gases. On the other hand the chemical elements on the first column at the left of inert gases have a strong tendency to attract an electron, this tendency decreases for elements on the left of the table because it then require more energy until the elements of column 14 where the number of electron in the external shell is equal to the number of missing electrons. These latter are the less reactive elements. When moving further toward the left, the missing electron number becomes higher than present electrons and then energy required to remove the last layer is lower than energy required completing it, thus elements in this case have tendency to give electron. Regarding the lines disposition, atomic number increases when moving toward the bottom of the table. When the number of electron increases, the distance of the electrons of external layer to the nucleus increases and consequently bonding energy decreases, furthermore, the high number of electrons on the lower layers act as a screen between the far electron and the nucleus of the element which enhanced the bonding energy decreasing and therefore the facility to give electron for elements of the left column and reversely the difficulty for the element on the right to attract electrons. This property of attracting electron is known as electronegativity and has been determined by Linus Pauling who established an electronegativity scale from 0 to 4. The most electronegative being F (4), and the less electronegative the Fr (0.7). The tendency to react for two elements increases with the difference of their electronegativity.

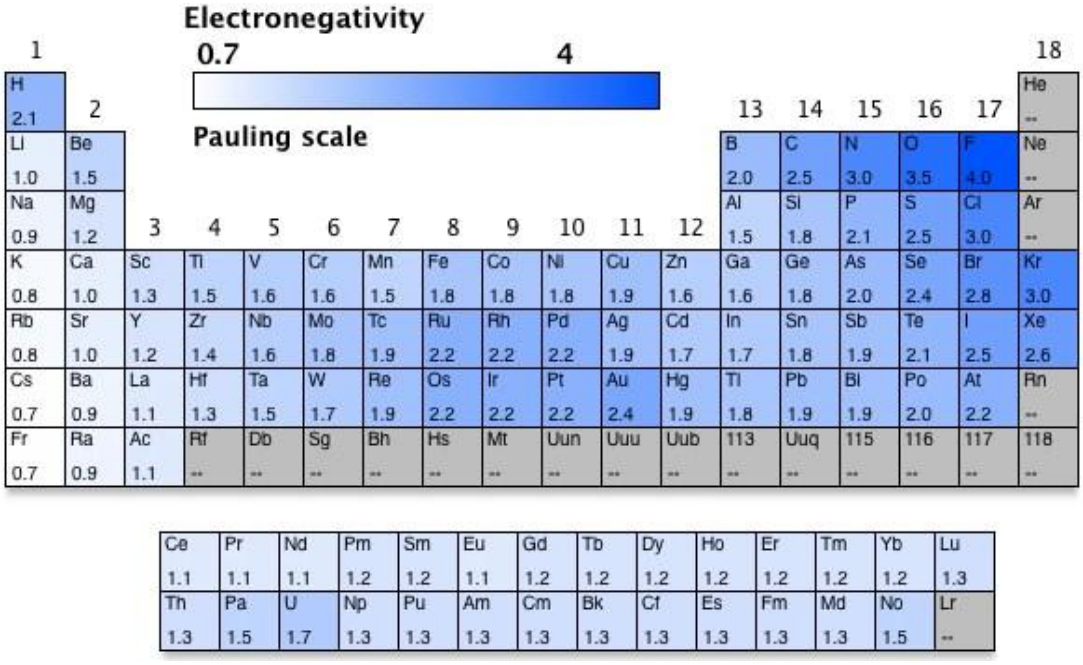

Figure 4.25 Periodic table of the chemical elements with their electronegativity. Electronegativity is a way for understanding the strength of a bond between atoms.

4.8.3 SiN_x films

For XPS measurement of SiN_x film we focus on silicon, oxygen and nitrogen electronegativity. For instance when silicon atom is bonded with nitrogen atom to form a Si-N bond, N atom which is more electronegative attracts the 2 electrons of the covalent bonding and thus the negative charge transfer from Si toward the N atom leaves locally a positive charge in the Si atom and therefore the electrostatic strength which link the electrons of this Si atom increases. It results from this phenomenon a shift of the core level toward higher energy. The number of electrons missing in the external shell determines the number of bonded electrons for a given atom. Electronic configuration of Si and N are:

$$Si: \quad 1s^2 2s^2 2p^6 3s^2 3p^2 \tag{4.95}$$

$$N: \quad 1s^2 2s^2 2p^3 \tag{4.96}$$

Therefore 4 and 3 electrons are required to complete the external layer of respectively Si and N. In the case of solid composed with Si and N atoms, the 4 missing electrons in Si external layers give rise to 4 covalent bonds whereas the 3 missing electrons of N give 3 bonds. Since covalent bonds are very strong, only the core electrons which are 1s, 2s and 2p for Si and 1s for N appear in the XPS spectra. The 5 possible configurations [4.29] for SiN_x solids are the ones represented on figure 4.26. Since electron core binding energy is shifted in the same way for every Si-N bond, the energy shift is directly proportional to the number N of atoms bonded with Si. SiN_x films deposited by PECVD do not only fulfil stoichiometry but also contain several different compositions for a same deposition condition [4.26, 4.30]. Therefore, Si peak on XPS spectra is a combination of these 5 configurations or in other words a sum of five peaks being further spaced by an equal shift as nitrogen atom number increases. The last peak corresponds to the stoichiometry Si_3N_4 and is around 397.4 eV [4.31]. However, a strong implicit assumption is that only the atoms on first vicinity of Si are involved but it is not always the case. Although we do not manage to deconvolute the N_{1s} peak and thus we cannot determine the different configurations contributions, this disorder in the film was useful to mention in order to understand the origin of the broadness C of the

dielectric function. On the other hand it has to be noted that the peak broadness is also a second order effect involving more than the atoms in the first vicinity.

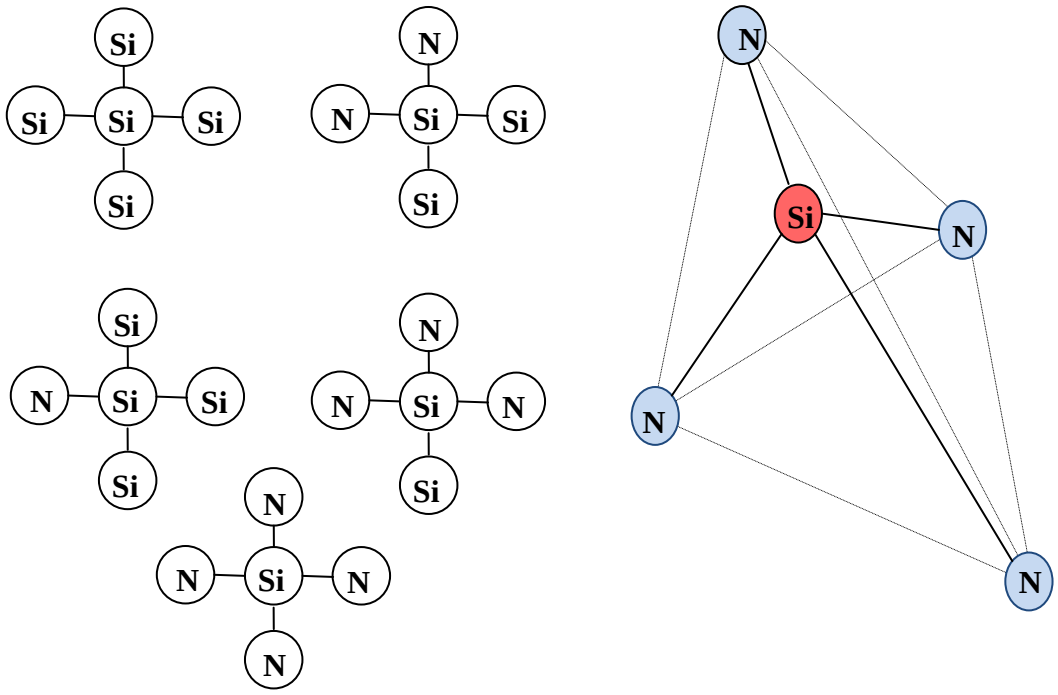

Figure 4.26 Configuration of Si bonds. The figure on the right represents a Si_3N_4 molecule. On the left every possible configuration are represented in SiN_x film.

- **Connection between refractive index and N to Si ratio**

Equation 4.32 gives the relation between the refractive index of SiN_x film and Si to N ratio [4.32]. A slightly different relation is given in references [4.29, 4.33] with a general connection between a-Si: H alloy and bond density.

$$n_f = 1.35 + 0.74\frac{[Si]}{[N]} \tag{4.97}$$

Sample N°	13	14	16	16B	17	18	19	20	21	22	23	24	25	26
[N]/[Si]	0.08	0.69	0.63	0.72	0.65	0.33	0.65	0.54	0.64	0.49	0.63	0.57	0.68	0.73
nf	X	2.42	2.52	2.38	2.49	3.63	2.48	2.71	2.50	2.87	2.53	2.65	2.44	2.37

Table 4.4 N to Si ratio and corresponding refractive index n_f for SiN_x film deposited on c-Si.

Since SiN_x is delimited in two regions: Si-rich from x=0 to 1.1 and N-rich for x>1.1, the analysed samples are all located in Si-rich region. However the refractive indices are much higher than the values which have been determined by ellipsometry.

4.9 Conclusion: Correlation between XPS and ellipsometry results

The low values of the refractive index determined by ellipsometry suggest the presence of porosity in the material. The connection between effective refractive index n_{eff} of a film with porosity fraction x_p and the refractive index n_f of the material without porosity is given by:

$$n_{f\,eff} = (1 - x_p)n_f + x_p \quad (4.98) \qquad (4.98)$$

In order to determine the porosity x_p we use equation (4.98) with n_{feff} and n_f corresponding respectively to the refractive index determine by XPS $n_{f\ XPS}$ and by ellipsometry. The results are presented on table 4.5. However, a so high porosity would result in very low passivation quality which is not the case since the measured SRV correspond to a quite good passivation.

	$n_{f\,xps}$	n_f ellipsometry	Porosity	SRV
16	2.52	2.022	0.33	280
16 B	2.38	2.021	0.26	x
19	2.48	1.773	0.48	373
20	2.71	1.804	0.53	406
21	2.5	1.786	0.48	354
22	2.87	1.779	0.58	202
23	2.53	1.821	0.46	94
26	2.37	1.843	0.38	86

Table 4.5 Estimation of porosity in SiN_x films deposited on c-Si.

Another way to estimate porosity in agreement with SRV results will be presented in chapter 6. The most important contribution of this chapter is the deduction of a simple method for comparing film structure with Si_3N_4 which correspond to the optimal film. This method consists of fitting only the amplitude A of the dielectric function. Since there is only one parameter to fit, the fit can be done for instance by dichotomy.

It has been seen at the beginning of this chapter that ellipsometry and XPS are used for the characterisation of the film structure and composition in order to allow a connection between PECVD conditions and passivating film quality. The optimisation of PECVD conditions will be presented on chapter 5.

BIBLIOGRAPHY CHAPTER 4

[4.1] H. Fujiwara, Spectroscopic Ellipsometry Principles and Applications, Edition Willey (2007)

[4.2] Handbook of Ellipsometry, Edited by H. G. Tompkins and E.A. Irene ,Edition Springer(2005)

[4.3] F.L. McCrackin *et al.*, Measurement of the thickness and refractive index of very thin films and the optical properties of surfaces by ellipsometry, J.Research of the National Bureau of Standards-A Phys. and Chem. 67A(4) ,363-377 (1963)

[4.4] D.W. Johnson, A Fourier series method for numerical Kramers-Kronig analysis, J. Phys. A: Math. Gen., 8(4) 490-495(1975)

[4.5] S.Jung *et al.*, The effects of the band gap and defects in silicon nitride on the carrier lifetime and the transmittance in c-Si solar cells , Solar Energy Materials & Solar Cells 95 (2), 546-550 (2011)

[4.5] R. Kärcher *et al.*, Electronic structure of hydrogenated and unhydrogenated amorphous SiN_x ($0 \leq x \leq 1.6$): A photoemission study, Phys. Rev. B 30(4), 1896-1910

[4.6] K. E.Oughstun , Velocity of energy transport for a time-harmonic field in a multiple-resonance Lorentz medium, J. Opt. Soc. Am. B 5(11), 2395-2398 (1988)

[4.7] R. Swanepoel, Determination of the thickness and optical constants of amorphous silicon, J. Phys. E: Sci Instrum. 16, 1214-1222 (1983)

[4.8] Y.M. Li, Thin-film coalescence in hydrogenated amorphous silicon probed by spectroscopic ellipsometry with millisecond-scale resolution, Phys. Rev. Letter 68(18), 2814-2817 (1992)

[4.9] S. Kageyama *et al.*, Dielectric function of *a*-Si: H based on local network structures, PHYSICAL REVIEW B 83, 195205-1-11 (2011)

[4.10] G.E. Jellison, Spectroscopic ellipsometry characterization of thin-film silicon nitride, Thin Solid Films 313-314, 193-197 (1998)

[4.11] P. Doshi, Characterization and optimization of absorbing plasma-enhanced chemical vapor deposited antireflection coating for silicon photovoltaics, Applied Optics 36, 7827-7837 (1997)

[4.12] G.E. Jellison *et al,* Spectroscopic ellispsometry characterization of thin-film silicon nitrid , Thin Solid Films 313-314, 193-197 (1998)

[4.13] Ferlauto et al, Analytical model for the optical functions of amorphous semiconductorsfrom the near-infrared to ultraviolet: Applications in thin film photovoltaics,J. Appl. Phys. 92,(5) (2002)

[4.14] G.E. Jellison *et al.*, Parameterization of the optical functions of amorphous materials in the interband region, Appl. Phys. Lett. 69, 371-

[4.15] J. Sancho-Parramon, *et al*., Optical characterization of HfO2 by spectroscopic ellipsometry: Dispersion models and direct data inversion, Thin Solid Films 516(22) , 7990-7995 (2008)

[4.16] M.Foldyna, Model dielectric function of amorphous materials including Urbach tail, Proceedings of SPIE 5445(1), 301-305 (2004)

[4.17] T.Datta *at al.*, Generalized model for the optical absorption edge in a-Si:H, Phys. Rev. B 39 (3), 1953-1954 (1989)

[4.18] M.Li *et al.*, An Ellipsometry Investigation of Nucleation and Growth of Electron Cyclotron Resonance Plasma Deposited Silicon Films, Presented at 39th AVS(1992)

[4.19] J. K. Saha *et al* ,Spectroscopic ellipsometry studies on hydrogenated amorphous silicon thin films deposited using DC saddle field plasma enhanced chemical vapor deposition system, Thin Solid Films 519 ,2863–2866(2011)

[4.20] K. Levenberg, A method for the solution of certain problems in least squares, Quart. Appl. Math., 1944, Vol. 2, pp. 164–168.

[4.21] D. Marquardt, An algorithm for least-squares estimation of nonlinear parameters,SIAM J. Appl. Math., 1963, Vol. 11, pp. 431–441.

[4.22] M. Serenyi *et al.*, Comparative analysis of amorphous silicon and silicon nitride multilayer, Thin Solid Films 515 ,3559–3562(2007)

[4.23] M.Green *et al.*, Optical properties of intrinsic silicon at 300 K , Progress in Photovoltaics, p.189-92, vol.3, no.3; (1995)

[4.24] Poruba *et al.*, Optical absorption and light scattering in microcrystalline silicon thin films and solar cells, J. Appl. Phys. 88(1), 148-160 (2000)

[4.25] Silicon Nitride: PALIK Vol. 1, p.774 fit to Tauc Lorentz (6.0eV to 1.0eV)

[4.26] J. Sancho-Parramon *et al.*,Optical characterization of ns-SiN:H in the infrared by spectroscopic ellipsometry, Applied Surface Science 253, 65–69(2006)

[4.27] G. T. Orosz *et al.*, Inelastic Mean Free Path Data for Si Corrected for Surface Excitation, Microsc. Microanal. 11, 581–585 (2005)

[4.28] I. Bertoti *et al.* , Characterization of nitride coatings by XPS, Surface and Coatings Technology, 194–203(2002)

[4.29] J.M. Lackneret al., Influences of the nitrogen content on the morphological, chemical and optical properties of pulsed laser deposited silicon nitride thin films, Surface & Coatings Technology 192 ,225– 230(2005)

[4.30] M.C.Poon *et al.*, Bonding structures of silicon oxynitride prepared by oxidation of Si-rich silicon nitride, Thin Solid Films 462– 463 ,42– 45 (2004)

[4.31] M.Blech *et al.*,Detailed study of PECVD silicon notride and correlation of various characterization techniques, 24^{th} PVSEC, 507-511 (2009)

[4.32] J. J. Mei *et al.*,Optical properties and local bonding configurations of hydrogenated amorphous silicon nitride thin films, J. Appl. Phys. 100, 073516-1-9 (2006)

[4.33] E. Dehan, Optical and structural properties of SiO_x, and SiN_x, materials, Thin Solid Films 266, 14-19 (1995)

Chapter 5

<a-Si:H and SiN_x film deposition by PECVD for passivation>

5.1 Generalities

Before entering in passivating film deposition process by PECVD it worth recalling that the aim of this work is to improve passivation of rear surface in order to reduce the wafer thickness with limiting electric charge carrier loss. In order to passivated the rear surface, intrinsic a-Si:H and SiN_x films have been deposited by PECVD. This chapter is a presentation of PECVD process which aims to understand how to optimize the conditions of deposition for approaching the structure corresponding to high passivating film.

5.1.1 Steps of Chemical Vapor Deposition (CVD) process

CVD process can be described [5.1] in five steps (figure 5.1). The first and second steps are gas processes whereas the three last steps are surface processes:

a) Gas mixture composed of reactant gas and inert diluted gases (for instance Argon) is introduced into the reaction chamber where stands the substrate to be covered. The different gas species react giving rise to the formation of growth precursors and byproducts.

b) Gas species move to the substrate growth surface.

c) Reactant are absorbed onto the surface

d) Atoms diffuse and film precursors are incorporated to form the growing film. This step is very important in regard with film quality since it determines to a large extent the coverage uniformity of the film. An improvement of diffusion (or migration possibility) results a better uniformity of the film and a better conformability to the sample topography as illustrated on figure 5.2 and as will be seen in section5.3.

e) Reaction byproducts are desorbed from surface and removed from the reaction chamber.

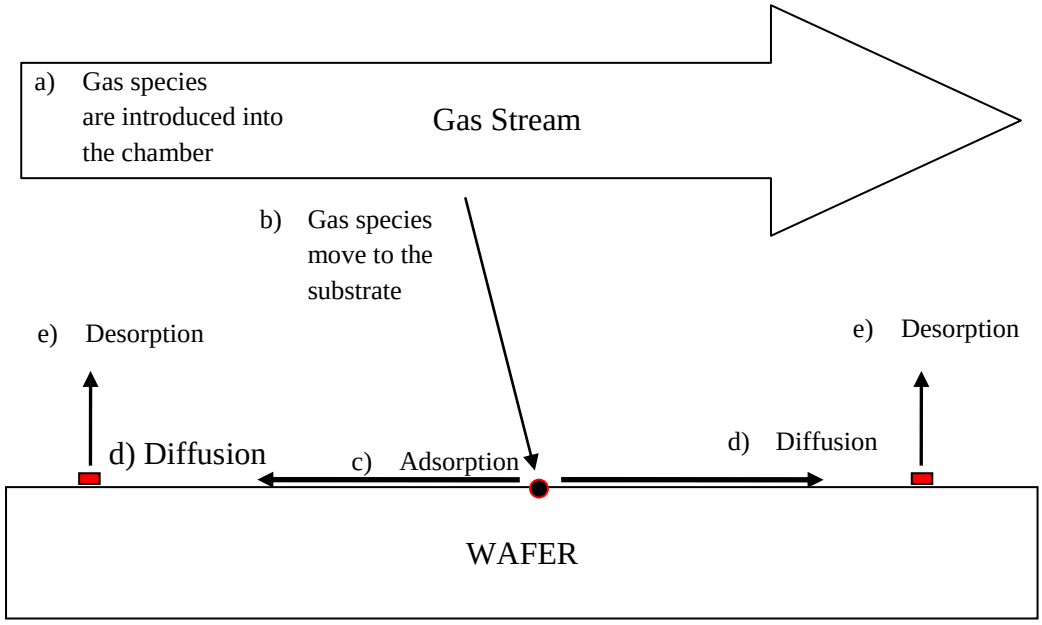

Figure 5.1 Steps of CVD process. For plasma enhanced CVD (PECVD) , the gas species molecules are dissociated by a RF or MW electromagnetic field whereas for CVD the gas molecules are dissociated by the high temperature. Cf. text for the description of the CVD and its phases (dissociation, transfer, adsorption, diffusion and desorption)

The energy which is required to drive reaction is supplied by several methods which are thermal method (i.e. heat), photons excitation and electrons hit. This latter is the PEVCD (plasma enhanced chemical vapor deposition) that has been used in this study for passivating silicon wafer.

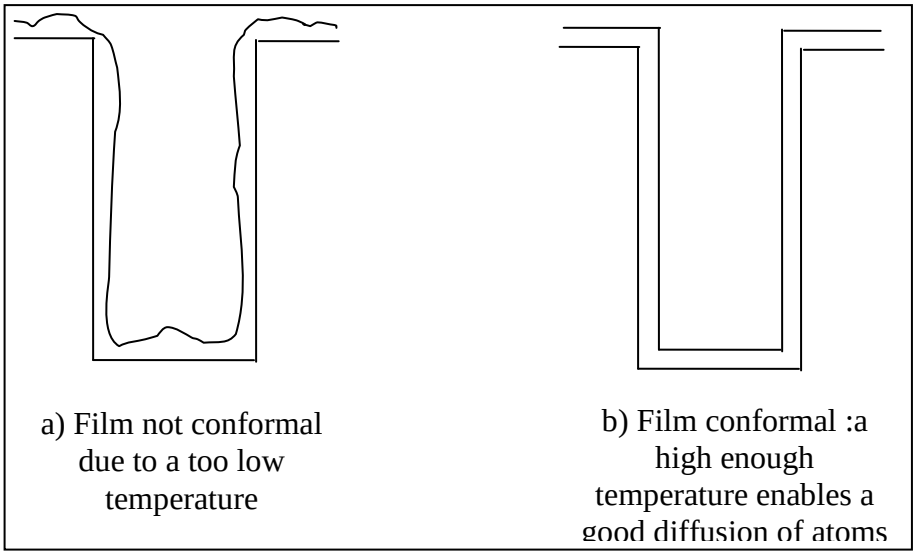

Figure 5.2 Conformability of film. A film is said conformal when its thickness is uniform. High diffusion and thus high temperature is required for having a uniform thickness.

For having a good conformability of the deposited film that is a uniform film thickness, diffusion coefficient has to be high enough to allow the species involved in the film growth, to move and stick to dangling bonds. If the sticking coefficient is too high, the species do not have enough time to find favorable sites and the growth rate of the film is high but the resulting film is rough. If the deposition rate is high due to high sticking, temperature has to be increased to have a higher diffusion at the surface and thus a smoother film (cf. section 5.3.).

It has to be noted that the use of plasma in PECVD add some differences in the growth process, among this difference is the fact that the impact energy of particle induces a local increasing of the temperature near the impact at the film-substrate interface and since diffusion increases with temperature, it improves reactant diffusion.

The parameters which have influence on the film growth are the temperature for the diffusion process, the partial pressure of reactant which is proportional to the gas concentration in the reaction chamber but also the crystal orientation. For instance the growth on crystal with orientation <111> is faster than <100> since more Si bonds are available at the Si surface for the former [5.2].

The regime of growth depends on the ratio between the surface reaction k_s and the gas phase coefficient h_g. If the surface reaction is much higher than the gas phase coefficient then the surface reaction rate is much higher than the gas transfer rate and therefore the growth process is limited by this latter as can be seen for instance on the relation linking the growth rate with h_g and k_s [5.3]. On the other hand for $h_g >> k_s$ the process is limited by the surface reaction rate which follows Arrhenius law ($\sim e^{-Ea/k.T}$), T being the substrate temperature and E_a the activation energy [5.1].

5.1.2 General steps of PECVD processes

Plasma is a partially ionised gas (process plasma ionisation is between 10^{-4} and 30% [5.4]), so one has on the one hand the negative charge i.e. the electrons and on the other hand the positive ions. Because of the very high ratio between ion and electron mass, the electron cannot transfer its energy to the plasma and thus keeps the accumulated energy of the plasma. Electrons can then increase their energy and behave like they were moving in a very high temperature ambiance. In other words plasma is in a non equilibrium state. While deposition of amorphous silicon or silicon nitride films requires temperature above 600°C in order to provide activation energy to dissociate

monosilane SiH_4 gas, PECVD deposition allows to deposit even at room temperature due to the very high energy provided by electron impacting on the SiH_4 gas [5.4].
Different gases are conducted at low pressure through separate pipe lines via mass flow controllers to the process chamber where a RF field is applied between 2 electrodes, or a MW field is applied by a distributed antenna. Under the influence of this periodic field, some of the gaseous atoms are separated into electrons and (mostly) positive ions. Electrons which have high mobility follow the alternating field. They acquire enough energy to decompose gas molecules by collision into various species depending on gas and the energy required for dissociation. Resulting species are deposited onto the growing film and are either incorporated or produce further reactions on the film surface.

PECVD can be divided into 4 steps. The first step concerns the interaction between electrons and reactant gas which generates the plasma; plasma dissociation rate and generated species depend mostly on power density and frequency. In a second step, the generated species fall onto the film surface, and positive ions are accelerated by the sheath [5.5] voltage. Frequency and power density effects will be described in section 5.2.2. The rates of collisions resulting in energy loss during this transport depend strongly on pressure. The third step is chemical reaction at the film surface, and the fourth is the incorporation of this species or reemission into the gas. For the same gas mixture this final step is strongly dependent on the fraction of the different components of the mixture. Steps 1 and 2 have an effect on film density, stress and possibly impurity incorporation while steps 3 and 4 influence film chemical composition and structure, for instance film crystallinity (cf.section.5.3.1.). Deposition rate increases with gas dissociation but is also limited by the chemical reactions taking place at the film surface.

5.2 Processes involved in the different steps of PECVD and external parameters

5.2.1 Processes in the gas phase

- **Gas dissociation**

The different species which are generated in the plasma come from the dissociation of the gas molecules and the way in which they interact together. For a-Si:H deposition, a gas mixture composed of SiH_4, H_2 and Ar is introduced in the gas chamber. For SiN_x films, the gas is a mixture of SiH_4 and NH_3. It has to be noted that SiN_x are also often

deposited with N_2 instead of NH_3 but this is not the case in this work. SiH_4 which is involved both for a-Si:H and SiN_x is the source of the Si in the film. When dissociation of monosilane SiH_4 occurs, different radicals are formed due to the impact energy of electrons. These latter provide the required energy to activate the dissociation reaction. Indeed, the reactions which generate these radicals correspond to configurations with more or less energy compared to the fundamental state. Decomposition of silane occurs in the following way:

$$e+SiH_4 \rightarrow H+SiH_3, 2H+SiH_2, 3H+SiH, 4H+Si \qquad Si \quad (5.1)$$

Table 5.1 summarises the threshold energy [5.40] of these radicals appearance:

Precursor	SiH_3	SiH_2	SiH	Si
Threshold (eV)	8.75	9.47	10.33	10.53

Table 5.1. Threshold energy for radical formation during PECVD process [5.40]

Compared to SiH_3, SiH_2 and SiH recombine more easily with SiH_4 giving rise to silanes of greater complexity than SiH_4 e.g. Si_2H_6, resulting in powder formation. Therefore silanes of highest complexity are not incorporated in the growing film **[**5.40]. It follows that it is the precursor SiH_3 which dominates in the formation of films deposited by PEVCD from silane. Nevertheless, other precursors play an indirect role on the properties of these films [5.6, 5.7]

It has to be noted that during the molecules dissociation of the gas mixture positive ions are also generated [5.7]. These ions contribute to the defect generation as will be seen in the next section about the transfer.

- **Chemical reactions**

The reactions which take place in the plasma depend on RF or MW power which provides the main part of energy required for dissociation, frequency which determines plasma density and dissociation rate, and pressure. High pressure increases the remaining time of the generated species in the chamber and thus increases both the probability of interactions and the probability of the neutral species to be deposited before being exhausted by the pump [5.8]. On the other hand the decreasing of the pressure results in an increasing of the electron energy and thus of the probability of gas

dissociation [5.9] which suggest an optimal pressure for having both a long residence time and high electron energy leading to high dissociation rate. These processes will be explained in more details in the case of a-Si:H and SiN_x PECVD in the section 5.3.2.

- **High dissociation rate and silane depletion**

For SiH_4-H_2 gas mixture, after the decomposition of H_2 a recombination reaction takes place between SiH_4 and H:

$$SiH_4 + H \rightarrow H_2 + SiH_3 \qquad (5.2)$$

Dissociation rate of the supply gas increases with applied power. This fact has in particular two important effects: When the silane dissociation is faster than silane supply, the reaction of atomic hydrogen and monosilane recombination cannot occur anymore and the amount of hydrogen due to silane dissociation at the surface can increase beyond the threshold flux giving rise to crystal formation (cf.section 5.3.1) even if the H_2 dilution is low [5.6] .This phenomenon is known as silane depletion which appears at high frequency and power. [5.6]. Before the occurring of silane depletion, the increasing of power leads as expected to a higher silane dissociation rate and thus to a higher deposition rate. However, when silane depletion occurs, the increasing of H amount leads to the etching reaction which slows the deposition rate [5.6].

- **Electrons density**

The ratio between the electron-neutral collision frequency ν_c [5.10-5.12] and the frequency of the applied power f is determinant parameter both for electron density in the plasma and their energy distribution. Indeed when the ratio $f/\nu_c >> 1$, the electron population with high energy is higher than when $f/\nu_c << 1$. The first condition is satisfied with MW PEVCD (2.45 GHz) and the last with RF PEVCD (13.56 MHz). On the other hand, the average energy of electron population in the plasma decreases with frequency. Therefore there is an optimal frequency in the VHF range where the electron density is maximal due to a large population of high electrons density and a high average energy of electrons population. Regarding the frequency that we use in this study (2.45 GHz and 13.56 MHz), plasma density is higher in MW PEVCD (the higher electron energy dominates on the lower average energy) which results in a higher deposition rate. This

point is particularly important regarding the defects generation. Since the damage due to impact energy is the result of sum of the impact of the ions falling onto the film surface with high kinetic energy. Damage can be seen as the product of ion flux density and ion bombardment energy during the deposition of a monolayer. It follows that for a given amount of high energy impacts, the damage is lower if this amount is distributed on many layers. In other words, for the same amount of high energy impacts, damage decreases with deposition rate.

5.2.2 Transfer

For low pressure gases, most of the voltage drops [5.13] across the cathode sheath [5.5] resulting from the periodicity of the applied voltage and the asymmetry between positive ions and electrons. Thus there is high electric field in the sheath and the ions will be strongly accelerated towards the cathode. Therefore, the cathode sheath potential determines the ion bombardment energy.

- **Formation of the sheath**

Most of the RF power is not consumed by the gas dissociation but by ions accelerating by a bias voltage through a sheath around the electrodes. This bias occurs when one electrode is connected to the RF power [5.14, 5.15]. Indeed, if this latter is large enough to let all the necessary current flow during each period, the electrode remains at a constant potential. On the other hand, the current flow is limited at the small connected and insulated electrode. However, there is a current flow in the chamber since electrons are attracted by the positive potential and ions by the negative one. During the half period when the applied potential is positive, electrons from the chamber are attracted toward the upper connected electrode. Since this electrode is insulated via the capacitor, the electrons cannot flow through the external circuit and thus they remain on this electrode adding a negative charge contribution to the applied voltage. Therefore, the potential decreases as the electrons are accumulated on the upper electrode. The higher is the potential of this latter, the higher is the acceleration of the electrons inside the chamber and thus their accumulation number by unit of time. Mathematically, this results in an exponential decrease of the positive potential with a time constant which is lower if the potential is higher [5.16]. During the second half-period when the potential becomes negative, positive ions are attracted toward the upper electrode but due to their much higher inertia, only a few are accumulated which results in a much lower contribution to the potential than the electron contribution. However, since the time

constant of the exponential decreases with the voltage, after several numbers of periods, the electron accumulation becomes equal to the ions accumulation and the periodic signal occurs around a mean value: the negative bias (cf. figure 5.3).

For simplifying the explanation of bias establishment, square periodic signal of intensity V_0 can be considered. If the signal is positive at the first half period, it drops by $2V_0$ in the second half period and increases by $2V_0$ when another cycle begins. When this periodic signal is applied on the upper electrode, electrons in the chamber are accelerated toward this latter. As electrons reach this electrode, the potential of this latter decreases in an exponential way with a time constant as low as the electrode potential is high. Thus, just before the change of polarity, the electrode potential is at a value $V_1<V_0$. After the change of polarity potential drops to the value (V_1-2V_0). Positive ions are attracted but due to their low mobility in regard with the signal period, upper electrode potential is still very close to (V_1-2V_0) at the end of the period. When the second period begins electrode is at V_1 and the process describes for the first period is repeated but due to the fact that $V_1<V_0$, time constant is higher. Potential decreases further during each cycle. After a sufficient number n of cycles, the electron attraction time constant is equal to positive ions attraction time constant and a steady state is established : the potential oscillates between $(V_0 - V_b)$ and $(- V_0 - V_b)$ where $V_b = (V_0 - V_n)$ is the bias voltage and V_n the value potential at the beginning of the next period. The voltage V (t) becomes the sum of the RF voltage and a negative DC voltage (the bias). A similar process occurs for sinusoidal signal and the upper electrode potential is the sum of the applied periodic potential and a negative bias potential V_b., This bias is involved in the positive ions acceleration toward the sample holder [5.5, 5.7, 5.10, 5.11, 5, 17].

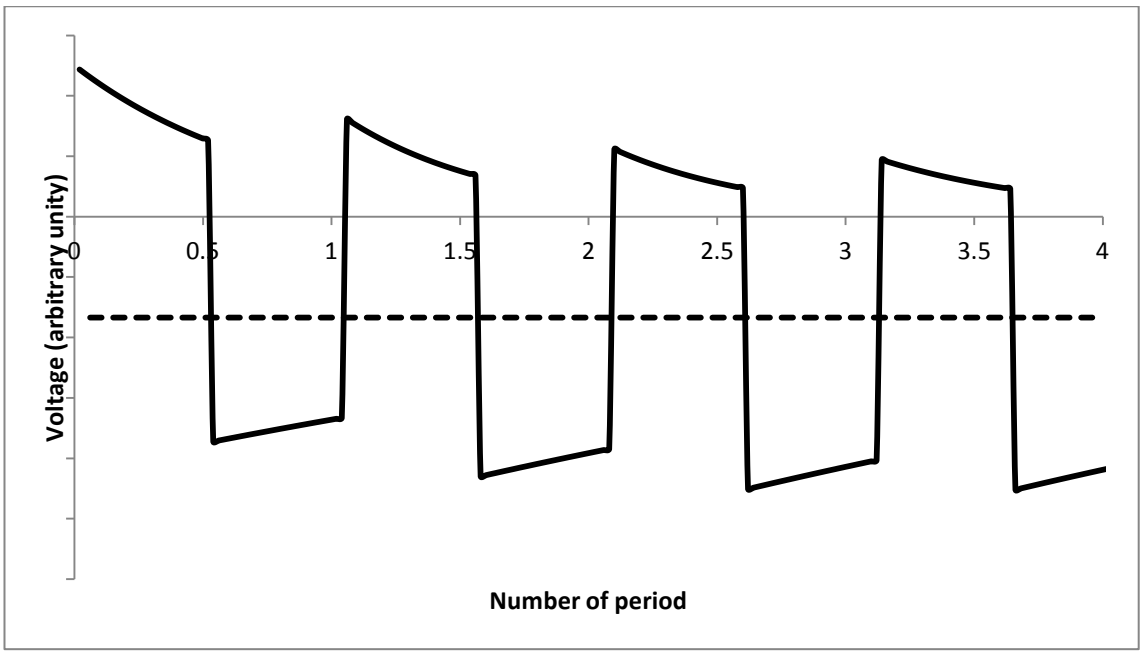

Figure 5.3 Establishment of the negative bias voltage. A bias voltage (in dash) is added to the RF voltage (in plain) after several RF periods. This bias voltage is the results of the difference between positive ion and electron inertia. Since positive ion cannot follow the alternative RF signal whereas electron can, negative bias appears (cf. text). A square signal has been chosen for illustrating this process but the signal is actually sinusoidal.

- **Individual and collective regimes**

While the major part of the potential between the two electrodes falls in the sheath region where positive ions are accelerated, the other part of the power is absorbed by the plasma electrons. Thus most electrons from the gas atoms are accelerated away from their equilibrium positions although still in the vicinity of the atoms and affected by the presence of the positive nucleons due to Coulomb interaction. The resultant motion at the temperatures present for plasma materials processing gives rise to oscillations with a frequency, known as the Langmuir or plasma frequency [1.13] and given by equation 5.3 where m_e is the electron mass , n_e the electron density and e the elementary charge:

$$\omega_p = \sqrt{\frac{n_e e^2}{m_e \varepsilon_0}} \qquad (5.3)$$

Ion acceleration is limited by ion plasma frequency which is given by equation 5.3 except that n_e is replaced by the ion density in the plasma and m_e by the ion mean mass. When the applied frequency is less than or not too high beyond the ion plasma frequency, positive ions accelerated towards the sheath can follow the potential variation V (t) and therefore each ion falls onto the film surface with energy

proportional to V (t). This is the individual regime. Köhler et al. have shown that for individual regime, the maximum energy of ion bombardment onto the grounded electrode is equal to V_{pp} / 4 where V_{pp} is the peak to peak RF voltage [5.14]. When the applied frequency is much higher compared with the plasma frequency, the potential variation is too fast in regard to ion mobility. Therefore ions are only subjected to the average value <V (t)> of V (t) and each of them reaches the film surface with the same impact energy: ions behaviour is collective [5.14, 5.18] The transition between these two regimes is not sharp and in the intermediate range of frequencies, impact energy distribution approaches the mean energy as the frequency is increased, resulting in a reduction of maximum impact energy. Therefore, for a given sheath potential, bombardment that can generate defects in the film is reduced when ion behaviour becomes close to the collective regime [5.19].

Among the other effects related to ion bombardment, it has been shown that surface roughness decreases with ion bombardment. A study has shown that the bombarding of film results in enhancing the film conformability and thus reducing the surface roughness [5.20] and improves the densification of the microstructure [5.21] due to the local enhancement of diffusion near the impact. This effect is strongly correlated with the increasing of intrinsic compressive stress [5.22]. Finally, strong bombardment inhibits the process of crystallite formation [5.23].

5.2.3 Adsorption, incorporation and desorption

The larger fraction of species involved in the film growth is reflected at the film surface and reintegrated in the plasma. A fraction β is adsorbed at the surface. The main interpretation of this phenomenon is given by Matsuda [5.7]: the species with Si- bonds falling onto the film surface are linked with a Si-H bond forming a Si-H-Si weak bond which is easily broken and then the Si- bond links with a Si-H bond in its vicinity, this process continues until the Si- bond of the species find a bare Si- bond at the surface (dangling bond) where it sticks to form a strong Si-Si bond. The sticking coefficient is the probability for sticking occurrence and is directly related to the number of dangling bonds at the film surface. In the model proposed by Matsuda, the dangling bonds in the film are generated by the abstraction of H by SiH_3. At temperature above 400°C, another process, H desorption, which was neglected at lower temperature starts to be dominant. The Si-H bonds in the film are broken due to the thermal agitation and give

rise to the dangling bond generation. Another model is proposed by Keudell et al [5.24] which does not consider the necessity for SiH_3 to abstract H but explains the film growth by insertion of SiH_3 into strained Si-Si bonds at the surface forming a penta-coordinated strained bond:

$$SiH_{3(g)} + Si\text{-}Si_{(s)} \rightarrow Si\text{-}SiH_3\text{-}Si_{(s)} \quad (5.4)$$

Obviously, this is not covalent bond but SiH_3 acts as a donor and the Si- bonds of the film surface as an acceptor [5.25]. However, only the model of Matsuda will be considered in this study. It has to be noted that the fraction β is usually around 0.3 but can increase to 0.5 [5.26] with conditions where SiH_x ($x < 3$) remains in high concentration near the film surface since these precursors are highly reactive with the film surface. This is the case of SiH_2 which becomes the dominant growth precursor when SiH_4 is very highly diluted in H_2 [5.27]. The a-Si:H film quality is then very low.

5.3 a-Si:H and SiN_x growth

The defects density in the a-Si:H films and its alloys is explained by the equilibration of weak Si-Si bonds by hydrogen atoms [5.28-5.31]. In this model the defect density is a function of the substrate temperature and the deposition rate. Substrate temperature determines the diffusion coefficient and deposition rate is determined by the sticking coefficient. Dangling bonds formation is due to the reaction:

$$H + \text{weak Si-Si bond} \rightarrow Si\text{-}H + \text{-}Si \quad (5.5)$$

Weak bonds density also increases with T. On the other hand, higher is T, higher is the H diffusion at the growing film surface and more the weak bonds tend to disappear via the upper reaction leading to strong Si-Si bonds and Si-H bonds. Therefore there is an optimum for T which corresponds to a maximal H diffusion and a minimal weak bond formation. The deposition rate should be slow enough to allow the H diffusion and thus the weak bonds elimination. Since H diffusion increases with T, T has to be increased when deposition rate is higher. Without entering into details, it has also to be mentioned that actually several types of dangling bond exist and some of them do not correspond to the energy defect commonly referred to as dangling bond [5.32].

5.3.1 a-Si:H

As seen in the section 5.2.1, several species are formed during SiH_4 and H_2 dissociation. Species like Si, SiH and SiH_2 are generated from the different dissociation levels of SiH_4 and can have a strong influence on film properties [5.6] but SiH_3 (silyl radical) is the dominant precursor [5.33]. When SiH_3 is adsorbed onto the surface, several possibilities occur: it can abstract a H atom from a Si-H bond to form SiH_4, or two adsorbed SiH_3 can react each other to form Si_2H_6. If the production rate of this latter is too high it is deposited onto the film forming powder on the sample. Indeed the formation of powder occurs when high silane species are produced in the chamber [5.34]. Both species return to the plasma gas. The other possibility is that SiH_3 sticks to –Si dangling bond and thus contribute to the film growth. The probability of SiH_3 from plasma to react with the surface whatever the result of this reaction (adsorption, recombination or sticking) is β. It is observed that for a-Si:H formation, the probability β does not depend on substrate temperature whereas the deposition rate remains constant until about 400°C where it drastically increases [5.7]. Deposition rate is directly related to the sticking of SiH_3. Indeed deposition rate can be seen as a measure of the number of stuck SiH_3. Thus the probability of sticking follows the same evolution as the deposition rate. On the other hand diffusion increases with temperature and thus higher is the temperature, higher the probability for SiH_3 to move to a dangling bond where it sticks.

For µc-Si:H, β is maximum (two times higher than β for a-Si:H at room temperature) and decreases until reaching the value of a-Si:H above 500°C. The deposition rate is two times lower than the a-Si:H. This is explained by the fact that SiH_3 is involved in surface reaction with sites with Si-H bonds and –Si dangling bonds. For high enough H_2 to SiH_4 ratio, excess H atoms from dissociation of H_2 saturate the totality of the dangling bonds. Thus the SiH_3 precursors can only stick on dangling bond issued from H abstraction by other SiH_3. The abstraction probability does not depend on T but only on SiH_3 flux. This can be understood by considering the equation 5.6 [5.35] linking the dangling bond time variation with the SiH_3 concentration at the film surface θ_{SiH3}, N_H and N_S respectively the number density of sites bonded with H and the number density of dangling bonds, C_a the rate constant of H abstraction, C_s and C_H respectively the rate constants of sticking and H desorption.

$$\frac{dN_S}{dt} = C_H(T).(N_H)^2 + C_a(T).N_H.\theta_{SiH3} - C_S(T).N_S.\theta_{SiH3} = 0 \quad (5.6)$$

Until the temperature is above 400°C, the abstraction of H is the dominant process. Figure 5.4 which represents the ratio of H abstraction rate to H desorption rate versus substrate temperature has been obtained using equation 5.6 using the values for the different coefficient given by Ganguly [5.35] , Kessel [5.18] and Höfer [5.36], the other parameters have been fitted for corresponding to literature results. This figure has therefore to be taken as an illustration and not as a rigorous result. When temperature is above 350°C, H desorption is not ever neglected [5.35] and above 400°C H desorption becomes predominant [5.7, 5.37]. Therefore, the number of dangling bonds which was almost constant below 350°C due to the constancy of abstraction rate, start to increases due to the formation of dangling bonds generated by H desorption above 350°C.

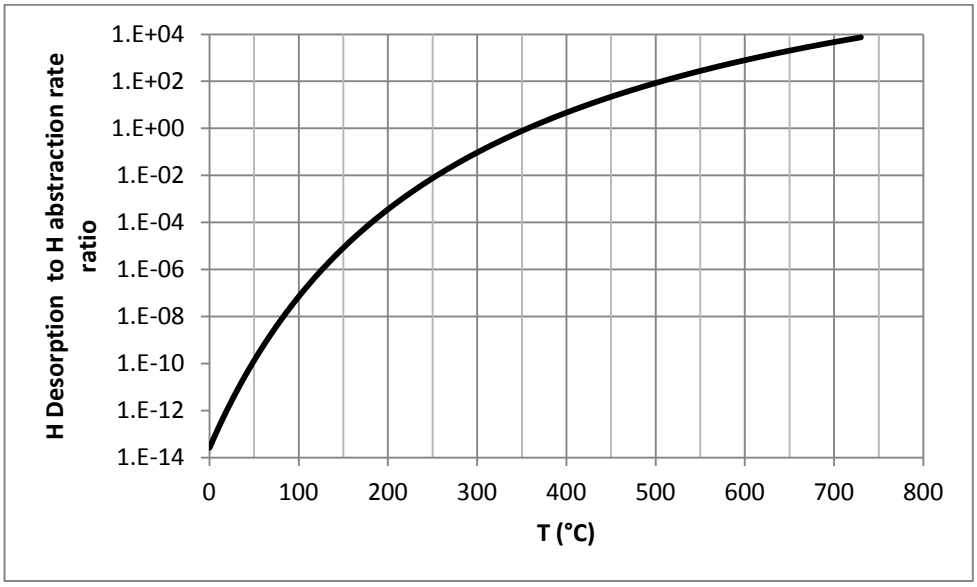

Figure 5.4 Schematic representation of the transition from abstraction process to desorption. The curve results from the ratio of desorption and abstraction terms of equation 5.6 respectively $C_H.N_H^2$ and $C_a.N_H.\theta_{SiH3}$.

On the other hand, for µc-Si:H, the sticking coefficient remains constant until 500°C because the Si-H bonding generated by the H flux at high H to SiH_4 ratio dominated on H desorption. However, at 500°C, the H desorption becomes predominant and almost all of the Si-H bonds are broken, therefore, the effect of H_2 in the plasma becomes neglected in regard with film growth and the film is a-Si:H even at high H_2 to SiH_4 ratio.

- **Crystallite formation**

Microcrystalline µc-Si:H formation is observed when the H_2 to SiH_4 ratio increases beyond a threshold [5.37-5.39]. Indeed, when silane is diluted with hydrogen, film quality changes, taking the amorphous configuration until a certain level of dilution; beyond this threshold, a transition occurs towards a nanocrystalline or even a microcrystalline film (µ-Si:H) .Then the crystallites' volume fraction increases with hydrogen to silane ratio in the gas [5.38]. The cluster interaction model and the chemical reactions taking place at the film surface can explain why crystallisation appears at high hydrogen to silane ratio. Microscopic stress in a-Si:H can help to understand the amorphous to crystalline transition in a-Si:H film when hydrogen concentration increases in the gas mixture. The origin of stress in a-Si:H can be explained by a cluster interaction model [5.40] **.** Indeed a-Si:H is constituted by silicon clusters with hydrogen at their boundaries. For high hydrogen content (hydrogen concentration, C_{Hyd} > 25 at %), Si-H_2 bonds dominate compared with Si-H bonds and clusters are small. These clusters attract each other and lead to tensile stress. On the other hand, for low hydrogen concentration C_{Hyd}, i.e. 5 < C_{Hyd} < 15 at %, Si-H bonds dominate and clusters are large. In this case, cluster interaction is repulsive and leads to compressive stress [5.40, 5.41]. As long as C_{Hyd} is in this latter range, compressive stress increases with C_{Hyd} since increasing C_{Hyd} means increasing Si-H bonds. When compressive stress increases the clusters tend to impose their local crystalline order on the nearest clusters. Hydrogen content in a-Si:H film higher than 17% is obtained when deposition occurs at substrate temperature at or below 250°C [5.42, 5.43] and indeed a study on a-Si:H film deposited at 250°C shows that the resulted films present a tensile stress [5.44] which means that C_{Hyd}>25 at %. This is also in agreement with the fact that at 250-300°C and beyond, the release of H from Si-H_2 gives films where Si-H configuration becomes dominant beyond 400°C and only Si-H configuration remains [5.45, 5.46]. It also explains why for temperature higher than 300°C H content is reduced [5.47] .Therefore for films deposited at a temperature higher than 300°C, the H concentration in the film is in the low H content range, thus increasing of crystallinity with hydrogen to silane ratio can be explained by the fact that increasing hydrogen dilution results in a higher hydrogen content in the growing film [5.48] and thus an increasing of the compressive stress. Compressive stress increases until crystallisation is activated leading to nanocrystallite formation and H content in the film starts to decrease [5.49]. When H_2 dilution is further increased, it leads to µ-Si:H formation

when hydrogen to silane ratio becomes high enough. It would be interesting to establish a parallel with grain boundary growth [5.50] in a polycrystalline material. It has also to be noted that the refractive index decreases with hydrogen content, for the low hydrogen content case, that is when compressive stress increases [5.51]. It has been seen previously that T has to be increased with the deposition rate in order to have a good diffusion of growth precursor and thus removing the defect. Reciprocally, it is possible to have a good a-Si:H quality even with high hydrogen dilution if the deposition rate is increased when T is higher since increasing the deposition rate enables to avoid the beginning of an epitaxial growth [5.42]. Eventually it has to be noted that when silane depletion occurs the H threshold at the surface can be reached even if there is no H_2 in the feed gas (cf. section 5.2.1.).

5.3.2 SiN_x

- **What is silicon nitride?**

Firstly the "perfect" structure of silicon nitride is the stoichiometric one Si_3N_4 which corresponds to a SiN_x with x of approximately 1.33. This stoichiometric Si_3N_4 is represented on figure 5.5 where a Si atom is at the centre of a tetrahedral structure and bonded with 4 N atoms. If we consider the unit cell of this structure , there is one Si in this unit cell and 4 N atoms shared by 2 other unit cells, thus there is 4/3 N atoms in the unit cells which gives the Si_3N_4. It is important to keep this representation in mind for understanding the different "states" of SiN_x. For Si_3N_4 the only existing bond is Si-N each Si being only bonded with an N atom and reciprocally. When x is below 1.33, Si-Si and Si-H bonds exist instead of Si-N bonds. The nature of the bond determines several properties of the film as residual stress and refractive index as will be seen later.

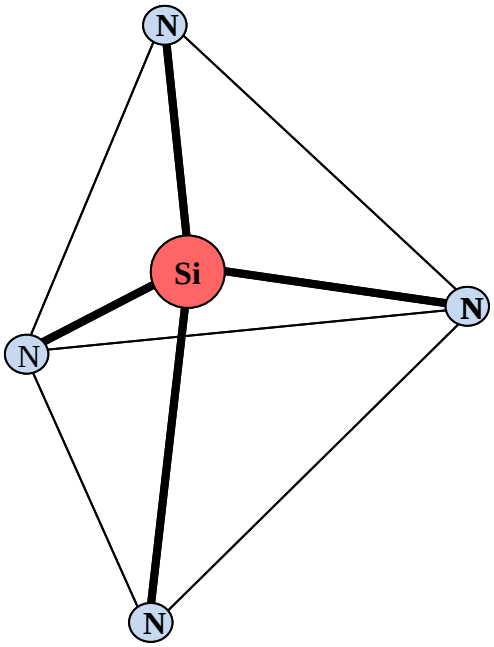

Figure 5.5 Unit cells of Si_3N_4 structure

- **SiN_x film production from dissociated gas mixture**

The energy corresponding to Si-H bond of SiH_4 is 3.30 eV (76 kcal/mol) whereas N-H bond is 4.05 eV (93.4 kcal/mol) [5.52]. Thus, when plasma electrons bring energy equal or higher than 4.05eV, the following reaction between SiH_4 and NH_3 can be activated.

$$3(SiH_4) + 4(NH_3) = Si_3N_4 + 24\ H \qquad (5.7)$$

However, this reaction is actually a summary of several mediated reactions in the gas and at the film surface as explained later. The stoichiometry required a PECVD temperature of 500°C whereas only 350°C is required for a gas mixture with SiH_4 -N_2 [5.53]. In this latter case, the ideal reaction is

$$3(SiH_4) + 2N_2 = Si_3N_4 + 12\ H \qquad (5.8)$$

This difference of temperature which is required for having stoichiometry is probably due to the fact that some of the hydrogen resulted from these chemical is incorporated into the film and is then desorbed when temperature is high enough. Since the reaction with NH_3 produced two times higher amount of H than with N_2, the films deposited

with NH_3 film have thus a higher H content and required a higher temperature for H desorption. Regarding the high content of hydrogen in film produced with NH_3, it is reported that film deposited with this method can contain up to 40% of H atoms [5.54]. Another reason is the fact that whereas the chemical reaction leading to SiN_x is mediated by growth precursor in the case of NH_3 as will be seen in the following, the N issue from N_2 dissociation and SiH_x radicals from SiH_4 are directly incorporated in the growing film [5.55]. However N_2 is strongly bonded with a triple bond and its dissociation required 9.8 eV (225.8 kcal/mole) [5.52], thus this study is limited to SiN_x deposition from SiH_4-NH_3 gas mixture.

The chemical reactions from SiH_4-NH_3 gas generate principally the following species: disilane: Si_2H_6, aminosilanes Si $(NH_2)_4$ and Si $(NH_2)_3$. Aminosilanes are the result of the reaction of SiH_x radicals with NH_x radicals. RF or MW power is the dominant parameter in regards with species ratio in the plasma because it provides the energy for dissociation. Since NH_3 dissociation required more energy, at a too low power for having enough NH_3 dissociation, Si_2H_6 is the dominant species [5.8].Si_2H_6 is issued from the SiH_3 radicals which react with each other through the following reaction:

$$SiH_3 + SiH_3 \rightarrow Si_2H_6 \qquad 6 \quad (5.9)$$

Thus the presence of Si_2H_6 is due to the fact that SiH_3 is the dominant species generated by plasma dissociation at low power. This means that NH_3 only acts as an inert gas. If the RF power is increased, the aminosilanes begin to be generated mostly $Si(NH_2)_4$ and due to the fact that SiH_3 reacts with the products of NH_3 dissociation, the Si_2H_6 concentration decreases. Then if the power is further increased $Si(NH_2)_3$ becomes the dominant aminosilane and indeed the evolution of the deposition rate follows the evolution of the $Si(NH_2)_3$ concentration which indicates that this latter is the major growth precursor [5.55]. If the RF power is still increased, Si_2H_6 concentration in the plasma decreases toward a minimum whereas aminosilanes concentration increases toward a maximum value where they remain constant. These limited values thus indicate a saturation of the gas dissociation. Although in a lesser part, pressure has also an influence in species generation. If the power is high enough to enable the dissociation of NH_3 and consequently the aminosilanes formation, the increasing of pressure results in higher SiH_4 consumption and lower Si_2H_6 formation. This is due to

the fact that raising the pressure is equivalent to increasing the interaction between species and therefore promoting the reactions which lead to aminosilane formation. This also explains the fact that deposition rate increases with pressure providing that NH_3 to silane ratio and power is high enough. On the other hand, as reported by Wei [5.9] NH_3 dissociation increases when pressure is lower since the mean free path of electrons is higher and thus their energy. Therefore there may be an optimum of pressure in regard with dissocation rate. However, for our concern the effect of pressure on gas dissociation has not enough importance in regard with its effect on bombardment and on plasma stability in order to avoid arcing [5.56].

- **SiN_x:H formation**

On figure 5.6, both dominant types of aminosilanes $Si(NH_2)_3$ and $Si(NH_2)_4$ are represented. From this figure several properties can be understood since film structure, refractive index, and stress in the film can be explained by the bonds present on these precursors. On $Si(NH_2)_3$ and $Si(NH_2)_4$, Si-N and N-H bonds are present whereas there is no Si-H bond which is in agreement with the fact that there are also no Si-H bonds in SiN_x:H films produced with NH_3 [5.8] since H is bonded with N in this case while with Si when N_2 is used [5.53].

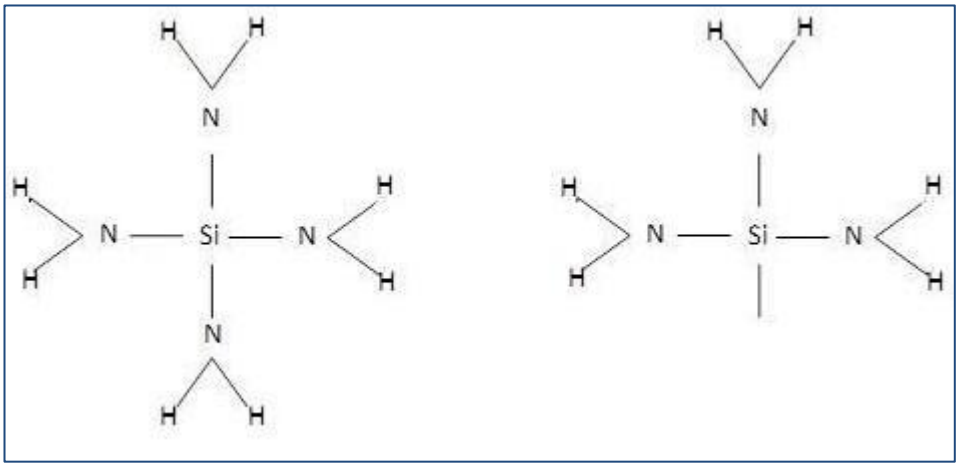

Figure 5.6 $Si(NH_2)_4$ and $Si(NH_2)_3$. These 2 aminosilane species result from the reaction between the species from NH_3 and SiH_4 dissociation. $Si(NH_2)_4$ and $Si(NH_2)_3$ are principals growth precursors of SiN_x films. No N-H bonds are present on these aminosilane but only Si-H and Si-N bonds. The nature of bonds explains the film properties.

These aminosilanes are incorporated in the film in the following way [5.8]: $Si(NH_2)_3$ are adsorbed at the film surface on a site with a N- bond, NH_2 group of adsorbed $Si(NH_2)_3$ reacts with another $Si(NH_2)_3$ in its vicinity by extracting a H atom

$$NH_2+H \rightarrow NH_{3(g)} \qquad (5.10)$$

NH_3 is reintegrated in the plasma and this reaction leaves a Si- and N- bond which link together to built the SiN_x:H film as illustrated on figure 5.7.

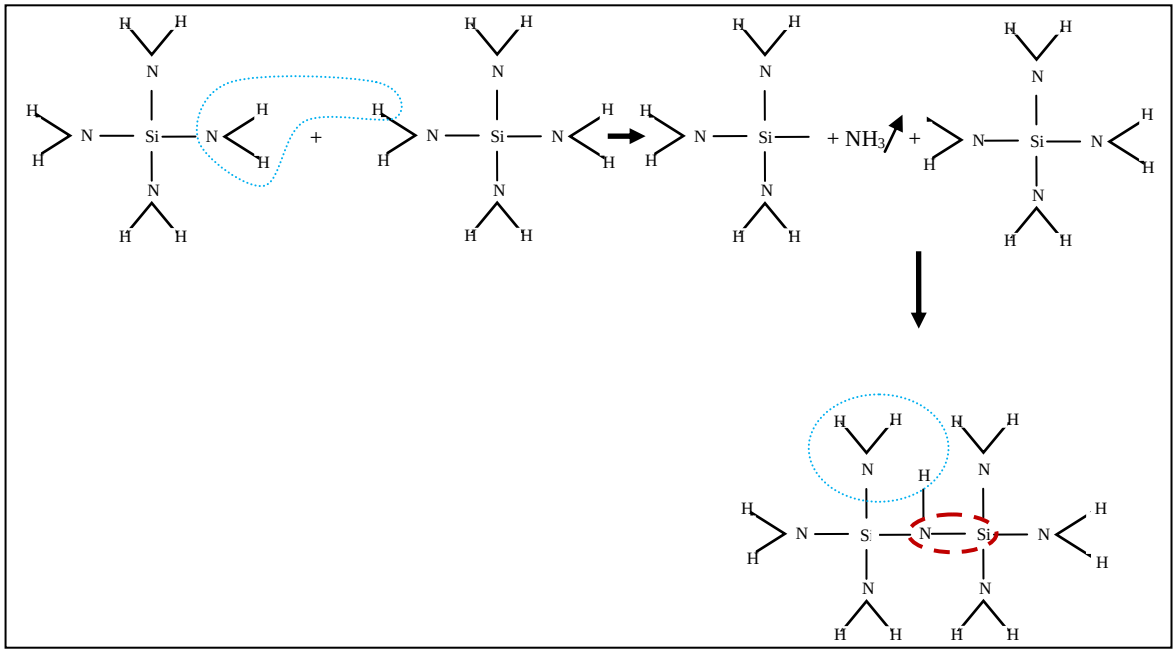

Figure 5.7 Process of aminosilanes incorporation in the SiN_x films. When aminosilane is adsorbed at the film surface, the NH_2 group of this aminosilane reacts with a H atom of a NH_2 group of another aminosilane and releases NH_3 and two dangling bonds Si- and -N. These 2 dangling bonds react and form Si-N bond.

If the substrate temperature is high enough to provide the heat required for completing the condensation, the process can be resumed by equation 5.11.

$$3Si(NH_2)_4 \rightarrow Si_3N_4+8NH_{3(g)} \qquad (5.11)$$

Nevertheless, for temperature below 500°C, the condensation is partial and the stoichiometry can only be approached.

- **Properties of SiN_x:H**

The SiN_x films can be divided in 3 ranges, from x=0 to 1.1, the film is said Si-rich, from x=1 to 1.33 the film is N rich, x= 1.33 corresponds to the stoichiometric Si_3N_4 material. The last range is x>1.33. For Si_3N_4, each Si is bonded with N and reciprocally as seen previously. When the N cannot be incorporated due to a too low NH_3 dissociation and a substrate temperature below 500°C , x<1.33 Si-Si bonds are present and as the deposition conditions become more favorable to N incoporation these bonds are progessively replaced by Si-N bonds until reaching stoichiometry if the conditions required are fullfilled. On the other hand films with x>1.33 are due to the replacement of Si-N by N-N or N-H bonds. On this latter case the x becomes higher than 1.33 not because of an excess of N incorporation but due to a lack of Si being replaced by H atoms [4.26]. On this latter range, x decreases with T_S and the N-H bonds are replaced by N-Si [5.8] The reason of x decrease is probably due to H desorption. However in this work SiN_x, only Si rich and near stoichiometric films are considered.

- **Evolution of film properties with N content**

In SiN_x:H films, Si-rich films have a high refractive index which decreases when the x fraction increases [4.4, 5.8]. More precisely this is the type of bond, Si-N or Si-H which play a determinant role both for defect density and optical properties. Regarding defects, Si-H bonds are bonded with energy lower than Si-N bond and thus have a higher probability to be broken leaving a dangling bond or in other words a defect. Since there is no Si-H bond in $Si(NH_2)_3$ and $Si(NH_2)_4$, as has been seen previously, a higher x correspond to a lower number of Si-H bond and therefore a lower defect density. Regarding the refractive index its evolution with x is directly related to intrinsic stress: N-H bonds and for a lower part Si-N bonds lead to tensile stress which decreases refractive index whereas Si-H and even more Si-Si bonds lead to compressive stress which increases refractive index [5.8, 5.57, 5.58] .

- **Relation between external parameters and film properties**

When the applied power is high enough to provide the energy required for NH_3 dissociation, x increases [4.4] with the NH_3 to SiH_4 ratio due to the fact that $Si(NH_2)_3$ and $Si(NH_2)_4$ are generated and then incorporated in the film in higher quantity. Since these latter do not have Si-H bonds but Si-N bonds, the compressive stress decreases in favour of tensile stress leading to a low refractive index and a higher energy band gap

[4.4]. More over it has been seen previously that the breaking of N-H bond required 4.05 eV while 3.3 eV is required for Si-H bond. In other words the dangling bond creation is easier with Si-H bonds and therefore a-Si:H should contain more defects than SiN_x:H films. Stress also depends on energetic bombardment: high ion bombardment energy leads to compressive stress [5.59] and thus decreasing the pressure leads to a diminution of the tensile stress by increasing the bombardment. Eventually the lowest stress configuration is for a refractive index of about n = 1.9 which corresponds to near stoichiometric Si_3N_4 [5.9, 5.59]. This near stoichiometric SiN_x film also corresponds to the lower SRV obtained by Schmidt with SiN_x passivation at 400°C [1.11]. We can therefore conclude that a film as close as possible to the stoichiometry is needed for having a good surface passivation. The main parameter for approaching stoichiometry is having a high temperature.

5.4 Experimentation

5.4.1 Film deposition by PECVD

In order to study surface passivation for reducing carrier recombination, p-type float zone monocrystalline wafers (FZ wafers, 8000 Ω.cm) have been chosen. Since these wafers are ultrapure monocrystalline silicon, the bulk recombination can be neglected during minority carrier lifetime measurement and thus carrier recombination can be entirely attributed to surface recombination. When the conditions were optimal, films deposited on Cz 1Ω.cm have been used. Prior to film deposition, wafers have been cleaned using RCA1 clean (NH_4OH: H_2O_2: H_2O at a ratio of 1:1:5, 70°C for 10 min), in order to remove organic residues, followed by a hydrofluoric acid (HF)-dip for removing the native oxide layer, and rinsing in deionised water as a finishing step: they were kept in deionised water until placed in the deposition chamber. Alternatively to HF cleaning, low power hydrogen plasma was used at 0.13 mbar for 10 min as indicated by several authors [5.61]. Deposition was realised by MW-PECVD at 2.45 GHz with a microwave generator type MW-GIRYJ 1540-1k-03 and by RF-PECVD at 13.56 MHz in a 2 parallel electrode, the 20 cm diameter upper electrode being connected to the RF power via an insulated capacitor and a matching net work and the other electrode being grounded. The distance between the 2 electrodes was 2 cm. The same PEVCD system has been used both for RF and MW. Indeed the PECVD system used in this work has the flexibility of being able to work with both microwaves (MW) and radio frequency (RF) excitation, from 13.56 MHz through VHF frequencies. This presents the advantage

of working at different frequency ranges with the same system and thus limiting variations in the other conditions, since it is known that deposited film quality is closely dependent on the system itself. In this study, standard RF and MW processing frequencies of 13.56 MHz and 2.45 GHz have been chosen for investigating deposition both in individual and collective plasma regimes. The influences of the other deposition parameters, namely pressure (P), substrate temperature (T), power and gas mixture have been investigated. The deposition time was 10 min for MW PECVD a-Si:H and 20 min for SiN_x MW PECVD and RF PECVD. Indeed, in general, deposition rate was more than 2 times higher for MW than for RF PECVD. Various pressures in the range 0.3–1.2 mbar were investigated for MW PECVD and 0.2 to 0.8 for RF PECVD. For a-Si:H film deposition the feed gas was composed of SiH_4, H_2 and Ar with various standard cm^3 per minute flow rates (sccm ratios). A description of the flow diagram can be found on reference [5.60]. For SiN_x deposition it was composed of SiH_4, NH_3 and occasionally Ar with various NH_3 to SiH_4 ratios. Due to the interactions between plasma and heating power, the temperature can hardly be maintained at a constant value particularly when SiH_4, H_2 and Ar gas mixture was used with MW frequency, temperature can decreased by 50°C in the worse case. Indeed we were forced to reduce the power of the heating supply for avoiding arcing. Arcing occurs when the voltage between plasma and the grounded wall of the chamber becomes high enough to lead to an electric field which exceeds the breakdown strength of the sheath. Arcing has to be avoided since it leads to unstable plasma, roughness of the film and introduction of the chamber wall material in the plasma [5.56]. From a heating power threshold arcing starts to occur with a frequency which increases with heating voltage until a maximum value where it causes the disjunction of the heating power. This excess in plasma potential is probably due to the fact that a part of the heating power voltage is absorbed by the plasma and should be avoided if the heating power is isolated enough to avoid a voltage transfer toward the plasma. However, it should be noted that the occurrence of arcing depends on the gas used for plasma. It is particularly strong with Ar at low pressure. Indeed pressure has a large influence on arcing [5.56] and in our experiments we have noted that by increasing the pressure arcing can be avoided. This latter fact may be due to the fact that since pressure is related to a high density of particles, it increases the dielectric strength of the sheath. Finally a considerable improvement appears when a more adapted heater has been installed allowing to reach temperature as high as 400°C with a relative stability.MW and RF PECVD system is presented on figure 5.8.

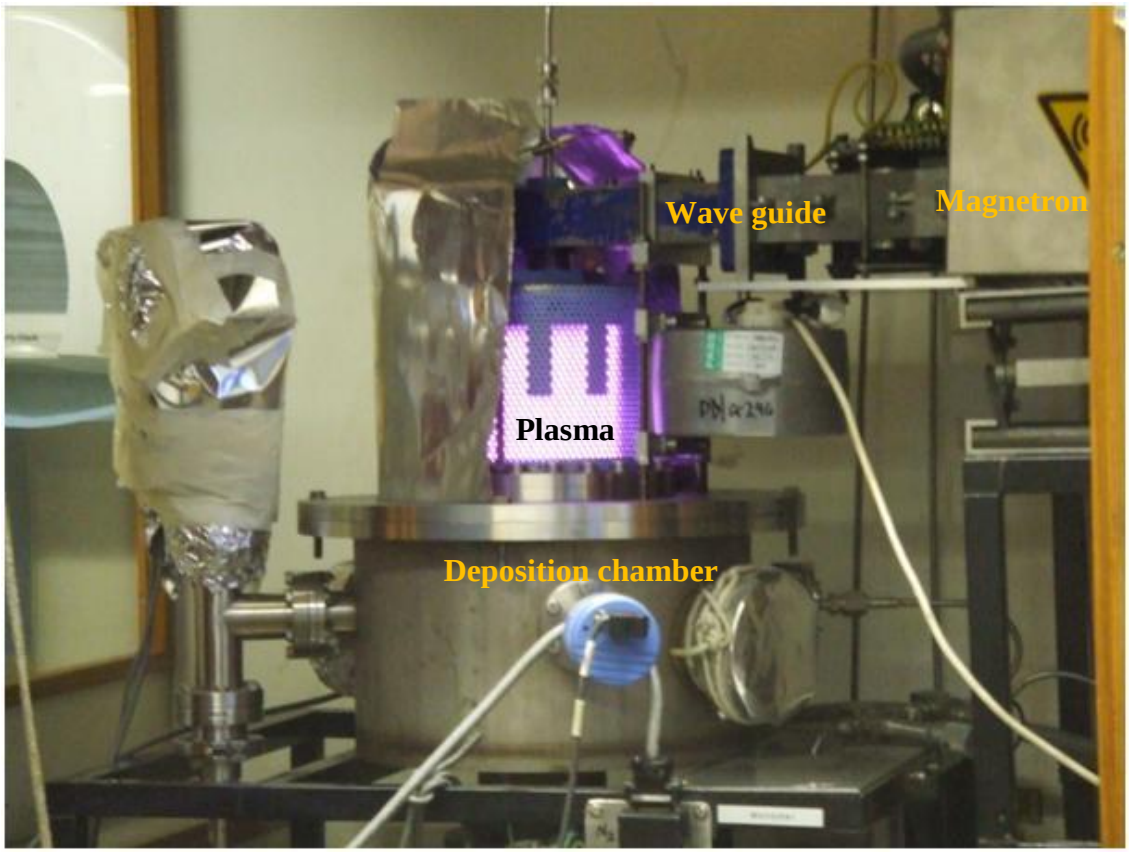

Figure 5.8 PECVD system: A photograph showing deposition chamber and glow discharge during a ME PECVD a-Si deposition. Magnetron and wave guide are associated with MW generator. The system is connected with a RF generator via a matching network for RF PECVD.

5.4.2 Consideration about the ratio between silane dissociation and supplied silane

It has been seen in section 5.3.1 that for the a-Si:H growth crystallite formation can appear due to a high H content at the film surface and that can occur even when SiH_4 is not highly diluted in H_2 in the case of silane depletion. Silane depletion occurs when the decomposition of silane is faster than the silane supply [5.6, 5.33, 5.62] which leads to the suppression of the recombination between SiH_4 and H atoms and thus to an increasing of H atoms at the film surface. In order to estimate the dissociation rate, we introduce in equation 5.12 the ratio R between the deposited mass of Si $m_{SiH4dep}$ and the total mass of SiH_4 provided by the gas supply $m_{SiH4tot}$. For this latter, the mass contribution of the 4 H is neglected. Several information can be deduced from the value of R. Firstly, when R is higher it indicates a higher deposition rate and thus a high silane dissociation rate. If R decreases with power or with addition of H_2 this can mean that there is H etching due to silane depletion.

$$R = \frac{m_{SiH4\ dep}}{m_{SiH4\ tot}} \tag{5.12}$$

The deposited silane can be roughly estimated by considering that the fraction of consumed silane corresponds approximately to the deposited volume rate of the film. Considering that the Si density is between 2.19 g.cm^{-3} and 2.29 for a-Si:H with a H content of respectively 12% at and 0.3 % at [5.63], and that the thickness of our MW PECVD a-Si:H films varies from 200 to 600 nm for a deposited times of 10 min, the volume per minutes can be estimated from the chamber dimension given on figure 5.9. The results are given in table 5.1.

Density g/cm3	2.19	2.2	2.21	2.22	2.23	2.24	2.25	2.26	2.27	2.28	2.29
Thickness nm/min	Mass of a-Si:H (mg)										
10	1.79	1.80	1.81	1.81	1.82	1.83	1.84	1.85	1.85	1.86	1.87
20	3.58	3.59	3.61	3.63	3.64	3.66	3.68	3.69	3.71	3.72	3.74
30	5.37	5.39	5.42	5.44	5.46	5.49	5.51	5.54	5.56	5.59	5.61
40	7.16	7.19	7.22	7.25	7.29	7.32	7.35	7.38	7.42	7.45	7.48
50	8.94	8.98	9.03	9.07	9.11	9.15	9.19	9.23	9.27	9.31	9.35
60	10.7	10.8	10.8	10.9	10.9	11.0	11.0	11.1	11.1	11.2	11.2

Table 5.1 Mass of deposited a-Si:H per minutes versus film density

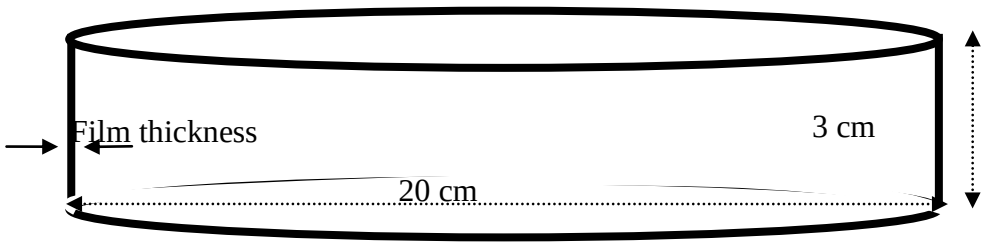

Figure 5.9 Volume of the deposited film including the walls of the deposition chamber and the 2 electrodes. The volume is the sum of product the 3 surfaces (the wall and the 2 electrodes) with the film thickness.

Considering that the density of silane is 1.35 mg/cm3 and the gas flow is 4 sccm, the silane mass provided per minute is 5.4 mg. Using equation 5.12, the result of the ratio R is given in table 5.2 for different film thicknesses and film density. Table 5.2 shows that for films deposited with a growth rate that exceeds 30 nm/min, the ratio becomes higher than 100% which does not make sense since it means that the dissociated silane would

be higher than the total silane flow. In this latter case we could guess in a first approach that the density is lower than 2.19 which suggest high porosity. Actually the presence of porosity in a-Si:H will be confirmed in chapter 6.

a-Si :HDensity g/cm3	2.19	2.2	2.21	2.22	2.23	2.24	2.25	2.26	2.27	2.28	2.29
Film thickness (nm/min)	Fraction of dissociated silane (%)										
10	33	33	33	34	34	34	34	34	34	34	35
20	66	67	67	67	67	68	68	68	69	69	69
30	99	100	100	101	101	102	102	103	103	103	104
40	133	133	134	134	135	136	136	137	137	138	139
50	166	166	167	168	169	169	170	171	172	172	173
60	199	200	201	201	202	203	204	205	206	207	208

Table 5.2. Results describing Silane depletion versus a-Si:H film density during the PECVD growth process

However, it has to be remembered that the dissociation rate has been considered equal to the deposition rate which neglects the time of transfer from the plasma to the film surface and the time of Si incorporation. Another point is the fact that the MW PEVCD a-Si:H films' thickness has a non homogeneity that can reach 50 %, the highest thickness being at the sample center. Therefore we can guess that the thickness on the wall is still lower on the chamber wall. However, although not exact, this estimation of R combined with other aspects can give a qualitative indication of the depletion possibility and the hydrogen content at the sample surface. Furthermore, since the silane flow used is always the same in our experiments, the knowledge of film thickness is enough for having this qualitative indication. A quantitative determination of silane depletion would require plasma diagnostic [5.64].

5.5 Conclusion

For both SiN_x and a-Si:H films, the main condition is the substrate temperature high enough to enhance the surface diffusion and the hydrogen desorption. For having a high passivating quality film with SiN_x, it is necessary to be close to the stoichiometry. Thus NH_3 to SiH_4 ratio has to be set in order to have a high enough incorporation of N atoms in the film. However it is necessary to have a high RF or MW power for dissociating NH_3. Regarding a-Si:H film it is important to limit the hydrogen concentration at the film surface below the threshold where crystallisation starts to occur. For this, H_2 to

SiH_4 ratio has to be low enough and silane depletion should be avoided. Regarding this last point, it has been seen that the estimation of R can only give a qualitative indication of the hydrogen content. The next chapter presents the results for the optimisation of the deposition parameters for a-Si and SiN_x films deposition with MW and RF PECVD. These parameters are temperature, pressure, ratio of the different component of the gas mixture and RF or MW power.

BIBLIOGRAPHY CHAPTER 5

[5.1] K.F. Jensen, Chemical vapor deposition principles and applications, Chapter 2, Edited by M.L. Hitchman and K.F. Jensen, Academic press (1993)

[5.2] A.M. Hashim et al., Carbonization layer obtained by acetylene reaction with silicon (100) and (111) surface using low pressure chemical vapor deposition, J.Appl.Sci. 8(9), 3473-3478 (2008)

[5.3] B. E. Deal et al. , General Relationship for the Thermal Oxidation of Silicon , J. Appl. Phys. 36, 3770-3778 (1965).

[5.4] Handbook of plasma technology p 16, Edited by S.M. Rossnagel, Noyes publication 1990.

[5.5] H.S Butler, plasma sheath formation by radio-frequency fields. Physics of Fluids, 1963. 6(9): p. 1346-1355.

[5.6] M. Kondo., An approach to device grade amorphous and microcrystalline silicon thin films fabricated at higher deposition rates. Current Opinion in Solid State and Materials Science, 2002. 6(5): p. 445-453.

[5.7] A. Matsuda, Microcrystalline silicon.: Growth and device application. Journal of Non-Crystalline Solids, 2004. 338-340: p. 1-12.

[5.8] D.L. Smith et al., Mechanism of SiN_xH_y deposition from NH_3-SiH_4 plasma, J. Electrochem. Soc. 137, 614-623 (1990)

[5.9] J.Wei et al., A new fabrication method of low stress PECVD SiNx layers for biomedical applications. Thin Solid Films,. 516 (16), 5181-5188 (2008).

[5.10] H.R. Koenig, Application of RF discharges to sputtering. IBM J. Res. Dev., 1970. 14(2): p. 168-171.

[5.11] S. Oda et al., Frequency effects in processing plasmas of the VHF band. Plasma Sources Science and Technology, 1993. 2(1): p. 26.

[5.12] M. Heintze et al., Analysis of high-rate a-Si:H deposition in a VHF plasma, J.Phys. D Appl.Phys 26, 1781-1786(1993).

[5.13] N. Spiliopoulos et al., Influence od discharge geometry on power dissipation and sheath impedances in siliane discharges, J.Appl.Phys 36, 4717-4721 (1997)

[5.14] Kohler, K., Frequency dependence of ion bombardment of grounded surfaces in rf argon glow discharges in a planar system. Journal of Applied Physics, 1985. 58(9): p. 3350-3355.

[5.15] A. Metze et al., Application of the physics of plasma sheaths to the modeling of rf plasma reactors, J.Appl.Phys. 60(9), 3081-387 (1986)

[5.16] Handbook of plasma technology p 59, Edited by S.M. Rossnagel, Noyes publication 1990.

[5.17] C. Mukherjee, Photoconducting a-Si:H films grown at high deposition rates by pulsing a VHF 100 MHz discharge. Thin Solid Films, 2003. 423(1): p. 18-26.

[5.18] A.V.Shah, Intrinsic microcrystalline silicon (μc-Si:H) deposited by VHF-GD (very high frequency-glow discharge) : a new material for photovoltaics and optoelectronics. Materials Science and Engineering B69–70 219–226 (2000).

[5.19] J. Dutta, Dependence of intrinsic stress in hydrogenated amorphous silicon on excitation frequency in a plasma-enhaced chemical vapor deposition process. J.Appl.Phys. 72(7), 3220-3222 (1992)

[5.20] T. Karabacak et al.,Growth front roughening in silicon nitride films by plasma-enhanced chemical vapor deposition, PHYS. REV. B 66, 075329 -1-10(2002)

[5.21] H. Rinnert et al., Enhanced hydrogen stability in a-Si:H thin films evaporated under a flow of energetic argon ions, Applied Surface Science 193 ,175–179 (2002)

[5.22] Y.Q. Fu et al.,Residual stress in amorphous and nanocrystalline Si films prepared by PECVD with hydrogen dilution, Materials Science and Engineering B 124–125 ,132–137 (2005).

[5.23] A. Parashar et al.,Influence of argon dilution on growth and properties of hydrogenated nanocrystalline silicon films, Solar Energy Materials & Solar Cells 94 ,892–899 (2010)

[5.24] A. Keudell et al., Direct insertion of SiH3 radicals into strained Si-Si surface bonds during plasma deposition of hydrogenated amorphous silicon films,Phys. Rev. 59(8),5791-5798 (1999)

[5.25] J.I. Masher, The chemistry of hypervalent molecules, Angewandte chemic international edition in English, vol.8 (1) 54-58 (1969)

[5.26] W. M. M. Kessels et al, Surface reaction probability during fast deposition of hydrogenated amorphous silicon with a remote silane plasma , J. Appl. Phys. 87 (7), 3313-3319 (2000)

[5.27] E. Amanatides et al., Gas phase and surface kinetics in plasma enhanced chemical vapor deposition of microcrystalline silicon: The combined effect of rf power and hydrogen dilution ,J. Appl. Phys. 90 (11), 5786-5798 (2001)

[5.28] W.M.M. Kessels et al. , On the growth mechanism of a-Si :H, Thin Solid Films 383, 154-160 (2001)

[5.29] W. Beyer, Diffusion and evolution of hydrogen in hydrogenated amorphous and microcrystalline silicon, Solar Energy Materials & Solar Cells 78 ,235–267(2003)

[5.30] S. C. Deane et al., Unification of the time and temperature dependence of dangling-bond-defect creationand removal in amorphous-silicon thin-film transistors, PHYS. REV. B 58(19),12625-12628(1998)

[5.31] D.Y. Kim et al.,Electrical properties of a-Si:H thin films as a function of bonding configuration , Solar Energy Materials & Solar Cells 93 ,239–243 (2009)

[5.32] Y. Bar-Yam et al.,Dangling bond in a-Si :H, Phys. Rev. Lett. 56(20), 2203-2206 (1986)

[5.33] MC.M. van de Sanden et al., Plasma chemistry aspects of a-Si :H deposition using an expanding thermal plasma, J.Appl.Phys. 84(5), 2426-2435(1998)

[5.34] A.Hasbi, Structural properties of hydrogenated amorphous silicon (a-Si:H) thin film grown via radio frequency plasma enhanced chemical vapor deposition (RF PECVD) , Master's thesis, Universiti Teknologi Malaysia, Faculty of Science (2005)

[5.35] G. Ganguly et al., Defect formation during growth of hydrogenated amorphous silicon, Phys. Rev B 47, 3661-3670

[5.36] U. Höfer et al., Desorption of hydrogen from Si (100) 2x1 at low coverages: the influence of π-bonded dimmers on the kinetics, Phys. Rev.B 45(16), 9486-9488 (1992)

[5.37] A. Matsuda, Growth mechanism of microcrystalline silicon obtained from reactive plasmas, Thin Solid Films 337, 1-6 (1999)

[5.38] Shah, A.V., Material and solar cell research in microcrystalline silicon. Solar Energy Materials and Solar Cells, 2003. 78(1-4): p. 469-491.

[5.39] J.Koh et al., Optimization of hydrogenated amorphous silicon p-i-n solar cells with two step I layers guided by real-time spectroscopic ellipsometry, Appl. Phys. Let. 73(11), 1526-1528 (1998)

[5.40] Alzar, G., Mechanical stress reduction in PECVD a-Si:H thin films. Materials Science and Engineering B, 1999. 65(2): p. 123-126.

[5.41] B. Stannowski et al., Amorphous-silicon thin-film transistors deposited by VHF-PECVD and hot-wire CVD, Journal of Non-Crystalline Solids 299–302 ,1340–1344(2002)

[5.42] A. Illiberi et al., Hydrogenated amorphous silicon based surface passivation of c-Si at high deposition temperature and rate, Phys. Status Solidi RRL 4, 206-208 (2010)

[5.43] W. M. M. Kessels et al., Hydrogenated amorphous silicon deposited at very high growth rates by an expanding Ar–H2–SiH4 plasma, J. APPL.PHYS.89(4) ,2404-2413 (2001)

[5.44] L. Cai et al.,Understanding the Effects of Stress on the Crystallization

of Amorphous Silicon, Journal of ELECTRONIC MATERIALS, 36, (3), 191-196(2007)

[5.45] W.M.M. Kessels et al,. Temperature dependence of the surface reactivity of SiH3 radicals and the surface silicon hydride composition
during amorphous silicon growth, Surface Science 547 L865–L870(2003)

[5.46] O. Salyk, Thermal Desorption Spectroscopy of Hydrogen from Amorphous Hydrogenated Silicon, Chem. Papers 50 (4) 177—182 (1996)

[5.47] Virzonis, D., Advanced Process Equipment for PECVD Silicon Nitride Deposition- An Experimental Study. Materials Science (MED Zyagotyra), 2006. 12(2).

[5.48] U. Kroll et al., Hydrogen in amorphous and microcrystalline silicon films prepared by hydrogen dilution, J. Appl. Phys. 80 (9), 4971-4975 (1996)

[5.49] T. Q.Trung et al, The effects of hydrogen dilution on structure of Si:H thin films deposited by PECVD, Journal of Physics: Conference Series 187 ,012035-1-6 (2009)

[5.50] Drolet, J. and A. Galibois, Altering the time cycle of heat treatment by preannealing prior to grain growth. Metallurgical and Materials Transactions B, 1971. 2(1): p. 53-64.

[5.51] Severens, et al., Characterization of Plasma Beam Deposited Amorphous Hydrogenatred Silicon. Vol. 67. 1995, Melville, NY, ETATS-UNIS: American Institute of Physics. 3.

[5.52] Kubacki, Low Temperature Plasma Deposition of Silicon Nitride to Produce Ultra-Reliable, High Perform-ance, Low Cost Sealed Chip-on-Board (SCOB) Assemblies. Components, Packaging, and Manufacturing Technology, Part A, IEEE Transactions on 1995. 18(3): p. 471-477.

[5.53] D.V. Tsu et al., Local atomic structure of silicon nitride and silicon diimide produced by remote plasma-enhanced chemical-vapor deposition , Phys.Rev.B 33(10), 7069-7076 (1996)

[5.54] A. El-amrani, Silicon nitride film for solar cells, Renewable Energy 33 ,2289–2293(2008)

[5.55] M. F. Romero et al. ,Plasma diagnostics and device properties of AlGaN/GaN HEMT passivated with SiN deposited by plasma-enhanced chemical vapour deposition, J. Phys. D: Appl. Phys. 43 ,495202 (2010) SiNx

[5.56] Y. Yin et al., Microarcing instability in RF PECVD plasma system, Surface & Coatings Technology 198 ,379– 383(2005)

[5.57] J.W. Lee et al., Bond density and physicochemical properties of a hydrogenated silicon nitride film, J. Phys.Chem.Solids 56(2), 293-299(1995)

[5.58] M. K. Gunde et al.,The relationship between themacroscopic properties of PECVD silicon nitride and oxynitride layers and the characteristics of their networks, Appl. Phys. A 74, 181–186 (2002)

[5.59] Mackenzie, K., et al., Stress Control of Si-based PECVD Dielectrics. ECS Meeting Abstracts, 2006. 501(9): p. 406-406.

[5.60] S. Jardine, PhD Thesis, Heriot-Watt University, 2006

[5.61] Y.B Park et al., Interfacial modification of amorphous substrates for microcrystalline silicon growth with in situ hydrogen plasma pretreatment, Phys. Stat. Sol. (a) 202, 2248-2453 (2005)

[5.62] S. Nunomura et al.,Time-dependent gas phase kinetics in a hydrogen diluted silane plasma, APPL.PHYS. LETT. 94, 071502-1-3 (2009)

[5.63] F. jansen et al.,Optical determination of the mass density of amorphous and microcrystalline silicon layers with different hydrogen contents, J. Non. Cryst. Sol. 227-230,876-879 (1998)

Chapter 6

Summary, Analysis & Discussion

On this chapter we try to make correlation between the different results of our film characterisation, PECVD conditions and passivating quality (or SRV value).

On figure 6.1, the plain line represents the results of the SRV measurement at $1x10^{15}$ cm^{-3} and the dashed line the maximum SRV. The samples are a-Si:H and SiN_x films deposited on FZ wafers with a resistivity of 8000 ohm.cm. Films deposited onto Cz wafers are not presented here because the optimisation has been exclusively done on FZ wafers. The Cz wafers were used as substrates for passivating film only after their optimisation. These samples from 1 to 46 are presented in a chronological order in abscissa. In a first approach, it would seem more appropriate to regroup the results by the 4 types of PECVD methods used for deposition which are MW PECVD and RF PECVD of a-Si:H and MW PECVD and RF PECVD of SiN_x. However, since some modifications have been made on the PECVD system as replacement of pump, flow controller and heating power, the conditions of deposition cannot be assumed to be the same even for a same set of external monitored parameters. Thus a chronological presentation highlights the improvement of the system in itself. Furthermore this way to present the results allows to see the general evolution of the passivation quality during the study. An extensive study of the influence of external parameters, which are temperature, pressure, RF or MW power and composition of the different gas in the gas mixture, would involve the investigation of every parameter separately. However, in order to save time and reach the milestone, the influence of the different parameters has not been studied separately but most of the time several parameters have been changed at the same time in a logical manner. Since the samples are analysed and compared individually due to the conditions that cannot be exactly the same because of unwanted changes in the deposition conditions like arcing for instance, the interpretation is sometime complicate and slighlty cumbersome to read. When the injection level is not mentioned, the SRV value is given for an injection level of $1x10^{15}$ cm^{-3} which corresponds approximately to the injection of high efficiency silicon solar cells as seen in chapter 2. Since wafers are FZ-Si of 8000 ohm.cm ($2.6x10^{11}$ cm^{-3}) , the effect of fixed charge is to reduce SRV at low injection (cf chapter 3). Therefore, SRV reaches a maximum for high injection level. Although this maximum SRV does not correspond to the loss of power for normal condition (injection around $1x10^{15}cm^{-3}$), it enables us to determine the defect density and thus the quality of the film since defect influence is not

compensated although moderated by the fixed charge at high injection. However, it can be seen, on figure 6.1 that the evolution from samples 1 to 46 of SRV at 10^{15} cm^{-3} follows the evolution of the maximum SRV. Exceptionally, when there is a consequent difference between the two evolutions, the maximum SRV is mentioned.

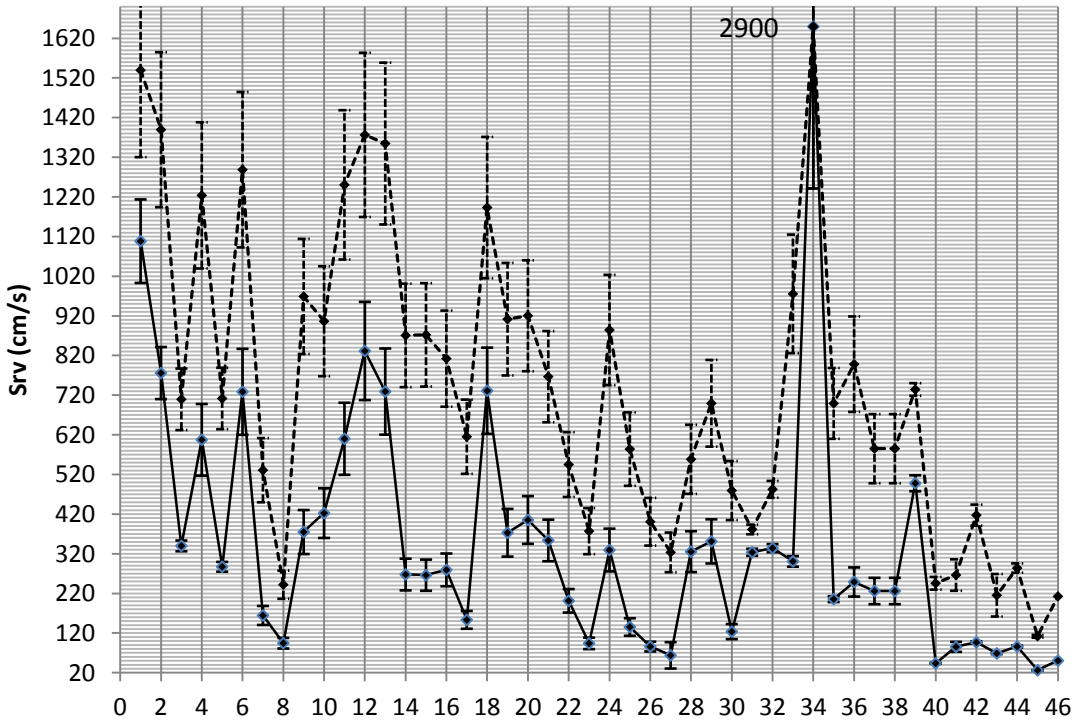

Figure 6.1 SRV for an injection level of 10^{15} cm^{-3} (plain) corresponding to one sun and maximal value of the SRV (dash) for samples 1 to 46.

6.1 PECVD a-Si:H films deposited with MW at 2.45 GHz

The first series presented on table 6.1 starts from sample 1 to sample 9. Passivating films are a-Si:H and are deposited with MW-PECVD. The range of the different parameters has been fixed in agreement with literature.

Sample N°	Pressure (Torr)	Temperature (°C)	ΔT (°C)	Power (W)	Mixture (sccm) SiH_4 : H_2 : Ar	Remarks	SRV (cm/s)	Growth rate (nm/min)
1	0.35	300	10	960	1 : 6 : 0	Flow of H_2 too high	1100	50
2	0.35	300	5	960	1 : 5 : 0	distance between electrode higher	776	x
3	0.35	300	5	1200	1 : 5 : 0	distance between electrode higher	340	70
4	0.35	280	50	1200	1 : 2.5 : 2.5	Arcing	610	x
5	0.7	315	40	1200	1 : 2.5 : 2.5		290	40
6	0.9	325	25	1200	1 : 2.5 : 2.5		730	x
7	0.9	330	50	1200	1 : 1 : 4		165	10
8	0.9	305	30	1200	1 : 0 : 5		95	x
9	1.2	325	30	1200	1 : 0 : 5	pressure between 1 and 1.5 torr	375	6

Table 6.1 Deposition parameters values, SRV and growth rate for MW PECVD processed a-Si:H films

Samples 1 to 3 are deposited almost in the same condition at a pressure of 0.35 torr and a gas mixture of SiH_4 : H_2 with the following proportion 1 : 5 sccm. The high value of the SRV for sample 1 is probably due to a too high H_2 to SiH_4 ratio (6 instead of 1). Indeed it can be seen on the following sample that the SRV decreases with the ratio. It has also to be noted that the distance between electrodes has been increased for samples 2 and 3 because it was first assumed that the high SRV (1100 cm/s) was due to a too low distance between electrodes. Indeed the passivation quality is better where there is a lower density of defects (cf. chapter 2) and a higher energy bombardment will induce more defects on the film. Although the bombardment energy is related to the velocity of the accelerated ions and thus depends on the electric potential between the electrodes, it has to be recalled that this potential is periodic. Therefore when changing the distance, the velocity changes. The SRV has effectively been reduced for sample 2 (760 cm/s) and in order to compensate the higher inter-electrode distance, the power has been increased to 100% (1200 W) for sample 3 resulting in a lower SRV (340 cm/s). Although SRV was improved, the distance between electrodes was not the real cause. Indeed, for a frequency of 2.45 GHz, it has been seen in chapter 6 that the acceleration of the ions does not follow the instant potential V(t) but the mean value and therefore bombardment increases with distance (ions are subject to a constant acceleration). As mentioned above, the reason for the very high SRV for sample 1 is probably due to a too high H_2 to SiH_4 ratio (6 instead of 5). Indeed it has been seen in chapter 5 that for passivation, amorphous films are wanted whereas microcrystalline structure arises for higher H_2 to SiH_4 ratio. It has also been seen in the same chapter that the phenomenon of silane depletion which suppresses the recombination reaction between SiH_4 and H leads to a strong increasing of H atoms at the film surface and to the etching of the film surface which results in a decreasing of the deposition rate and indeed the growth rate of sample 1 (50 nm/min) is lower than for sample 2 (70 nm/min) whereas the other conditions are similar. This fact drives us to reduce this ratio and in order to keep the total flow rate at a constant value, Ar has been added. For sample 4, SRV increases (610 cm/s) probably due to a too low temperature with a strong temperature drop indicated on table 6.1 by $\Delta T=50°C$ (it has to be noted that ΔT is equal to the initial temperature minus the final temperature) and arcing inside the chamber which is known to damage the film quality (cf. chapter 5). Although passivation quality is worse with high H_2 to SiH_4 ratio it can be seen that the temperature is more stable ($\Delta T \leq 5°C$) with a mixture with only H_2 and SiH_4. Ar induces electric discharges in the chamber (arcing) at high heating power and thus it is difficult to maintain high temperature. For sample 5,

pressure has been increased to 0.7 torr in order both to reduce the arcing and the bombardment and thus the defect density. Since pressure is the measurement of the ion impact occurrence, ion velocity can be reduced by increasing pressure, and SRV was reduced to 290 (cm/s). The reduction of the growth rate to 40 cm/s is probably due to etching by the ions Ar^+ [6.1] and indeed as can be seen clearly in table 6.1, the growth rate decreases when the Ar flow increases. The growth rate values suggest that the etching effect of Ar^+ is stronger than etching by H atoms which is probably due to the fact that Ar^+ ions are accelerated toward the film surface by the sheath voltage whereas it is not the case of H atoms and it is therefore necessary to increase the pressure in order to limit the impact energy onto the film surface. For sample 6, pressure was further increased to 0.9 torr but unexpectedly SRV increases (730 cm/s) probably due to arcing. In sample 7, H_2 to SiH_4 ratio has been reduced to 1 resulting in a SRV of 165 cm/s. This latter has been further reduced, by replacing the H_2 flow by Ar, to 95 cm/s. It has also to be noted that it is the best SRV obtained in this work at 300°C for a-Si:H. Regarding the fact that high temperature is the predominant condition for having good passivation i.e. low SRV, it would be interesting to use the same value for pressure (0.9 torr), gas mixture ([SiH_4: Ar] = [1: 5]), power (1200 W) and frequency (2.45 GHz) at 400°C.

For MW PECVD of a-Si:H at 1200 W and 300°C, SRV is lower when H_2 to SiH_4 is reduced to 1 or better when H_2 is totally replaced by Ar in parallel with the increasing of pressure until 0.9 torr.

6.2 PECVD SiN_x films deposited with MW 2.45 GHz

The second series (cf. table 6.2.) from sample 10 to 17 including 30 was deposition of SiN_x:H films with microwave PECVD from a gas mixture of SiH_4 and NH_3. Pressure was previously optimized at 0.8 torr.

Sample N°	Pressure. (torr)	Temp (°C)	ΔT (°C)	Power (W)	Mixture (sccm) $SiH_4 : NH_3$	Remarks	SRV (cm/s)
10	0.8	345	5	1200	1 : 6	quick drop of temperature	420
11	0.8	324	20	1200	1 : 12	quick drop of temperature	610
12	0.8	305	15	1200	1 : 5	temperature drop quickly until 290 °C	830
13	0.8	310	15	960	1 : 1.5 : 2.5*	powdery surface *addition of H_2	730
14	0.8	310	10	960	1 : 4		270
15	0.8	315	20	960	1 : 5		265
16	0.8	320	50	960	1 : 12		280
16B	0.8	320	50	960	1 : 15		810
17	0.8	300	10	1200	1 : 5		155
30	0.8	300	10	1200	1 : 10		125

Table 6.2 Deposition parameters values and SRV for MW PECVD SiN_x films

It is difficult to explain why SRV increases so highly from sample 10 (420 cm/s) to 12 (830 cm/s). The conditions of sample 12 and 15 are similar except that temperature is about 10°C higher for sample 15 and power is 80% the value of the power used for sample 12. There is also similar condition for sample 11 and 16 where initial temperature is around 370°C for sample 16 and 350°C for sample 11. Although the dropping of temperature is higher for sample 16 (ΔT=50°C), this dropping occurs during the whole time of deposition regularly whereas it occurs very rapidly for sample 11 at the beginning and remains at its lower level throughout the deposition. Since the last sample of the series (sample 17) corresponds to the lowest SRV of the series (155 cm/s), and was deposited at 1200 W and at 300°C, the higher power (1200 W) and the too low temperature (300°C) are not the reason for the higher SRV for sample 12 (820 cm/s) compared with sample 15 (265 cm/s at 960 W and 315 °C)) and sample 11 (610 cm/s at 1200W) compared with sample 16 (280 cm/s at 960 W). The cause of the high SRV is probably the quick dropping of the temperature at the beginning of the deposition. For the following sample, although temperature tends to decrease, this decreasing has been controlled by manually adjusting the heating power during the deposition in a way to avoid electric discharge. The relatively low SRV value for

sample 17 is probably due to the more stable temperature. By comparing maximum SRV, it seems that increasing the NH_3 to SiH_4 ratio to 12 reduces slightly the defect density. In order to confirm the benefit of higher ratio, conditions of sample 17 have been repeated for sample 30 except for the ratio which has been increased to 10. This has led to a small improvement of the SRV (125 ± 20 cm/s instead of 155± 20 cm/s) but this lower SRV compared to sample 17 can be due to uncertainty. Although the high ratio seems better for SiN_x:H MW-PECVD we cannot consider that parameters have been optimized except for pressure (0.8 torr.)

6.3 PECVD SiN_x films deposited with RF 13.56 MHz

The third series (table 6.3) starts from sample 18 to 29 including samples 31, 36, 37, 40 and 44 to 46. SiNx:H films have been deposited by RF-PECVD (13.56 MHz).

Sample N°	Pressure (torr)	Temperature (°C)	ΔT (°C)	Power (W)	Mixture (sccm) $SiH_4 : NH_3$	Remarks	SRV (cm/s)
18	0.2	290	10	10	1 : 9.5		730
19	0.2	300	1	7.5	1 : 5		370
20	0.8	295	5	20	1 : 7.5		405
21	0.5	300	3	15	1 : 5		355
22	0.8	300	3	20	1 : 7.5		200
23	0.8	345	10	15	1 : 10		95
24	0.2	350	30	15	1 : 5	arcing	330
25	0.8	360		20	1 : 7.5		135
26	0.5	300	2	15	1 : 5		85
27	0.5	345	5	10	1 : 7.5		65
28	0.8	340	5	30	1 : 10.5		325
29	0.8	340	1	30	1: 10		350
31	0.8	265	5	20	1 : 5		325
36	0.8	340	5	20	1 : 5		250
37	0.8	345	5	20	1 : 5		225
40	0.5	387	2	30	1 : 5		45
42	0.5	386	5	30	1 : 5		95
44	0.8	405	5	15	1 : 10		85
45	0.3	400	1	15	1 : 7.5		25
46	0.5	405	5	20	1 :10 : 2	Ar added by mistake	50

Table 6.3 Deposition parameters values and SRV for RF PECVD SiN_x films

For this series in order to save time, a method developed by G. Taguchi [6.2] has been adapted to find the optimum range for the external parameters. For a more extensive study of the effect of 4 parameters i.e. pressure, temperature, power and NH_3 to SiH_4 ratio, with 3 levels (table 6.4) for each parameter, 3^4 depositions are required. Using Taguchi method which limits the study to the first order effect, only 9 depositions are required (table 6.5). Indeed in this method, 2 couples of values (e.g. P_1 with T_1) cannot be repeated and therefore the correlations between parameters (2^d and 3^{rd} order effects) are not taken into account. It is equivalent to an independent study of the parameters' influence.

Level setting	pressure	Temperature	Power	Ratio
1	P1	T1	Pw1	R1
2	P2	T2	Pw2	R2
3	P3	T3	Pw3	R3

Table 6.4 Levels of the external parameters for PECVD deposition

Run	pressure	Temperature	Power	Ratio
1	P1	T1	Pw1	R3
2	P2	T2	Pw1	R1
3	P3	T3	Pw1	R2
4	P1	T3	Pw2	R1
5	P2	T1	Pw2	R2
6	P3	T2	Pw2	R3
7	P1	T2	Pw3	R2
8	P2	T3	Pw3	R3
9	P3	T1	Pw3	R1

Table 6.5 Parameters combinations for 3 levels and 4 parameters for PECVD deposition

Actually, the applied power does not follow exactly the Taguchi method on every sample. We would expect a more random evolution of the SRV if the method was strictly applied. Actually the evolution of the SRV is more oriented toward a decreasing because the setting of the parameters has been adjusted in order to reach a low SRV more rapidly. The 3 levels of the RF power which were 7.5,15 and 20 W have been increased to 10, 20 and 30 W. Sometimes deposition conditions have been also reproduced for several samples. For instance, samples 20 and 22 have been deposited with the same conditions. The first of this series, sample 18, shows the highest SRV (730 cm/s) of the series. For this sample, the NH_3 to SiH_4 ratio was 10 which corresponds to a NH_3 flow of 30 sccm, the RF power was 10 W, the temperature 300 K

and the pressure was 0.2 torr. The XPS analysed N to Si ratio in sample 18 is around 0.3 which is very low as can be seen on table 4.4. It has been seen that the NH_3 dissociation requires more energy than SiH_4. Here the power is relatively low compared to the high flow rate of NH_3 which is probably the reason for the poor N concentration in the film. The non reactive NH_3 seems to have a negative influence on the film quality. Firstly it seems difficult to explain why N content decreases when NH_3 flow is increased with a too low power. Indeed it is expected that the effect of having a low power would only be to reach a limit value for the fraction of dissociated NH_3 and thus for the N content in the film. Thus, it is expected that a too high NH_3 flow in regard with power would have a neutral effect. However, even if this excess of NH_3 is not dissociated it does not mean that it does not absorb power leading to a reduction of effective power for the gas dissociation. Indeed, the dissociation results from a high excitation of NH_3 bonds but even if the power is not enough for breaking these bonds, a part of the power can still be absorbed by the vibrating bonds of NH_3. Therefore we suggest that a too high NH_3 flow results in a decrease of the effective power. Sample 23 has also been deposited in a NH_3 flow of 30 sccm and although N/Si is 0.62 which is almost two times more than sample 18, the N concentration is still low since it is expected that the higher is the NH_3 to SiH_4 ratio, the higher is the N concentration in the film. Compared to sample 18, 3 factors explain the increasing of N/Si. The RF power is 15 instead of 10 W, the pressure is 0.8 instead of 0.2 torr and the temperature is 350 instead of 300°C. All these parameters increase the NH_3 dissociation; RF power and temperature provide more energy and increasing of pressure increases the dissociation probability. However, assuming that the N to Si ratio in the film depends on NH_3 dissociation, it seems that the fraction of NH_3 dissociated is lower than for samples 19, 21, 25 and 26 where the NH_3 to SiH_4 ratio is lower. Furthermore, sample 19 has the highest N/Si (0.72) and a NH_3 flow of 16 sccm which corresponds to the lowest NH_3 to SiH_4 ratio (5). Pressure (0.5 torr) and temperature (300°C) are lower than for sample 23 and thus provide less energy for NH_3 dissociation. However, the fact that N/Si is 0.72 shows that more NH_3 has been dissociated. The same remark can be made for samples 19 and 21 where the NH_3 flow is 16 sccm. Furthermore sample 19 uses the lowest RF power (7.5 W). For sample 16, N/Si is 0.67 for a relatively high NH_3 to SiH_4 ratio (7.5) which corresponds to a NH_3 flow of 24 sccm. However, the RF power (20 W), temperature (360°C) and pressure (0.8 torr) are high. Therefore we can deduce that for a too high NH_3 flow rate, the non reacted NH_3 has a negative effect on the incorporation of N in the film. It can also be noted from the XPS sample where thickness has been determined that N/Si decreases

with the deposition rate (figure 6.4.). Except for sample 22 which has the maximum deposition rate (10.3 nm/s) and relatively low SRV of 200 cm/s. The SRV decreases with the deposition rate which can be attributed to a too high deposition rate compared to the diffusion coefficient resulting in a non uniform film. Sample 22 is also the film with the lowest N incorporation (N/Si=0.49). It has also to be noted that sample 20 which has been grown with the same condition has a similar N to Si ratio (0.54) and a high deposition rate (8.5 nm/min) but a very high SRV (405 cm/s). Thus the N content of the two films and the high deposition rates during their deposition seem to be in agreement with the setting of the parameters. However it will be seen in the section 6.5 that although N content follows qualitatively what is expected (cf. figure 6.4), [N]/ [Si] is actually under evaluated. On the other hand it was expected a higher SRV for sample 22 due to its high deposition rate (10.3 nm/min). The SRV of sample 22 is lower because of a lower defect density. This can be seen in figure 6.2 where the SRV at high injection level is higher for sample 20. Regarding samples 21 and 26, the same remark can be made about SRV as is obvious in figure 6.3 but the incorporation of N is largely higher in sample 26. Regarding the fact that for almost all the SiN_x films deposited after sample 21, the SRV are lower, this improvement could be due to an amelioration of the system: the upper electrode has been redesigned.

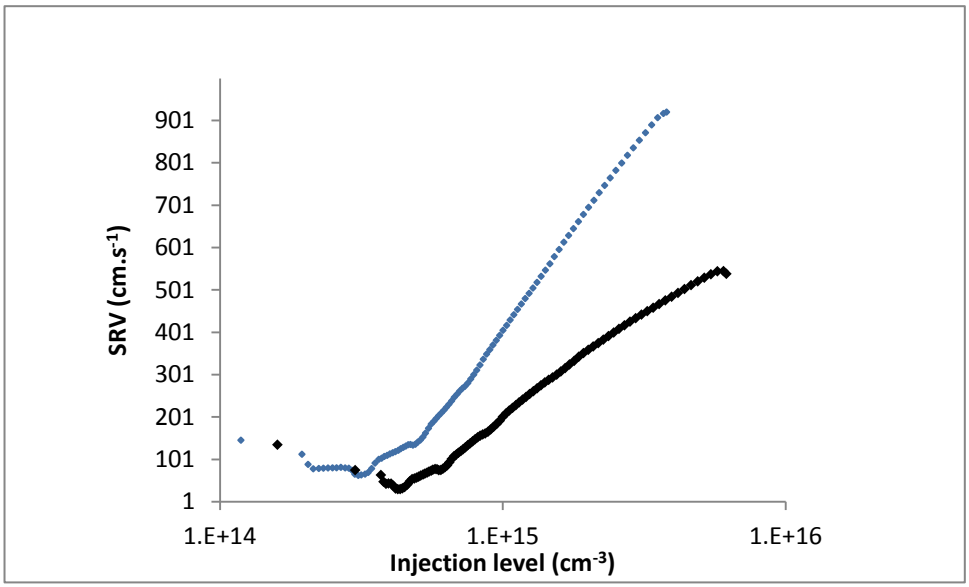

Figure 6.2 SRV versus injection level of sample 20 (in blue) and 22 (in black).This figure illustrates that the SRV of sample 20 is higher at injection level $\Delta n=10^{15}$ cm^{-3} because of a higher defect density. If it was due to a higher positive charge density, SRV for sample 22 would increase faster than for sample 20.

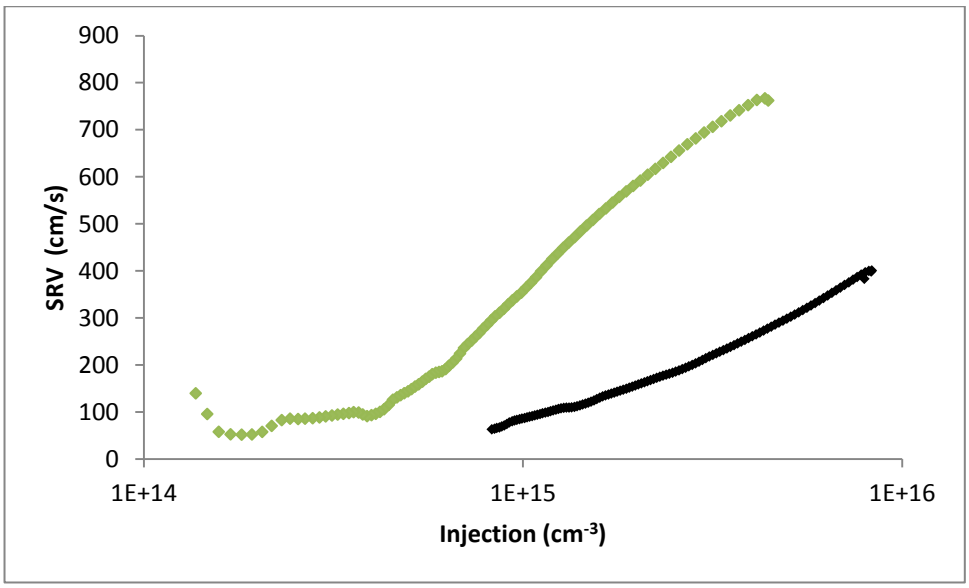

Figure 6.3 SRV versus injection level of sample 21 (in green) and 26 (in black). This figure illustrates that the SRV of sample 21 is higher at injection level $\Delta n=10^{15}$ cm^{-3} because of a higher defect density. If it was due to a higher positive charge density, SRV for sample 26 would increase faster than for sample 21.

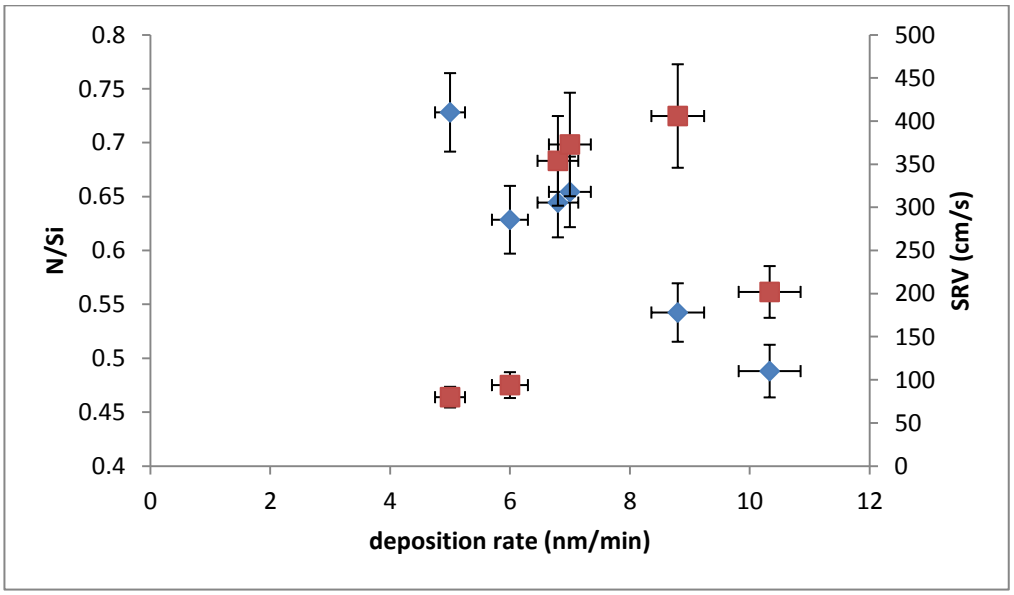

Figure 6.4 Evolution of N content (in blue) and the SRV (in red) versus deposition rate. N content in the film decrease with deposition rate whereas SRV increases. This figure shows that N incorporation and passivation quality are for low deposition rate.

The last samples of the series, samples 43 to 46 are deposited at 400°C. Over all the parameters, increasing temperature to 400°C especially improved the passivation

quality whatever the values chosen for the other parameters in agreement with what has been seen in chapter 5. However, reducing the pressure from 0.8 torr to 0.3 torr enables to reduce the SRV from 85 to 25 cm/s in agreement with the fact that for 13.56 MHz RF PECVD, having low pressure reduces the tensile stress. (Pressure has not been reduced to 0.2 torr in order to maintain temperature at 400°C since the plasma becomes too instable at low pressure.) Sample 45 is the lowest SRV of all of the samples. Its maximum SRV is 110 cm/s which correspond to a very low defect density. Although samples 40 and 42 have a low SRV, their maximum SRV are still high (245 and 420 cm/s) compared to samples deposited at 400°C. However, the temperature is only 25 °C higher for the 3 last samples which is relatively low and should not bring a consequent amelioration regarding the diffusion. However, since has been seen in chapter 5, hydrogen desorption becomes considerable near 400°C, the improvement is surely due to this latter phenomenon combined with a temperature high enough to provide a high diffusion. On contrary, if H desorption would occur with a too low diffusion, the dangling bond density and thus the defect density would increase drastically leading to a high SRV. Here, because of the high diffusion, species can stick to the dangling bond and remove the defects.

6.4 PECVD a-Si:H films deposited with RF 13.56 MHz

In the series from sample 32 to 35 (table 6.6), a-Si:H films have been deposited by RF PECVD following Taguchi method. Power was fixed at 30 W and therefore only 3 parameters are studied with 2 levels which required 4 runs. A last run, sample 43, has been added at 400°C using the best settings of the previous runs.

Sample	Pressure (torr)	Temperature (°C)	ΔT (°C)	Power (W)	Mixture(sccm) SiH_4 : H_2 : Ar	Remarks	SRV (cm/s)
32	0.2	250	10	30	1 : 1 : 2		335
33	0.5	300	10	30	1 : 1 : 2		300
34	0.2	250	10	30	2 : 1 : 1	Powdery sample	1650
35	0.2	300	10	30	2 : 1 : 1	Slightly Powdery sample	205
38	0.5	300	5	30	2 : 0 : 2		225
39	0.2	300	5	30	1 : 1 :2		500
43	0.8	400	10	30	1 : 1 : 2		70

Table 6.6 Deposition parameters values and SRV for RF PECVD SiN_x films

The lowest SRV of the Taguchi series from sample 32 to 35 is sample 35 with SRV of 205 cm/s. However on this sample the gas mixture is not appropriate, SiH_4 flow is too high which results in powder on the sample due to higher silane formation. Furthermore the maximum SRV of sample 32 (485 cm/s) is only 70% of the maximum SRV of sample 35 (700 cm/s) and this is actually the lowest maximum of the series after sample 43. The fact is that mixture 2: 1: 1 is not appropriate. This is more obvious at low temperature (250°C). Lowering the pressure until 0.2 torr seems to decrease the SRV. Although SRV of sample 32 (335 cm/s) deposited at 0.2 torr is very slightly higher than SRV of sample 33 (300 cm/s) deposited at 0.5 torr, the maximum SRV of sample 32 (485 cm/s) is much lower than for sample 33 (975 cm/s). Therefore the defect density of sample 32 is much lower than in sample 33 (this is the only case of all the samples presented on the figure 6.1. where the evolution of SRV at $1x10^{15}cm^{-3}$ is so opposite to the evolution of the maximum SRV). For 13.56 MHz RF PECVD of SiN_x film, lowering the pressure is necessary for increasing the bombardment energy and thus for reducing the tensile stress. It can be assumed that the same process is involved for RF a-Si:H. However, for the added sample (sample 43) of the series, a high pressure was necessary in order to maintain temperature at 400°C with a heating power low enough to avoid electric discharges. Indeed it has been seen that for the MW PEVCD, the presence of Ar induces more electric discharges and instability in temperature. This last sample has the lowest SRV of the a-Si:H samples (70 cm/s) with a maximum SRV of only 215 cm/s showing that the defect density is very low. Regarding the added samples, 38 is deposited in the same conditions as sample 33 but H is replaced by Ar. As for MW PECVD, the replacement of H improves the SRV (225 instead of 300 cm/s). On the other hand it is difficult to explain why SRV is so high (485 cm/s) for sample 39 whereas it was expected that lowering the pressure and changing the gas mixture would result in an improvement. However the maximum SRV of 39 (735 cm/s) is very close to the maximum SRV of sample 35 (700 cm/s). Furthermore, for samples 32 and 39 the SRV versus injection on figure 6.5 do not show a fixed charged effect as strong as for samples 33 and 35. Therefore the lower values for samples 33 and 35 at 10^{15} cm^{-3} are due to a higher fixed charge density and not to a lower density of defects.

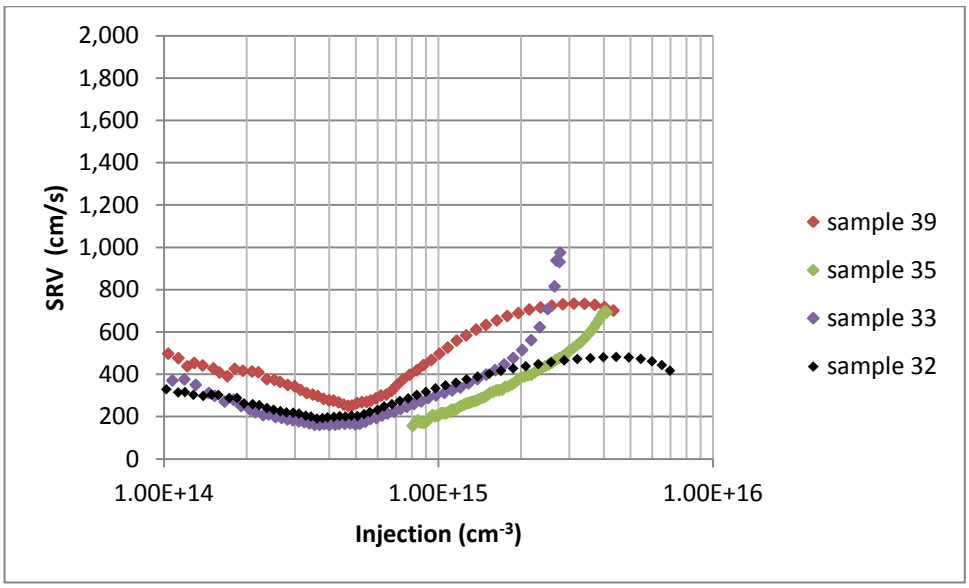

Figure 6.5 SRV of samples 32, 33, 35 and 39 versus injection level. SRV is strongly reduced and until higher injection level for sample 33 and further more for sample 39 than for samples 32 and 39. This is due to a higher fixed charge for sample 33 and even higher for sample 35. The lowest defect density is for sample 32 then sample 39, 35 and 33. The higher defect density of sample 33 can be seen by the stronger increase of the SRV at higher injection level.

In conclusion, films deposited with a gas mixture of NH_3 and SiH_4 at 13.56 MHz present the best passivating quality with a lowest SRV of 25 cm/s. Although a high temperature of 400°C is the predominant condition, furthermore reducing the pressure to 0.3 torr is required. Temperature of 400°C is also the most important condition for RF PEVCD a-Si:H films giving an SRV of 70 cm/s. This is due to the fact that high temperature provides the combination of a high diffusion of the species adsorbed onto the film surface and the occurrence of hydrogen desorption: regarding the fact that for temperature lower than 300°C, low pressure improves the passivation quality, it will be interesting to make deposition of a-Si:H at 400°C with a lower pressure if the problem of temperature stability can be solved. Indeed for SiN_x films deposited at 400°C and 0.8 torr, the SRV was 85 cm/s. Therefore we can expect SRV as low or lower than that with SiN_x at 0.3 torr.

6.5 Determination of N content in the film and porosity

Table 6.7 presents the PECVD parameters and the results of N to Si ratio in the films determined by XPS. The results for the films deposited at 2.45 GHz shows that when the power is high enough for dissociating NH_3, the nitrogen content in the film increases as expected.

Sample	Pressure(Torr)	Power (W)	NH3/SiH4	T (°C)	TYPE	N/Si
13	0.8	960	1.5	310	MW	0.08
16	0.8	960	12	320	MW	0.63
16B	0.8	1200	15	320	MW	0.72
17	0.8	1200	5	300	MW	0.65
18	0.2	10	10	290	RF	0.33
19	0.2	7.5	10	300	RF	0.65
20	0.8	20	5	295	RF	0.54
21	0.5	15	7.5	300	RF	0.64
22	0.8	20	7.5	300	RF	0.49
23	0.8	15	10	345	RF	0.63
24	0.2	15	5	350	RF	0.57
25	0.8	20	7.5	360	RF	0.68
26	0.5	15	5	300	RF	0.73

Table 6.7 PECVD conditions and [N]/[Si] determined by XPS

The comparisons of the refractive index values determined by ellipsometry has led at the end of chapter 4 to the determination of porosity in samples 16, 16B, 19-23 and 26. However it has been concluded that the high corresponding porosity cannot be in agreement with the low SRV values. These results suggest that the values of N to Si ratio in the films determined by XPS are not accurately determined. The refractive index of samples 16 and 16B correspond to Si_3N_4 which results from the fact that the Tauc-Lorentz function corresponds to Si_3N_4 as can be seen on table 4.1. Furthermore, table 4.1 shows that the thickness of these two samples is very low (respectively 11 and 4.5 nm) which is due to a low deposition rate (1 and 0.5nm/min). It is reported in reference [5.47] that a low NH_3 to SiH_4 ratio results in low refractive index, higher porosity, higher deposition rate and low nitrogen content in the film. The low refractive index actually resulted in higher porosity since low nitrogen content should lead, if there were no porosity, to high refractive index. The porosity is itself due to high deposition rate since as seen in chapter 5, when the deposition rate is too high the diffusion of growth precursor is too low. Samples 16 and 16B combine both very low deposition rate with highest refractive index of the series and highest NH_3 to SiH_4 ratio as can be seen on table 6.8 and thus it is very probable that these films are effectively close to a Si_3N_4 structure and present a negligible porosity. On table 6.8, the 3rd and 4th columns present the value of [N]/ [Si] in the films and the corresponding refractive index determined with equation 4.97. The 5th and 6th columns present the value of the refractive index determined by ellipsometry and the corresponding [N]/ [Si] for a film without porosity. Sample 16B corresponds to the highest NH_3 to SiH_4 ratio and the lowest deposition rate. Furthermore the dielectric function of this film is very close to Si_3N_4. For this sample

[N]/ [Si] is equal to 0.73. Although it is a strong assumption, we suggest that the value of [N]/ [Si] determined by XPS should be corrected to be 1.33 which is the [N]/ [Si] value for Si_3N_4. Therefore we assume that the [N] to [Si] ratio determined by XPS is under evaluated for every samples and has to be multiply by 1.33/0.73.

Sample N°	NH3/SiH4	$(N/Si)_{XPS}$	nf XPS	nf ellipsometry	N/Si ellipsometry
16	12	0.63	2.52	2.04	1.07
16B	15	0.72	2.38	2.01	1.16
19	10	0.65	2.48	1.80	1.63
20	5	0.54	2.71	1.80	1.64
21	7.5	0.64	2.50	1.78	1.72
22	7.5	0.49	2.87	1.82	1.58
23	10	0.63	2.53	1.82	1.57
26	5	0.73	2.37	1.84	1.50

Table 6.8 [N] / [Si] and corresponding refractive index determined by XPS and ellipsometry.

The corrected values of [N]/ [Si] are presented on table 6.9. The refractive index has been calculated with equation 4.97 and the porosity with equation 4.98. The resulting porosity is low enough to allow good passivation in agreement with our SRV measurements.

Sample	N/Si	n_{th}	Porosity
16	1.16	1.99	0.05
16B	1.33	1.91	0.00
19	1.20	1.97	0.17
20	1.00	2.09	0.27
21	1.18	1.98	0.20
22	0.91	2.17	0.30
23	1.16	1.99	0.17
26	1.35	1.90	0.07

Table 6.9 [N]/ [Si], corresponding refractive index and porosity after correction

The ellipsometry fitting has been done after conversion of the Tauc-Lorentz function by EMA with void fraction corresponding to the value of porosity on table 6.9 and Tauc-Lorentz material with all parameters setting at the values of Si_3N_4 except the amplitude A. Table 6.10 presents the new value of amplitude A, refractive index and MSE.

Sample N° (Porosity)	Amplitude A	n_f without porosity	MSE (chapter 4)	MSE
16 (5%)	139.8	1.99	1.7	1.7
19 (17%)	124.3	1.91	1.0	1.0
20 (27%)	176.1	1.97	5.9	5.5
21 (20%)	142.8	2.09	4.2	4.6
22 (30%)	184.4	1.98	13.2	10.3
23 (17%)	146.6	2.17	2.1	1.9
26 (7%)	123.1	1.99	5.8	6.3
44 (29%)	152.5	2.12	16.8	14.1
45 (17.8%)	144.3	2.08	4.0	2.3

Table 6.10 Ellipsometry results after addition of porosity

The MSE has been in general slightly reduced. Porosity has then been determined by ellipsometry for samples 44-46 which result in a good improvement of MSE. Table 6.11 gives the corresponding values of x in SiN_x.

SAMPLE N°	x
44	1.17
45	1.01
46	1.09

Table 6.11 value of x for SiN_x

Sample 45 has the lowest SRV probably due to the fact that the pressure is lower than for samples 44 and 46 which reduce the tensile stress and the porosity. However its N content is still too low and it will be interesting to repeat the deposition in a future work with higher NH_3 to silane ratio.

This study shows that SiN_x samples present a mean porosity of 20.5% and up to 30%. As expected samples 45 and 46 have porosity lower than the mean porosity since higher temperature improves diffusion. However, it is difficult to explain why sample 44 has a high porosity of almost 30%. It is also the sample with the highest SRV of samples grown at 400°C. The lowest SRV have a dielectric function closer to Si_3N_4. For instance samples 45 and 46 have amplitude around 143 which is not very far from the Si_3N_4 amplitude equal to 131.636 (cf. chapter 4 section 4.7).

The structure of the films has been estimated and all the samples are located in the region of Si-rich films. However the best SRV correspond to the highest values of x. Elmiger has reported on a study of the in-situ carrier lifetime measurement of the

lifetime during PECVD deposition of SiN_x films that the lifetime decreases strongly at the beginning of the film deposition and then increases until reaching 30 nm thickness where lifetime remains constant [6.3] . The high value of SRV (810 cm/s) for sample 16 B is certainly due to its very low thickness (4.5 nm). Sample 16 which has a thickness a bit higher (11nm) provides a value of SRV as low as 280 cm/s and indeed the thickness of samples 16B and 16B are in the range of the increasing of the lifetime reported by Elmiger. Therefore, we can expect by increasing the deposition time to have a very low SRV. The predominant factor for having this stoichiometric film is a high NH_3 to silane ratio combined with a high power in order to provide NH_3 dissociation and a low deposition rate which enables the diffusion process. However from an industrial point of view having a too long deposition time is not wanted since it involves a higher consumption of energy and a lower production volume.

Regarding a-Si:H samples, the porosity suggested by the fact that some values for the dissociated SiH_4 fraction are higher than 100% on table 5.2 is confirmed by these results. Indeed the porosity should be higher for a-Si:H film because deposition rate is higher than for Si_3N_4. It would be interesting to fit the Cody-Lorentz function of a-Si:H films by adding porosity as an 8^{th} parameter. However, since porosity is largely related to the diffusion which changes with temperature, the porosity of the film is surely also graded due to any decreases of temperature during a-Si:H deposition (cf table 6.1 and 6.7). Furthermore it is expected that porosity is higher near the top of the film. Since a-Si:H films have a lower passivating quality than SiN_x and are harder to fit by ellipsometry, the investigation of porosity has been omitted.

Finally, after optimization of PECVD conditions for films deposited on Fz 8000 ohm.cm wafers, 3 films labeled 2527, 2530 and 2532 have been deposited on Cz 1 Ohm.cm wafer. SiN_x films have been deposited at 13.56 MHz with the optimal conditions used for sample 45. These conditions have not been changed because films on Cz wafers have been deposited before deducing that higher NH_3 to silane ratio should improve passivation.

6.6 PC1D simulations

On figure 6.6, the evolution of the injection level (or excess carrier concentration) versus distance from front of the solar cell is represented. As explained in chapter 2 these values have been calculated in order to fix the value of S_0 for the calculation of SRH recombination rate. For Cz 1ohm.cm wafer, the injection level is around $3.5x10^{14}$ cm^{-3}.

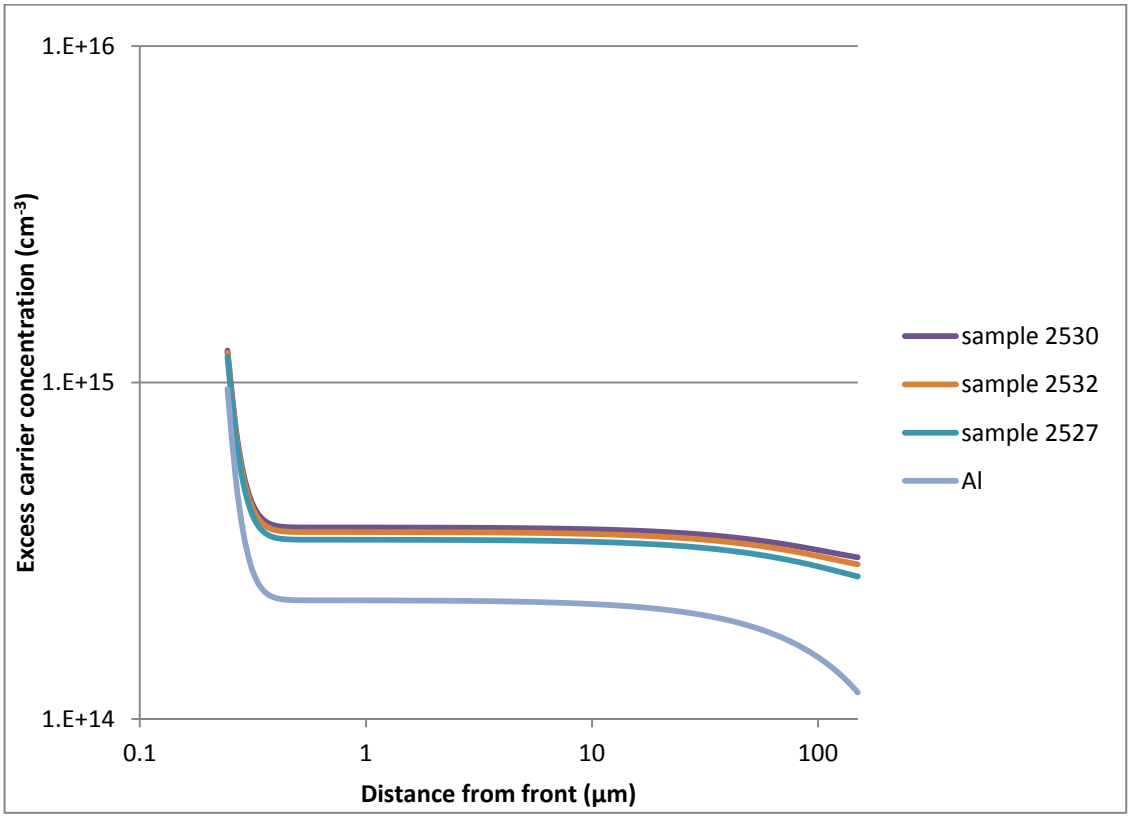

Figure 6.6 Excess carrier concentration generated by light for a one sun AM 1.5 G spectrum (corresponding to sun illumination in real conditions). Sample 2527-2530 and 2532 are 1 ohm.cm wafers coated with SiN_x PECVD.

Figure 6.7 represents the results of the PC1D5 simulation with an illumination of one 1sun and an AM 1.5G spectra. The details have been explained in chapter 2. The SRV values at $3.5x10^{14}$ cm^{-3} for Cz wafers in agreement with the injection level at one sun which is represented on figure 6.6.

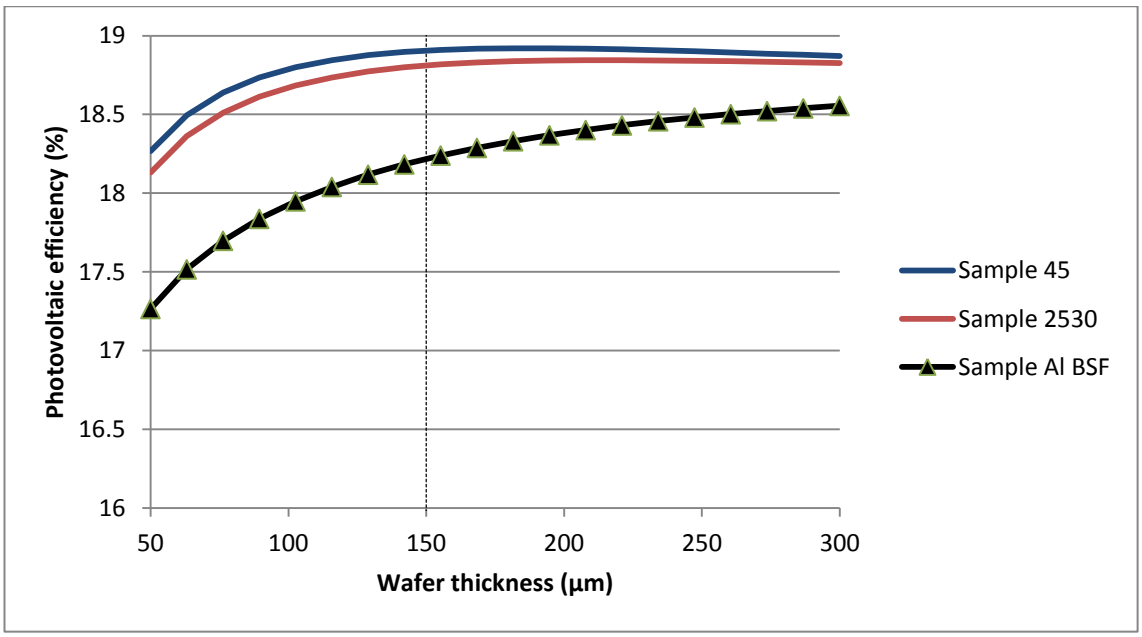

Figure 6.7 Photovoltaic efficiency versus wafer thickness for SiN_x films deposited by PECVD on 1ohm.cm Cz wafers. The curve for sample 45 is actually the photovoltaic efficiency that would be obtained for a Cz 1ohm.cm wafer coated with a film with characteristic of sample 45 (cf. figure 3.49 in chapter 3). Sample 2530 characteristics are given on figure 3.51. Sample Al BSF corresponds to Cz 1ohm.cm wafer coated with Al. The highest efficiency is almost 19% at 150 µm and corresponds to an improvement of 1.7% compared with Al BSF.

On this work, it has been shown that LGBC Si solar cell with a thickness equal to 150 µm instead of 300µm can provide an efficiency of almost 19% after deposition of SiN_x film by PECVD on Cz 1 ohm wafer. This represents on improvement of 1.7% compared with passivation with Al coating. The simulation which gives the highest efficiency corresponds to a Cz 1 ohm.wafer coated with a film which has a maximum defect of $1.47x10^{11}$ $cm^{-2}.eV^{-1}$ and a fixed charge density Q_f of 10^{11} cm^{-2}. This film provides a passivation with a SRV of 295 and 200 cm/s respectively at an injection level $\Delta n=3.5x10^{14}$ and 10^{15} cm^{-3}. A record-low SRV of 4 cm/s at $\Delta n=10^{15}$ cm^{-3} has been obtained by A.G. Aberle [3.1] with PECVD SiN_x passivation on 1.5 ohm.cm wafers. However the values of the defects parameters given in reference [3.1] are a film with a maximum defect density equal to $3.5x10^{10}$ $cm^{-2}.eV^{-1}$ and a fixed charge Q_f of 10^{11} cm^{-2} which corresponds to a SRV of 68 cm/s at $\Delta n=10^{15}$ cm^{-3}. The best SRV in this present work is thus 50 times higher than the world record-low SRV but only 4 times higher than the usual SRV values. Moreover our SRV value is low enough for achieving the goal of this work that is keeping high efficiency (19%) with a thin silicon wafer.

BIBLIOGRAPHY OF CHAPTER 6

[6.1] J.Zhu *et al.,* Plasma pretreatment on Si(111) substrates for the growth of ZnO thin films, J.Cryst.Growth 303, 655-658 (2007)

[6.2] G.Z Yin *et al.*,Orthogonal design for process optimization and its applications in plasma etching, Solid State Technology, 127-132(1987)

[6.3] J.R. Elmiger *et al.,* Investigation of Silicon Nitride films for Silicon Solar Cells, MRS Proceedings, 426, 129 (1996)

Chapter 7

<Conclusions>

7.1 Highlights of the thesis

A part of the research work for this thesis took place in the context of a jointly funded project by EPSRC/TSB and the National Renewable Energy Center (NaREC) of the U.K. for contributing to the improvement of the PV technology based on silicon solar cells by reducing the manufacturing cost and silicon consumption. One of the requirements for achieving this goal is a high passivation quality on the rear surface of the wafer. The aim of this work was to optimise PECVD conditions for silicon-based films in order to produce passivating coatings on the rear surface of silicon wafers, in the future for lower thickness LGBC solar cells without a loss of photovoltaic efficiency. Although SiN_x and a-Si:H high quality passivating films with very low SRV have been deposited in the past by different groups after optimisation of the deposition parameters, their results depend on the type of PECVD system used. Indeed if industrial systems are quite standard, the experimental systems used in research are not and extended over a large range. Thus it is not enough to reproduce the deposition conditions by using the parameter values mentioned in the literature. On the other hand since very good results have already been obtained with some PECVD systems worldwide it was not interesting to limit our work to the optimisation of the deposition conditions only to our system. Therefore even if the first goal was to find the required parameters for having low SRV under 1 sun illumination, it was required to understand as much as possible why having these values is necessary. It was also required to have a criterion which does not depend on a particular PECVD system but allows adaptability to others.

Passivation quality resulted from PECVD conditions but it is not possible to optimise directly the PECVD parameters from interpretation of passivation quality. However, passivation quality is directly related to film structure and film structure itself can be understood from PECVD conditions. Film structure is thus the link between PECVD condition and passivation quality. Chapter 3 was focused on passivation quality which has been determined by the mean of SRV measurement. Chapter 4 described the film structure which has been estimated from ellipsometry and XPS. Chapter 5 was mainly a review of PECVD a-Si:H and SiN_x films for optimisation of PECVD parameters.

The expected PV efficiency for a silicon solar cell with rear surface passivated with a-Si:H and SiN_x film has been determined in chapter 2 by using public software –PC1D-5- for the simulation of LGBC solar cell behaviour in order to investigate the evolution of the PV efficiency with the wafer thickness at different passivation quality that is different value of the SRV.

The comparison of simulations and experimental results in chapter 3 have led to the estimation of defect density in the film and fixed charge density at the interface of the silicon wafer and the film. Moreover, it has shown when the SRV value was increased or decreased by this fixed charge. Indeed, for low injection level, depending on the ratio between this fixed charge concentration and the doping concentration, there is either an accumulation of charge carrier at the surface or a repulsion leading to inversion that is when minority carrier concentration becomes higher than the majority carriers. In this latter case SRV is drastically reduced. On the other hand, when there is charge carrier accumulation the SRV increases. At high injection level when the fixed charge effect can be neglected in regard to excess carrier concentration, the SRV tends toward a constant value. At this high injection level the value of the SRV is directly related to the defect density. The value of the fixed charge density (around $1x10^{11}$ cm^{-2}), is in the same range for all of the samples, both a-Si:H and SiN_x films, thus the value of the fixed charge is probably intrinsic to the interface between Si and a-Si alloy films.
At this stage, the film parameters have been determined by fitting the experimental values with the theoretical SRV expected with SRH theory. This theoretical SRV has been obtained from a computer code implemented for this work.

Another aspect of this work was the optimisation of the PECVD conditions for a-Si:H and SiN_x passivating film. It has been shown that using SiN_x was better for achieving this goal mainly regarding the film characterisation by ellipsometry. The structure of a-Si:H film varies with film depth because it is difficult to keep temperature at a constant value with the gas mixture used for a-Si:H deposition. The a-Si:H films are more difficult to characterise than SiN_x films since 7 parameters are required whereas only 4 for SiN_x films and the parameters values of the Tauc-Lorentz dielectric function of SiN_x films can be interpreted in a more systematic way and the structure of these films can be "monitored".
Furthermore it is known that Si_3N_4 film provides the best passivation with SiN_x film. A simple method using spectroscopic ellipsometry has been thus developed for checking if

our SiN_x film was close to Si_3N_4 whereas the precise deduction of x in SiN_x would require and extended knowledge of the dielectric function parameters and other characterisation techniques. This method consists on setting all of the dielectric function parameters to the values corresponding to Si_3N_4 except the amplitude of the dielectric function which has to be fitted to the experimental values determined by ellipsometry. If the amplitude is close to the Si_3N_4 amplitude value that means that the film structure is close to Si_3N_4.

Regarding PECVD conditions our experimental values show that the optimal conditions are a low pressure for reducing tensile stress but high enough to maintain a stable temperature, a NH_3 to silane ratio high enough to produce N-rich SiN_x films and a RF power high enough to dissociate NH_3 molecules. However the most important parameter is temperature which has to be maintained at 400°C in order to ensure both high diffusion of the growth precursor and hydrogen desorption. This confirms what has been previously shown by other authors, particularly Schmidt and Vetter. Furthermore a very important technical point is the fact that in order to reach this temperature of 400°C without damage caused by electrical discharge in the deposition chamber, the heating voltage should be very well isolated from the RF or MW power in order to avoid electrical arcing. More generally, pressure has to be as low as possible for reducing tensile stress and film roughness but high enough to maintain the temperature at 400°C. High NH_3 to silane is required combined with a high enough power to ensure the dissociation of NH_3 since better passivation is expected for N-rich SiN_x films. An important point is the fact that in RF PECVD the NH_3 flow required for having a high dissociation is limited by a low RF power. We have suggested, based on N/Si measurement by XPS that it is due to the fact that a part of the power is lost by absorption by vibrating bonds of non-dissociated NH_3. On the other hand high power provided by MW PECVD combined with high NH_3 to silane ratio has led to films close to stoichiometry at 300°C. Furthermore these latter films have a very low porosity. However due to very low deposition rate, the film thickness was too low to provide low SRV. It will be very interesting to repeat the deposition with the conditions of sample 16B at 400°C in a future work.

Finally, the possibility of having a SRV of 295 cm/s at an injection level corresponding to an intensity one sun ($\Delta n=3.5x10^{14}$) has been demonstrated. This corresponded to a film passivated with a maximum defect energy level density of $1.5x10^{11}$ $cm^{-2}.eV^{-1}$ and a fixed charge density Q_f equal to $2x10^{11}$ cm^{-2}.

This film provides a passivation with a SRV of 200 cm/s for $\Delta n=10^{15}$ cm^{-3} whereas the record-low SRV is 4 cm/s at $\Delta n=10^{15}cm^{-3}$.On the other hand the SRV value (order of magnitude of) our film is close to the usual range of high passivation with SiN_x (10-100 cm/s) and is low enough for achieving the goal of this work that is keeping high efficiency (19%) with a thin silicon wafer.

The main contributions arising out of this work are:

- An adaptation of the method used in PC1D-5 to film wafer passivated with a-Si:H and SiN_x film. Indeed, this software uses the SRH theory for simulating the recombination behaviour via a single defect energy level whereas defect in a-Si:H and SiN_x film generates a quasi-continuum defect level distribution in the bandgap. Furthermore a fixed charge density Q_f at the interface between the silicon substrate and the passivating film can change the recombination rate by several order of magnitude depending on the value of Q_f the doping of the substrate and the ratio between the electron and the hole capture cross section Thus the method used for recombination in PC1D-5 has been extended to include the fixed charge density influence and the energy level distribution.

- The introduction of two quantities, that we have called electron capture probability section and hole capture probability section, is an efficient mean for describing and understanding the SRV evolution with the injection level for interface with a fixed charge density and energy level distribution in the bandgap. The research efforts have resulted in the proposition of a new method for determining the parameters of defect level Gaussian distribution from the SRV function with injection level. This method which consists of comparing the experimental SRV values of a PECVD film deposited on 3 wafers having respectively a low an intermediate and a high doping should be implemented in a further work.

- An adaptation of Sinton photo conductance decay measurement to the direct determination of SRV without the mediation of minority carrier lifetime. This enables to extend the SRV measurement to a wider range of injection level.

- A rapid method for estimating how close is the structure of a SiN_x films from Si_3N_4 structure.

7.2 Future directions

Although some significant outcomes of the research efforts have been listed in the previous section, it is felt worthwhile to describe some of the offshoots that could well be taken up at a later stage for additional contribution. Some of these aspects are described as below:

First of all the determination of the parameters of the Gaussian distribution of defects energy levels could be improved by the method described in section 3.8 of chapter 3.

Regarding spectroscopic characterisation, using ellipsometry, it will be interesting to push further the determination of the Tauc-Lorentz parameters in order to have a better estimation of the SiN_x composition this would require a better understanding of the physical meaning of the model parameters, particularly the bandgap energy E_G, the resonance energy $E_{n0,}$ and the broadness C of the corresponding peak. The relation between E_G and the N content of SiN_x films is already well established in literature as well as its connection with hydrogen content. It would be interesting in a further work to study the link between the dielectric polarisation modes of vibration and E_{n0}, and between the broadness of the peak C and the statistics of the atom configurations in the vicinity of Si.

Regarding the optimisation of PECVD conditions for SiN_x deposition, it has been assumed in chapter 6 from XPS results that when the NH_3 to SiH_4 is too high with respect to RF or MW power, the non dissociated NH_3 does not only acts as an inert gas but absorbs a part of the RF power which results in a decrease of dissociated NH_3. It would be interesting to do an extensive investigation of NH_3 to SiH_4 ratio with respect to RF power in order to determine the percentage of absorbed power when NH_3 concentration is increased for a fixed SiH_4 concentration and RF power.

Finally it is necessary to manufacture LGBC solar cell with rear surface passivated with SiN_x film in order to confirm the results of the simulation.